Inversion of Disorder Signatures in Complex Systems



Fábio Rangel Duarte Filho

A thesis submitted for the degree of
Doctor of Philosophy

School of Physics
Trinity College Dublin

2025

Declaration

I, Fábio Rangel Duarte Filho, hereby declare that this thesis has not been submitted as an exercise for a degree at this or any other university and it is entirely my own work; That I was involved in a number of collaborations, and where it is appropriate my collaborators are acknowledged for their contributions.

I agree to deposit this thesis in the University's open-access institutional repository or allow the Library to do so on my behalf, subject to Irish Copyright Legislation and Trinity College Library conditions of use and acknowledgement. I consent to the examiner retaining a copy of the thesis beyond the examining period, should they so wish (EU GDPR May 2018).

Fábio R. Duarte Filho
November 25, 2024

Abstract

In an attempt to understand nature, we are constantly seeking the causal factor behind everyday observations. We categorise this kind of endeavour as an inverse problem - the problem of inverting the arrow of time, the direction of measurement, to understand the instrumental parameters that brought a system into its current state. In this thesis, we will approach inverse problems in the realm of condensed matter physics to devise a methodology capable of revealing the primary factors behind observed spectral signals. With this method, we will be able to identify the structural properties of a variety of systems from the nano to the mesoscopic scale, revealing the different types of disorder found within.

In particular, we will approach two major systems - the transition metal dichalcogenide (TMD) Molybdenum Disulfite (MoS_2), and the neuromorphic random nanowire network of memristors. After having established the theory to approach disordered crystals, we will apply the devised inversion methodology to recover the concentration of chalcogen vacancies in the MoS_2, the most common type of disorder in this system. This will be done for a variety of quantities including a qualitative inversion of experimental measurements. Later we will analyse this system with an extra level of complexity by introducing $AuCl_3$ coordinated complexes on the TMD surface as disorder. The weak effect that this scatterer has in the spectral functions offers a challenge to our inversion method. By performing this inversion, we will probe the reliability of the methodology. Finally, we will shift gears into treating nanowire networks of memristors that can assume a particular conductive behaviour denominated "winner takes all", where the sourced current travels through one single path within the network. We will identify and characterize the network parameters responsible for this neuromorphic behaviour and predict its occurrence.

The work presented in this thesis contributes to the development of research on inversion problems in condensed matter physics and opens the door for

quantitative work in the field of inversion, as well as for tackling the inverse problem of signal-based material design. By obtaining domain over the field of inverse problems, we are one step closer to observing and controlling matter to our will.

Publications

Publications resulting, partially or wholly, from this work:

- **F R Duarte**, S Mukim, A Molina-Sánchez, Tatiana G Rappoport and M S Ferreira
  Decoding the DC and optical conductivities of disordered MoS_2 films: an inverse problem
  New J. Phys. **23** 073035 (2021)

- **F. R. Duarte**, S. Mukim, F. Matusalem, D. Grasseschi, A. R. Rocha, Leandro Seixas, Christiano J. S. de Matos and M. S. Ferreira
  Decoding disorder signatures of $AuCl_3$ and vacancies in MoS_2 films: from synthetic to experimental inversion
  J. Phys.: Condens. Matter **36** 495901 (2024)

- **F. R. Duarte**, S. Mukim, C. G. Rocha and M. S. Ferreira
  Identifying Winner-Takes-All Emergence in Random Nanowire Networks: an Inverse Problem
  Physical Chemistry Chemical Physics (2024) DOI: 10.1039/D4CP03242J

Acknowledgements

First and foremost, I would like to express my respect and gratitude to Prof. Mauro Ferreira, who was my supervisor during this PhD program. Mauro always demonstrated great engagement and exemplary commitment to the realisation of science - be it in health or while facing serious illness - all while never abandoning his good and light humour. His scientific integrity is something to aspire to in an academic career. Thanks to his availability and flexibility I managed to conclude this PhD that started in the midst of a global pandemic. In this theme, I extend my gratitude to Dr Shardul Mukim, my senior in the theory and modelling group, who was also always available to help me and ready for engaging discussions.

The work done here in Ireland was also only possible thanks to the support I had in Brazil during my upbringing and the support given here by my lovely wife. Even while far from home, I could always count on the care offered by my mother, so I also express my respect to her and my late father, who provided a strong foundation which allowed me to pursue this academic realisation.

Needless to say, I write this thesis today because I stand on the shoulders of the great giants of the past, who laid down the scientific principles and technology that enabled the realization of this research. Hence, I also pay my respects to them. This work was also possible thanks to all the collaborators I had all over the world. I give my thanks to Felipe M. and Daniel G., and their respective supervisors Dr. Alexandre R. and Dr. Christiano M. Special thanks go to Prof. Tatiana R., my Master's degree supervisor and Prof. Claudia G., who engaged thoroughly with our group in the research of neuromorphic devices.

Last but not least, I offer my deep and sincere respects to my beloved Gurudeva Shrii Shrii Anandamurti, whose intuitional science offered me a practice that, among other realizations, gave me the mental fortitude necessary to tackle one of the most difficult subjects of science.

List of Figures

1.1 Illustration of the deconvolution process showing the original, the convoluted image with a Gaussian blur and the result of the deconvolution using Point Spread Function, an analytical inverse technique commonly used in biological microscopy based on the wave behaviour of light (which causes the ringing at the edge of the image) [14]. 5

2.1 Infinite linear chain in the pristine case (**a**) and with one in the case with one disorder (**b**). The disordered case can be interpreted as one device D connected on the left and on the right by semi-infinite leads LL and RL. 16

2.2 Semi-infinite left lead (LL) connecting its semi-infinite surface Green's function ($g_{00} = SGF$) to the surface Green's function g_{11} of the device (D) via perturbation $\hat{V}$ from the unperturbed state (**a**) to the perturbed one (**b**). 21

2.3 Principal planes for different dimensions. 24

2.4 First steps of the iterative calculation of the Green's function of the device. 26

2.5 Transmission for a 1D lattice of 100 single-orbital sites ($\epsilon_0 = 0$, $\epsilon = 0.5$, $t = -1$). Each curve contains a different number of disordered orbitals, N_d. Note that the curves for $N_d = 0$ and $N_d = 1$ are symmetrical to $E = 0$. This is because these systems have inversion symmetry, so no matter what direction the wave comes from, the result will be the same. In the case $N_d = 0$, there is no disorder, so the inversion symmetry is evident. In the case $N_d = 1$, there is one disorder that can be placed at any point in the system but, because the system is connected by semi-infinite leads with the same onsite energy ϵ_0 as the pristine orbitals, this effectively results in a one-orbital system with the disordered onsite energy ϵ connected by two semi-infinite leads, and this system is naturally symmetric. For any case $N_d > 1$, the relative positions between the scatterers will cause different propagation of the GF, resulting in unpredictable transmission signals (up until $N_d = D$, the entirety of the device). 27

2.6 **a)** Average over 10^4 transmission calculations for a 1D lattice of sizes ranging from 50 to 1000, all with 20% disorder concentrations ($\epsilon_0 = 0$, $\epsilon = 0.5$, $t = -1$). Note that the average transmission values decrease as the system size increases, which can be seen in **b)** when looking at the same energy value of E=0.5eV. This illustrates the effect of Anderson localization in the calculation of transmissions. 28

2.7 Parametrization of hexagonal lattices into principal planes for **a)** Armchair and **b)** Zigzag cases. All solid black lines represent the same hopping value and the dashed lines show the vertical reflection plane and separate two consecutive principal planes. The difference in the iteratively calculated transmission can be seen in the graph **c)**, depicting the positive part of the transmission spectrum using graphene parameters for a ribbon of 30x16 atoms. 30

2.8 Normalized Chebyshev Polynomials of the first kind of degree n from 0 to 5. 33

2.9 Square lattice transmission of 1000 systems for each different substitutional disorder concentration. The dashed line represents the configurational average of each concentration. The solid curves represent one transmission calculation whose concentration is indicated by its colour. Together, they illustrate the configuration distribution in the transmission space. The black solid line is the transmission for the pristine case and the black regions under it are the regions where the distributions of each curve overlap one another. 45

2.10 **a)** 25x8 square lattice transmission CAs for $N_c = 1000$ systems for different substitutional disorder concentrations. The dashed black line is the transmission of the input configuration with a concealed concentration. **b)** Square difference between some CAs and the input transmission. **c)** The misfit functional result displays a minimum at $n = 2\%$, coinciding with the dashed red line, which represents the original concealed concentration value of the input configuration. 50

2.11 **a)** 3072x3072 armchair graphene nano-ribbon transmission CAs with $N_c = 10$ for different vacancy concentrations. The dashed black line is the transmission of the input configuration. **b)** The misfit result with a minimum between $n = 2\%$ and $n = 3\%$, illustrating a case where the minimum is not clear. **c)** The misfit result displays a minimum at $n = 2.4\%$, coinciding with the original input concentration (dashed red line). 53

2.12 Two systems **a)** and **b)** with the same number of scatterers, but in different configurations. 54

2.13 Inversion error α as a function of the longitudinal size L (in unit cells) of graphene systems with substitutional impurities. Devices of all sizes contained a fixed impurity concentration of n = 4%. [80] 55

3.1 MoS_2 in 1H structural phase TMD illustration (purple sphere = Mo, yellow sphere = S) of: **a)** and **b)** side view. **c)** top-down view with unit cell. **d)** Standard orientation of crystal shape showing two layers and the bonding nature - Van der Waals for the inter-layer interaction and covalent for inter-atomic interactions (bi-colour cylinder). 61

3.2 **a)** Comparison between the band structure calculated from the maximum localized Wannier functions tight binding parameters (solid black) and the one calculated via DFT (dashed red). Note the direct band-gap present at momentum Γ. **b)** Illustration of the density of states spectrum (black) and DC conductivity (red) for the pristine MoS_2 case from these parameters. 66

3.3 **a)** Longitudinal conductivity at temperature $T = 0$K comparison between 8% concentration CA of 100 configurations (dashed red) and an input configuration of concealed disorder concentration (solid blue). The discrepancy is shown in the filled green curve. **b)** Misfit function $\chi(n)$ in arbitrary units averaged over 10 distinct input configurations displaying a minimum at 4%. For the sake of comparison, the vertical (red) line indicates the real concentration n_p of the input configuration. 69

3.4 **a)** Optical conductivity at temperature $T = 0$K comparison between 6% concentration CA and input configuration. **b)** Misfit function $\chi(n)$ in arbitrary units averaged over 30 distinct input configurations with the minimum at 4%. The error bars are smaller than the point markers. For the sake of comparison, the vertical (red) line indicates the real concentration n_p of the input configuration. 70

3.5 Comparison between longitudinal conductivity misfit functions with CAs at temperature $T = 0$K and input configurations of disorder concentration of $n = 4\%$ at temperatures $T = 0$K (black) and $T = 300$K (red) averaged over 10 realizations and with minima marked by the lines with the respective colour. Note that both results are not only practically identical but most importantly, have their minima at exactly the same concentration. 71

3.6 Vacancy peaks formed within the conduction gap due to the presence of vacancies illustrated at different vacancy concentrations. Each curve represents a configurational average of 40 configurations with a specific concentration. The heights of the peaks are proportional to the increased presence of S vacancies displayed, illustrating the electronic resonances caused by this disorder. 73

3.7 Behavior of the mean standard deviation as a function of the point density and the energy range covered. Statistical distribution for 50 different input configurations with CA of 50 configurations $\sigma_{\langle\chi_{50}\rangle_{50}}$. 74

3.8 **a)** AFM height profile and topographic image (inset). **b)** Optical image (inset) and Raman Spectrum. **c)** Pholuminescence spectrum. 77

3.9 MoS_2 BGFET devices. Schematic of a back-gated field effect transistor (alumina) under the MoS2 channel on the left and optical image of the fabricated devices showing the lateral structure on the right. 79

3.10 **a)** Comparison between simulated MoS_2 conductivity containing different vacancy concentrations (coloured) and experimental conductivity data for various MoS_2 systems (black), each of which contains unknown vacancy concentration. **b)** Histogram of the minima of the different misfit functions for each black curve of a). The black dot and red bar indicate the Gaussian mean and standard deviation of the minima distribution at 1.8 $\pm$ 1.1 %. The area in green represents the expected range of vacancy concentration previously reported for this method of fabrication. 80

3.11 Misfit function in black for the machine learning optical conductivity interpolated data based on the numerical data whose misfit function result is shown in red. The model still predicts the minimum correctly while providing via approximation more resolution around it, allowing for fine probing of different input configuration concentrations with lower computational costs. . . 83

3.12 Configurational average corresponding to 8% disorder randomly distributed in the device represented in Blue. In Red, machine learning optical conductivity shows very good prediction with the numerical result. 83

4.1 **a)** Standard orientation of crystal shape for the $(MoS_2)AuCl_3$ disorder unit cell (purple sphere = Mo, yellow sphere = S, golden sphere = Au, green sphere = Cl). **b)** Electronic band structure of **I -** pristine MoS_2 and **II -** $AuCl_3$-adsorbed MoS_2 calculated via DFT (red dashed lines) and the corresponding MLWF one (black solid lines). The agreement between the curves is such that it makes them hardly distinguishable. 89

4.2 **a)** Linear chain with substitutional disorders. **b)** Linear chain with adsorbed disorders. **c)** Transmission results configuration average over ten thousand configurations with 5% disorder concentration in a 100-orbital linear chain for the pristine, substitutional and adsorbed cases. The hopping to the adsorbed disorder t_A is one-fifth of the lattice hopping t and the disorder onsite energy ϵ_d is 0.5 (a.u.) higher than the lattice onsite energy ($\epsilon_0 = 0$). 91

4.3 **a)** Average convergence comparison between adsorbed impurities and substitutional at 5% concentration in relation to the average done with ten thousand curves. Each step on the horizontal axis signifies an increase in the number of configurations used to compose the probing average. Note that the adatom case converges more rapidly at first, reaching at 1000 configurations the same level of conversion that the substitutional case reaches at around 9000. **b)** Comparison between average transmission of systems with adsorbed orbitals. Each curve is an average of ten thousand configurations with adsorption concentrations: 0% (Pristine), 5%, 10% and 100%, showing curves with very similar signatures almost on top of each other. 93

4.4 Difference between unit cell hopping reach in the cases of a lattice composed of **a)** primitive cells and **b)** supercells. Here, only the hoppings for the central Mo atom are shown to facilitate visualisation. 95

4.5 Intra-gap effect of the disorder shown in averages over 40 configurations. The heights of the peaks **I** are proportional to the increased presence of $AuCl_3$. The concentrations of $AuCl_3$ are exaggerated to illustrate both peaks in the same scale. The heights of the peaks **II** are proportional to the increased presence of S vacancies. In the inset, we can see the case for typical concentrations of 1% $AuCl_3$ and 2% S vacancies in the purple log-linear plot. 97

4.6 **a)** Longitudinal conductivity at temperature $T = 300$K comparison (filled green region) between 1% $AuCl_3$ concentration CA (dashed red line) and input configuration signal (solid blue line) containing unknown $AuCl_3$ concentration. The CA is composed of 40 configurations and all systems have a 1% concentration of S vacancies. **b)** Misfit function $\chi(n)$ in arbitrary units averaged over 20 distinct inversion instances with minima at 0.5% $AuCl_3$ concentration. The vertical (red) line indicates the real concentration of the input configurations. 98

5.1 **a)** Scanning electron microscopy image of an NWN made of Ag/PVP core-shell nanowires with wire density of 0.49 nanowires/μm^2. Courtesy of the authors of reference [232]. **b)** Computationally generated random nanowire network geometry with a density of 0.67 nanowires/μm^2. The black lines represent the coated metal nanowires (in our case simulated to be Ag/PVP core-shell nanowires). The red vertical lines represent the metallic leads acting as electrodes. 103

5.2 Schematics of core-shell nanowire contact points depicting the main resistance contributions in our circuit model. Three nanowires made of a metallic core (internal silver cylinders) are coated by a dielectric material (outer blue cylinders) and are in direct contact at two locations: at left and right positions with respect to the bottom nanowire depicted horizontally. At each contact point, two distinct voltage nodes or terminals are created (red spheres). The resistance inside a wire segment (orange resistor symbol) is described by a static Ohmic resistance given by $R_{in} = \rho\ell/\Omega$ with ρ being the resistivity of the core metallic material, ℓ the length segment between the two voltage nodal points, and Ω the wire cross-sectional area. A variable resistive junction j used to model the inter-wire dynamic conduction is represented by the black resistor symbols and is characterized by a junction resistance R_j which is a function of the parameters A_j and α_j defining the phenomenological power law $R_j = I^{-\alpha_j}/A_j$ being I the amount of current flowing through the junction. . . 106

5.3 Surface colourmaps of the conductance junction model as a function of source current (I) and A_j, parameters in the junction conductance power law given by $\Gamma_j = A_j I^{\alpha_j}$. This conductance value is capped by two cut-off values defining an HRS and an LRS that the junction can endure. The resistance of the junction $R_j = 1/\Gamma_j$ cannot be larger than $R_{HRS} \sim 10^4$ kΩ and cannot be lower than $R_{LRS} = 12.9$ kΩ known as the quantum of resistance. The three panels show three important junction model cases that one needs to consider to subsequently understand the formation or not of WTA states in NWNs: **a)** $\alpha_j = 1.3$, illustrating junctions with $\alpha_j > 1$, **b)** $\alpha_j = 1$, and **c)** $\alpha_j = 0.7$, illustrating junctions with $\alpha_j < 1$. 108

5.4 Log-log plots of the NWN conductance evolution as a function of the sourced current. The NWN geometry adopted here is shown in Fig. 5.1b. The junction power law conductance model parameters (given in arbitrary units) used in **a)** are for fixed $A_j = 0.01$ and three distinct curves taken for $\alpha_j = 0.8, 1.0, 1.2$. In **b)**, A_j was reduced (and fixed) to $A_j = 0.1$ and the same α_j exponent values as in a) were used. 111

5.5 **a)** Colour band representation depicting the CAs composed of 100 configurations, which was used in the misfit minimization. Each colour band is defined between two CA curves. The configurations had $A_j = 0.05$ and distinct α_j values as depicted by the colour code. The dashed line is the input conductance evolution for a NWN evolved only up to the TG stage with an unknown α_j exponent. **b)** Misfit function $\log(\chi)$ versus α_j curve, with a clear minimum at $\alpha_{min} = 1.1$, revealing the correct exponent used in the input conductance curve before the power-law regime in the evolution. 115

5.6 Average misfit function χ plotted as a function of exponent α_j, developing a minimum at $\alpha_{min} = 1.1$, corresponding to the actual value of the input systems. The current limits of integration considered in the calculation of χ for the inversion is $I_{min} = 0$ to $I_{max} = 0.2$ (arbitrary units) and fixed $A_j = 0.05$ (arbitrary units). The error bars correspond to the standard deviation in χ computed over an ensemble of 60 inversions. 116

5.7 **a)** The same NWN as in Fig. 5.1b. Here only the nanowire segments between junctions are shown - nanowire "dead ends" are not depicted. **b-d)** Current maps obtained at the conductance state at $I = 0.25$ which corresponds to a state at the transient regime (TG) (see Fig. 5.5a). The power law prefactor was fixed at $A_j = 0.05$. Each panel shows the current color map for a given α_j value: b) $\alpha_j = 0.9$, c) $\alpha_j = 1.0$, and d) $\alpha_j = 1.1$. In the panels, $\alpha \equiv \alpha_j$. $\alpha_j > 1$ evidences the early stages of a WTA scenario whereas in the cases where $\alpha_j \leq 1$, a multiple path scenario is seen. 117

5.8 Surface contour plot of the logarithm of the misfit function in terms of α_j and A_j. The crossing of the horizontal and vertical dashed lines indicate the minimum of the $\log(\chi)$ surface, matching the parameters initially set for the input NWN system which were $\alpha_j = 1.1$ and $A_j = 0.05$. 118

5.9 Fixing $\alpha_j = 1.1$ in Fig. 5.8, one can visualize the misfit function (average) plotted in terms of A_j; the minimum is located at $A_{min} = 0.05$, corresponding to the original prefactor set in the input NWN system. The distribution of χ was computed from 60 different inversions with standard deviations shown as error bars. 119

5.10 Surface contour plot of the logarithm of the misfit function in terms of α_1 and α_2. In this case, the power law exponents for each junction in the NWN case were arbitrarily assigned to $\alpha_1 = 0.9$ and $\alpha_2 = 1.2$. Note that now, since the misfit function cannot differentiate between the variables, this graph will be symmetric along the identity line (save some oscillations from the stochastic CA calculations). This implies that we have two possible minima, one at $\alpha_1 = 0.9$ and $\alpha_2 = 1.2$ and the symmetric one at $\alpha_1 = 1.2$ and $\alpha_2 = 0.9$. 120

5.11 Surface contour plot of the logarithm of the misfit function in terms of α_μ and α_σ. In this case, the power law exponents for each junction in the NWN case were randomly assigned following a Gaussian distribution of mean α_μ and standard deviation α_σ. The crossing of the horizontal and vertical dashed lines indicates the minimum of the $\log(\chi)$ surface, matching the Gaussian parameters initially set for the input NWN system which were $\alpha_\mu = 1.2$ and $\alpha_\sigma = 0.2$. 121

B.1 Magnetic susceptibility calculation for a one-dimensional lattice of 1.000 sites with varied concentrations of magnetic disorder. **a)** CAs for different disorder concentrations and the plot of one input signal with a 5% concentration of magnetic impurities (black). **b)** The misfit function distribution of 500 minimization samples with input functions containing 5% concentration of disorder. 133

C.1 **a**) Pristine infinite linear chain of harmonic oscillators with mass m and elastic constant κ. **b**) Disordered case with the transmission setting including right and left leads. Here the disorder is represented by a single impurity of mass m_d. 136

C.2 **a**) Phonon transmission CAs for different concentrations of disorder ($m_d = 2m$). We can also see the function $\Upsilon(\omega, T = 300K)$ that will later modulate the transmission for the thermal conductivity calculation. **b**) Misfit function averages and standard deviations for ten thousand input functions and minimum at 5% concentration, marked by red line. **c**) CA distributions at $E = 2.0$. 140

C.3 **a**) CAs for the phononic contribution to the thermal conductivity of linear chain of harmonic oscillators with different concentrations of disorder. **b**) Misfit function averages and standard deviations for ten thousand input functions and minimum at 5% concentration, marked by red line. 141

List of Acronyms

AC	Alternate Current
CA	Configurational Average
CPGF	Chebyshev Polynomials Green's Function
CVD	Chemical Vapour Deposition
DC	Direct Current
DFT	Density Functional Theory
GF	Green's Function
HRS	High Resistance State
LRS	Low Resistance State
NWN	Nanowire Network
SGF	Surface Green's Function
TB	Tight Binding
TG	Transient Growth
TMD	Transition Metal Dichalcogenide
WTA	Winner Takes All

Contents

1 Introduction **1**

1.1 Inverse Problems 1

1.2 Inverse problems in Condensed Matter Physics 3

1.3 Approaching Signal Inversion 5

1.4 Signal Inversion on Disordered Devices 6

1.5 Characterizing Neuromorphic Devices 7

1.6 Thesis Layout 8

2 Theory and Methods **11**

2.1 Theoretical Modeling 11

2.1.1 Electronic Structure and Tight Binding 11

2.1.2 Green's Function 16

2.1.3 Dyson's Equation 18

2.1.4 Kubo Formalism for Transmission 23

2.1.5 Green's Function Iterative Algorithm 25

2.1.6 Green's Function Polynomial Expansion 31

2.1.7 Density Functional Theory Parametrization 40

2.2 Inversion Method 42

2.2.1 Approaching the Inversion Problem 43

2.2.2 Inverse Problem Ill-Posedness 47

2.2.3 The Inversion Algorithm 48

2.2.4 Ergodic Assumption 52

2.3 Summary 56

3 Inversion for MoS_2 Vacancy Characterization **59**

3.1 MoS_2: a Transition Metal Dichalcogenide 60

3.1.1 Disorder in TMDs and Vacancies 62

3.1.2 Characterization of TMDs 63

3.2 Inversion on Synthetically Disordered MoS_2 64
3.3 Validating the Ergodic Assumption 72
3.4 Inversion of Experimental Data 75
3.5 Interpolation Method for CA Generation 81
3.6 Summary 84

4 Inversion on MoS_2 Films Functionalized with Gold 87
4.1 Functionalization of TMDs 87
4.2 Adsorption Impact on Transmission 90
4.3 Supercell Approach 94
4.4 Obtaining Gold Concentration via Inversion 96
4.5 Summary 100

5 Inversion on Neuromorphic Systems 101
5.1 Memristive Nanowire Networks 101
5.2 The Winner Takes All Identification Problem 103
5.3 The Junction Power Law Conductance Model 105
5.4 The Network Conductance Evolution 109
5.5 Inversion of Conductance Evolutions 112
5.6 Determining Winner Takes All Occurance 114
5.7 Multiple-Material Network Characterization 118
5.8 Summary 122

6 Conclusion 123
6.1 Thesis Summary 123
6.2 Future Work 125
6.2.1 Quantitative Experimental Assessment 125
6.2.2 Material Design 126
6.3 Final Words 127

A Chebyshev Polynomial Green's Function Algorithm 129

B Magnetic Susceptibility Inversion 131

C Inversion of Phononic Quantities 135

Bibliography 142

From this we arrive at the conclusion that the mind never enjoys the original object; it enjoys only the reflected shadows of the original object. Catching the shadows of the physical world, people mistakenly believe that they have realized their goal. If the mind really desires to enjoy something, it should adopt the opposite course.

– Shrii Shrii Anandamurti

Chapter 1

Introduction

1.1 Inverse Problems

Among the challenges surrounding science and humanities, there is a particular set of problems which are concerned with uncovering the causal factors behind specific observations. These problems may vary in complexity, but in the end, they share a similar format. From detective work attempting to reconstruct a crime scene, to archaeology attempting to reconstruct past civilizations. From the problem of the origin of life wondering about the cause of our existence to the philosophical hard problem of consciousness wondering about the cause of our selves. All these problems have the goal of uncovering the reason behind different conjectures while only having information regarding the current, seemingly uninformative, present state. Nonetheless, hidden within these different present enigmas, lie the signatures of their causes. As wondering creatures, we feel uncomfortable whenever there is a gap in our knowledge. At the same time, we find great satisfaction when we find the puzzle piece that complements our understanding of reality.

This family of problems are denominated *inverse problems* for, instead of directly inferring the outcome out of specific initial conditions that strictly obey a set of fundamental laws, we attempt to do the inverse - from the observed final state, obtain the possible initial conditions or the laws governing these events. For this reason, inverse problems serve, among many other roles, as a pillar for the implementation of the scientific method. Here, we aim to form knowledge regarding the causal factors behind empirical observations, and, through hypothesis, reasoning, experiments and analysis we are able to

reproduce our observations and understand their cause. Needless to say, the physical sciences are full of inverse problems. In this thesis, we will approach inverse problems in the realm of condensed matter physics, particularly problems that aim to decode the structural information of various devices. But before I introduce this set of problems, let us try to understand the scope of inverse problems by considering a well-known example.

Take the concept of dark matter - by observing how light from distant stars bends on its way to the Earth, we infer the existence of gravitational lenses of a type of mass that does not interfere with electromagnetic waves [1]. We have an observation in hand, a signal of some sort, and wish to determine what is the cause of that signal, and which of the candidates will satisfy that description. We can draw a parallel to a particular scenario: suppose there is an unknown object inside a black box. You cannot observe it directly, but you are able to cast lights on it from different directions and observe the shape formed on the opposite side of the box. The more projections you analyse, the clearer becomes your concept of the original object. Naturally, the more angles you have available to cast your light from, the more precise your result will be. Likewise, the physicists hope that by studying the dark matter natural phenomena in different ways, from multiple angles, we will eventually either be able to project the unknown into the spaces of knowledge we already have or, in the evermore refined pursuit of an answer, we reveal a novel dimension of knowledge priorly unknown to us. While neither of these happens, the unknown remains a mystery.

As long as an inverse problem remains unsolved, the lack of information caused by the limited knowledge we can extract from our different projections will hold the door open for multiple interpretations and possible solutions. This is a persistent characteristic of inverse problems. A problem that lacks a unique solution is considered to be an *ill-posed problem* and this is a challenge that all inverse problems face. In the context of dark matter, the ill-posedness is evident in the amount of promising candidates to fit the role. In order to tackle this problem, certain constraints need to be put in place to turn *ill-posedness* into a *well-posedness*. Because we are aware of this ill-posedness populating the frontier of knowledge, we can avoid repeating Michelson's slight oversight [1] and, instead, say that it is most likely that physical sciences will

[1] "While it is never safe to affirm that the future of Physical Science has no marvels in store even more astonishing than those of the past, it seems probable that most of the

never be absolutely established for we will always be short of uncovering a new uncharted projection-space of knowledge lying just beyond the edge of our current understanding. In this way, qualitative and quantitative work are both equally necessary for scientific progress.

This sets the tone for the correct approach to inverse problems. Let us now see what kinds of inverse problems we are interested in in this thesis and how to address them.

1.2 Inverse problems in Condensed Matter Physics

Despite their pervasiveness, inverse problems are not the only type of problem in the sciences. More abstract, theoretical sciences deal with equivalently abstract problems such as conjecture proofs, classification, and properties of equation solutions, as can be seen in the list of unsolved Millennium Prize Problems. Whereas more practical sciences are concerned with performance optimization problems for example in the area of energy generation, transfer and storage. In physics, problems such as the grand unification between fundamental forces, paradoxes from the combination of quantum mechanics and general relativity (such as the black hole information paradox or the quantum nonlocality), quantum computing and quantum cryptography thresholds, and many more, fall into other categories. The difference between these problems and inverse problems is that the solutions for the first ones do not necessarily rely on the reconstruction of observations, rather they are either predicting observations beyond our current measurement technological capacity, they exist solely in the abstract field detached from empirical experimentation or they exist in the practical field of established theory as direct or forward problems in which one aims to obtain the final effects given the original causes.

In this thesis, we will focus on theoretical problems that come within the scope of empirical measurements. Particularly, we will deal with inverse problems in the realm of condensed matter physics with a focus on the characterization and design of physical systems. The inversions here initiate from

grand underlying principles have been firmly established and that further advances are to be sought chiefly in the rigorous application of these principles to all the phenomena which come under our notice. It is here that the science of measurement shows its importance — where quantitative work is more to be desired than qualitative work. An eminent physicist remarked that the future truths of physical science are to be looked for in the sixth place of decimals." - Albert A. Michelson, 1894, dedication of Ryerson Physical Laboratory.

different measurable and calculable signals from mesoscopic solid-state devices with the goal of identifying the intrinsic properties responsible for the observed outcome. In other words, in the case of characterization, one question we may ask here is:

> *Given an arbitrary signal quantifying a given observable of a device susceptible to a type of disorder, what is the concentration of that disorder in the device?*

Other questions may involve probing the type of disorder or the magnitude of a system property. The presence of disorder is what sets the difficulty and uniqueness of this inverse problem. Usually, signals from disordered systems will be pervaded with noise, making the identification of particular signatures very difficult. On the other hand, disorder is what makes the problem interesting - not only does it make the device itself unique by altering its properties, but disorder is what gives this problem a non-trivial solution.

Currently, the inverse problem of characterization is approached via more direct ways such as scanning transmission electron microscopy (STEM), and different kinds of spectroscopy such as photoluminescence and Raman spectroscopies. The success of these approaches, especially in STEM imaging, relies on the "over-measurement" of the sample, *i.e.*, measurements are taken with enough resolution so that the atomic structure of the sample is clear and defined, leaving no room for wonder, no allowable deviation. In other words, projections from every known direction are taken, decreasing the degrees of freedom of the unknown up to (or almost to) zero. This represents a very successful inversion and displays the peak of technological progress in the area of material characterization. The downside is that such an extensive measurement requires a respectively extensive set-up - the cost of performing this measurement and analysing the data is high both performance-wise and monetarily due to the cost of necessary instruments. What I propose here is that we try to perform this inversion with less "over-descriptive" measurements. Instead, would it be possible to obtain structural information about our device solely by analysing a spectral signal such as electrical conductivity?

In this setting, inverse problems are particularly practical. We understand the fundamental laws necessary to describe disordered mesoscopic systems at a quantum level, including the different equations devised to theoretically calculate various observables. Thanks to that, we can devise a tool capable of solving signal-based inversion problems for characterization, which facilitates

the usage of these systems in practical applications by simplifying and contributing to the characterization process.

1.3 Approaching Signal Inversion

Signal inversion is a well-studied problem [2, 3] that pervades the areas of medical physics [4,5], image deconvolution [6,7] and geophysics [8–12] to name a few. In each of these areas, different techniques have been devised tailored to solving the specific inverse problem of that domain.

In medical imaging, for example, the inversion of signals can be approached by considering the measurement, a model for noise, which is considered detrimental to the imaging process, and a "prior model", which takes care of the ill-posedness around the inversion by restricting the sought parameters [13]. These models are derived for each inversion scenario and together serve to construct an analytical model for inverting different signals such as MRI, electrocardiac potential and photo-acoustic or ultrasound modulation tomography, with the goal of obtaining their pristine form - here, the disorder poses a hindrance to the final result and has to be filtered out of the measurement.

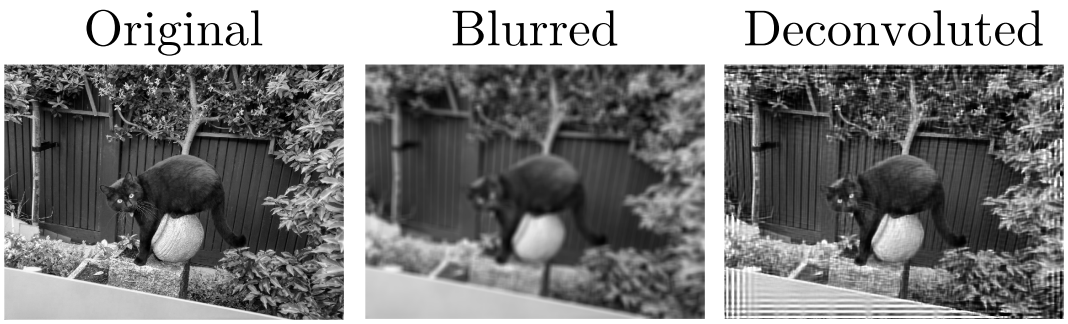


Figure 1.1: Illustration of the deconvolution process showing the original, the convoluted image with a Gaussian blur and the result of the deconvolution using Point Spread Function, an analytical inverse technique commonly used in biological microscopy based on the wave behaviour of light (which causes the ringing at the edge of the image) [14].

Image deconvolution - the reconstruction of an image convoluted by disorder - in itself is a form of inverse problem that has an established methodology behind its inversion. By employing regularization methods to image signals and their Fourier transforms, a family of approximate solutions is used to reconstruct an original image via their combination regulated by the optimized

regularization parameter [15]. Regularization can be performed via multiple different analytical, iterative or statistical methods such as least-square solutions, conjugate gradient and maximum-likelihood to name a few [16, 17]. Medical physicists often rely on image deconvolution techniques to treat its images.

In geophysics, problems such as locating the epicentre of a seismic event (including tsunamis), travel-time tomography, and acoustic surveys are prime examples of inverse problems. Given the unpredictable nature of the object of observation, the methods to approach these problems tend to be of a statistical nature, such as monte-carlo methods, gaussian-distributed error least-squares or least-absolute-value criteria, and others similar to the statistical approaches used in medical physics [18, 19].

1.4 Signal Inversion on Disordered Devices

In most of the approaches, the noise or disorder in the signal is treated as a hindrance to obtaining the final reconstructed result. For our case, however, the noise itself caries valuable information, for within the seemingly incomprehensible signal, lies the impetus of the disorder characteristic signature. We do not wish to throw out the baby with the bath water, so we make maximum utilization of those signatures to construct a method for inverting these signals and obtaining the information shrouded within it.

Because of the unpredictable variations in observable signals that occur when scatterers assume different positions in a device, deterministic methods fail to offer us a good solution for this inverse problem. Instead, we approach the problem of disorder characterization by employing a statistical Bayesian method similar to the maximum likelihood estimation while at the same time availing of the disorder signature information contained in the noise by performing Monte-Carlo averagings. As we will more thoroughly see in Chapter 2, the method used in this thesis for solving the inverse problem relies on the definition of a likelihood function as a parameter of the disorder concentration termed here as *misfit function*. The misfit function terms contain statistical information of the observable over the configurational space of scatterer placements and, by comparing it to an input signal, the target of the inversion, we are able to extract the likelihood of disorder concentration. By minimizing the misfit function (maximizing the likelihood), we can obtain the most probable

disorder concentration of the input sample. This characterization is substantiated by delimitating the possible parameters of the problem - in this way, we contour the ill-posedness of our inversion.

This method has been studied in the past few years and the range of its application has been steadily increasing. We have successfully employed it to obtain disordered structural information on a variety of hosts for one or more concomitant types of disorder. We also employed it to obtain spatial information on the disorder placement in the host system and treated scatterers of different natures such as impurities with magnetic moments [20–22]. In this thesis, I will expand even more the scope of application of this method by challenging it with large systems with a complex structural description on various scales as well as by employing it to obtain hidden information regarding the emerging conductivity evolution of neuromorphic networks.

It is worth mentioning that within the realm of condensed matter physics, there are other statistical methods that aim to perform various types of inversions. For example, some methods aim to stabilize or extend the inversion results from experimental measurements via statistical analysis [23, 24], while others aim to statistically select potential materials or atomic configurations by performing a set of candidate simulations [25, 26]. Other methods rely on machine learning techniques to identify or predict such candidates and properties [27–29], or for the general design of materials based on recursive inverse algorithms [30, 31]. These methods are powerful tools for each inversion application but are not quite suitable to solve the problem of device characterization from system signatures. The method proposed in this thesis bridges this gap, offering a generalizable approach to characterization via inversion and contributing to the research of inversion problems in condensed matter physics.

1.5 Characterizing Neuromorphic Devices

Among the current challenges in condensed matter physics is the search for materials whose electrical properties mimic the function of the brain [32, 33]. In this thesis, I offer a contribution to this effort with the aid of our devised inversion method.

By studying the functioning of nano-wire networks of memristors, whose resistance activations mimic some aspects of neurons, under progressive current evolutions, we observe the emergence of a global behaviour similar to how one

models brain-like behaviour in artificial neural networks [34]. In certain conditions, we can distinguish the emergence of a Winner-Takes-All conductivity path - a preferred path for the flow of current. By associating the occurrence of this phenomenon to a self-similar parameter that dictates the rate of the resistance evolution in the junctions of the networks, we are able to employ our inversion method to tackle the following question:

> *Given the early uninformative stages of the conductivity evolution as a function of the current of a nanowire network of memristors, can I determine if a winner-takes-all path will emerge?*

Similar to the previous inversion problems, here we are trying to obtain information about the network composition by analysing one of its signals. Note, however, that in this case, the problem faces a different degree of subtlety - no longer are we dealing with disorder in the form of scatterers, but here the disorder is present in the very geometry of the device - and we wish to obtain from the global behaviour of the system the information of a parameter whose action is limited to the micro-scale of individual memristors.

1.6 Thesis Layout

In the following chapter, Chapter 2, I will lay the theoretical framework necessary for the calculation of conductivity signals in disordered devices as well as introduce and exemplify our method for solving the inversion problem. Here we will deal with the fine properties of this method that enable its functioning such as the way we deal with the ill-posedness of the problem and the ergodic principle that serves as the foundation for the operation of this method.

From Chapter 3 onwards, I will submit the method to novel scenarios and test its implementation with the goal of probing the scope of its application. In Chapter 3 we will study how the method works on a complex system - MoS_2 - composed of multiple orbitals and attempt to obtain the concentration of sulfur vacancies that serve as our scatterers. Here we will go one step further and analyse what is the feasibility of employing this method on experimental transconductivity data by performing a qualitative inversion to obtain values for vacancy concentrations.

In Chapter 4, I will advance on the path of increasing complexity and try to invert conductivity signals to obtain the concentration of a novel type of scatterer in the form of adsorbed complexes, whose signatures are very weakly

present in our spectrum. From the understanding of the functioning of the method laid out in Chapter 2, we expect that weak scatterers will present a greater challenge for this inversion method. In this chapter, we will put it to the test and once more expand the frontiers of its application.

In Chapter 5, we will approach the problem of winner-takes-all occurrence on nano-wire networks of memristors as described in the previous section. This will configure a shift in the approach we take for the inversion, changing completely our systems both in scale and in modelling, the concept of disorder and the goal of the inversion. This will demand an introduction to the model behind the calculations of conductivity evolution that will serve as components for our inversion equation.

Finally, in Chapter 6, I will conclude the thesis, offering a summary of the work done and of our findings. In this chapter, I will also comment on the future works available for this research topic such as pursuing the problem of material design, a very pertinent inverse problem with extremely impactful repercussions in the realm of condensed matter physics.

Chapter 2

Theory and Methods

Having introduced the main topic of this work, let us build the foundations necessary for tackling the projects proposed in the following chapters.

The current chapter is divided into two major sections. In the first one, I lay out the theoretical tools - the modelling and formulations - necessary for the calculation of transmission functions in disordered systems and their derived quantities. In the second section, I offer a detailed framework for the inversion methodology used throughout the thesis and exemplify it in simple scenarios.

2.1 Theoretical Modeling

In this thesis, we aim to study the use of inversion methods to identify how impurities can alter the properties of various systems. With this in mind, the first step of this endeavour is to establish the language with which we will articulate and substantiate the elements of observation. In other words, we are to use the current solid-state paradigms that can provide a description and analysis for general atomic and molecular lattices, in special disordered ones. That said, let us explore the theory behind the modelling of choice and the respective derived formulations that we will use in this work to access their properties.

2.1.1 Electronic Structure and Tight Binding

We can model atomic and molecular systems in various ways depending on the desired output and the scale of the interactions of interest. For exam-

ple, by using the density matrix approach, one can model small-scale atomic and molecular systems with great precision via the density functional theory (DFT) method using the Khon-Sham equations (or, non-self-consistently, via the Harris functional like in DFTB applications) [35, 36]. Alternatively one can try to completely determine the electronic wave function of closed-shell systems via the Hartee-Fock method along with the Born–Oppenheimer and mean-field theory approximations ignoring electron correlation [37, 38]. When dealing with a periodic lattice, one can straightforwardly apply Bloch's theorem, which offers an *ansatz* for the solution of the Shroedinger Equations [39]. Yet another approach, more suitable for larger systems, is to treat the electronic wave function in real space as a linear combination of the atomic orbitals of the system (LCAO) and use the single-electron states to calculate the band structure based on empirical parametrization as in the tight binding model [40, 41]. The ultimate goal of the different models is to describe the system at the appropriate level of complexity in such a way that the elements of interest can be mathematically represented and the Schroedinger equations for such a system can be straightforwardly tackled.

When dealing with crystalline structures, as we will, one may be tempted to resort to Bloch's theorem to express the electronic wave functions in the lattice as periodic-modulated reciprocal plane waves, but this approach is only practical when dealing with a pristine structure. Once we add disorder to the system, we lose the periodicity, making it more interesting, but also more tricky to be described in the reciprocal space. In this case, a real-space model of the system offers the necessary level of description and flexibility to implement disorder. With that in mind, the Tight Binding (TB) model suits best our problem. The TB model provides a good balance between accuracy and scalability. On one hand, it allows access to analytical expressions for the case of simple electronic structure materials, and on the other, it offers accuracy and numerical functionality when dealing with more complex structures.

The TB model is derived from the assumption that the nuclei of the atoms are stationary, which means that their atomic orbitals form a static orthonormal basis. This is a safe assumption on the basis that the electronic degrees of freedom have much faster dynamics than those of the underlying atomic structure. The next assumption is that the electrons of a lattice are firmly bound to these orbitals in such a way that the total electron single-particle wave function $|\Psi\rangle$ can be represented as a linear combination of isolated atomic orbitals

$|n\rangle$,

$$|\Psi\rangle = \sum_n \phi_n |n\rangle \ , \tag{2.1}$$

where ϕ_n are complex coefficients. With this orthonormal basis of atomic orbitals (also known as tight-binding orbitals), we can use the Schrodinger Equations to write the eigenvalues of a system's Hamiltonian in terms of the tight-binding coefficients. Considering that our system is in adiabatic conditions, we can write the time-independent Schrodinger Equation:

$$E |\Psi\rangle = \hat{H} |\Psi\rangle \, . \tag{2.2}$$

Using the expression for $|\Psi\rangle$ of Eq.(2.1), we reach:

$$E = \frac{\sum_{nm} \phi_n^* \langle n| \hat{H} \phi_m |m\rangle}{\sum_{nm} \phi_n^* \phi_m \langle n|m\rangle}. \tag{2.3}$$

Since this is an orthonormal basis ($\langle n|m\rangle = \delta_{nm}$), the denominator is reduced to $\sum_n \phi_n^* \phi_n = 1$. The ground-state eigenvalue can be found then by minimizing E with respect to the eigenstate coefficients [42]:

$$\frac{\partial E}{\partial \phi_n} = \frac{\partial E}{\partial \phi_n^*} = 0 \ \Rightarrow \tag{2.4a}$$

$$0 = \frac{\partial E}{\partial \phi_n^*} = \frac{\sum_m H_{nm} \phi_m}{\sum_{nn} |\phi_n|^2} - \left(\frac{\sum_{nm} \phi_n^* \phi_m \langle n| \hat{H} |m\rangle}{\sum_{nm} \phi_n^* \phi_m \langle n|m\rangle} \right) \frac{\phi_n}{\sum_{nn} |\phi_n|^2} \, , \tag{2.4b}$$

where H_{nm} is the expected value of $\hat{H}$ connecting orbitals m and n. From Eq.(2.3) and considering the unitary norm of the coefficients of this basis set, we reach:

$$0 = \sum_m H_{nm} \phi_m - E \phi_n \, . \tag{2.4c}$$

We can then write this eigenvalue equation in matrix form:

$$E \begin{bmatrix} \phi_1 \\ \phi_2 \\ \vdots \\ \phi_N \end{bmatrix} = \begin{bmatrix} H_{11} & H_{12} & \cdots & \\ H_{21} & H_{22} & & \\ \vdots & & \ddots & \\ & & & H_{NN} \end{bmatrix} \begin{bmatrix} \phi_1 \\ \phi_2 \\ \vdots \\ \phi_N \end{bmatrix} . \tag{2.5}$$

Resolving this set of linear equations, we can determine the coefficients of the linear combinations of atomic orbitals, identifying the electronic states of our system and their dispersion relation. Expressing the electron wave function in terms of the atomic orbitals allows us to maintain a real-space resolution of our wave function, which is necessary when we are dealing with disordered systems that lack translational symmetry. The expected values of our Hamiltonian can be expressed as:

$$\langle \hat{H} \rangle = \langle i | \frac{\hat{p}^2}{2m} + \hat{V} | j \rangle = \begin{cases} \epsilon_i & \text{, if } i = j, \\ t_{ij} & \text{, if } i \neq j, \text{ for } n \text{ and } m \text{ nearest neighbours,} \\ 0 & \text{otherwise.} \end{cases} \tag{2.6}$$

On the left-hand side of the equation we have the Hamiltonian expressed in terms of the kinetic energy of the electron in an orbital plus the electric potential, which can, for example, be given by the coulomb interaction between the electron in an orbital and the different orbitals. In this representation, the orbital index also contains information about its absolute position in the lattice. Note that this Hamiltonian does not account for electron-electron interaction terms, which is fundamental for the simplicity of the tight-binding method, decoupling its calculations and allowing for easy computation of large systems. On the other hand, it is causal for the TB models' lower accuracy in comparison to first-principle calculations such as DFT. On the right-hand side of Eq.(2.6) the values ϵ_i are the on-site energies for every orbital, and t_{ij} are the hopping energies from orbital $|i\rangle$ to the neighbour orbital $|j\rangle$. The expected values of the Hamiltonian are the degrees of freedom of the model, and they are selected to best fit experimental or first-principle theoretical results, as we will later see in this chapter on Section 2.1.7.

Only nearest neighbours are considered in this modelling, so if the orbitals $|i\rangle$ and $|j\rangle$ are far enough apart, $t_{ij} = 0$. The definition of "nearest neighbours", however, is fairly loose. The idea is to account only for the local inter-orbital interactions because the further one goes, the weaker and more complex the interactions become, and the model tends to disagree with ab initio calculations. In this sense, for simple modelling, the "nearest neighbours" might be the immediate neighbouring atoms. However, if one can stipulate the model parameters t_{ij} from ab initio calculations themselves, one can take into consideration further neighbours without much problem. This combines

the precision of ab initio calculations with the simplicity and efficiency of the TB model, allowing for simulations of materials in the mesoscopic scale. This is the approach we take in this thesis.

One may point out that when choosing a real space parametrization, the size of the Hamiltonian matrices scales directly with the number of orbitals in the system, bringing computational challenges both due to the memory needed for storage and due to the inversion operation cost, especially as the system size and/or level of description is enhanced. Later in this section, I will present techniques that deal with these issues. For now, let us use a simple system to exemplify and illustrate our modelling and calculations.

The Linear Chain

The most simple system we can model is a one-dimensional infinite linear chain of single-orbital atoms. Verily, this is but a toy model, since we seldom observe a one-dimensional system in nature, much less an infinite one. Nonetheless, it serves to illustrate how the modelling and calculations are carried out in an uncomplicated manner. Let us take a linear chain as illustrated in Fig. 2.1a.

Assuming each atom is composed of one single orbital with the same onsite energy ϵ_0 and hopping energy $-t$ to first nearest neighbours, the Hamiltonian expectation value matrix would assume the tri-diagonal shape

$$\langle \hat{H} \rangle = \begin{bmatrix} \ddots & \ddots & & & 0 \\ \ddots & \epsilon_0 & -t & & \\ & -t & \epsilon_0 & -t & \\ & & -t & \epsilon_0 & \ddots \\ 0 & & & \ddots & \ddots \end{bmatrix} . \tag{2.7}$$

Here we can index the orbital as their unique position in the linear chain. So far, this represents a pristine system and it can be straightforwardly solved in the reciprocal space. The moment we add disorder, as shown in Fig. 2.1b, we immediately break the translational symmetry of our system. Yet, the system can still be thought of as two semi-infinite linear chains connected by the foreign orbital. This separation organically introduces the spatial delimitation of three regions: the left lead, or the pristine semi-infinite region arriving from the left, the right lead, the right counterpart of the left lead, and the device,

which houses the disorder and marks the region of interest in the system. In fact, this nomenclature is not coincidental, for when dealing with mesoscopic devices, the leads (metal wires that introduce the voltage potential) connected at the edges of the system, can be considered semi-infinite perfect conductors in the scale of the device. Naturally, we can expand the device region to have any size we want and any disorder concentration while keeping the property of being but a connection between the left and right leads.

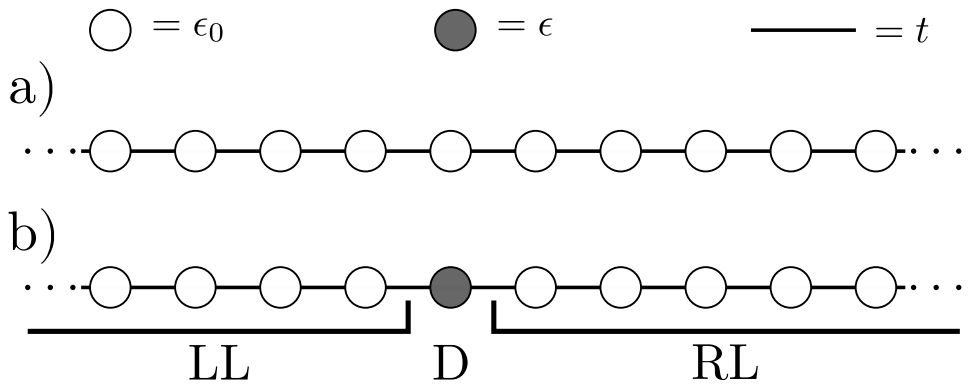


Figure 2.1: Infinite linear chain in the pristine case (**a**) and with one in the case with one disorder (**b**). The disordered case can be interpreted as one device D connected on the left and on the right by semi-infinite leads LL and RL.

2.1.2 Green's Function

From now on, for the rest of this chapter, we will not be operating directly on the Hamiltonian of the device, but instead, we will be using its Green's Function (GF) [43]. Given a linear operator $\hat{\mathcal{L}}$ with a complete set of eigenfunctions:

$$\hat{\mathcal{L}} |n\rangle = \epsilon_n |n\rangle \ , \tag{2.8}$$

its Green's function operator ($\hat{G}$) is defined as the solution of the inhomogeneous differential equation:

$$\left[z\mathbb{I} - \hat{\mathcal{L}}\right] \hat{G} = \mathbb{I} \, , \tag{2.9}$$

where z is a complex number. If we want to evaluate these operators on this basis set to find the expectation values, we operate basis vectors from the left

and from the right:

$$\langle n| \left[z\mathbb{I} - \hat{\mathcal{L}}\right] \hat{G} |m\rangle = \langle n| \mathbb{I} |m\rangle \ , \tag{2.10a}$$

$$\langle n| z\hat{G} |m\rangle - \langle n| \hat{\mathcal{L}}\hat{G} |m\rangle = \langle m|n\rangle \ . \tag{2.10b}$$

Since this is a complete basis-set, we can introduce the identity:

$$\sum_{n'} |n'\rangle \langle n'| = \mathbb{I} \Rightarrow \tag{2.10c}$$

$$z \langle n| \hat{G} |m\rangle - \sum_{n'} \langle n| \hat{\mathcal{L}} |n'\rangle \langle n'| \hat{G} |m\rangle = \langle m|n\rangle \ . \tag{2.10d}$$

Now, if $\hat{\mathcal{L}}$ is hermitian and has $|n\rangle$ as its eigenvector, then $\langle n| \hat{\mathcal{L}} = \epsilon_n \langle n|$, which gives us:

$$z \langle n| \hat{G} |m\rangle - \epsilon_n \sum_{n'} \langle n|n'\rangle \langle n'| \hat{G} |m\rangle = \langle m|n\rangle \ , \tag{2.10e}$$

because this is an orthonormal basis set, $\langle n|n'\rangle = \delta_{nn'}$,

$$z \langle n| \hat{G} |m\rangle - \epsilon_n \sum_{n'} \delta_{nn'} \langle n'| \hat{G} |m\rangle = \delta_{nm} \ , \tag{2.10f}$$

$$z \langle n| \hat{G} |m\rangle - \epsilon_n \langle n| \hat{G} |m\rangle = \delta_{nm} \ , \tag{2.10g}$$

$$(z - \epsilon_n) G_{nm} = \delta_{nm} \ , \tag{2.10h}$$

$$G_{nm} = \frac{\delta_{nm}}{z - \epsilon_n} \ . \tag{2.10i}$$

In the last expression of Eq.(2.10i), we can see that the GF has a pole at $z = \epsilon_n$, but, since we chose $\hat{\mathcal{L}}$ to be hermitian, ϵ_n is a real value and we can overcome the ill definition by adding a small imaginary part to z. By considering the completeness relation of Eq.(2.10c), Eq.(2.10i) can be alternatively be written in operator form as:

$$\hat{G} = \sum_n \frac{|n\rangle \langle n|}{z - \epsilon_n} \ . \tag{2.11}$$

Note that the resulting GF for this operator is diagonal. Since we chose to represent the operator $\hat{\mathcal{L}}$ on the basis of its eigenvectors, $\hat{\mathcal{L}}$ is diagonal. $z\mathbb{I}$ is also diagonal and the inverse of a diagonal operator is also diagonal. In the case of TB modelling, this hermitian linear operator $\hat{\mathcal{L}}$ is our tight-binding

Hamiltonian $\hat{H}$ of disconnected orbitals, and the basis formed by $|n\rangle$ is the basis of orthonormal atomic orbitals. Now, the differential equation of interest as specified in Eq.(2.9), is our Schrodinger Equation, where z is our energy E plus a small imaginary part $i\eta$. Here the GF becomes an auxiliary tool to solve the Schrodinger equation and is given finally by:

$$\hat{G}(E) = \frac{\mathbb{I}}{z - \hat{H}}\,. \tag{2.12}$$

In case we choose to use the ket notation formulas defined above in the space representation, our states become continuous and the sums over n become integrals over $\boldsymbol{r}$. Because of the presence of poles, we approach these integrals via Cauchy's residue theorem and depending on the curve we choose to close the contour integral in the complex plane, the imaginary part of z has a different signal, giving us different forms of the GF:

$$\hat{G}^{\pm}(E) = \lim_{\lambda \to 0} \hat{G}(E \pm i\lambda)\,, \tag{2.13}$$

where G^+ can be equivalently termed as the retarded Green's Function and G^- as the advanced Green's Function due to their possible interpretation as propagators that carry causal information from different points in time.

The GF is a function of the Hamiltonian that carries all the information of the system and at the same time, its off-diagonal elements carry the physical meaning of propagation of the electronic wave through the orbitals of our system. This makes GFs extremely powerful tools to tackle various problems, in particular those involving transmission and scattering as we will see later in this chapter.

2.1.3 Dyson's Equation

The question that arises then is: how do we calculate the Green's Function of a Hamiltonian with connected orbitals? After all, in our TB modelling, the nearest neighbour orbitals are connected via the hopping parameters. In this case, the pure orbitals are no longer eigenvectors of our Hamiltonian and we can no longer use the equations above to obtain the matrix elements of the GF. We can approach this problem by considering that each connection is a potential that acts as a perturbation to our disconnected Hamiltonian such

that:

$$\hat{H} = \hat{H}_0 + \hat{V} \tag{2.14}$$

From this, using Eq.(2.9), we define our GF of the perturbed system as:

$$\left[z\mathbb{I} - \hat{H}\right]\hat{G} = \mathbb{I} \Rightarrow \tag{2.15a}$$

$$\left[z\mathbb{I} - \left(\hat{H}_0 + \hat{V}\right)\right]\hat{G} = \mathbb{I}, \tag{2.15b}$$

$$\left[z\mathbb{I} - \hat{H}_0\right]\hat{G} = \mathbb{I} + \hat{V}\hat{G}, \tag{2.15c}$$

$$\hat{G} = \frac{\mathbb{I}}{z\mathbb{I} - \hat{H}_0} + \frac{\mathbb{I}}{z\mathbb{I} - \hat{H}_0}\hat{V}\hat{G}. \tag{2.15d}$$

But the term $\frac{\mathbb{I}}{z\mathbb{I}-\hat{H}_0}$ is exactly the definition of the GF for the unperturbed Hamiltonian of Eq.(2.12). Let's call it $\hat{g}$:

$$\hat{g} = \frac{\mathbb{I}}{z\mathbb{I} - \hat{H}_0} \Rightarrow \tag{2.15e}$$

$$\hat{G} = \hat{g} + \hat{g}\hat{V}\hat{G}. \tag{2.15f}$$

And this is the definition of Dyson's Equation [44]. From Eq.(2.15f), we can see that in order to calculate the GF of a connected system, it is not necessary to invert a complicated Hamiltonian. Instead, if we can express our Hamiltonian in terms of a perturbation plus a disconnected Hamiltonian which GF we know, we can obtain the GF for the perturbed case. If now we want to obtain the matrix elements of our GF $\hat{G}$, we operate it with our vectors:

$$\langle n|\,\hat{G}\,|m\rangle = \langle n|\,\hat{g}\,|m\rangle + \langle n|\,\hat{g}\hat{V}\hat{G}\,|m\rangle \Rightarrow \tag{2.16a}$$

$$\langle n|\,\hat{G}\,|m\rangle = \langle n|\,\hat{g}\,|m\rangle + \sum_{n'n''}\langle n|\,\hat{g}\,|n'\rangle\,\langle n'|\,\hat{V}\,|n''\rangle\,\langle n''|\,\hat{G}\,|m\rangle = \tag{2.16b}$$

$$G_{nm} = g_{nm} + \sum_{n'n''} g_{nn'}V_{n'n''}G_{n''m} \tag{2.16c}$$

This is a general equation that serves for any perturbation on a Hamiltonian with known GF $\hat{g}$. This equation will have a closed-form expression when $\hat{V}$ is a short-range potential. In the special case in which $\hat{H}_0$ is the matrix of disconnected onsite energies and $\hat{V}$ are the connecting hoppings, we can

decompose the perturbation $\hat{V}$ as a series of short-range connections:

$$\hat{V} = \sum_n V_{nn+1} = \sum_n \left(|n\rangle\, t\, \langle n+1| + |n+1\rangle\, t\, \langle n| \right) \text{ , and} \tag{2.17}$$

$$g_{nm} = \begin{cases} g_{nn} & \text{, if } n = m, \\ 0 & \text{otherwise.} \end{cases} \tag{2.18}$$

$$V_{nm} = \begin{cases} t & \text{, if } m = n+1, \\ 0 & \text{otherwise.} \end{cases} \tag{2.19}$$

Making one of these perturbations at a time on the disconnected Hamiltonian, we have from Eq.(2.16c):

$$G_{nn} = g_{nn} + g_{nn} V_{nn+1} G_{n+1n}. \tag{2.20a}$$

From the same equation using the same perturbation between n and $n+1$:

$$G_{n+1n} = g_{n+1n+1} V_{n+1n} G_{nn} \Rightarrow \tag{2.20b}$$

$$G_{nn} = g_{nn} + g_{nn} V_{nn+1} g_{n+1n+1} V_{n+1n} G_{nn}, \tag{2.20c}$$

$$G_{nn} = \frac{g_{nn}}{1 - g_{nn}\, t\, g_{n+1n+1}\, t} \tag{2.20d}$$

Where we fully write the element of $\hat{G}$ in terms of the known elements of $\hat{g}$. Like this, we can obtain every other matrix element and slowly include the other connections of Eq.(2.17) until we build the entire connected system.

Let us now consider a different case. In the linear chain example illustrated in Fig. 2.2, if we know the Hamiltonian of the unperturbed system ($\hat{H}_0$)and its GF $\hat{g}$, and we know what potential $\hat{V}$ should connect the device and the lead, we can establish this connection by using Dyson's equations to calculate the GF $\hat{G}$ of the connected Hamiltonian ($\hat{H}$) and write it again as

$$\begin{aligned} \hat{H} &= \hat{H}_0 + \hat{V}\,, \\ \hat{G} &= \hat{g} + \hat{g}\hat{V}\hat{G}\,. \end{aligned} \tag{2.21}$$

This equation is particularly useful numerically if we are concerned with the GF elements at the sites around the perturbation $\hat{V} = |0\rangle\, t\, \langle 1| + |1\rangle\, t\, \langle 0|$. If we want to go from the scenario illustrated in Fig. 2.2a to the one in Fig. 2.2b,

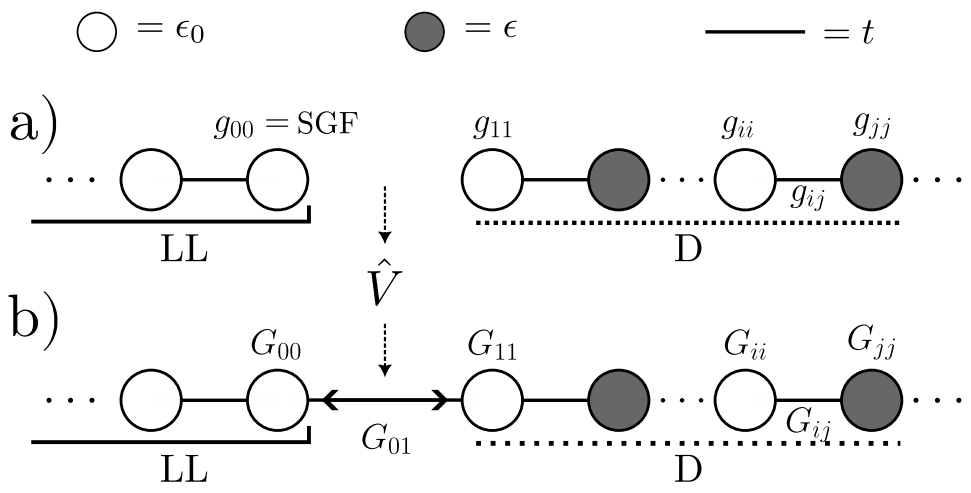


Figure 2.2: Semi-infinite left lead (LL) connecting its semi-infinite surface Green's function ($g_{00} = SGF$) to the surface Green's function g_{11} of the device (D) via perturbation $\hat{V}$ from the unperturbed state (**a**) to the perturbed one (**b**).

the resulting $G_{11} = \langle 1| \hat{G} |1\rangle$, for example, is given by:

$$G_{11} = g_{11} + g_{10}t_{01}G_{11} + g_{11}t_{10}G_{01}\,, \tag{2.22a}$$

and since the unperturbed $g_{10} = 0$ due to the absence of the connection,

$$G_{11} = g_{11} + g_{11}t_{10}G_{01}\,. \tag{2.22b}$$

We now write the Dyson's equation for our unknown $G_{01} = \langle 0| \hat{G} |1\rangle$:

$$G_{01} = g_{01} + g_{00}t_{01}G_{11} + g_{01}t_{10}G_{01}\,, \tag{2.22c}$$

and since the unperturbed g_{01} is also zero,

$$G_{01} = g_{00}t_{01}G_{11}\,. \tag{2.22d}$$

Substituting this value in Eq.(2.22b), we finally arrive at:

$$G_{11} = g_{11} + g_{11}t_{10}g_{00}t_{01}G_{11} \quad \Rightarrow \tag{2.22e}$$

$$G_{11} = \frac{g_{11}}{1 - g_{11}t_{10}g_{00}t_{01}}\,. \tag{2.22f}$$

For completeness, if we were interested in any other value G_{ij}, instead, a similar sequence of equations would lead to the general expression for lead-device coupling (still assuming $g_{01} = g_{10} = 0$):

$$G_{ij} = g_{ij} + \frac{g_{i0}t_{01}\left(g_{1j} + g_{11}t_{10}g_{0j}\right) + g_{i1}t_{10}\left(g_{0j} + g_{00}t_{01}g_{1j}\right)}{1 - g_{00}t_{01}g_{11}t_{10}}\,. \tag{2.23}$$

Note that each of the values g_{i0}, g_{i1}, g_{0j}, and g_{1j} can be zero depending on if the sites i or j belong or not to the lead or the device. Nonetheless, as we will soon see, the value of G_{11} proves to be especially relevant for calculating the transmission using the iterative algorithm.

Before we proceed to the numerical transmission calculation, there is one more analytical result we can derive from Dyson's equations above. We have in hands both the Hamiltonians for the lead and for the device, yet, we can only invert the Hamiltonian of the device if we wish to calculate its complete GF matrix - the same cannot be done for the lead case since it is an infinite matrix. So the question arises as to how to calculate the g_{00}, or the Semi-infinite linear chain surface Green's Function (SGF).

If we simply picture the semi-infinite linear chain as a series of connections between principal planes g_{11} containing the same GF (in the 1D case the GF of one single pristine orbital), one can extrapolate that if we take the limit where the number of connected principal planes goes to infinity, *i.e.* a series of infinite equal perturbations, the GF of the last plane will converge to the value for the SGF S. This convergence implies that, in the event of implementing an additional equal perturbation to the SGF, both the unperturbed SGF g_{00} and the perturbed SGF G_{11} will have the same values S. If we enforce this condition on Eq.(2.22e), we reach:

$$S = G_{11} = g_{00} \qquad \Rightarrow \tag{2.24a}$$

$$S = g_{11} + g_{11}t_{10}St_{01}S\,, \tag{2.24b}$$

assuming $t_{10} = t_{01} = t$ and writing g_{11} as g, we can write:

$$S = \frac{\frac{1}{g} \pm \sqrt{\left(\frac{1}{g}\right)^2 - 4t^2}}{2t^2}\,. \tag{2.24c}$$

But $\frac{1}{g}$ is simply the Hamiltonian for one single orbital with onsite potential ϵ_0:

$$\left(\hat{\mathbb{I}}\epsilon_0 - \hat{H}\right)\phi = 0 \qquad \Rightarrow \qquad \text{(2.24d)}$$

$$\frac{1}{g} = (E - \epsilon_0) \qquad \Rightarrow \qquad \text{(2.24e)}$$

$$S = \frac{(E-\epsilon_0) \pm \sqrt{(E-\epsilon_0)^2 - 4t^2}}{2t^2}\,, \qquad \text{(2.24f)}$$

which is the analytic expression for the semi-infinite linear chain surface Green's function. Of the two solutions possible given by the plus or minus sign, we chose the one that ensures the density of states remains positive, *i.e.*, the sign that will make the Green's Function imaginary part negative.

2.1.4 Kubo Formalism for Transmission

With the device and its GF properly defined, we can start to inquire about the transmission properties of the system as the device changes in size or disorder concentration, and even as the disorder changes in nature. For this, we can employ Kubo's formalism in TB modelling to express the transmission tensor as a function of the GF of the system [45–48]

$$\Gamma(E) = \frac{4e^2}{h}\mathrm{Tr}\left[\tilde{G}_{ii}(E)V_{ij}\tilde{G}_{jj}(E)V_{ji} - V_{ji}\tilde{G}_{ij}(E)V_{ji}\tilde{G}_{ij}(E)\right] \quad , \qquad (2.25)$$

here the indexes i and j label two consecutive principal planes in the direction of the propagation ($j = i \pm 1$). These principal planes can be thought of as cross-section areas of orbitals in 3D structures with the normal vector pointing in the direction of the propagation. In the 2D case, these planes are reduced to lines of orbitals orthogonal to the direction of propagation, and in the 1D case to a point, or a single orbital (see Fig. 2.3). $\tilde{G}$ is a combination of the G^+ and G^- GFs of the system such that $\tilde{G} = \frac{1}{2i}(G^+ - G^-)$. It is evaluated at energy E and separated into its sub-matrices for the respective principal planes (G_{ii} and G_{jj}) and their off-diagonal sub-matrices (G_{ij} and G_{ji}). Finally, V_{ij} is the connecting operator matrix between the principal planes, which expresses the off-diagonal Hamiltonian sub-matrices relative to two consecutive planes. Simplifying this analysis to a 1D, single orbital linear chain case, the GF G_{ii} becomes the GF for a site i in the linear chain, and V_{ij} becomes the hopping in between sites t_{ij}.

Eq.(2.25) is an outcome of considering the current flow to happen in one single direction and of applying current conservation on the single-particle Kubo formula [47]. Indeed, after some consideration, it is easy to deduce via continuity that the current that flows between two consecutive sites must be the same as the current flowing in the rest of the sites (or planes) of the system if those are connected in series. This implies that having complete knowledge of the GFs of two consecutive principal planes is enough to calculate the transmission for the entire system, regardless of disorder concentration or positioning.

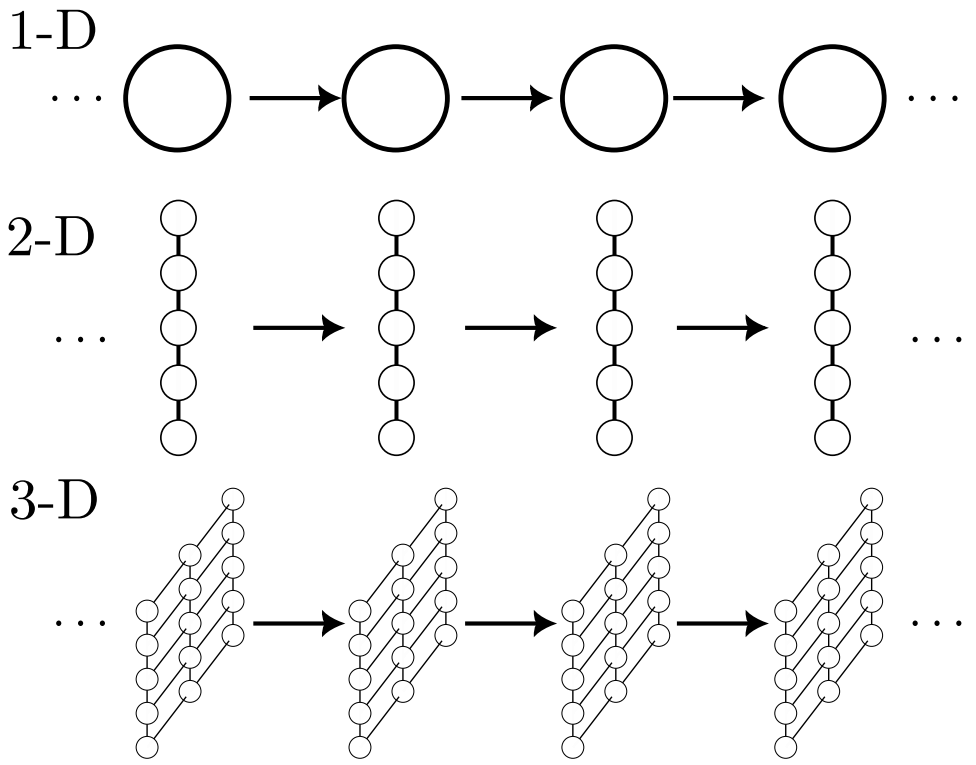


Figure 2.3: Principal planes for different dimensions.

Writing the transmission as a function of the GF immediately equips us with multiple tools, both analytical and numerical, that we can avail of to perform the transmission calculations from a Hamiltonian. In particular, the connecting characteristic between the regions of our system allows us to employ Dyson's equation for a perturbation to calculate the total GF of the system based on the GFs of each region. In this case, the perturbation added is in the form of a short-range potential behaving as the inter-region hopping, assuring that Dyson's series will have a closed-form solution. This inter-region hopping

takes the unperturbed state of two separate regions to the perturbed state that contains the connection.

2.1.5 Green's Function Iterative Algorithm

Since we know the complete Hamiltonian of our device, including all the disorder positions, and since this matrix is finite, one can, in principle, invert it to obtain the GF of the device. This inversion however is extremely costly and the number of numerical operations scale with the cube of the size of the device, or $\mathcal{O}(D^3)$. This is the price for acquiring the information of the full system of orbitals and how they interconnect through their hoppings and onsite potentials. But, for the purpose of calculating the transmission function of the system, this amount of information is superfluous. In fact, from Eq.(2.25) all we need is two consecutive submatrices of the GF of the system, the GFs of two consecutive principal planes (or two consecutive orbitals in 1D).

We can start with a device with disconnected orbitals, each of which has a very simple GF expressed by the inverse of its onsite potential. By employing Dyson's equations for every connection, one at a time, we can calculate the whole GF of the device from start to finish. Of course, calculating every GF element through Dyson's equations as implemented in Eq.(2.23) would be the same as inverting the matrix with extra steps. But, through the iterative approach that I am about to present, we do not need to calculate the effect of the perturbation in the whole device and connections every time we add an extra orbital - we are only concerned with the effect that each connection has on the GF of the last site or the surface GF of the device. In this way, we can step-by-step add orbitals until we reach the end of the device, at which point we will have the exact GF element for the last orbital and no other. We have already explored a similar idea when we calculated the SFG in Eq.(2.24f) - this equation grants us only the surface GF, or the GF of the last orbital of a semi-infinite linear chain, and the rest of the GF matrix remains unstudied. One can recover the other GF elements based on the SGF and the Hamiltonian if necessary with further calculation.

This is where Eq.(2.22f) proves to be very useful for it is the exact equation we need to calculate the surface GF of the device iteratively. For 1D, writing the onsite potential of the orbital to be connected i as ϵ_i (which can assume different values), and writing the connecting potential, or hopping, as t, we

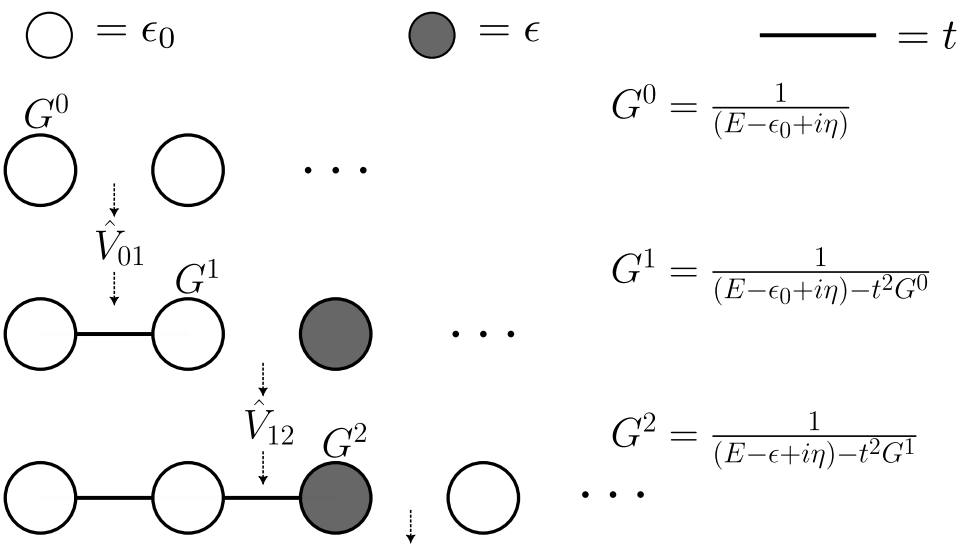


Figure 2.4: First steps of the iterative calculation of the Green's function of the device.

can express the GF of this orbital i after the connection as:

$$G^i = \frac{1}{(E - \epsilon_i + i\eta) - t^2 G^{i-1}}\,, \tag{2.26}$$

where G^{i-1} is the result of the previous iteration or the GF of the first orbital $G^0 = \frac{1}{E-\epsilon_0+i\eta}$ in case $i = 1$. Note that we added an infinitesimal imaginary value $i\eta$ to the energy, which guarantees that we will not encounter any singularity points in the root of the denominator which generally leads to numerical overflow errors. In this 1D case, the complexity of this approach scales linearly with the size of the system with $\mathcal{O}(D)$. For higher dimensions, this approach will scale as $\mathcal{O}(D \cdot d^3)$, where D is the number of principal planes in the direction of propagation and d is the number of orbitals in each principal plane.

Through equation 2.23, we can retroactively calculate the GF elements of other sites to obtain two consecutive principal planes, but we might not need to employ it. A smart choice of the consecutive principal planes is the end of the device and the beginning of the right lead. This approach relieves us from having to do any retroactive calculations inside the device and takes advantage of the analytical solution for the SFG of the lead (Eq.(2.24f)).

All that is left to be done is to implement the connection between the right lead and the device, again via Dyson's equation by calculating the surface GF of the device with the connection as a perturbation, recalculate the SGF of the

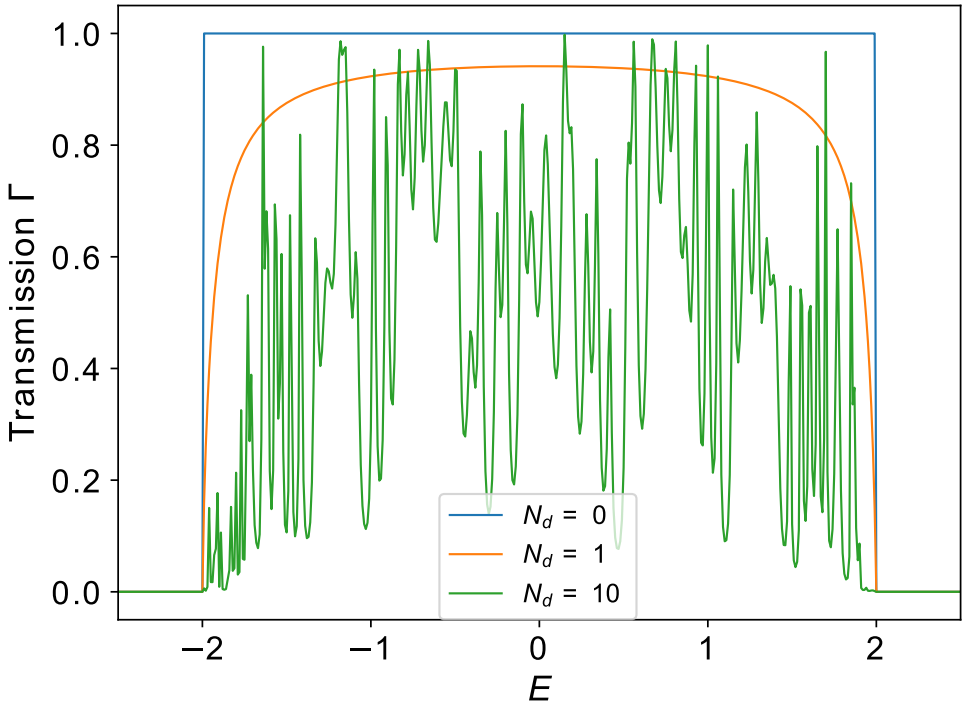


Figure 2.5: Transmission for a 1D lattice of 100 single-orbital sites ($\epsilon_0 = 0$, $\epsilon = 0.5$, $t = -1$). Each curve contains a different number of disordered orbitals, N_d. Note that the curves for $N_d = 0$ and $N_d = 1$ are symmetrical to $E = 0$. This is because these systems have inversion symmetry, so no matter what direction the wave comes from, the result will be the same. In the case $N_d = 0$, there is no disorder, so the inversion symmetry is evident. In the case $N_d = 1$, there is one disorder that can be placed at any point in the system but, because the system is connected by semi-infinite leads with the same onsite energy ϵ_0 as the pristine orbitals, this effectively results in a one-orbital system with the disordered onsite energy ϵ connected by two semi-infinite leads, and this system is naturally symmetric. For any case $N_d > 1$, the relative positions between the scatterers will cause different propagation of the GF, resulting in unpredictable transmission signals (up until $N_d = D$, the entirety of the device).

lead after the perturbation based on the new surface GF of the device, and we have all the values to input into the Eq.(2.25) for the transmission function of the system. This result can be seen in Fig. 2.5.

It is worth mentioning that this iterative approach can be used to calculate the SGF of the leads by iteratively adding new pristine orbitals until the value converges in relation to some tolerance. Despite being a good exercise for numerical calculation, this approach is computationally very expensive and less accurate in comparison to the implementation of the analytic solution of

Eq.(2.24c), which can be used for principal planes of any dimension.

Anderson Localization

Since we are dealing with a uniformly distributed disorder in a 1D system, Anderson Localization of our electron wave functions is bound to happen. This will consequently impact our transmission values as a function of the system size, as shown in Fig. 2.6. Especially, in Fig. 2.6b, we can see the characteristic exponential decay of transmission as a function of size due to the localization effect.

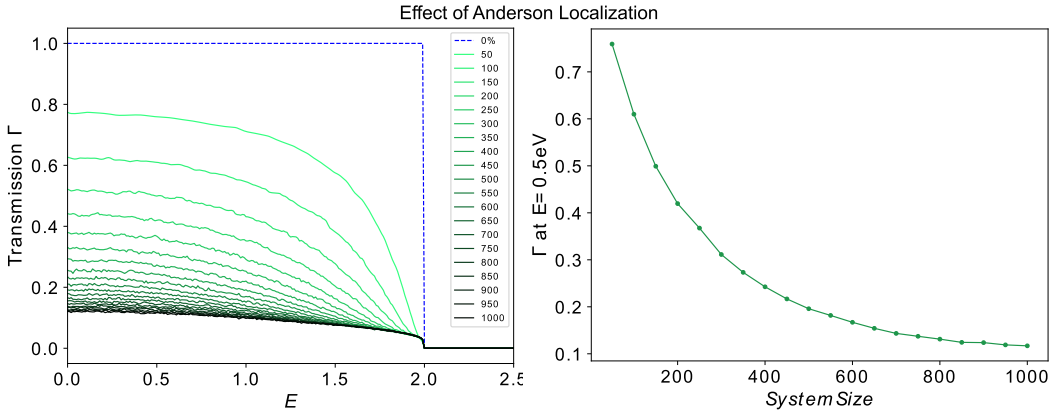


Figure 2.6: **a)** Average over 10^4 transmission calculations for a 1D lattice of sizes ranging from 50 to 1000, all with 20% disorder concentrations ($\epsilon_0 = 0$, $\epsilon = 0.5$, $t = -1$). Note that the average transmission values decrease as the system size increases, which can be seen in **b)** when looking at the same energy value of E=0.5eV. This illustrates the effect of Anderson localization in the calculation of transmissions.

This phenomenon is also present in the 2D case, with a different intensity. It is relevant to note that this localization effect affects equally all the transmission functions of systems with the same size, regardless of their disorder concentration values. Therefore, as long as we maintain the system size constant in our calculations, we are able to compare the transmission functions on an equal footing. Another condition we need to impose is that the system size shall not be much greater than the disorder localization length. If we meet both these conditions, we will be able to extract information from the comparison between different transmission functions, despite the Anderson localization effect.

Hexagonal Lattice

The iterative equations and generalized approach presented in the previous paragraphs will not change drastically from 1D to 2D systems, but in the 2D case, the resulting transmission functions will provide modelling for more realistic material applications. Yet it is worth noting some of the differences in the approach, particularly for hexagonal lattices, where the definition of principal planes can be slightly more intricate in comparison to a plain square lattice.

When viewing hexagonal lattices in a preferred direction, their repetition pattern can assume two distinct configurations: the zigzag form or, by rotating it 30°, the armchair form. Each of these configurations will yield a distinct transmission function and answer differently to the introduction of disorder. The hexagonal to principle plane parametrization is illustrated in Fig. 2.7 as well as the difference in transmission caused by the change in geometry.

Note that for the armchair case, the principal planes alternate to their mirror image at each step, in other words, they repeat only every second plane. This brings about a limitation in the transmission calculation: if we consider the semi-infinite leads to also possess this hexagonal structure and the left and right leads to be a reflection of each other, the connection to the device must be to planes of opposite chirality. This implies that the device must have an even number of principal planes so that the first and last principal planes match the necessary chirality for connection to the left and right leads.

For the zigzag case, on the other hand, the principal planes are the same at every iteration and are not mirrors of one another, but the SFGs for the left and right leads are different. That is because the chosen consecutive plane representation does not have reflection symmetry (observe the dashed lines in Fig. 2.7) like in the armchair case or the case of other geometries such as the square lattice, which causes the emergence of a virtual anisotropy in the propagation calculation of waves. In this way, the reflection of the left lead, which is calculated by propagating its Green's Function from the infinite left to the right, is not equivalent to the right lead. Instead, the right lead needs to be calculated by propagating its Green's Function from the infinite right to the left, taking into account the anisotropy of this representation and without changing the orientation of the crystal.

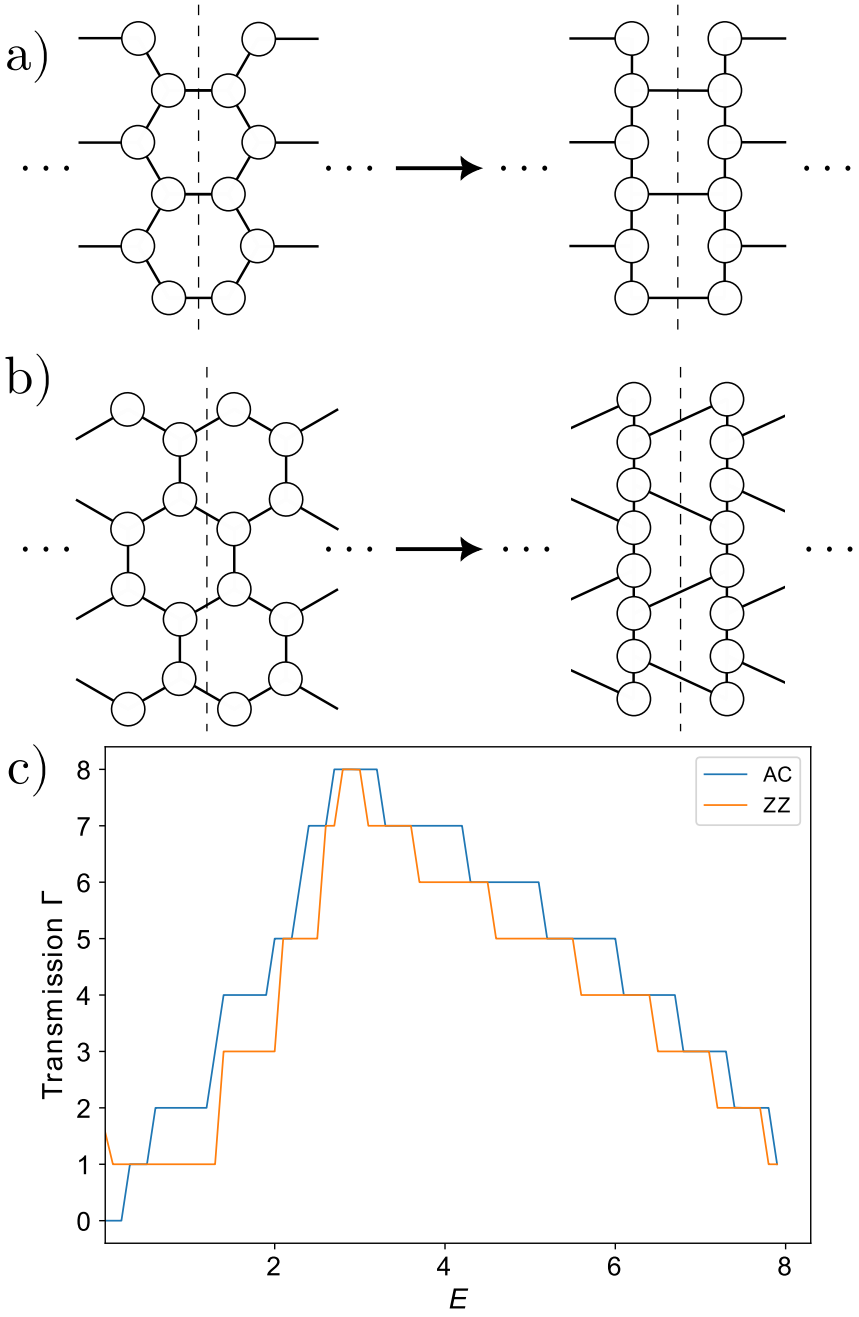


Figure 2.7: Parametrization of hexagonal lattices into principal planes for **a)** Armchair and **b)** Zigzag cases. All solid black lines represent the same hopping value and the dashed lines show the vertical reflection plane and separate two consecutive principal planes. The difference in the iteratively calculated transmission can be seen in the graph **c)**, depicting the positive part of the transmission spectrum using graphene parameters for a ribbon of 30x16 atoms.

2.1.6 Green's Function Polynomial Expansion

As soon as we start working with higher dimensionality, the computational cost of the iterative method becomes glaring, especially if we are interested in simulating large, realistic systems with many orbital sites in multiple directions. Furthermore, if we are interested in increasing the resolution of our transmission function simulations to cover more energy points (E) for a higher point density, we will find ourselves with an increased complexity of $\mathcal{O}(D \cdot d^3 \cdot E)$ per simulation. Later in Sec. 2.2.4 we will understand that the accuracy of the inversion method presented in this thesis is directly proportional to the system size, the energy density, and the spectrum range of the calculation, all of which add to the overall cost. To escape this rapidly increasing computational cost, our best strategy is to give up the exact for the very good approximate.

So far, we have fully employed our paradigm-dependent theory to devise the exact solution for our model, and, despite human fascination for the perfect, this exactness comes with proportional cost. Luckily, when it comes to practical concrete applications our system description can never be absolute, our models never account for every effect nor is our theory ever complete. This allows for some leeway to employ approximations as long as our deviations are small enough compared to the scale of interest.

Polynomial Methods

By the end of the past century, many efforts had been made to circumvent the complexity problem of calculations at the cost of dropping the requirements for a complete and exact knowledge of the spectrum and pursuing, instead, the best approximate description [49]. The first natural approach was already considered from the early days of quantum mechanics - to expand the spectral quantities in terms of its power moments, which can be very efficiently iteratively calculated. To remedy the numerical instabilities arising by iterations utilizing ordinary power moments of the energy, polynomials of the energy were suggested instead. The polynomials worked well to properly weigh the power moments of the energy at the boundaries of the spectrum, but alongside, they brought another complication - Gibb's oscillations.

Gibb's oscillations occur when a polynomial series describing a non-smooth function is truncated at a finite value. Due to the overshooting nature of the polynomial expansions, oscillations emerge near the not continuously differen-

tiable points. This became known as the Gibbs phenomenon. To deal with this, the Kernel Polynomial Method (KPM) was coined [49, 50]. The kernel would serve as a wrapping function, a regularisation factor to ensure the oscillations were being taken care of in the right places. The kernel is responsible for smoothing the function's discontinuous points to improve the convergence of the polynomials approximation [51].

For simple calculations such as the density of states, we use kernels such as the one derived by Jackson [52] or Lorentz kernel for its parametrization flexibility. For more complex calculations such as conductivity or optical conductivity, another approach shows better efficiency. Because in these cases we are dealing with a second-order correlation function, simple polynomial expansions of the Hamiltonian will not suffice, instead, we apply the polynomial expansion method directly with its Green's function operator.

These methods can have linear or quasi-linear scalability in the case of sparse matrices (depending on the quantity being calculated) or quadratically otherwise [53]. The matrices we are concerned with in this work, despite being big in size, can be considered sparse because the orbitals interaction range is relatively small in comparison with the system size - the interaction ranges only up to close neighbours. This low resource scalability is the reason why polynomial methods are now used to approach a variety of problems involving correlation, responses, or Green's functions of large matrices (in cases such as density of states, static correlations, or dynamic correlations) [53–55]. It also became a component for multiple methods such as Monte Carlo simulations and Cluster Perturbation Theory (CPT) [49].

Polynomial Expansion

Introducing a function scalar product between integrable functions $f(x)$ and $g(x)$ in a certain interval $[a, b]$

$$\langle f|g\rangle = \int_a^b dx\, w(x) f(x) g(x)\,, \tag{2.27}$$

where $w(x)$ is a weight function, one can find a complete set of polynomials $p_n(x)$ such that they fulfil orthogonality relations

$$\langle p_n|p_m\rangle = \delta_{n,m}/h_n\,, \tag{2.28}$$

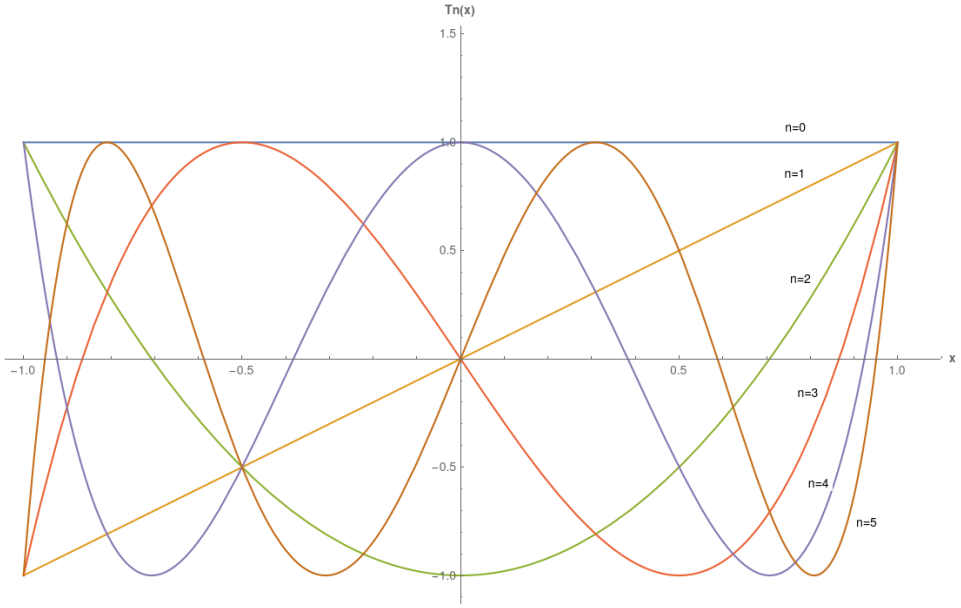


Figure 2.8: Normalized Chebyshev Polynomials of the first kind of degree n from 0 to 5.

with $h_n = 1/|\langle p_n|p_n\rangle|$ granting the normalisation. The completeness and orthonormality of this set of polynomials allows us to express, through this scalar product, a function $f(x)$ in terms of the $p_n(x)$:

$$f(x) \equiv |f\rangle \ , \tag{2.29a}$$

$$|f\rangle = \sum_{n=0}^{\infty} \frac{|p_n\rangle \langle p_n|}{\langle p_n|p_n\rangle} |f\rangle \ , \tag{2.29b}$$

$$f(x) = \sum_{n=0}^{\infty} \nu_n p_n(x) \qquad \text{with } \nu_n = \langle p_n|f\rangle \, h_n \, . \tag{2.29c}$$

In principle, for a function expansion, any type of orthogonal polynomial can be used, but some have been better studied than others [49, 50]. From all the rising families of polynomials in the 90's studies, the Chebyshev polynomials proved to be of outstanding fast convergence. This family of polynomials expansion also has a close relation to the Fourier transform [56], which is an important characteristic for the derivation of optimal kernels for finite order expansions.

Chebyshev polynomials are of two kinds, but only the first kind is bounded

inside the interval of definition $[a, b] = [-1, 1]$. We express this kind as

$$T_n(x) = \cos[n \arccos(x)] \,, \tag{2.30}$$

or equivalently via its recursion relations as

$$\begin{aligned} T_0(x) &= 1 \,, \\ T_1(x) &= x \,, \\ T_n(x) &= 2xT_{n-1}(x) - T_{n-2}(x) \,. \qquad (n \geq 2) \end{aligned} \tag{2.31}$$

Given the weight function $w(x) = (\pi\sqrt{1-x^2})^{-1}$ we can define a scalar product using Eq.(2.27) and derive these polynomials orthogonality relation as

$$\langle T_n | T_m \rangle = \frac{1 + \delta_{n,0}}{2} \delta_{n,m}. \tag{2.32}$$

Finally, using Eq.(2.29c), a function $f(x)$ can be expressed in terms of a series of this kind via

$$f(x) = \frac{1}{\pi\sqrt{1-x^2}} \sum_{n=0}^{\infty} \frac{2\mu_n}{1 + \delta_{n,0}} T_n(x), \tag{2.33}$$

with the modified coefficients, or moments of the expansion, μ_n given by

$$\mu_n = \int_{-1}^{1} dx \, f(x) T_n(x). \tag{2.34}$$

From these equations, we can appreciate the power of the polynomial method - once the moments (2.34) are known, we can recover $f(x)$ for any x from Eq.(2.33) with little cost of the order of $\mathcal{O}(N)$, where N is the number of moments used. Verily, the moment calculations themselves are the most expensive part of the simulation.

Naturally, because the Chebyshev polynomials are defined only in the $[-1, 1]$ interval, we need to re-scale our quantities to fit in the same interval, in our case, we need to re-scale our Hamiltonian. Because our Hamiltonian depends on the eigenvalues ϵ of its matrix, to fit the $[-1, 1]$ interval a simple linear transformation of the Hamiltonian and all energy scales is needed:

$$\begin{aligned} \tilde{H} &= (H - a_+)/a_-, \\ \tilde{\epsilon} &= (\epsilon - a_+)/a_-. \end{aligned} \tag{2.35}$$

Given the extremal eigenvalues of the Hamiltonian, ϵ_{min} and ϵ_{max}, the scaling factors above read

$$a_- = \frac{\epsilon_{max} - \epsilon_{min}}{2 - \eta}\,, \tag{2.36a}$$

$$a_+ = \frac{\epsilon_{max} + \epsilon_{min}}{2}\,, \tag{2.36b}$$

the parameter η being a small cutoff to avoid stability problems near the boundaries of the interval $[-1, 1]$. It can be adapted as a function of the resolution of the expansion, *i.e.*, for a finite N order expansion, η can be written as $\eta = 1/N$.

Chebyshev Polynomials Green's Function Method

We have already discussed in the previous sections how powerful is to approach spectral calculations by availing of Green's Functions as tools. The alternate perspective provided by analyzing Kubo's formula in the light of the GFs simplifies the numerical approach we employ to solve these equations. Now we employ the Chebyshev polynomial expansion to approximate the value of these GFs. The Chebyshev Polynomials Green's Function method (CPGF) provides great accuracy, fast convergence, and displays uniform resolution over the calculated spectrum [49, 53, 57]. This polynomial expansion also has a reduced dependency on kernels since the GFs are usually calculated accounting for an infinitesimal imaginary part ($i\eta$) in the energy, which provides a smoothing effect in the shape of the spectral function.

To expand the GF of a system (Eq.(2.4)) in Chebyshev polynomials of the Hamiltonian, we use first the identity [58]

$$e^{-ixz} = \sum_{n=0}^{\infty} \frac{2i^{-n}}{1 + \delta_{n,0}} J_n(z) T_n(x), \qquad |x| \leq 1, \tag{2.37}$$

where $J_n(z)$ is the Bessel function of first kind, along with Eq.(2.33) to write

$$\hat{G}(E + i\lambda) = \frac{1}{i} \int_0^{\infty} dt\, e^{i(E+i\lambda)t} \left[\sum_{n=0}^{\infty} \frac{2i^{-n}}{1 + \delta_{n,0}} J_n(t) T_n(\hat{H}) \right]. \tag{2.38}$$

This Laplace transform of the Bessel function has the solution [59]

$$\int_0^\infty dt\, e^{-st} J_n(t) = \frac{1}{\sqrt{1+s^2}} \left(\sqrt{1+s^2} - s\right)^n , \tag{2.39}$$

which, in the equation above, results in

$$\begin{aligned} \hat{G}(E+i\lambda) &= \sum_{n=0}^{\infty} g_n(E+i\lambda) T_n(\hat{H}) \,, \\ g_n(z) &\equiv \frac{2i^{-1}}{1+\delta_{n,0}} \frac{\left(z - i\sqrt{1-z^2}\right)^n}{\sqrt{1-z^2}} \,. \end{aligned} \tag{2.40}$$

Or, iteratively

$$\begin{aligned} g_0(z) &= \frac{1}{i\sqrt{1-z^2}} \,, \\ g_1(z) &= 2(z - i\sqrt{1-z^2}) g_0(z) \,, \\ g_n(z) &= (z - i\sqrt{1-z^2}) g_{n-1}(z) \,. \end{aligned} \tag{2.41}$$

Note that, since we are calculating the GF from its polynomial expansion, we no longer need to be concerned with the propagated GF as in the iterative approach of the previous section.

To calculate the conductivity, we re-write Kubo's formula in terms of Green's function of the Hamiltonian as in the Kubo-Bastin formulation [60]. Ignoring electron-electron interaction we can then write the Kubo formula for longitudinal conductivity in the direction x as

$$\sigma_{xx}(\mu, T, \lambda) = \int dE\, f(\mu, T, \hat{H}) \sigma_0(E, \lambda), \tag{2.42}$$

where $f(\mu, T, \hat{H}) \equiv 1/(1 + e^{-(\mu - \hat{H})/k_B T})$ is the Fermi-Dirac distribution for a chemical potential μ and temperature T and σ_0 is the conductivity at $T = 0$ [53]:

$$\sigma_0(E, \lambda) = \frac{2\hbar e^2}{\pi\Omega} \mathrm{Tr}\left[\mathrm{Im}\hat{G}(E+i\lambda)\hat{v}_x \mathrm{Im}\hat{G}(E+i\lambda)\hat{v}_x\right], \tag{2.43}$$

where Ω volume of the sample and $\hat{v}_x = [\hat{x}, \hat{H}]/i\hbar$ is the velocity operator. Using our Chebyshev Green's Function expansion of Eq.(2.40), we can write

Eq.(2.43) as

$$\sigma_0(E,\lambda) = \frac{2\hbar e^2}{\pi\Omega}\sum_{n,m=0}^{N-1} \mathrm{Im}[g_n(E+i\lambda)]\mathrm{Im}[g_m(E+i\lambda)]\mathcal{V}_{nm}, \tag{2.44}$$

with

$$\mathcal{V}_{nm} = \mathrm{Tr}\left[\hat{v}_x T_n(\hat{H})\hat{v}_x T_m(\hat{H})\right] \tag{2.45}$$

being our conductivity expansion moments. Given the eqs. 2.41 for the GF moments of the Hamiltonian Chebyshev expansion, the trace in Eq.(2.45) is the only quantity left to be evaluated. Yet another technique is employed to tackle this: stochastic evaluation of traces.

Stochastic Evaluation of Traces

Extremely good approximations have been made in the past to evaluate the traces of large matrices [49, 61, 62]. This method consists of evaluating the trace through random vectors.

For an arbitrary basis $\{|i\rangle\}$, random vectors are defined as

$$|r\rangle = \begin{pmatrix} \xi_1^r \\ \xi_2^r \\ \vdots \\ \xi_D^r \end{pmatrix}, \quad r = 1, 2, \cdots, R \tag{2.46}$$

with each of its components ξ_i^r being a random complex number that obeys the following distribution:

$$\begin{aligned} &\langle\langle \xi_i^r \rangle\rangle = 0, \\ &\langle\langle \xi_i^r \xi_j^{r'} \rangle\rangle = 0, \\ &\langle\langle \xi_i^{r\star} \xi_j^{r'} \rangle\rangle = \delta_{i,j}\delta_{r,r'}, \end{aligned} \tag{2.47}$$

being $\langle\langle \cdots \rangle\rangle$ the statistical average operation:

$$\langle\langle \xi_i^r \rangle\rangle = \lim_{N\to\infty} \frac{1}{N}\sum_{i=0}^{N} \xi_i^r. \tag{2.48}$$

With that, one can evaluate the trace of a Hermitian operator $\hat{H}$ defined in the same basis $\{|i\rangle\}$, *i.e.* with matrix elements $H_{ij} = \langle i|\,\hat{H}\,|j\rangle$. Its trace is

then given by

$$\Theta = \lim_{R\to\infty} \frac{1}{R} \sum_{r=1}^{R} \langle r| \hat{H} |r\rangle \,, \tag{2.49}$$

which can be statistically averaged to get

$$\begin{aligned} \langle\langle\Theta\rangle\rangle = \left\langle \left\langle \lim_{R\to\infty} \frac{1}{R} \sum_{r=1}^{R} \langle r| \hat{H} |r\rangle \right\rangle \right\rangle &= \lim_{R\to\infty} \frac{1}{R} \sum_{r=1}^{R} \sum_{i,j=1}^{D} \langle\langle \xi_i^{r\star} \xi_j^r \rangle\rangle H_{ij} \\ &= \sum_{i=1}^{D} H_{ii} = \mathrm{Tr}(\hat{H}). \end{aligned} \tag{2.50}$$

The approximation for the trace calculation comes when we do not use $R \to \infty$ random vectors to determine our momentum, rather we use a small number of random vectors $R \ll D$ which causes fluctuations that can be found by calculating $(\delta\Theta)^2 = \langle\langle\Theta^2\rangle\rangle - \langle\langle\Theta\rangle\rangle^2$. We get for the fluctuation [49, 63]

$$(\delta\Theta)^2 = \frac{1}{R} \left(\mathrm{Tr}(H^2) + (\langle\langle |\xi_i^r|^4 \rangle\rangle - 2) \sum_{j=1}^{D} H_{jj}^2 \right), \tag{2.51}$$

from which one can determine the relative error

$$\frac{\delta\Theta}{\Theta} \approx \frac{1}{\sqrt{DR}}. \tag{2.52}$$

That means that not only the error decrease with the number of random vectors used R, but the dimension D of our system too. In our case, because we are interested in relatively large systems, most of the time very few random vectors will be needed, granting fast calculations of the conductivity momenta.

CPGF for Longitudinal Conductivity and Optical Conductivity

Applying this trace approximation to our Eq.(2.45), we can write our moments as [53]

$$\mathcal{V}_{nm} = \frac{1}{R} \sum_{r=1}^{R} {}_n \langle \bar{r}| \hat{v}_x |r\rangle_m \,, \tag{2.53}$$

where

$$\begin{aligned} |r\rangle_m &= T_m(\hat{H})\,|r\rangle \quad \text{and} \\ |\bar{r}\rangle_n &= T_n(\hat{H})\,|\bar{r}\rangle \quad \text{, with} \\ |\bar{r}\rangle &= \hat{v}_x\,|r\rangle\,. \end{aligned} \tag{2.54}$$

These can then be calculated recursively for $n, m = 0, \cdots, N-1$.

As discussed before, due to the lack of translation symmetry of our Hamiltonian, we make these calculations using the position space. Defining the quantities

$$\psi_n^{(r)}(x_k, y_k) = \langle x_k, y_k | r\rangle_n\,, \qquad \phi_m^{(r)}(x_k, y_k) = \langle x_k, y_k | \bar{r}\rangle_m\,, \tag{2.55}$$

with k being the index for site coordinates ($k = 1, \cdots, D$). Then I can rewrite Eq.(2.53) as

$$\mathcal{V}_{nm} = \frac{1}{R}\sum_{r=1}^{R}\sum_{k,k'=1}^{D} \phi_m^{(r)}(x_k, y_k)\psi_n^{(r)}(x_{k'}, y_{k'})\,\langle x_k, y_k|\hat{v}_x|x_{k'}, y_{k'}\rangle\,. \tag{2.56}$$

The last term can be written, from the velocity operator definition, as

$$\begin{aligned} \langle x_k, y_k|\hat{v}_x|x_{k'}, y_{k'}\rangle &= i(x_{k'} - x_k)\,\langle x_k, y_k|\hat{h}|x_{k'}, y_{k'}\rangle\ , \\ &= i\Delta_x(k, k')t_{kk'}\,, \end{aligned} \tag{2.57}$$

where $\Delta_x(k, k')$, is the longitudinal distance between the orbitals k and k' in the x direction and $t_{kk'}$ is the off-diagonal Hamiltonian matrix element between orbitals k and k', or the hopping between these orbitals.

This marks a great decrease in the inversion cost of our Hamiltonian from the exact $\mathcal{O}(D^3)$ to the approximate $\mathcal{O}(D^2)$ with high accuracy in large systems given by Eq.(2.52). Furthermore, because we are dealing with a sparse Hamiltonian, the quantity of computational steps drops from $\mathcal{O}(D^2)$ to $\mathcal{O}(D \times z)$, where z is the number of first neighbour connections and $\vec{\tau}$ are the specific lattice vectors:

$$\mathcal{V}_{nm} = \sum_{k=1}^{D}\phi_m^{(r)}(x_k, y_k)\sum_{\vec{\tau}}^{z}\tau_x\psi_n^{(r)}(x_k + \tau_x, y_k + \tau_y)\,\langle x_k, y_k|\hat{h}|x_k + \tau_x, y_k + \tau_y\rangle\ . \tag{2.58}$$

concluding the calculation for the DC conductivity. A diagram for the numer-

ical implementation of this method is available in Appendix A.

In the same fashion, we can calculate the optical conductivity, another second-order correlation function at finite temperature. For the Anderson model for optical conductivity, we can write the regular part ($\omega > 0$) of the optical conductivity as a function of frequency ω as [49, 64]

$$\begin{aligned} \sigma(\omega) &= \frac{1}{\omega}\int_{-\infty}^{+\infty} dE\, j(E, E+\omega)[f(E) - f(E+\omega)] \quad \text{, with} \\ j(E, E') &= \frac{1}{\Omega}\sum_{n,m} |\langle n|J_x|m\rangle|^2 \delta(E-\epsilon_n)\delta(E'-\epsilon_m), \end{aligned} \tag{2.59}$$

where $J_x = -it\sum_i (c_i^\dagger c_{i+x} - c_{i+x}^\dagger c_i)$ is the x component of the current operator with $(c^\dagger, c)$ being the electron creation and annihilation operators; $|m\rangle$ and $|n\rangle$ are eigenvectors of $\hat{H}$ with eigenvalues ϵ_m and ϵ_n and Ω is the area of the system. The quantity $j(E, E')$ can then be expanded in a series of Chebyshev polynomials with the expansion moment μ_{lm} being calculated as [64]

$$\mu_{lm} = \frac{1}{\Omega}\mathrm{Tr}\left[T_l(\hat{H})J_x T_m(\hat{H})J_x\right]. \tag{2.60}$$

This trace can then be calculated similarly to Eq.(2.45) and the resulting function be wrapped by a kernel. A Chebyshev Green's function approach to this calculation can be seen in references [57, 65, 66].

Note that for this quantity, we perform an extra sum over the energies of the system compared to the DC case. This makes it so that the optical conductivity functions carry more *dense* information about the system and, as we will later see, this is responsible for a more precise inversion when using our method.

2.1.7 Density Functional Theory Parametrization

With the model and formulations established, the only ingredient remaining to perform the numerical calculations is the value of the Hamiltonian parameters, which will describe, in our TB modelling, the onsite potentials of the orbital and the inter-orbital potentials, or hoppings. They are, nonetheless, an essential piece of the calculation for the precision of these parameters will dictate the precision and applicability of the calculated spectral functions. We aim to perform calculations with a high level of realism so that the inver-

sion procedure finds applicability beyond the realm of theoretical calculations, *i.e.* in real-life scenarios. For this, we employ the Density Functional Theory (DFT) [67,68] method to obtain TB parameters originating from *ab initio* calculations. By acquiring parameters this way, we promote the TB modelling from a semi-empirical approximate description to a reliable quantitative calculation tool [69].

As opposed to the simplified tight-binding Hamiltonian of Eq.(2.6), the DFT one includes the electron-electron interaction term, resulting in the expression:

$$\hat{H} = \hat{T} + \hat{U} + \hat{V}\,, \tag{2.61}$$

where the Hamiltonian ($\hat{H}$) is expressed in terms of the kinetic energy ($\hat{T}$), the electron-electron interaction ($\hat{U}$) and the external potential ($\hat{V}$), which is determined by the system in hands. The addition of the electron-electron turns the problem into solving a coupled many-body Schrodinger Equation, massively increasing the complexity. From DFT theory, one can map this many-body problem into a single-body one by writing the observables as functionals of the electron ground-state density. This, however, introduces the cost of complicating the potential $\hat{V}$ by introducing an exchange-correlation term that has to be solved self-consistently. The single-particle potential assumes then the form:

$$V_s(\boldsymbol{r}) = V(\boldsymbol{r}) + \int \frac{n(\boldsymbol{r'})}{|\boldsymbol{r} - \boldsymbol{r'}|} d\boldsymbol{r'} + V_{XC}\,, \tag{2.62}$$

where $V(\boldsymbol{r})$ is the external potential, the integral comprises the electron-electron Coulomb repulsion, and V_{XC} is the exchange-correlation potential, which is a functional of $n(\boldsymbol{r})$ and whose form is not generally known. The electron density $n(\boldsymbol{r})$ is written in terms of the system's orbitals as:

$$n(\boldsymbol{r}) = \sum_i |\phi(\boldsymbol{r})|^2\,. \tag{2.63}$$

Since V_{XC} depends on $n(\boldsymbol{r})$ and $n(\boldsymbol{r})$ comes from the solution of the eigenvalue equation involving $V_s(\boldsymbol{r})$, we end up with a self-consistent set of equations.

Note that the calculations in the previous sections could all be modelled directly from a DFT approach, but this brings two major problems. Firstly, because of the self-consistent calculation of the exchange-correlation function, the computational cost of performing DFT calculations is far superior to that of TB calculations, especially as the system size increases. Not only there is a

superior level of detail in the definitions of the electrostatic potentials, but also the self-consistent equations demand expensive long converging loops [35, 69]. Secondly, DFT is best suited for performing calculations of periodic structures when using planar waves basis-sets [69–71], which is not our case once disorder is added to our system. Yet, DFT can still prove extremely useful for the task at hand.

One strategy employed in this work is to use the first-principles DFT to derive the TB parameters of a collective set of orbitals defining a grid of multiple unit-cells (a super-cell) of our pristine system and later implement disorder in the form of modified values for onsite potentials and hoppings. The other approach, as we will see in more detail in Chapter 4, is to use DFT parametrization for periodic structurally disordered settings, that is, to derive parameters for entire super-cells containing one kind of structural disorder such as vacancies, adatoms, extra hoppings, *etc.*, and utilize the entire disordered super-cell parametrization as a singular disorder to replace pristine super-cells of our original system with a given concentration [72, 73].

Although this approach possesses some resemblances, it is not the same as the DFTB (Density-Functional Tight Binding) one, which casts the TB energy parameters calculation as a function of the electron density in a form that is relatable to DFT calculation expanded around a reference density [36, 74]. Instead, the TB parameters here are derived via Wannier Function maximum localization, a form of mapping the DFT self-consistent electronic structure results into a smaller set of atomic orbitals of interest (given by the Wannierization of a specific system) [75–79].

2.2 Inversion Method

Having laid down the necessary toolset for the theoretical calculations, let us now study how to apply it to solve inverse problems. In this section, we are mainly concerned with the inverse problems involving disordered solid-state devices. The solution we propose here will be optimized to obtain structural information from different spectral signals of these systems by extracting information from the disorder characteristic signatures. For that, we will avail of stochastic techniques to approach the inversion problem in contrast to analytical models of inversion. That said, the methodology proposed in the following pages has proven itself extremely powerful and may find application in other

scenarios and disciplines.

2.2.1 Approaching the Inversion Problem

Inversion problems are remarkably intricate ones. As we will see in the next pages, a varied number of challenges present themselves when we attempt to solve such a kind of problem. Let us present these problems and solutions gradually to familiarize ourselves with the problem we propose to solve throughout this thesis.

Let $\Gamma_I(E)$ be a measured signal relative to a spectral quantity of an unknown system that we want to characterize. Assuming realistic variance regarding the purity of our sample, this system will find itself in a certain configuration of many possible ones, a configuration in which we expect the realistic system to be subject to unknown concentrations of multiple different types of disorder. The specific configuration which we aim to characterize (*e.g.* to determine the value of the disorder concentrations) we call the *input configuration.*

Say this $\Gamma_I(E)$ is the DC conductivity of such input configuration, and by observing and operating on this signal we want to identify the concentration n_I of any specific disorder. The first step is to model the pristine version of this system theoretically, using the tools described in the previous sections. We then introduce to this model the specific disorder in an arbitrary concentration n and calculate that desired spectral quantity for N_c different cases, each with a different configuration of disorder placement. This will leave us with multiple signals $\Gamma_i(E, n)$, with $i = 1, \cdots, N_c$. Each one of these configurations yields a different, unique conductivity signal. If we want to recover the original Γ_I by naively observing each separate signal, we would have to compare the input to every single one individually trying to find a match. To find this match is to solve the inverse problem, for then we would have access to the configuration that generated the match to our input. It is theoretically possible to find our input configuration this way if N_c is large enough to cover all possibilities, but we would have to calculate the conductivity for

$$N_c = {}_nC_r = \frac{D!}{(nD)!((1-n)D)!} \tag{2.64}$$

different configurations where D is the system size. For a typical bidimensional

system presented later in this thesis, this would mean approximately 10^{173} configurations conductivity calculations. These calculations would have to be repeated for each concentration value n we wish to probe until we find the precise configuration at concentration n_I. Needless to say, this is not feasible with current processing power.

Luckily we do not need to rely on such a brute-force approach. It is possible to solve the inverse problem in a much less costly way, but be aware that there is no free lunch. If we want to find the exact configuration of the system with 100% precision, we have to use the approach described above. Yet, we can redefine our problem in such a way that the precision and guaranteed information can give way to lower computational complexity and a realistic shot to solve the problem. Once again, just like in the previous section, we give up the mathematically exact for the very good approximate. Let us see how we can approach the problem in such a reasonable way.

Often we are not concerned with the atomic position of the impurities in the system for most of our macroscopic measurements are a result of the combined effect of the relative position of the scatterers. Especially when dealing with transmission functions, the relative position of the scatterers holds paramount importance, as we can read from Eq.(2.43), where the velocity operator is responsible for extracting these scattering relative distances. Furthermore, in the process of fabrication of real devices seldom do we get to pick the scatterer positions, they are effectively randomly placed. In this way, we can let go of our first degrees of freedom, contributing to lowering the cost of our inversion.

Yet another step can be made in this direction by freeing the positional degrees of freedom of the first scatterer as well as the distance and angular degrees of freedom that determine its connection to the other ones. That is the same as assuming that the scatterers are isotropically distributed in our system and that there is no preferred direction in our interaction. The system and its output can then be determined by the number of scatterers, or if the dimensions of the system are also fixed (yet another degree of freedom), we can refer to these systems by their scatterer concentration. Behind this approximation rests the assumption that every host system with the same concentration of a certain disorder will behave similarly. In the systems and quantities that we will cover in this thesis, these assumptions hold. But that is not always the case. As illustrated in Appendix B, if the calculation of the quantity of interest has a preferred direction and/or a source point within the

system, we can no longer rely on these approximations.

An immediate consequence of relaxing the requirement for the exact is the emergence of errors, and we have to be prepared to handle them. By grouping every host with the same concentration of disorder under the same label, we start to effectively consider average effects and no longer individual signals. We hope that these different configurations will behave similarly enough so that the distribution of their signals will center around an average signal with some small standard deviation, this standard deviation being the measurement of our error, or of how off we usually are when we reduce the complete description of the disordered configuration to its concentration value average. An example of this can be seen in the square lattice case in Fig. 2.9.

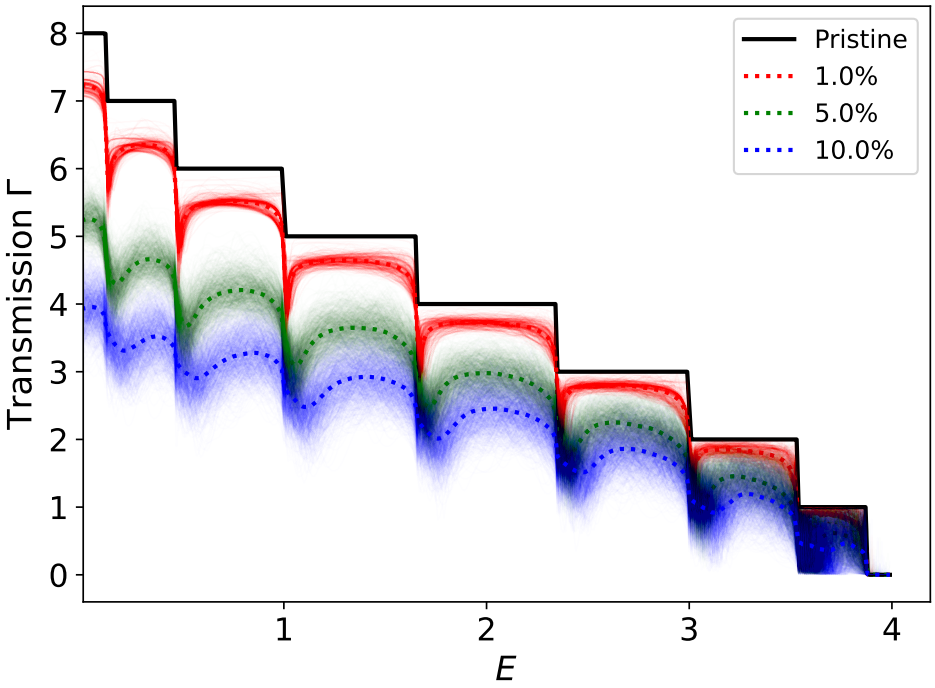


Figure 2.9: Square lattice transmission of 1000 systems for each different substitutional disorder concentration. The dashed line represents the configurational average of each concentration. The solid curves represent one transmission calculation whose concentration is indicated by its colour. Together, they illustrate the configuration distribution in the transmission space. The black solid line is the transmission for the pristine case and the black regions under it are the regions where the distributions of each curve overlap one another.

This brings out the stochastic character of our inversion method, which can be interpreted to be a Monte-Carlo-like approach to inversion. When we

assume the averages converge with a small finite number of configurations, we reduce the number of calculations needed to identify systems for a determinate concentration value. This average, then, becomes the representative of that set of configurations. The convergence rate to reach an average that carries the characteristic signature of our disorder is a function of the quantity being measured as well as the dimensionality of our system. In general, the more information is input into this calculation, the greater will be the convergence. The amount of information is also dictated by the ergodic principle behind this averaging and we will return to discuss it later in section 2.2.4.

As soon as we introduce a distribution with a relevant standard deviation, we introduce along with it a resolution for our measurements. For example, we may be able to identify the difference between a signal originating from a system of concentration of 1% and that of 1.01% by using the costly, exact approach mentioned before, but the same would be harder to do in our proposed stochastic averaging approach. If the effect of the 0.01% increase in scatterers is not sufficiently strong to separate the distributions with enough distance in relation to their standard deviation so that there is no significant overlap, then there will not be sufficient resolution to identify the different concentrations. This is illustrated in a region of the spectrum of Figure 2.9 close to 4 eV, where the transmission distributions of different colours overlap forming a black region where one can no longer differentiate between the distributions. In such regions, there is not enough information to differentiate between the concentrations of interest and if one uses only this region for inversion calculations, the method will yield a high error. This may be seen as a shortcoming if we are interested in this level of precision, but if our typical values are further apart, this represents instead the release of another degree of freedom from our problem. That is because we effectively discretized our problem in the concentration space, with the resolution given by our standard deviations. In this setting, we can only identify concentrations that are far enough apart while assuming that similar disorder concentrations will have a similar impact on the signal.

This approximation framework is enough to redefine our inversion problem in such a way that the cost of reaching the solution is small enough for our computational resources. Based on it, we can now devise an algorithm for inverting signals as we will soon see in section 2.2.3. However, an important aspect of inversion problems is yet to be discussed - we have to determine if

such a problem has a unique solution in the first place.

2.2.2 Inverse Problem Ill-Posedness

Inverse problems universally suffer from one common issue - we often do not know what the problem precisely is. In other words, these are often ill-posed, or ill-defined problems, problems that can be interpreted in different ways and yield more than one solution [2, 3, 13]. Inverse problems originate when we attempt to determine the cause of an effect and a unique solution to these problems is only possible if the question is asked appropriately - if enough constraints are set up so that there is no room left for ambiguity.

Take the example of a shadow. If someone sees a circular shadow cast on a wall, one may be quick to think that the body casting the shadow is a sphere. Yet many objects would be just as good candidates, such as a disk, a cylinder, or a combination of semi-circular objects to name but a few. The problem of acquiring the caster of the shadow is in essence the same as that of acquiring the configuration from its spectral function. In the condensed matter case, we are observing the projection of a Hamiltonian of the system (the object) into the conductivity space (the wall) due to the effect of measurements at different energies (the light cast at different positions). They are both inverse problems.

The ill-posedness for the case of spectral inversion is apparent when a certain signal could be generated by multiple different systems. Be it different hosts with the same spectral behaviour, different types of disorder in a host that can generate similar signatures when in certain concentrations, or systems of different sizes and shapes, all are examples of possible solutions for the same spectral inversion. I emphasize especially the case of different types of disorder since these are the most unpredictable ones when dealing with real systems and experimental measurements. A plethora of disorder types can behave as scatterers in our system, and while some are expected to be present in a range of concentrations, lots are unpredictable, a consequence of the different fabrication methods. Each of these impurities can cause an alteration in our signal that can interfere with the characterization via the inverse method. For example, as we will later see in Chapter 3, vacancies are an expected disorder in MoS_2 films and they have a particular effect on the conductivity gap. By inverting the system based on these characteristic signatures we can identify the concentration of vacancies, but if unknown impurities are present in real-

istic systems whose scattering affects the same energies, we may overshoot or undershoot the real vacancy concentration value.

Yet we have an inversion problem at hand and to solve it we will have to surrender to the unknown so we can, at the same time, try to probe it. Among all possible realistic impurities in our system, we will have to make an executive decision and pick the few most reasonable ones - either those that would have the greatest impact on our spectral signal or those that we know are the most likely to be present. This is precisely the way we circumvent the ill-posedness of the inversion problem. By the way with which we covertly phrased the previous section, the presented problem did have a unique solution. We delimitated the problem by imposing the host material and the measured quantity, the type of disorder we were introducing, the size and dimension of the system, and the expected range of disorder concentrations. All these served to qualify the problem and enforce one possible solution.

Yet these manoeuvres are not to be taken mindlessly. As we are about to see, the algorithm for solving our inversion is based on the minimization of a misfit functional, that guarantees an optimum solution in our configuration space. And here lies the intricacy of the problem - we are *guaranteed* to reach a solution. This means that regardless of how reasonable the configurational space delimitations are, one will always find a configuration that will minimize the misfit function. For example, I could try to invert a signal originating from a MoS_2 film with vacancies by probing it on the configurational space of graphene with adatoms, and inevitably, among all the configurations I probe, I will find one that yields a better fit to the solution than the others.

In summary, ill-posedness is an ever-present issue looming over the attempts to solve inverse problems. To avoid it, it is essential to have a minimum amount of information that will allow us to make the best-educated guess we can to approach the inversion of a signal.

2.2.3 The Inversion Algorithm

Following the approach described in the previous sections, we can devise an algorithm to identify the best solution for the inverse problem in a configuration space.

Let us reduce the problem assuming that the host lattice, size, and disorder type of the system that generated our signal $\Gamma_I(E)$ is known. Let us

also assume that this signal is a measurement of the electrical transmission of the system within a certain spectral range $E \in [E_i, E_f]$ and that the possible disorder concentration values lie within a range $n \in [n_i, n_f]$. From this information, we can populate our configuration space with stochastic Configurational Averages (CAs), each average being performed over N_c configurations such that

$$\langle \Gamma(E,n) \rangle_{N_c} = \frac{1}{N_c} \sum_{m=1}^{N_c} \Gamma_m(E,n) \ . \tag{2.65}$$

We then compare our input function $\Gamma_I(E)$ to each n instance of the CAs $\langle \Gamma(E,n) \rangle_{N_c}$ at every energy value, and the discrepancy calculated by the integration in energy of their difference squared is stored in the misfit functional χ (see Fig 2.10):

$$\chi(n) = \frac{1}{E_i - E_f} \int_{E_i}^{E_f} dE \ \left(\Gamma_I(E) - \langle \Gamma(E,n) \rangle_{N_c} \right)^2 . \tag{2.66}$$

Here, our signals Γ can either be the transmission coefficients, as we have showcased in the previous sections for the cases of the linear and bidimensional chains, or the conductivity of, *e.g.*, Eq.(2.42). For the case that our signal of interest is the conductivity, it is worth noting that the fermi conductivity at temperature $T = 0K$, σ_0, is equivalent to the electrical transmission Γ of Eq.(2.25) (note the similarity between the expressions of Eq.(2.25) and Eq.(2.43) - in the first one, the imaginary part of G is captured by the tilde operation in $\tilde{G}$, whereas in the second one the connecting potential V_{ij} is captured by the velocity operator $\hat{v}_x$).

By minimizing this functional with respect to n we determine which of the CAs our input configuration signal $\Gamma_I(E)$ is more similar to, *i.e.*, this minimum indicates the most likely disorder concentration in our original sample, n_I. If our assumptions were right, this result is the solution for the inverse problem and we have successfully characterized the input configuration by identifying its disorder concentration value.

Now we have an answer for the inversion problem, but note that all approximations made beforehand to devise this algorithm can be individually lifted and we can increase the complexity of this inversion problem arbitrarily. For example, we can add a second, third, or more different kind of disorder and attempt to minimize our misfit function simultaneously for all of them [80] - this would scale the proposed algorithm exponentially as $\mathcal{O}(n_c^d)$, where n_c is

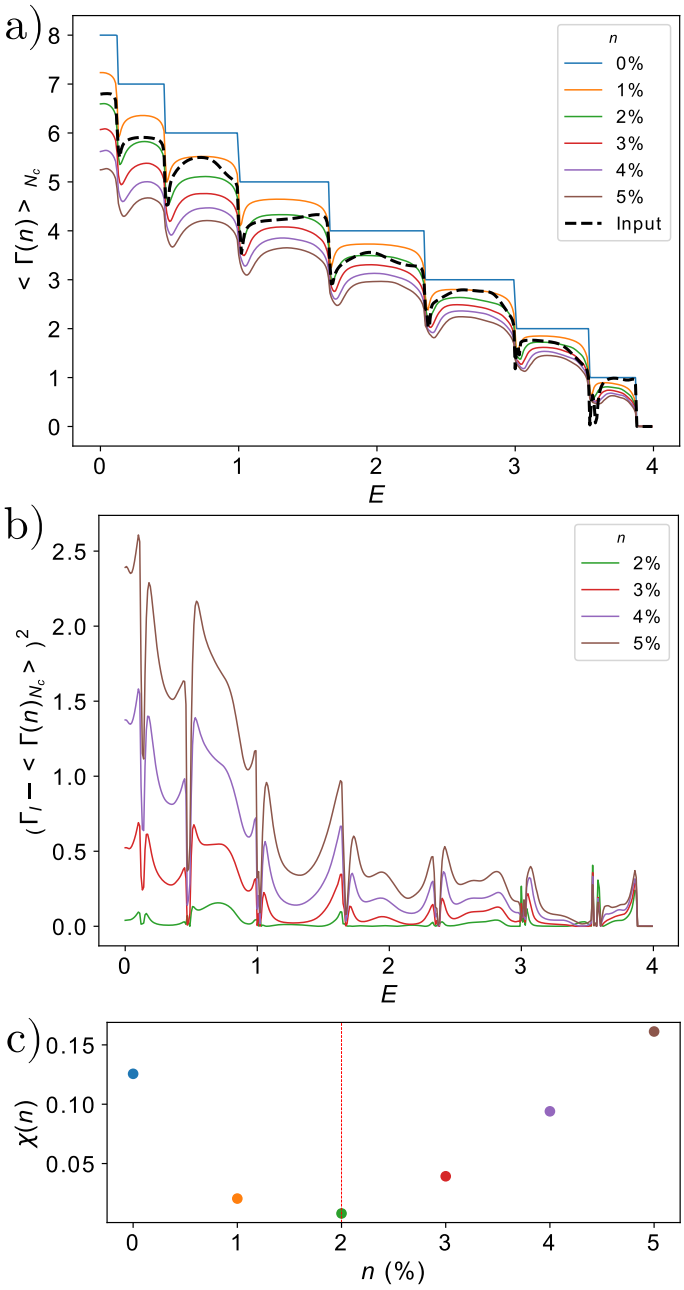


Figure 2.10: **a)** 25x8 square lattice transmission CAs for $N_c = 1000$ systems for different substitutional disorder concentrations. The dashed black line is the transmission of the input configuration with a concealed concentration. **b)** Square difference between some CAs and the input transmission. **c)** The misfit functional result displays a minimum at $n = 2\%$, coinciding with the dashed red line, which represents the original concealed concentration value of the input configuration.

the number of concentration values and d the number of disorder types. Each introduced disorder type would effectively introduce a new dimension to our minimization problem. A way to circumvent this exponential growth in the cost is to perform a dynamic minimization of $\chi(\{n\}_d)$, which would require an on-demand calculation of CAs. Another way of increasing such complexity is if we forfeit the isotropic approximation and try to identify the spatial localization of the scatterers. By removing the vertical or horizontal symmetry of the leads that probe our system, we allow for spatial-dependent transmission signatures that carry information regarding the spatial placement of disorder, from which we can perform the inversion to recover the approximate input configuration [21].

Likewise, the work presented in the following chapters showcases the application and reliability of this method in scenarios with gradually increased complexity, lifting certain approximations or tackling more complex quantities and larger systems. For now, let us see how to apply this method in a simple system.

Inversion of DC Longitudinal Electrical Conductivity Signals

With this detailed tool set in hand, we can illustrate our method by applying it in a few different scenarios. Firstly, let us consider a scenario in which we have a sheet of graphene that we know contains disorder in the form of vacancies. We measure its DC conductivity in one direction and obtain an input signal as a function of the energy $\Gamma_I(E)$. We wish to characterize this sample with regard to the concentration of vacancies present, so we calculate our CAs in such a way that the configuration space is populated around the vicinity of a first educated guess.

For this example, let us consider the space between 0% to 5% vacancies. We can see the CAs and the input signal as well as the misfit functional $\chi(n)$ in Fig. 2.11. Here, the conductivity signals were calculated using the CPGF method via the High-Performance Quantum Transport Software KITE [65]. Now we are dealing with a large graphene nano-ribbon, which is why the discontinuities present in the graphene transmission of Fig 2.7c cannot be seen here.

In the first misfit result shown in Fig. 2.11b, the minimum is located at $n = 2\%$, but due to the expected quasi-parabolic behaviour of the misfit function

in the vicinity of a minimum, we can expect that the true concentration should lie between the values of $n = 2\%$ and $n = 3\%$. We test this hypothesis by populating the CA space between the two values of concentration that yield the lowest misfit values and extract a misfit result with a better resolution, as shown in Fig. 2.11c, where the minimum at $n = 2.4\%$ is sharp and clear.

Appendix C provides another application of this method - where we aim to perform the inversion based on phononic transmission signals - changing the paradigm from fermionic transmission to a bosonic one.

2.2.4 Ergodic Assumption

Our quest for solving the inverse problem lies intrinsically in the search for information hidden in different signals. Naturally, the more information one has, the closer one gets to reaching a good solution for the inverse problem. The straightforward way of obtaining more information is, in our case, to increase the number of configurations which signals compose our database. More data makes the CAs more precise resulting in a more accurate minimization. However, this is not the only way of acquiring information and, from the way we pose this problem, one can infer that it possesses the property of ergodicity.

Ergodicity is the concept that a stochastic motion within a finite system will eventually cover all the space of possible movements in such system and, consequently, the average behaviour of the movements within the system can also be extracted from that motion [81]. In other words, there is an equivalency between observing one stochastic event for a long time and observing the average of multiple stochastic events for a short time. Here we are not concerned with the temporal average of the position of the electron in our system, but with an analogous energy average of the transmission of the electron in our system. Just as, given enough time, the stochastic motion of a particle will cover the space of possible positions in a finite space, similarly, given enough energy points, the electron scatterings will cover the space of possible transmissions. That is to say that observing the effect of our randomly placed scatterers on the transmission of an electron with different starting energies is as informative as observing the transmission of this electron in varied systems with a different disorder configuration.

From Fig. 2.12, we can illustrate this principle. Assuming the electron to propagate as a free particle plane wave, scattering at the coloured scattering

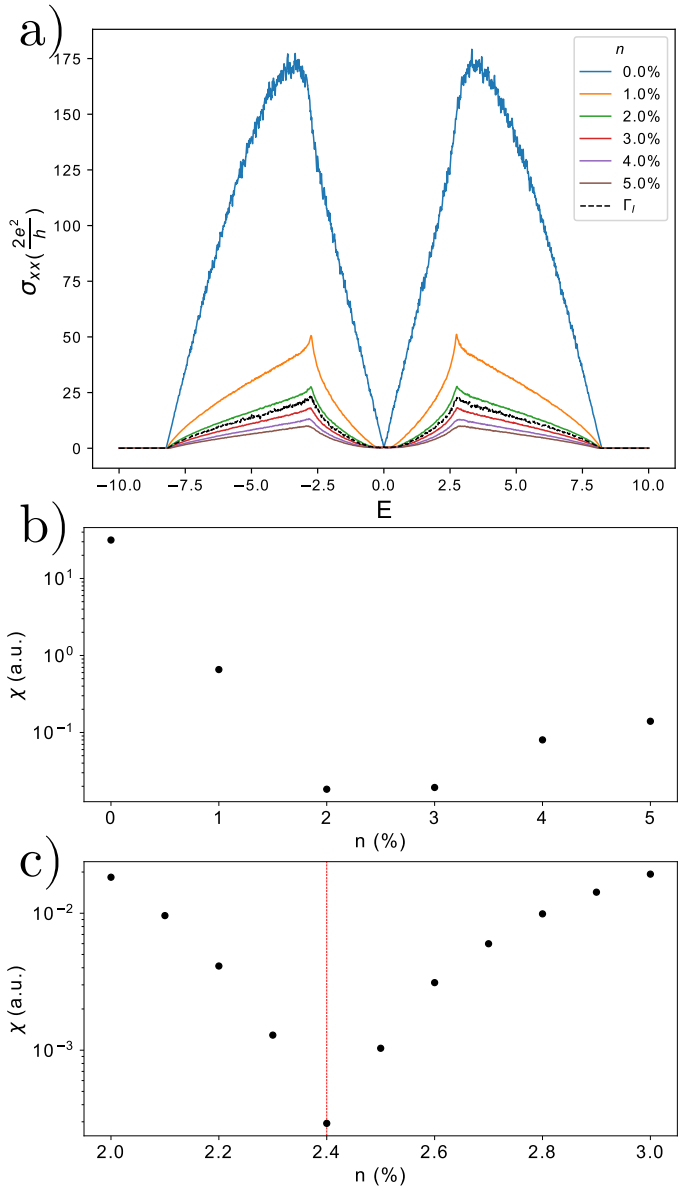


Figure 2.11: **a)** 3072x3072 armchair graphene nano-ribbon transmission CAs with $N_c = 10$ for different vacancy concentrations. The dashed black line is the transmission of the input configuration. **b)** The misfit result with a minimum between $n = 2\%$ and $n = 3\%$, illustrating a case where the minimum is not clear. **c)** The misfit result displays a minimum at $n = 2.4\%$, coinciding with the original input concentration (dashed red line).

points, the top and bottom configurations of this image will result in plane waves with different phase differences $\psi_B(E)$ and $\psi_R(E)$. These different results give us different bits of information for the propagation in a system that contains five scatterers. However, if we allow the calculation in a different en-

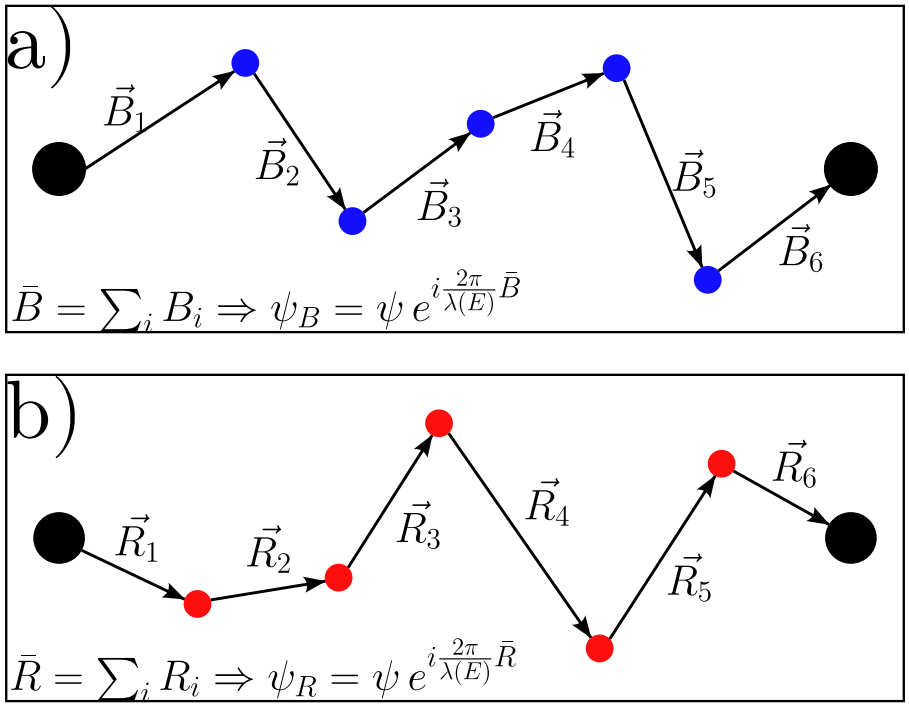


Figure 2.12: Two systems **a)** and **b)** with the same number of scatterers, but in different configurations.

ergy value, we can show that, as long as we can continuously sweep the energy spectrum, there will always be an energy E' in which $\psi_B(E') = \psi_R(E)$, as long as $\lambda(E') = \lambda(E)\frac{\bar{B}}{\bar{R}}$. This shows that probing one configuration at an energy point is equivalent to probing a different configuration at another energy point and, therefore, one can get as much information varying the energy as one can varying the scatterer placement of the system.

When, in Eq.(2.66), we average the square difference of one electron transmission over energy, we are effectively treating each energy point independently and with the same weight in our average. Consequently, just as much as an inversion of a new configuration would give us more data, so would an inversion with a higher energy point density. In this sense, the CPGF method for the conductivity calculation excels in solving inverse problems because, after the moment calculations are done, one can get the value of the transmission for as many energy points as one desires with a very low computational cost. As long as the chosen resolution for the energy spectrum doesn't surpass the one given by the error of the measurement associated with the system size and the number of polynomials chosen, the increase in resolution will translate to

an increase in meaningful information. Later, in Chapter 3, I will demonstrate this ergodicity of the inversion problem by performing a parametric experiment on a particular inversion procedure.

Impact of Self-Averaging

Keeping with that theme, another way we can capture more information about the disorder's signature is to simply observe a larger system. If the system is large enough, it can be broken down into smaller subsystems that possess the same concentration of randomly placed disorder. These subsystems effectively serve as novel configurations carrying information about that disorder concentration. In the process of calculation of the spectral quantity over the large system, the properties of the smaller systems contained within contribute to the final result. In the end, we obtain the average behaviour of the disorder signature of the smaller systems. This is the self-averaging property of disordered systems. This self-averaging property was also used to our advantage before when we performed the stochastic evaluation of traces (see Eq.(2.52)).

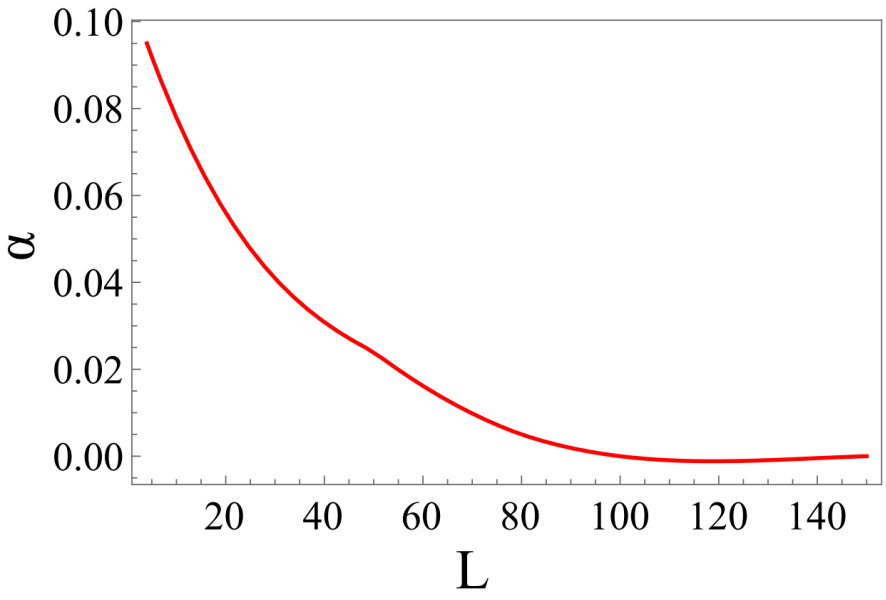


Figure 2.13: Inversion error α as a function of the longitudinal size L (in unit cells) of graphene systems with substitutional impurities. Devices of all sizes contained a fixed impurity concentration of n = 4%. [80]

Naturally, since the accuracy of our misfit function relies on configurational averages over a large number of configurations, the self-averaging property of

these disordered systems contributes to the information contained in the configurational average. Consequently, the larger the system we consider in our configurational average, fewer configurations are needed to obtain a CA convergence. This impacts the scaling properties of our misfit function, as can be seen in Fig. 2.13. The larger the system size we use to generate the quantities employed in our misfit function calculation, the lower the error of our misfit function prediction (relative comparison between the predicted concentration given by the misfit function minima in relation to the actual disorder concentration that generated the input function).

2.3 Summary

In this chapter, we systematically laid out the theory necessary to describe, simulate and operate on various systems and their properties, with special attention given to disordered media. We introduce the tight binding for real-space modelling of the disordered systems, the Green's function for their application in the Kubo formulas in conjunction with Dyson‘s equations, and finally the approximative Chebyshev Polynomial Green Function method to deal with large complex systems. Each technique explanation was followed by an application or example, aiming to provide a solid understanding of each particular tool.

This tool set allowed us, then, to introduce the inverse problem with a focus on the characterization of materials. We dove into the theory behind and surrounding the inversion problem, addressed its ill-posedness, and offered a systematic solution via an inversion method. The use of the inversion method was showcased in simple cases, preparing us for the work in the next chapters. Finally, we were introduced to the ergodic assumption behind the functioning of the method, revealing the foundational work behind our averages and approximations.

It is worth mentioning that the inversion method as laid out in this chapter may bear some resemblance to regression deep learning techniques used in machine learning. For example, the misfit function can be re-interpreted as a cost function while the CAs may be regarded as training sets. While we do not make use of machine learning techniques in the work presented in this thesis, later in Chapter 3, we demonstrate the possible use of machine learning to reduce the cost of populating the CA configurational space, aiding our

inversion.

Now, having provided a systematic framework to solve the inversion problem and applied it to simple systems, the next step in the development of the inversion tool is to gradually increase the complexity of our problem and systems. By increasing the complexities of the target simulation, exploring the scope of the inversion accuracy in extreme cases and exploring its application with multiple different systems, we are able to gauge how reliable this inversion procedure truly is. In the next chapters, we will apply these tests to the inversion method aiming to consolidate its scope and application.

Chapter 3

Inversion for MoS_2 Vacancy Characterization

In the previous chapter, we presented all the theoretical tools necessary to perform the spectral calculations of different systems using a tight binding model. We also introduced the method we apply to solve inverse problems like characterization, which we exemplified using a simple system. That theoretical introduction brings forth two very pertinent questions:

1. Can this inversion method, which demonstrates efficacy when handling simple systems, deal with realistic systems - systems whose description may rely on dozens of orbitals and that are large enough to have practical application?

2. Will this method be capable of inverting real signatures, generated by experimental measurements - will it have a practical use?

In this chapter, I intend to answer these two questions as well as explore other frontiers in the application of this method. I will test its robustness by characterizing the vacancy concentration in simulated mono-layer MoS_2 via the inversion of different spectral signals. In the meantime, we will see how signatures of different quantities can impact the result of the inversion as well as the effect a realistic temperature can have on these results. Later, we will test the application of the method on experimental transconductivity signals for CVD-grown MoS_2 and analyse the characterization results against the expected values.

3.1 MoS_2: a Transition Metal Dichalcogenide

The discovery of graphene along with all its applications and properties led to the start of a hunt for new planar materials with similar or complementary uses [82, 83]. By 1935, it was argued by Peierls and Landau that the free-standing two-dimensional sheet of atoms could not exist in nature as the long-range order would break down due to the thermal fluctuations and meltdown the 2D sheet into a three-dimensional bulk [84]. Graphene, then, emerged with a different physics that bridges quantum electrodynamics and condensed matter physics [85], which would open the path for investigation of a larger number of 2D layered materials.

Although extremely innovative, graphene still lacked an electronic bandgap, which is essential for optoelectronic applications. Multiple attempts to engineer this bandgap have been reported [86–91], but often these attempts would interfere with the mobility or mechanical properties of the material. This research leveraged the chase for components that would possess a naturally forming bandgap, which brought us to the layered Transition Metal Dichalcogenides (TMDs). The TMDs became one of the highly studied families of materials due to their quasi-two-dimensional crystallographic structure and its electronic and mechanical properties [92–99]. Their bandgaps include such a wide range of sizes that all visible and infrared parts of the spectrum are covered [100]. Other than these, one can highlight materials like hexagonal boron nitride (h-BN), borophene, phosphorene, silicene, germanene, and MXenes, which also became heated topics in research [101–106].

TMDs are semiconductors of the form MX_2, where M is a transition metal atom typically from groups 4-7 (Mo, W, and Re) and X is a chalcogen atom such as S, Se or Te. Examples of TMDs are, therefore, molybdenum disulfide MoS_2, molybdenum diselenide $MoSe_2$, tungsten disulfide WS_2 or tungsten diselenide WSe_2. In bulk form, the TMDs are layered materials with each layer of the compound consisting of three atomic layers in which the transition metal one is sandwiched between two others formed by the chalcogens as illustrated in Fig. 3.1. The layers have strong intralayer bonding given by covalent chemical interactions while possessing weak interlayer van der Waals-like bonding [107]. This allows the isolation or fabrication of two-dimensional TMDs via methods such as exfoliation [108, 109] or chemical vapour deposition [110, 111].

Much like graphene, the layered TMDs possess dramatically different prop-

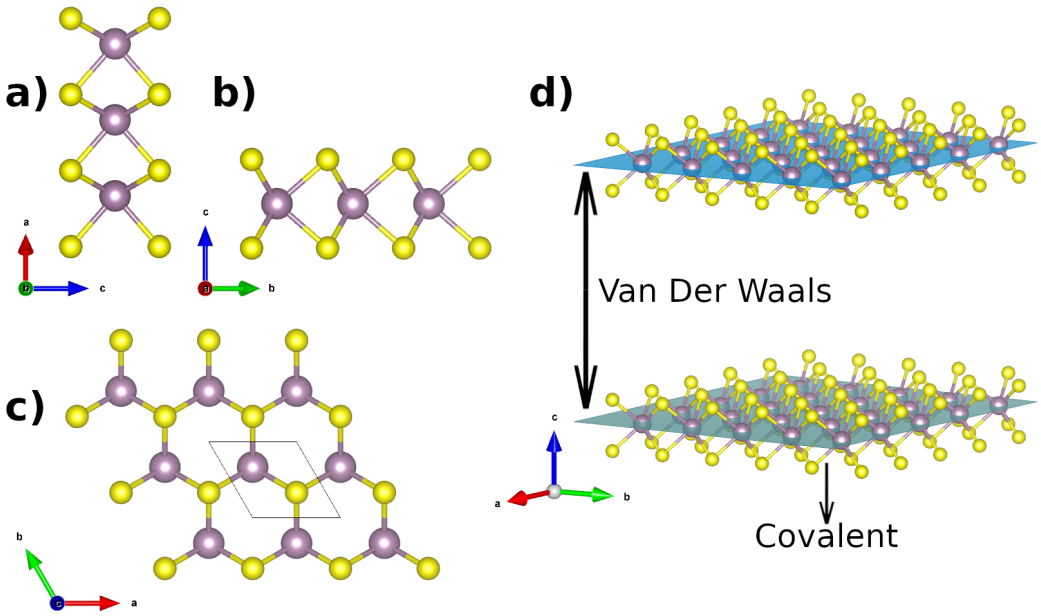


Figure 3.1: MoS_2 in 1H structural phase TMD illustration (purple sphere = Mo, yellow sphere = S) of: **a)** and **b)** side view. **c)** top-down view with unit cell. **d)** Standard orientation of crystal shape showing two layers and the bonding nature - Van der Waals for the inter-layer interaction and covalent for inter-atomic interactions (bi-colour cylinder).

erties compared to their bulk counterparts. They reveal a direct bandgap in monolayer form, while possessing an indirect bandgap in bulk form except for a few cases (GaSe and $ReSX_2$) [112,113]. The direct bandgap is a highly sought-after property for optical conductivity purposes once the energy needed to raise the electrons to the conduction band does not change the electronic crystal momentum, which makes the light absorption process more efficient. The tunable bandgap in TMDs is accompanied by strong photoluminescence and large exciton binding energy, making them promising candidates for a variety of optoelectronic applications [114,115], including solar cells, photo-detectors, light-emitting diodes, and photo-transistors [116–119].

TMDs have shown a vast range of applications. From fundamental studies of valleytronics and Raman spectroscopy [120–124] to applications in biomedicine, catalysis, electronics, photonics, power generation, power storage, and others [92,95,116–118,125–128]. Particularly, these ultrathin semiconductors possess huge potential to be made into ultra-small and low-power transistors that are more efficient than the state-of-art silicon-based ones due to their electronic

properties and mechanical flexibility [95]. This makes them good candidates for novel materials that cope with the increasing demand for ever-shrinking electronic devices. The synthesis of TMDs and 2D materials is still an active research area with the main methods involving exfoliation and chemical vapor deposition. The main challenge is mass production, *i.e.* scalability while maintaining atomic thickness precision [108, 129–131]. More recently, this issue has been approached with a variety of new strategies [132–137].

Of all TMDs, MoS_2 deserves special attention. It is a well-established semiconductor with low toxicity and high thermal and chemical endurance [138, 139]. By varying the number of layers, one can produce bandgaps with energies that fall in the solar spectrum range around the visible light and, thus, allow the MoS_2 employment for photovoltaic and photocatalytic applications [140–143]. The electronic properties of MoS_2 are also sensitive to external pressure and strain, both of which affect the insulating gap and, under particular conditions, can induce an insulator-metal transition [144]. MoS_2 belong to the group of TMDs with promising application in valleytronics because, among other reasons, their conduction band minima and valence band maxima are located at degenerate, but nonequivalent valleys due to the presence of heavy metal atoms [145–147].

3.1.1 Disorder in TMDs and Vacancies

So far, the main application of our inversion methodology is the characterization of disordered systems. An inversion could still be performed on a pristine system, and while being a challenging inverse problem overall, it is the trivial case for the method introduced in this thesis. An interesting characterization relies on the expectation of some quantity of disorder of one or more types, so it is relevant to understand what type of disorder can be expected to be present on MoS_2 thin films.

Disorder can be introduced in many ways such as substitutional, adsorption, vacancies, or interstitials to name a few and while normally seen as detrimental to the properties of a crystalline material, the introduction of disorder can unlock new properties in the system, with each type of disorder inducing a particular effect on the properties and spectral quantities of the system [148, 149]. The doping of TMDs is also useful for creating n-type and p-type semiconductors, which can be applied in p-type semiconductor-based

complementary metal-oxide semiconductors (CMOS-)FET and other p-n junctions based optoelectronic devices [115,150]. N-type MoS_2 can be achieved by hydrogen adsorption and oxygen chemisorption while niobium and nitrogen doping form p-type MoS_2 [150]. In such components, if a more reactive metal is used in contact with the MoS_2 layer, chemical reactions can create defects in the TMD, altering its properties [151]. Another example is the native defects in TMDs which, similarly to graphene, can also induce the formation of local magnetic moments [152–154].

Vacancies are native point defects that strongly influence the transport and optical properties of semiconductors [138,155–159]. Vacancies behave like traps holding electrons, holes, or excitons, introducing new energy states and the effects of this disorder increase in lower dimensions due to the tighter localization of the electron wavefunction [160]. The vacancies can be created artificially via thermal annealing [161,162], α-particle irradiation [163,164], or electron beam irradiation [165,166]. During the manufacturing of TMD monolayers, however, some degree of disorder is inevitable and it is certain to affect the otherwise perfect crystalline structure of these layered materials. Due to the type of atomic bonding in monolayer TMDs, a structural disorder in the form of vacancies of the chalcogens is one of the most likely to occur [107,167], making it a good candidate for the type of disorder we will employ in the implementation of our inversion methodology for MoS_2.

3.1.2 Characterization of TMDs

The natural, or possibly engineered, occurrences of these defects and their aforementioned effects on spectral quantities motivate us to seek a form of characterizing these materials in a cheap and simple manner. Typically, characterization techniques such as scanning transmission electron microscopic imaging, photoluminescence spectroscopy and Raman spectroscopy are the tools employed experimentally for the characterization of TMD samples [136,168–173]. While these are extremely powerful methods for characterization, they require expensive experimental setups and equipment. Not only that, but they are subject to practical limitations such as sample sensitivity or image interpretation that introduce avenues for systematic errors in the results.

Measurement of spectral quantities such as the electrical DC conductivity, on the other hand, usually requires simpler and cheaper standard experimental

setups of two or three-terminal devices. Suppose we can obtain information regarding the material composition from such measurements. In that case, we can make characterization much more accessible, allowing, for example, characterization in harsh environments such as in space, celestial objects or the deep sea - in this scenario, our inversion method becomes very valuable. It is important to stress that, despite the convenience of this proposed method, we are not suggesting that other characterization methods should be abandoned. Rather, by introducing a cheap alternative way for characterization, our process seeks to complement the existing procedures contributing to increased accuracy in the results.

In the following pages, I will demonstrate the efficacy of the method in dealing with complex, realistic systems such as TMDs, paving the way for realistic applications.

3.2 Inversion on Synthetically Disordered MoS_2

In the previous section, we introduced the system which we aim to characterize: MoS_2 with vacancies. Now we are tasked to obtain as much information as possible about the nature and the level of disorder present in such a system so we may assess its impacts on the electronic and optoelectronic properties of the material. To accomplish that, we will first determine the parametrization of such a system in multi-orbital tight binding modelling via *ab initio* calculations, allowing us to simulate the complex structure of MoS_2 using real space Hamiltonians. Then we will perform the calculations to obtain the spectral functions - the DC and the optical electrical conductivities - of the simulated system and use them to fill out the respective configurational averages (CA) configuration spaces. In possession of this data, we will be able to perform the inversion of an arbitrary input signal with an unknown concentration of vacancies to reveal the concentration value by the method introduced in Chapter 2. This input signal can either be an experimental measurement or a simulated one. To investigate the scope of the inversion method in this new scenario, however, we first approach it with the inversion of synthetic signals, because in this way, we can access the initial conditions of the generating configuration to assess the success of the inversion procedure.

Parametrization and Calculation

Despite sharing a hexagonal structure similar to graphene (which we used for illustration as the target for inversion in the previous chapter), the unit cell of TMDs is far more complex and requires multiple orbitals to be properly described. While the graphene toy model could be described using one orbital per atom, for the case of MoS_2, we will need at least 13 orbitals in the unit cell - 5 for the Mo atom and 4 for each S atom - increasing the complexity of the system. Furthermore, as the unit cell complexity rises, larger has to be the simulated lattice to account for the effects of each orbital interaction accurately - especially if disorder is randomly placed in the system. This makes it so that the simulations of disordered TMDs with a random distribution of defects become tremendously expensive computationally when using *ab initio* methods such as density-functional theory (DFT) for the calculation of spectral functions [144, 174]. Instead, we apply the calculation methods introduced in Chapter 2 via the high-performance software KITE [65,175–177]. By using the Chebyshev Polynomial Green's Function method on tight binding modelled lattices, extensive numerical calculations can be performed on large systems with a relatively low computational cost.

Yet we still make use of *ab initio* DFT calculations for the parametrization of our system. By simulating a small lattice accounting for one unit cell and its first nearest neighbours, we can localize the Wannier functions of the system and obtain the tight binding parameters for each orbital onsite energy and the hopping parameters to every other orbital in that unit cell and in the neighbouring ones [78, 79]. In this way, we make use of the realistic level of description provided by *ab initio* calculations while at the same time enabling a fast simulation of disordered media by employing real-space tight binding modelling.

To obtain this real-space Hamiltonian for MoS_2, we performed DFT calculations with the help of our collaborator at the University of Valencia. The calculations were done within the local-density approximation, using the Quantum Espresso numerical packages [178]. We employed norm-conserving and fully relativistic pseudopotentials [179, 180], and generated a basis of atomic orbitals using Wannier90 [181, 182] for MoS_2 that includes the s, p_x, p_y and p_z orbitals of the chalcogen atoms and the five d orbitals of the Mo one (see exact composition of states at K in Ref. [183]). The tight binding Hamiltonian

obtained with Wannier90 is exported to KITE with PythTB scripts [184]. Its band structure and density of states are consistent with DFT calculations [185] and multi-orbital tight binding models [186–189] and can be seen in Fig. 3.2a.

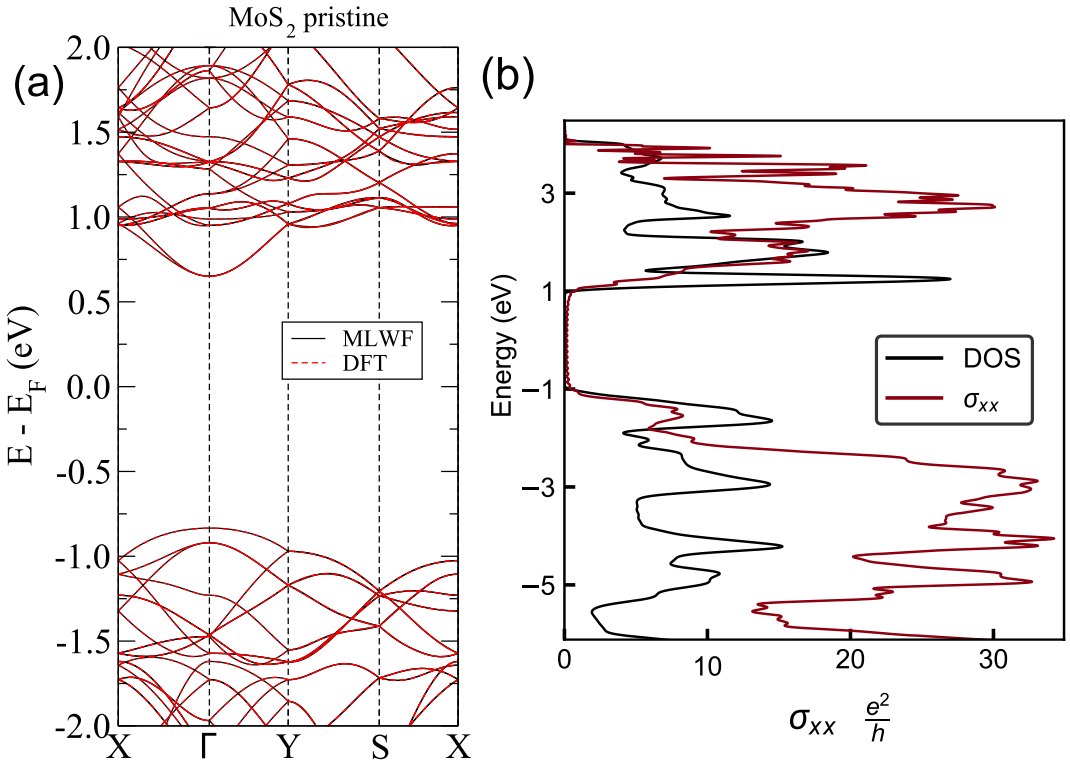


Figure 3.2: **a)** Comparison between the band structure calculated from the maximum localized Wannier functions tight binding parameters (solid black) and the one calculated via DFT (dashed red). Note the direct band-gap present at momentum Γ. **b)** Illustration of the density of states spectrum (black) and DC conductivity (red) for the pristine MoS_2 case from these parameters.

The conductivity calculations were carried out on KITE [190], an efficient quantum transport software for real-space tight binding simulations, capable of handling an extremely large number of atomic orbitals. It is based on Chebyshev polynomial expansions [49, 191] and provides excellent accuracy levels without being too demanding in terms of computational resources. Furthermore, its real space formalism is ideally suited to study disorder effects on materials. Spectral properties such as Density of States (DOS) [192], DC conductivity [53, 55, 185, 193], and optical conductivity [194] are some of the combined outputs of these calculations and can be easily tested against a variable degree of structural disorder. It is thus possible to create a collection of spectral quantities results for different configurations and concentrations of

disorder.

The equivalence between increasing the number of configurations in the CA part of the calculation and increasing the number of integrated energy points enables us to replace having a configuration average containing large amounts of functions with one with fewer functions that carry a higher energy point number - be it by increasing the energy point density or by spanning a wider range of the spectrum. This makes KITE particularly suitable because when using a polynomial method, the output from KITE is evaluated at as many energy points as desired without changing the computational demands since it provides the function for the whole energy spectrum [49, 190]. Therefore, the number of configurations N_c needed in the CA part of the calculation as expressed in Eq.(2.65) may be reduced without impacting the inversion accuracy.

With that in mind, we obtained numerous results for the longitudinal DC conductivity and optical conductivity spectral function, both calculated through KITE. All calculations were carried out with 64×64 unit cells comprising a total of 13 orbitals per unit cell (4 orbitals for each S atom and 5 orbitals for the Mo atom) with a finite concentration of disorderly distributed chalcogen vacancies, which in the case of the MoS_2 are sulfur (S) vacancies. For each function, 256 moments of Chebyshev polynomials expansion were used for 9 different random-vector trace calculations. Our results for clean samples are consistent with previous theoretical analyses based on multi-orbital tight binding Hamiltonians [187, 195, 196]. Despite working with small system sizes, few random vectors and few polynomial moments, the inherent noise of the polynomial approach in the form of Gibbs oscillations should be averaged out when calculating the CA. The same can be said about the quantity $\langle\chi\rangle$ regarding the input configurations noise. This feature of the calculation appears to contribute to the efficiency of the method, allowing for low-cost calculations without loss in precision.

One specific set of vacancy positions is arbitrarily chosen to define the input configuration, which in this case contains $n_p = 4\%$ of vacancies. Note that this information is not used in any part of the subsequent calculation, except for testing the inversion success at the end. Fig. 3.3a captures the essence of the inversion approach by showing the conductivity spectrum of the input configuration (blue solid line) together with a CA calculation with $N_c = 100$ configurations for $n = 8\%$ of vacancies (red dashed line). This comparison

is made to extract the misfit functional value for the concentration $n = 8\%$. There is quite a discrepancy between the two curves, suggesting that 8% is not the real vacancy concentration in the configuration that generated $\Gamma_p(E)$. This can be concluded from observing the green-filled curve, which measures the absolute value of the deviation between the red and blue curves. From Eq.(2.66), the integration of the square of such deviation curve leads to the misfit value of $\chi(8\%)$.

Repeating this process for different concentrations n, we get the misfit function $\chi(n)$, seen in Fig. 3.3b. The distinctive minimum at $n = 4\%$ coincides with the exact vacancy concentration n_p contained in the input configuration which is evidence of a successful inversion. The same procedure was repeated 10 times with distinct input configurations and each time the inverted concentration was compared with the real value, leading to a normal statistical distribution of the misfit function $\langle\chi(n)\rangle_{10}$. The standard deviation associated with this distribution appears in the figure in the form of error bars. One input configuration is enough for performing the inversion. However, to assess the accuracy of the inversion we must repeat the process several times with different configurations to obtain statistical information for a given concentration. The higher the number of input configurations used, the higher the statistical significance of the data.

Regarding previously made claims of generality and robustness [80], the inversion must be tested with an input function other than the electrical conductivity. Although more computationally demanding, the optical conductivity is a suitable candidate. Following similar steps to the ones taken earlier, the spectral optical conductivity for an input configuration as well as for numerous other configurations were calculated. Shown in Fig. 3.4a are the input signal (blue solid line) together with its CA counterpart (red dashed line) for an arbitrary concentration value of $n = 6\%$. Once again, the concentration-dependent misfit function $\chi(n)$ is generated when the deviation between the two curves is integrated over energy. Fig. 3.4b depicts $\chi(n)$ for concentration values between 1% and 8%. Reassuringly, even though the input signal is of a different nature and looks very different to the one used in Fig. 3.3a, the inversion finds exactly the same answer with a distinctive minimum at $n = 4\%$.

Remarkably, the error bars in this case are of comparable sizes to the DC conductivity inversion even in cases where the CA calculation involved considerably lower N_c values ($N_c = 10$). While the DC conductivity at a given

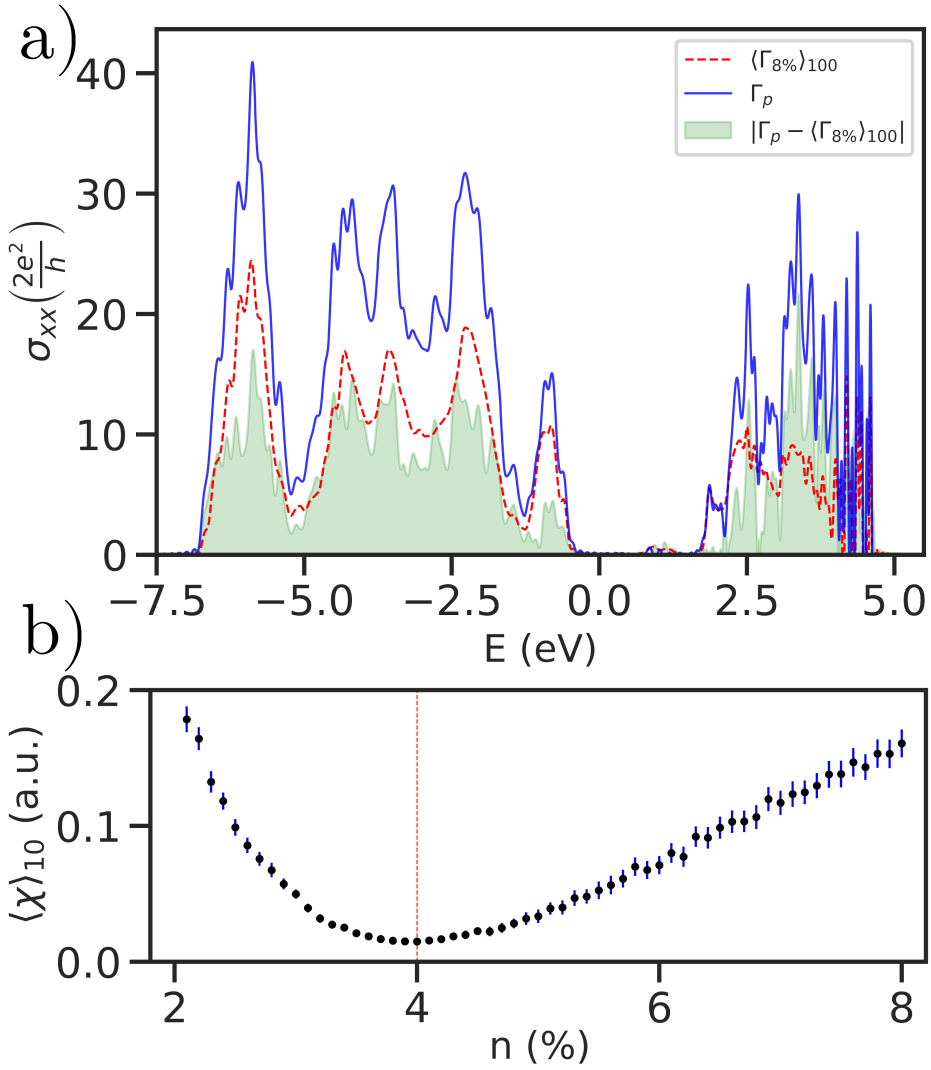


Figure 3.3: **a)** Longitudinal conductivity at temperature $T = 0$K comparison between 8% concentration CA of 100 configurations (dashed red) and an input configuration of concealed disorder concentration (solid blue). The discrepancy is shown in the filled green curve. **b)** Misfit function $\chi(n)$ in arbitrary units averaged over 10 distinct input configurations displaying a minimum at 4%. For the sake of comparison, the vertical (red) line indicates the real concentration n_p of the input configuration.

energy depends only on the states at that particular Fermi level, the optical conductivity calculation for each energy point takes as input the energy values in a range of the order of $\hbar\omega$ around the Fermi level of the calculated point. In other words, the optical conductivity calculations involve a larger volume of states which, according to the ergodic principle is equivalent to a larger number of iterations. This ultimately translates into a greater accuracy for

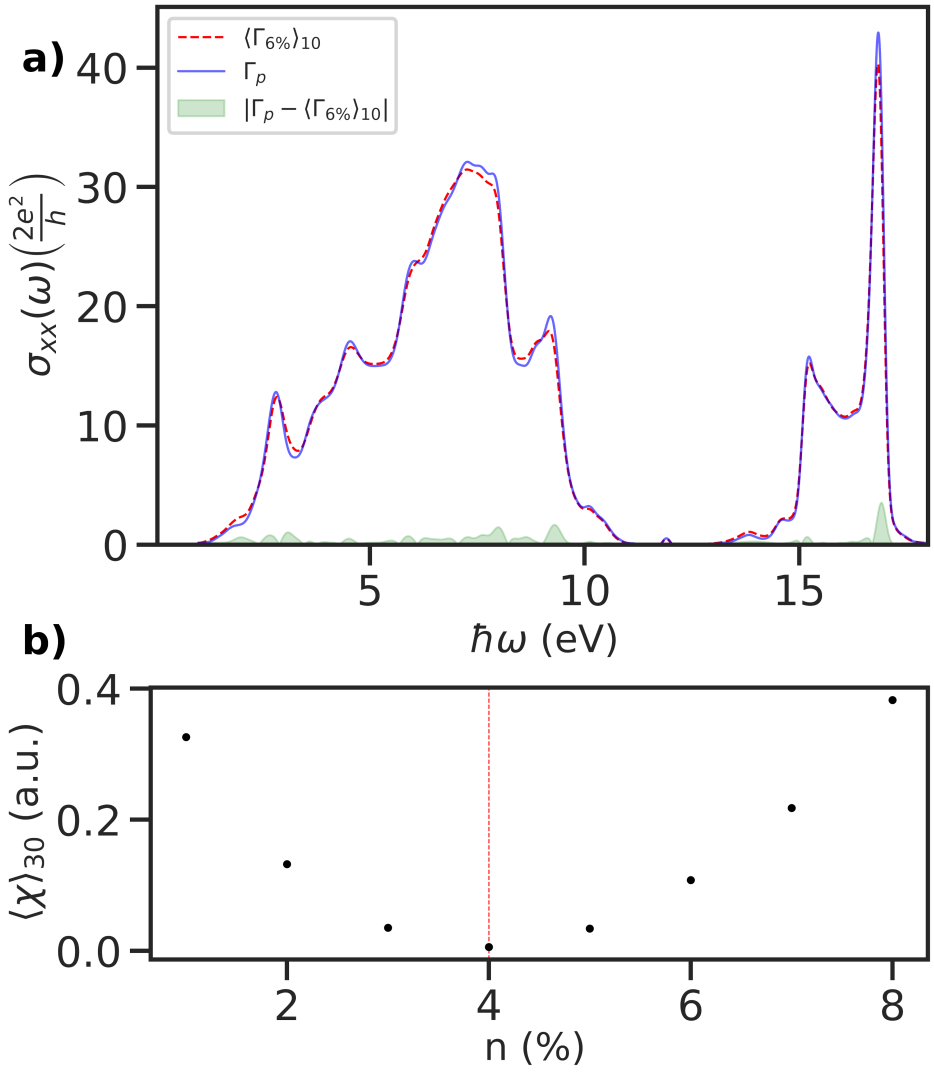


Figure 3.4: **a)** Optical conductivity at temperature $T = 0$K comparison between 6% concentration CA and input configuration. **b)** Misfit function $\chi(n)$ in arbitrary units averaged over 30 distinct input configurations with the minimum at 4%. The error bars are smaller than the point markers. For the sake of comparison, the vertical (red) line indicates the real concentration n_p of the input configuration.

the misfit function calculation.

Notice that the calculations were carried out at temperature $T = 0$K. Even though this is not a typical experimental temperature, the method still works in the case of relevant temperatures, as discussed in Reference [80]. The effect of typical experimental temperatures is much smaller than the correlation length of our conductivity energy integrations and therefore meaningful information

can still be extracted from Eq.(2.66) at higher temperatures. In fact, one could use the same low-temperature CA calculations for obtaining misfit functions from room temperature input functions provided its correlation length stays greater than the temperature effect. This is illustrated in Fig. 3.5 where we can see a comparison between misfit functions with different temperature settings. When using input functions at room temperature with a CA calculated at $T = 0$K, the misfit function minimum remains well distinguished at 4%, *i.e.* when compared to the input functions calculated at $T = 300$K. This serves as confirmation that the thermal effects on the calculation do not interfere with the minimization, which facilitates the method calculations by allowing for the simple $T = 0$K CA calculations to act as the basis for the inversion of signals obtained at typical experimental temperatures. It goes without saying that for the case where both the CA and input functions are at high temperatures, the method will also work provided the temperature-induced changes are lower than the energy correlation length of our function. This condition is broken only in the case of extreme temperatures many orders of magnitude higher than room temperature.

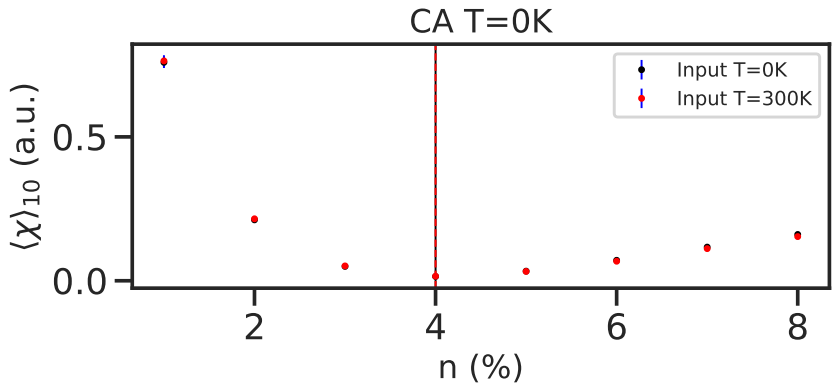


Figure 3.5: Comparison between longitudinal conductivity misfit functions with CAs at temperature $T = 0$K and input configurations of disorder concentration of $n = 4\%$ at temperatures $T = 0$K (black) and $T = 300$K (red) averaged over 10 realizations and with minima marked by the lines with the respective colour. Note that both results are not only practically identical but most importantly, have their minima at exactly the same concentration.

Vacancy-Induced Resonances

One of the most notable signatures of the disorder is the emergence of conductivity within the energies of the gap between the conduction and valence bands. Due to the absence of atoms in an otherwise periodic crystalline structure, we can observe the formation of localized electronic states. These states create electronic resonances that can be observed in the density of states of the system. Consequently, these resonances are also reflected in the conductivity signals and can be observed between the conductivity bands. Fig. 3.6 illustrates the MoS_2 with vacancies conductivity spectrum similar to the curves presented in Fig. 3.3, but zoomed in the spectral interval between the bands. Here we can see how the presence of vacancies promotes the emergence of transport in energy ranges that would otherwise be inert. This particular disorder signature is crucial for identifying the presence and quantity of vacancies since it is the first signal that one can observe when increasing the energy of the system above the Fermi level. Later in this chapter, we will avail of this feature to compare experimentally measured signals against our conductivity calculations.

It is worth noting that electronic resonances are not the only type of resonance emerging from the presence of vacancy in the system. One example is the photoluminescence resonance, which measurement carries information about the presence of vacancies [119, 160, 197], Magnetic resonances, more prevalent when there are vacancies of the transition metal, but also occur in the case of chalcogen vacancies [153, 154]. Vibrational local modes of resonance that emerge from the break of translational symmetry and can be perceived via Raman spectroscopy [124, 171]. Finally, valleytronics can also be observed due to the lifting of valley degeneracy inducing small energy resonant states [198, 199].

All these resonant effects carry the unique signatures of the disorder and may be candidates to identify the presence of vacancy by implementing the inversion method on the relevant spectral signals.

3.3 Validating the Ergodic Assumption

In the previous chapter, on subsection 2.2.4, we introduced the concept of the ergodicity behind the misfit function calculation, now we can subject our inversion procedure to a parametric experiment to validate this assumption. The

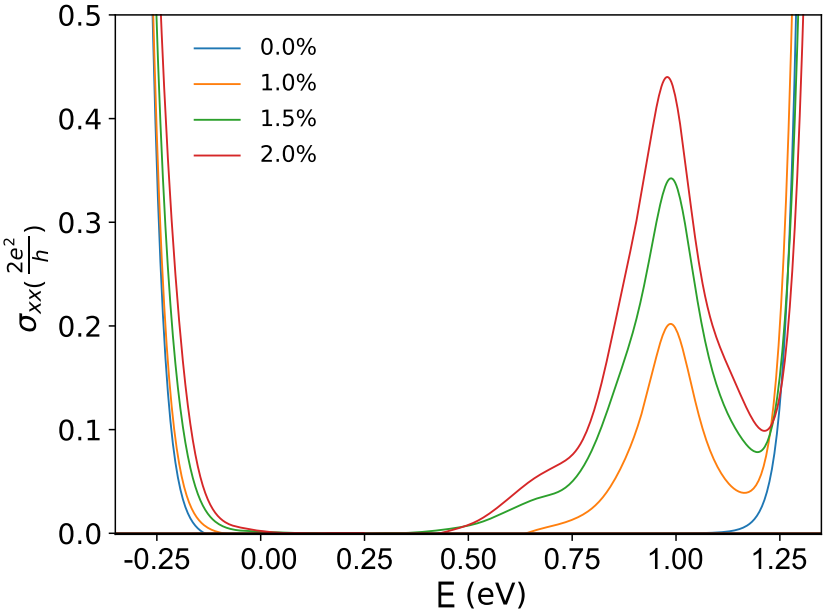


Figure 3.6: Vacancy peaks formed within the conduction gap due to the presence of vacancies illustrated at different vacancy concentrations. Each curve represents a configurational average of 40 configurations with a specific concentration. The heights of the peaks are proportional to the increased presence of S vacancies displayed, illustrating the electronic resonances caused by this disorder.

underlying questions then become: what is the role of the integral of Eq.(2.66), and how impactful are the integration parameters in the misfit function precision?

The integration plays a significant role in identifying with precision the real impurity concentration because, as we have seen in the last chapter, the fluctuations of the spectral signal of a configuration as a function of energy are equivalent to fluctuations relative to different configurations at fixed energy. Therefore, performing this integration over a greater spectral range is equivalent to augmenting the number of disordered configurations taken into account for the CA calculations. Furthermore, the integration itself never happens in the continuum spectrum since we are approaching the disordered system spectral functions via numerical calculations instead. This means that the integration energy step is an essential parameter in determining the amount of information being extracted from the signal. By reducing the number of energy points involved in generating the misfit function, there should be a threshold below which the inversion accuracy drops quite significantly.

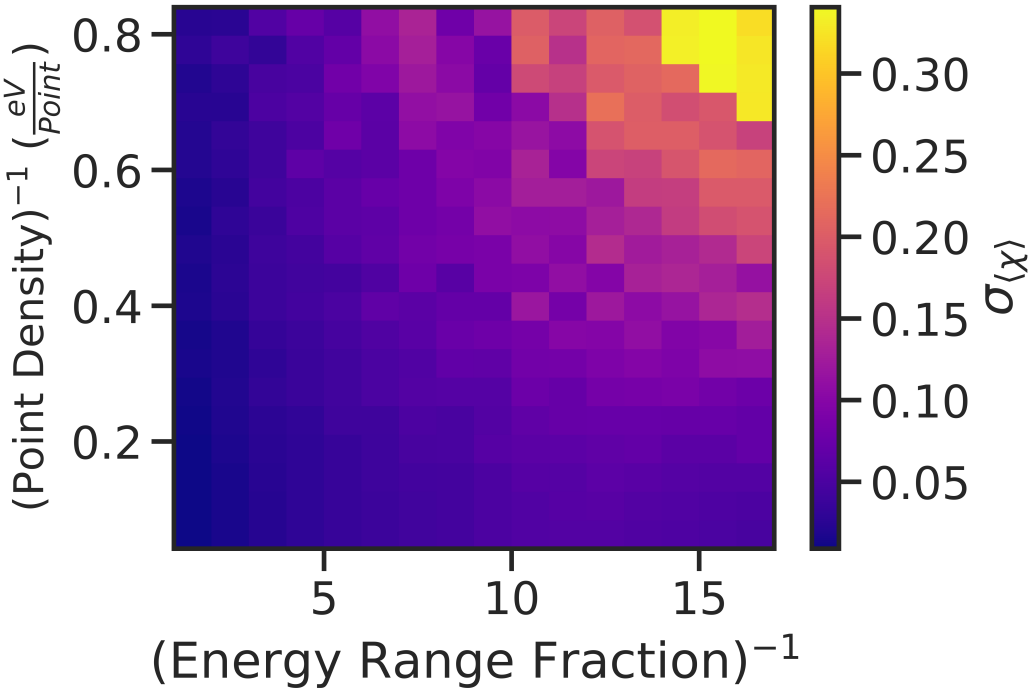


Figure 3.7: Behavior of the mean standard deviation as a function of the point density and the energy range covered. Statistical distribution for 50 different input configurations with CA of 50 configurations $\sigma_{\langle\chi_{50}\rangle_{50}}$.

This implies that both integration parameters have a strong impact on the accuracy of the misfit function, and that is indeed the case as quantified in Fig. 3.7 - a colour plot of the standard deviation associated with the inversion accuracy as a function of the reciprocal of two quantities, namely the energy range fraction and the integrated point density. The energy-range fraction refers to the proportion of the electronic band structure taken into account in the inversion calculation. The point density refers to how dense an energy mesh was used in the integration of Eq.(2.66) and determines the energy step size. The plot unmistakably shows that the higher the density of points or the spectral range used, the lower the standard deviation we get from the same number of configurations in the CA calculation. Furthermore, the bright spot on the top right of the plot indicates that the inversion accuracy drops if both the point density and the energy range fraction are reasonably low. This means that for a sufficiently wide energy range fraction, the integration point density may be lowered to fairly small values without impacting the inversion accuracy and vice versa. Most importantly, having a high value

on both these parameters saves us from excessive CA calculations, lowering the computational cost of the inversion procedure. This highlights again the usefulness of the CPGF method on CA calculations as mentioned in section 2.2.4.

It is worth emphasizing that the accuracy analysis of Fig. 3.7 not only validates the ergodic assumption behind the inversion methodology but also demonstrates the robustness and efficiency of this inversion method. In both cases, it was possible to pinpoint the exact concentration of defects contained in the probing system with great accuracy even when decreasing the amount of data used for the configuration averages. This behaviour was seen for input configurations with defect concentrations of up to 8%. Finally, it is worth pointing out that this study also suggests that the applicability of the method can be extended to any type of spectral function besides the DC and optical conductivities. Combined with the CPGF method, it can determine the disorder concentration of realistic systems with a reasonably low computational cost and points to possible on-demand inversion of experimental spectral signals. On attempting such inversion from an experimental setup, it is important to consider the possible relevant disorder types on the system at hand, such as different scatterers, and calculate the CA accordingly. The method can then easily be extended for the case of multiple disorder types as seen in reference [80].

3.4 Inversion of Experimental Data

As stated earlier, vacancies are the most likely type of disorder to naturally occur during the fabrication of TMDs and this is the reason why we chose to analyse this type of disorder in this chapter. In fact, vacancy occurrences are so common that even when attempting to fabricate pristine MoS_2 systems via methods such as chemical vapour deposition (CVD), one will end up with systems containing some non-negligible amount of vacancies. Moreover, to preserve the purity of the material sample, much care is taken to avoid condemnations during the fabrication procedure and, as a result, structural defects are the ones most likely to be present. Therefore, these defects will be, for the most part, responsible for the variation between the spectral measurements of different material samples created under the same conditions and procedures. This natural variation provides a great opportunity to test our

inversion method with non-synthetic measurements in an attempt to identify the amount of vacancies in different samples.

So far, to implement our inversion method, we generated DC conductivity curves from synthetic systems populating our CA space and creating a basis for discrepancy comparison with our synthetic input signal. Now, we have access to a set of transconductivity data of different CVD-grown MoS_2 samples obtained via a three-point measurement experimental setup as seen later in Fig. 3.9 - the source voltage, the gate voltage and the drain, where the source and drain are kept constant and the gate voltage is systematically altered to change the electric field in the sample, resulting in a shift in the system's fermi-level. These samples have completely unknown structural configurations, but, given the fabrication method, we assume they contain some noticeable quantity of vacancies, which prompts us to perform the inversion by comparing them with our synthetic calculated CAs. Given that our CAs were generated from first principle parametrization in a TB modelling, we expect them to behave similarly to real conductivity signals and, based on that assumption, we carry out this inversion of the experimental data.

As we have carefully laid out in section 2.2.2, much care has to be taken when defining our inverse problem, especially in the present scenario, where we do not have complete information about the composition of the samples. Verily, even while preserving our sample purity assumption, there are still multiple different kinds of structural disorder which could influence the variations observed in the transconductivity signals. Yet, for the sake of simplicity, we assume that only chalcogen vacancies are causing the signal variations and allowing us to perform qualitative signal inversions availing of our previous CA calculations. In this way, we are effectively projecting all other possible types of structural disorder of the system into the vacancy disorder space. That is, their possible contributions to the spectral variation are being interpreted as vacancy contributions, virtually shifting the prediction of vacancy occurrence up or down. A thorough inversion procedure would require all possible types of structural disorder to be considered in the misfit function calculation and, in turn, this would exponentially increase the complexity of the problem. Nonetheless, to consider the perceived effects on the transconductivity signals to be predominately caused by vacancies is still a good approximation given the strong impact vacancies have on TMDs, especially in the early parts of the conductivity spectrum following the transition gap as we have seen in section

3.1.1.

Material Fabrication and Measurement

The transconductivity experimental measurements were possible thanks to a collaboration with experimental physicists and chemists from Mackenzie Institute and UFRJ who fabricated the samples as described below.

MoS_2 flakes were synthesized on 300 nm thick SiO_2/Si substrates using the chemical vapour deposition (CVD) method. Here, MoO_3 (6mg) and NaCl (24 mg) powders were mixed and placed in an alumina boat in the high-temperature zone of the CVD furnace. The substrate was placed facedown above the alumina boat containing the NaCl/MoO_3 mixture. Meanwhile, 140 mg of pure sulfur was placed in another alumina boat in a low-temperature zone. Both alumina boats were placed at a distance of 22 cm along the quartz tube furnace. First, a flow rate of 600 sccm of high-purity argon (Ar) gas was passed through the experimental setup for 15 min to purge the quartz tube. Subsequently, a flow rate of 200 sccm (Ar) was maintained during the growth process. The Sulphur temperature was 250 ºC. The growth temperature to obtain MoS_2 monolayers was T= 850 °C (high-temperature zone) for 10 min and after that, the system was cooled down.

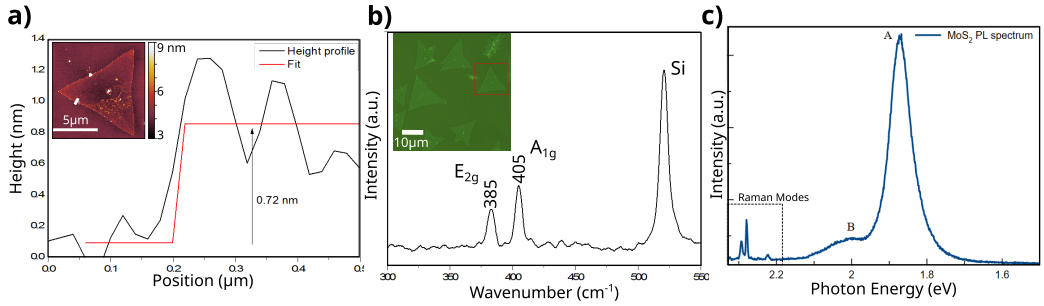


Figure 3.8: **a)** AFM height profile and topographic image (inset). **b)** Optical image (inset) and Raman Spectrum. **c)** Pholuminescence spectrum.

Optical and atomic force microscopies performed the Monolayer MoS_2 flakes morphological characterization. AFM measurements were performed using an NT-MDT Solver Next microscope equipped with feedback sensors, ensuring a Noise XY of less than 0.3 nm and a Noise level Z (RMS in the band of 10 - 1000 Hz) typically at 0.03 nm. Non-contact mode imaging was employed, utilizing a Force Modulation AFM Probe featuring a Platinum Overall

Coating, a force constant of 3 N/m, resonance frequency of 75 kHz, and dimensions of 225 μm length and 28 μm width. The formation of triangle-shaped nanocrystals with a mean lateral dimension of approximately 20 μm is observed (inset in Fig. 3.8a and b). The thickness of these triangular crystals determined by the height profile of AFM measurements (Fig. 3.8a) is around 0.7 nm, confirming the formation of monolayers. The Raman spectra (Fig. 3.8b) also confirm the flake's monolayer nature by the presence of two Raman-active modes at the Γ point: E^1_{2g} at around 385 cm^{-1} and A_{1g} at 405 cm^{-1}, with a frequency difference of 20 cm^{-1}, typical of monolayer. A strong signal between 665 and 620 nm can be observed in the Photoluminescence spectra (Fig. 3.8c), which corresponds to A and B direct excitonic transitions. For Raman and Photoluminescence measurements, a confocal Raman spectrometer (WITec Alpha 300R) was utilized, incorporating a 100X objective lens and a 532-nm laser line with a laser power of 0.5 mW.

Back-gated field effect transistors were fabricated using a 50nm alumina (Al_2O_3) film as the gate oxide and a stack of Pt/TiN/p++Si as the back gate electrode. First, CVD-grown MoS_2 was transferred onto the alumina sample. The sample was spin-coated with A6 PMMA, followed by electron-beam (e-beam) lithography to specify the 2 µm channels, and then separated out by sulfur hexafluoride (SF_6) etch under 5^oC for 30s. After each step, the sample was rinsed in acetone for 30 min, followed by a rinse in IPA. To define the source and drain contacts, the sample was spin-coated with methyl methacrylate (MMA) followed by A3 PMMA. The electron-beam lithography source and drain contacts were then patterned and further developed using a 1:1 mixture of 4-methyl-2-pentanone (MIBK) and IPA for 60s. 40nm of Ni and 30 nm of Au were deposited onto the patterns using electron beam (E-beam) evaporation. The evaporated materials were lifted off by immersing the sample in acetone for 30 min, followed by an IPA final rinse.

Back-gated field effect transistors (BGFETs) were designed and fabricated (Figure 3.9), to extract the drain current (I_{DS}) versus the back gate voltage (V_{BG}). The transconductance per width (g_m/W, where $g_m = dI_{DS}/dV_{BG}$) versus V_{BG} was used as the input function $\Gamma_I(E)$ for the inversion procedure to extract the approximate vacancy concentration on the MoS_2 flakes. The calculated average field effect mobility (μ_{FE}) was 15 $\pm$ 10 cm^2/V^{-s}, which is comparable to the mobility values reported for exfoliated single crystal material [200]. The ON state current was found to be approximately 120 μA/μm at

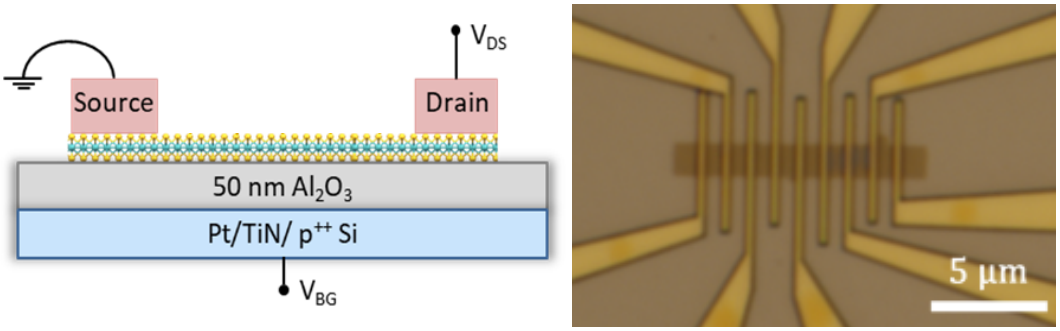


Figure 3.9: MoS_2 BGFET devices. Schematic of a back-gated field effect transistor (alumina) under the MoS2 channel on the left and optical image of the fabricated devices showing the lateral structure on the right.

$V_{DS} = 8$V and $V_{BG} = 10$V. The calculated subthreshold slope (SS) was 350 mV/decade.

Inversion Results and Discussion

With 23 transconductivity signals from different CVD-grown MoS_2 samples with unknown structural configurations in hand, we can compare them to our previously synthetic generated CAs to obtain the plot of Fig. 3.10a. In this figure, we observe a spectrum region within the conduction gap, similar to Fig. 3.6, and we can see the effect of increasing vacancy concentrations on the height of the peaks of conductivity. Since these are the first signal of conductivity that emerges after the valance band, we can assume that, as we increase the fermi energy of the system by changing the back-gate voltage, the measured transconductivity will contain information regarding these peaks.

The relationship between the back-gate voltage and the change of fermi-energy caused by it was not clear from the experimental setup due to undocumented gains. However, the measured transconductivity matches precisely the expected conductivity values giving us certainty in the y-axis and leaving us with one extra degree of freedom in the x-axis to fit the experimental curves. In Fig. 3.10a, we implemented an artificial gain on the x-axis so that the derivatives of the conductivity with respect to the energy of experimental curves would match those of the calculated case. In this way, we attempt to put both experimental and theoretical conductivities on the same footing so we can employ our inversion method. With the assumption that the system is composed solely of MoS_2 and S vacancies, we can invert the experimen-

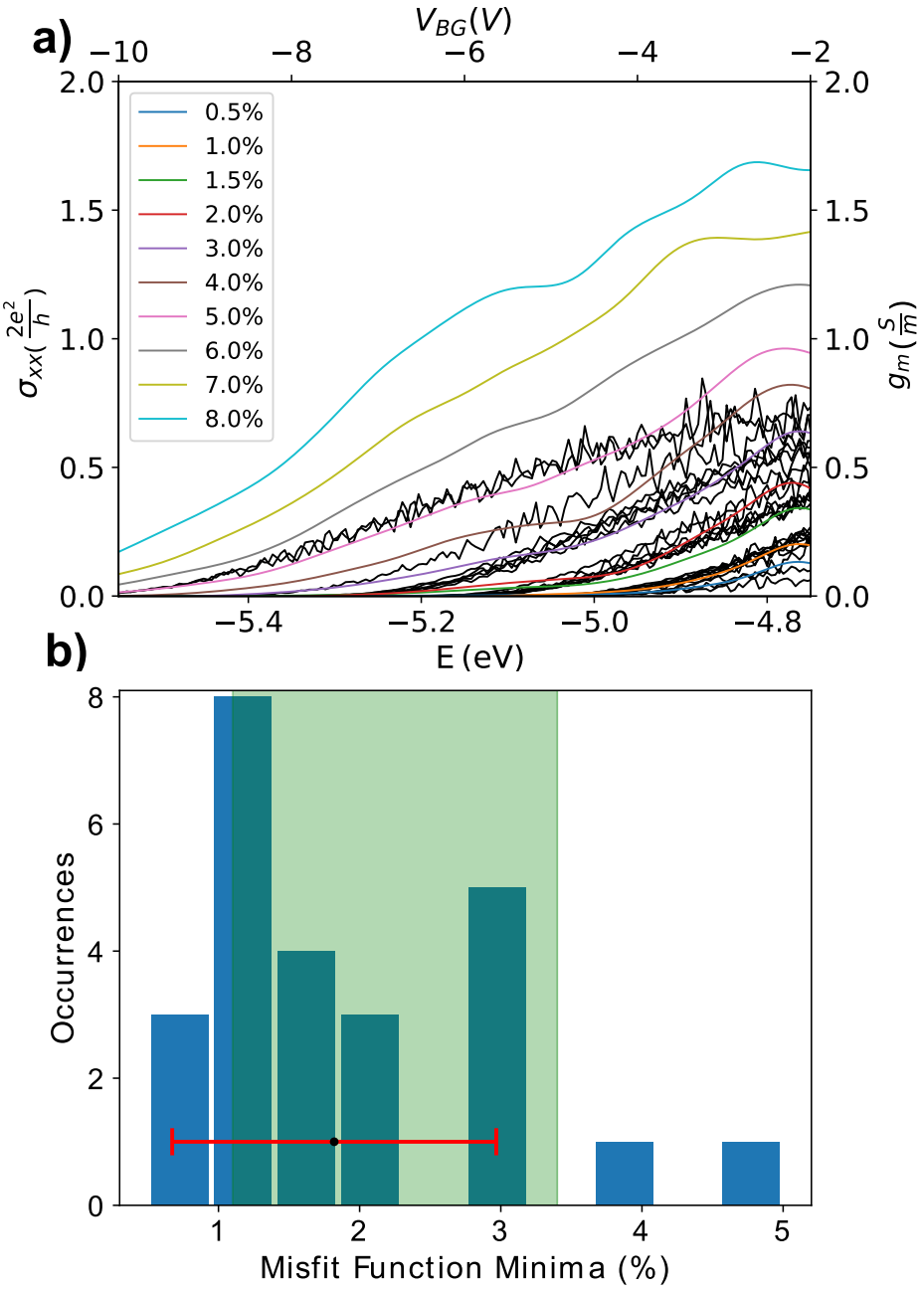


Figure 3.10: **a)** Comparison between simulated MoS_2 conductivity containing different vacancy concentrations (coloured) and experimental conductivity data for various MoS_2 systems (black), each of which contains unknown vacancy concentration. **b)** Histogram of the minima of the different misfit functions for each black curve of a). The black dot and red bar indicate the Gaussian mean and standard deviation of the minima distribution at 1.8 ± 1.1 %. The area in green represents the expected range of vacancy concentration previously reported for this method of fabrication.

tal data to obtain the misfit functions minima. Fig. 3.10b plots a histogram of the occurrences of each minimum found for their respective concentration positions.

Despite the lack of complete and direct information regarding our samples, we can still avail of some indirect information. By analysing previously reported vacancy concentrations of CVD-grown MoS_2 films [201–203], we can obtain indirect structural information regarding CVD-grown MoS_2 and use it to assess our inversion results. We find via our calculations that the inverted vacancy concentrations fall within and around the expected range of 1.2% to 3.4% of vacancy concentrations for CVD-grown MoS_2. This expected range is illustrated in Fig. 3.10b as the shaded green area.

This result configures a qualitative success of the inversion method implementation on experimental signals. A more impactful experiment would be to quantify the accuracy of the method by comparing the inversion results with the measured characterization of each sample whose spectral signal was inverted. Unfortunately, the characterization of the samples mentioned above was not possible due to limitations in the project's experimental laboratory and the availability of the samples. Despite this handicap, the results provided are still significant as they illustrate a direct application of the inversion method on input signals generated from experimental data. This achievement bridges the gap between synthetic inversion algorithms and realistic applications of the inversion tool, expanding the frontiers of inversion science. Furthermore, it establishes that tools of such type can be employed as a reliable mechanism for material characterization, and, promisingly, material design.

3.5 Interpolation Method for CA Generation

It is clear by now that populating the configurational average space is crucial for the success of the proposed inversion. By increasing the grid density of our CA space calculations, we can determine the result of the inversion with higher accuracy as long as the mesh point separations are not smaller than the standard deviation length associated with the configuration distribution for each CA calculation. However, we have also concluded that the calculations of reliable CAs (CAs obtained from a high enough amount of configurations) are computationally expensive and, in order to increase the accuracy in the inversion-target parameter space, we would need more CA points. Moreover,

finer CA meshes demand CAs calculated from a more definite distribution (with lower standard deviation), which demands more system configuration calculations and consequently further increases the cost of the CA mesh. For this reason, the CA calculations are currently the bottleneck of our inversion method and, if one could introduce yet another approximation method to derive the CAs more easily, one could facilitate the overall application of this inversion methodology.

One way of doing so is to approximate the expression of our CA to its first-order expansion with respect to the disorder concentration n, and evaluate it around $n = 0$ to extract the parameter β such that [204]:

$$\langle \Gamma(E, n) \rangle \approx \Gamma_0(E) - n\beta(E)\,, \tag{3.1}$$

where $\langle \Gamma(E, n) \rangle$ is the CA of the disorder concentration n we wish to approximate, $\Gamma_0(E)$ is the spectral function of the pristine system, and all the contribution of the disorder concentration is expressed in the term $n\beta(E)$, with $\beta(E)$ being the first order expansion coefficient. In other words, we are considering in this approximation that any CA with a disorder concentration n will be proportional to the pristine system minus a linear contribution with the concentration value n of the energy-dependent coefficient $\beta(E)$. Note, however, that this is a rather big assumption - it states that whatever contribution a specific disorder has in the spectral signal, the configurationally averaged contribution grows linearly as a function of the disorder concentration. This may be a good assumption at low concentrations, but as the disorder concentrations get higher and the scatterers have the opportunity to interact strongly with the host or between themselves (either directly or mediated by the host system), these interactions may assume a variety of forms which are not easily described by the linear approximation.

With this context, we can avail of the approximation in Eq.(3.1) to generate CAs for more values of the concentration n using interpolation supported by machine learning instead of calculating them via brute force. Fig. 3.11 shows a misfit function calculation where the points in red are the results of numerically generated CAs and the points in black are from CAs obtained via the interpolation method. Note that the 33 black points result from interpolating solely the 7 numerical points shown in red, which cut our calculation cost almost five-fold. Naturally, the more numerical data available, the better

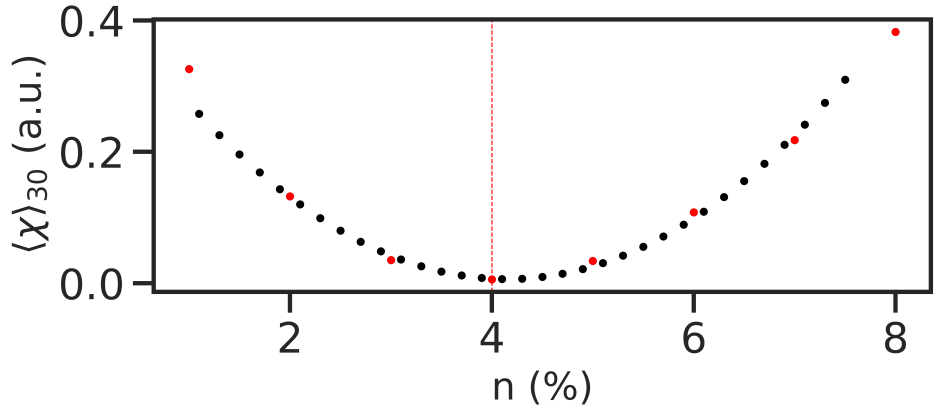


Figure 3.11: Misfit function in black for the machine learning optical conductivity interpolated data based on the numerical data whose misfit function result is shown in red. The model still predicts the minimum correctly while providing via approximation more resolution around it, allowing for fine probing of different input configuration concentrations with lower computational costs.

the interpolation approximation is, but also more expensive will the general calculation be.

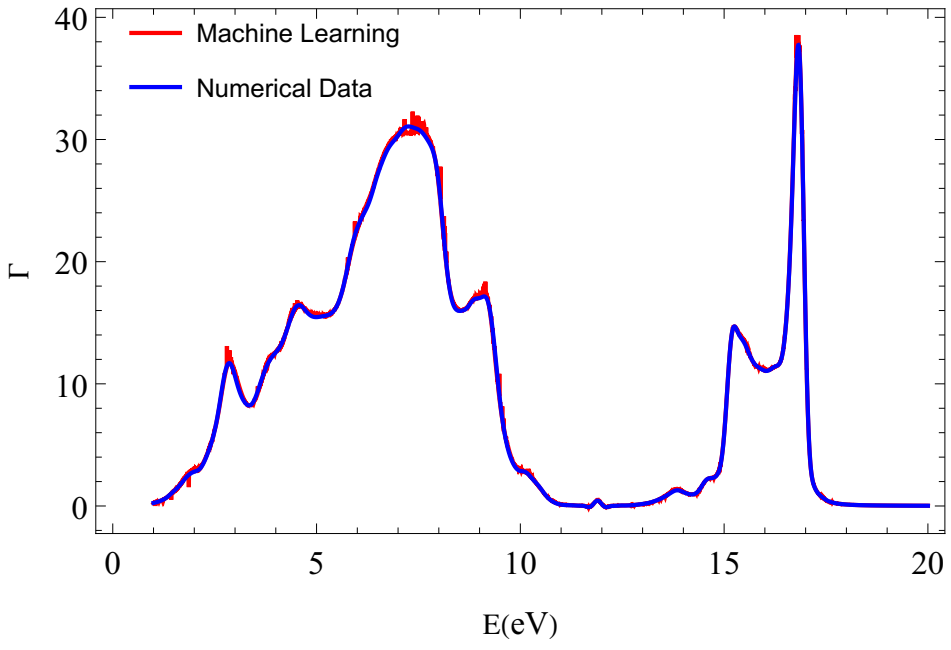


Figure 3.12: Configurational average corresponding to 8% disorder randomly distributed in the device represented in Blue. In Red, machine learning optical conductivity shows very good prediction with the numerical result.

In this way, machine learning becomes a very handy tool capable of gener-

ating CA spectral functions and it does so at a low computational cost without losing details of the quantum signatures of the disorder at low concentrations. Fig. 3.12 demonstrates a good prediction of MoS_2 optical spectrum CA corresponding to 8% of disorder with the numerically calculated optical spectrum in blue and the machine learning result in red. Both images illustrate the same model trained over only 7 numerical CA calculation points, which highlights the efficacy of this approach.

Wolfram Mathematica provides predefined machine learning tools called Predict and Classify to define a model. Both tools can generate the output corresponding to concentration and energy in this case. The model uses numerically computed CA spectrums as the training examples. The CPGF-calculated spectrum provides a large number of energy points to train the model, aiding its accuracy. It is worth pointing out that while more sophisticated machine-learning techniques are available to model quantum transport [205, 206], this is by no means an essential ingredient of the proposed inversion method but one that can speed up the inversion calculations and improve its resolution.

3.6 Summary

In this chapter, we introduced the MoS_2 TMD and its characteristic types of disorder. We applied the inversion method and calculations derived in Chapter 2 to invert the spectral signals of this system to characterize its vacancy concentration. As input signal for the inversion, we used at first instance the synthetic DC and AC conductivity of the material, both of which returned an accurate result for the inversion. The major challenge that marks this procedure is the complex simulation for realistic spectral quantities of disordered MoS_2 systems, and we tackled this challenge by modelling the systems using a combination of TB and DFT tools and CPGF calculations. Meanwhile, we took advantage of the flexibility of the CPGF calculations to illustrate the ergodic principle in action and validate our previous assumption. We then introduce the next instance of our characterization, which takes experimental transconductivity data from CVD-grown MoS_2 films and compares them with our realistic synthetic CAs to obtain a qualitative characterization of the original systems. Despite not having the experimental characterization of the samples, we were able to verify the inversion results by comparing them with the quantity of vacancies expected to be present on CVD-grown MoS_2. The

chapter ends with a proposition for increasing the performance of the inversion method by introducing an alternative way of calculating the CAs, which calculations are the bottleneck of our operation. With the help of machine learning algorithms, we can interpolate extra CA signals based on a few ones calculated previously decreasing the computational cost associated with our method.

Thus we have shown that information about the composition of disordered structures is contained and can realistically be extracted from seemingly noisy conductivity response functions via an efficient inversion methodology. These results can be extrapolated to other simple or complex materials, given that our method is not material-dependent and works from simple electronic structures such as graphene [80] to more complex materials such as the case shown here with MoS_2. This marks an expansion in the range of applications of our methodology, enabling its use in a variety of systems and quantities and most significantly, it reveals its possible implementation on inversions of experimental signals. The remarkable robustness and versatility of this methodology suggest that structural and compositional information about disordered quantum devices can also be extracted from physical signals other than DC or optical conductivities.

That said we can confidently answer yes to both questions posed at the beginning of the chapter - the inversion method is capable of handling realistic systems, and it demonstrates promising application on experimental signals. In the following chapter, I will dive deeper into the capabilities of this method by approaching the characterization of MoS_2 systems containing a type of disorder with a characteristic signal in the conductivity spectrum that poses a greater challenge for the inversion procedure overall. I will analyse how the method fares with this challenge once again probing the frontiers of its application.

Chapter 4

Inversion on MoS_2 Films Functionalized with Gold

In the previous chapter, we explored how our inversion methodology can be used to recover vacancy concentration on MoS2 from synthetic and experimental signals. We tackled that problem to answer questions regarding the scope of application of our method. In this chapter, I will dial up the complexity of the problem by attempting the inversion to characterise a type of scatterer with an extremely weak signature in the conductivity spectrum. The disordered system of choice is the MoS_2 functionalized with adsorbed $AuCl_3$ molecules. This new challenge will demand a more complex description of our system translating to more complex calculations and this stress test will ultimately assert the applicability of our inversion method in more challenging conditions.

4.1 Functionalization of TMDs

Much has already been said about MoS_2 and TMDs in our previous chapter, so let us focus here on understanding our new type of scatterer, which appears as a result of the functionalization of our system.

TMD can be functionalized via chemical functionalization [207–210], physisorption [211, 212] or other non-bond-forming methods [213, 214] to introduce new properties or enhance existing ones such that their range of applications is broadened. These include tuning electrical or optical properties [197, 215–217], catalytic properties [218, 219] and mechanical proper-

ties [220, 221]. Note, however, that because the metals of TMDs are located in the central layer of the film (see Fig. 3.1), they are hardly reachable from the surface, which makes them inaccessible for adsorption. The chalcogens, on the other hand, are exposed on the surface, but due to their being mostly saturated with covalent connections, they also tend to be chemically inactive. These two points make TMDs tend to be inert and their functionalization becomes a tricky task [222]. This reduces the number of possible functionalizations which limits the effect such a procedure can have on the properties of the material. One approach to circumvent this is to make use of the naturally occurring or fabricated lattice defects of our system to house our coordinated complexes, making it possible to overcome this chemical inertness [223–226]. This kind of approach, however, makes modelling the problem slightly more complicated - because the functionalization is linked to the occurrence of structural defects for allocation, the different types of disorder cannot be treated independently.

One of the possible types of functionalization that do not rely on the presence of lattice defects for passivation or substitution is the introduction of adsorbed $AuCl_3$ via the formation of S-Au-Cl coordination complexes $[Au(MoS_2)Cl_x]$ on the TMD surface chalcogens (see Fig. 4.1a) via bonding with the lone pair electrons of S. This functionalization introduces high exciton-to-trion ratios in the photoluminescence spectrum, and enhances the thermal boundary conductance of the system, while also allowing for Fermi level tuning via p-type doping [227]. The independence between the coordination of S-Au-Cl_3 complexes and the presence of other defects, in particular S vacancies, allows for an uncomplicated combination of both types of disorder when modelling the mesoscopic systems. It enables us to introduce multiple types of disorder without the danger of clash and, since the chalcogen vacancies are commonly formed defects, as we have previously discussed in Chapter 3, it is essential to consider the occurrence of such defect in various situations including when in the presence of other types of disorder. Another reason why we decided to focus on this specific functionalization is that the presence of S-Au-Cl coordination complexes reportedly did not interfere measurably with the carrier mobility of the MoS_2 system [227], indicating that any contribution this type of disorder may have on the conductivity spectrum is a minimal contribution. This reveals an ideal opportunity to verify the resolution power of our inversion method - if the inversion succeeds even in such extreme conditions, we can safely extend

the range of application of our method.

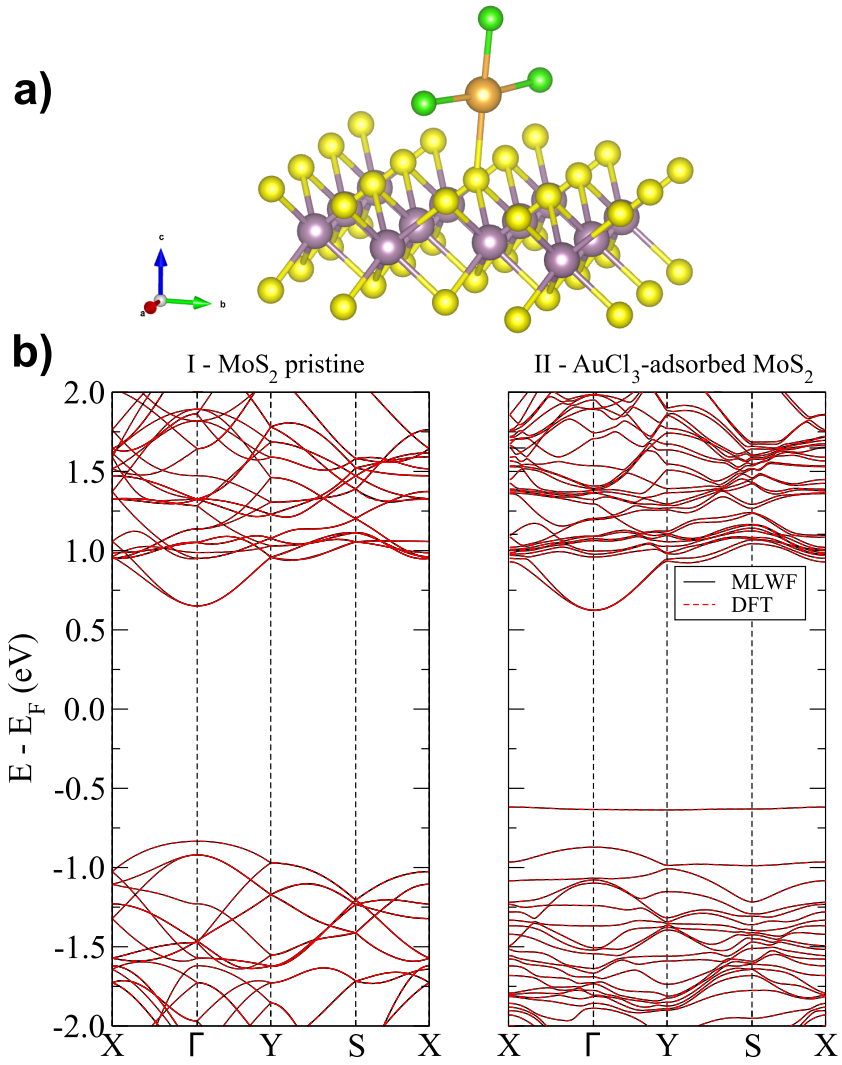


Figure 4.1: **a)** Standard orientation of crystal shape for the $(MoS_2)AuCl_3$ disorder unit cell (purple sphere = Mo, yellow sphere = S, golden sphere = Au, green sphere = Cl). **b)** Electronic band structure of **I -** pristine MoS_2 and **II -** $AuCl_3$-adsorbed MoS_2 calculated via DFT (red dashed lines) and the corresponding MLWF one (black solid lines). The agreement between the curves is such that it makes them hardly distinguishable.

Verily, it is expected that absorbed elements and complexes such as this one, with one point of connection to the lattice, will not contribute directly to the transmissions in the 2D plane, since, in a first approximation, the electrons will not pass through these atoms in their longitudinal motion, given the direction

of the electrical field. In this case, the CPGF moment calculations of Eq.(2.53) would yield zero since the velocity operator is perpendicular to the bonding direction. Nonetheless, these compounds still contribute to the transmission in an indirect way by altering the lattice and the Green function of the sites around them. This extra consideration promotes an unprecedented increase in complexity, once simple or complex *ab initio* models of the adsorption-lattice pair that focus on one unit cell are not enough to describe the effect the adsorption causes on the surrounding lattice. Instead, one has to observe the impact of the compound on its vicinity from first principles to notice the mechanisms through which the electric properties will change.

4.2 Adsorption Impact on Transmission

To illustrate how adsorbed elements modify the transmission of a system, we can examine a simplified version of the problem using the straightforward transmission calculation via the iterative Green function method explained in Chapter 2. For this instance, we will ignore the effect that the adsorbed complex has on the orbital positions of the system.

Let us observe a 1D linear chain of atoms of onsite potential ϵ_0 and hopping t. To capture the difference between a substitutional type of disorder and an adsorbed one, let us consider three scenarios for the linear chain: a pristine case, a case with concentration n of substituted orbitals and a case with the same concentration n of adsorbed orbitals. In Fig. 4.2, we can observe the disordered systems and the resulting average transmission value over a thousand configurations for $n = 5\%$. Once again we are performing calculations in 1D and the effect of Anderson localization is pertinent. However, since we are not changing the size of the system in the following calculations, we can make the following comparisons freely.

A few remarks are in order when simulating the system with adsorbed impurities. Firstly, note that the hopping to the adsorbed orbital t_A is smaller than the host lattice inter-orbital hoppings. This is to be expected since the adsorbed type of bonding is generally weaker than the host system internal bonds - this is especially true for the MoS_2 case, as we have discussed above. Secondly, note that the effect of the adsorption in the transmission is energy-dependent. Because of the weak bonding, the transmission signature of the adsorbed case is weaker than that of the substitutional case with the exception

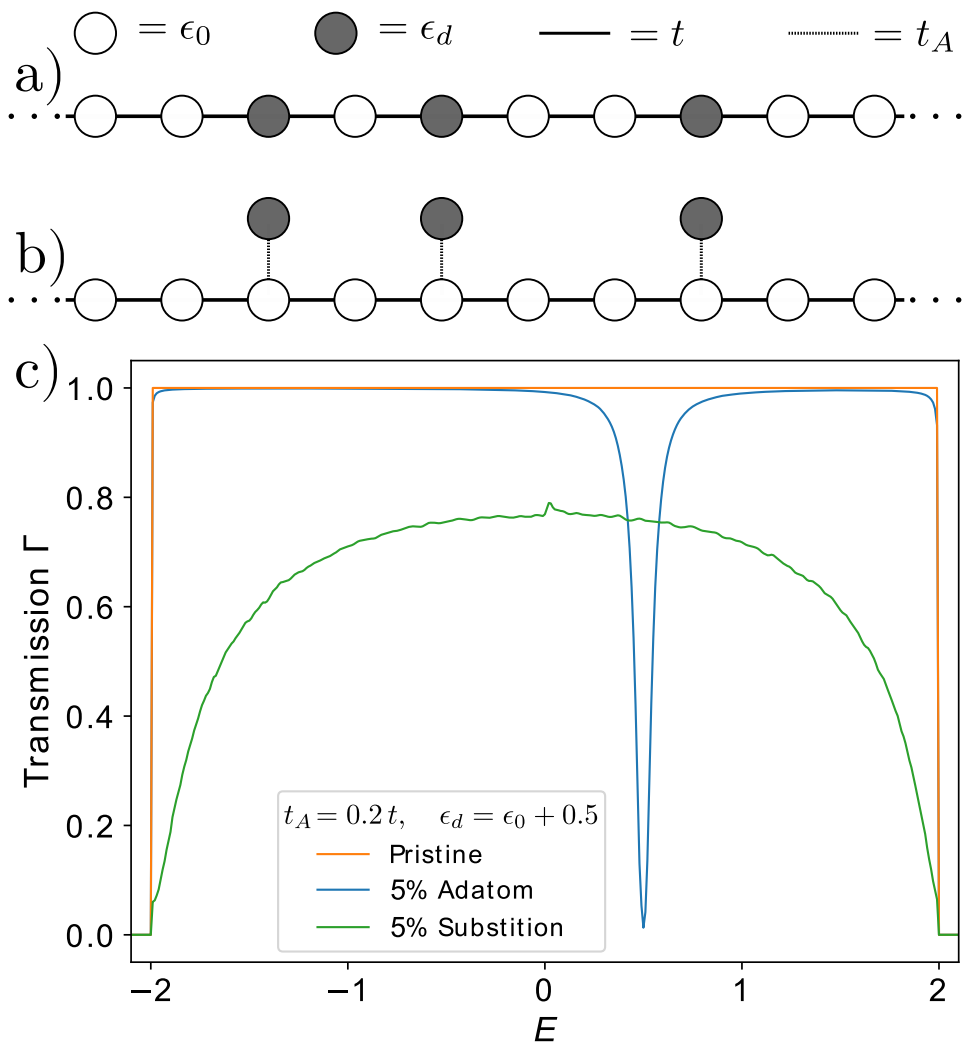


Figure 4.2: **a)** Linear chain with substitutional disorders. **b)** Linear chain with adsorbed disorders. **c)** Transmission results configuration average over ten thousand configurations with 5% disorder concentration in a 100-orbital linear chain for the pristine, substitutional and adsorbed cases. The hopping to the adsorbed disorder t_A is one-fifth of the lattice hopping t and the disorder onsite energy ϵ_d is 0.5 (a.u.) higher than the lattice onsite energy ($\epsilon_0 = 0$).

of one small energy interval. Around the energy value of the onsite potential of the adsorbed disorder (ϵ_d), we observe a peak in the transmission signature. It is mostly through this resonance with the system that the adsorption alters the transmission. We can observe this analytically if we consider the following scenario: Suppose I want to come up with a substitutional disorder with onsite energy ϵ_D such that its effect on the system is equivalent to that of an adsorbed one. For that, the disconnected Green function of the disordered site g_D will

have to equate the disconnected Green function of the adatom's anchor G_A (the orbital in the lattice to which the adatom is connected). From Eq.(2.22f), we can use Dyson's equation to obtain the Green function of the anchor connected to the adatom as:

$$G_A = \frac{g_0}{1 - g_0 t_A g_A t_A}, \tag{4.1a}$$

where

$$g_0 = \frac{1}{z - \epsilon_0} \quad \text{and} \quad g_A = \frac{1}{z - \epsilon_A}, \tag{4.1b}$$

with z being the complex energy value $(E + i\lambda)$, ϵ_0 being the pristine host onsite potential and $\epsilon_A (\equiv \epsilon_d)$ and t_A, the onsite potential and hopping to the adatom orbital respectively. We equate this to our proposed disorder Green function:

$$g_D = G_A \quad \Rightarrow \tag{4.1c}$$

$$\frac{1}{z - \epsilon_D} = \frac{g_0}{1 - g_0 t_A g_A t_A} \quad \Rightarrow \tag{4.1d}$$

$$\epsilon_D = \epsilon_0 + \frac{t_A^2}{z - \epsilon_A}. \tag{4.1e}$$

which shows that our made-up disorder onsite potential would have a dependency on energy, not only that but this dependency peaks at $E = \epsilon_A$, which is responsible for the resonance effect we observe in Fig. 4.2c (dampened by the imaginary value of the energy $i\lambda$). Note also that as the energy moves away from this value in any direction, the second term of Eq.(4.1e) tends to zero and our made-up disorder onsite potential tends to the pristine host onsite potential $\epsilon_D \to \epsilon_0$.

A curious consequence of this resonance-induced impact on the transmission is that different configurations of the same disorder concentration will yield very similar transmission curves for most of the spectrum, leaving a small range with variations. This results in quicker averaging, as depicted in Fig 4.3a, which shows the average convergence when averaging over ten thousand configurations of the adsorbed case compared to the substitutional one. This implies that lower configurations would be needed to build a reliable configurational average as within a thousand configurations, the adatom average

reaches a deviation as low as the one reached in the substitutional case at around nine thousand. Another consequence is that the strength of the disorder signature is mostly determined by the resonance value and its dampening, while less so by the disorder concentration, as shown in Fig 4.3b. This by itself would be detrimental to the inversion procedure, since the curves of different disorder concentrations would not be easily distinguishable within the resolution of the different configurational averages distribution. In the realistic case approached in this chapter, however, this simple model is not enough to describe the complex impact of the adsorbed impurities in the system, which is responsible for a set of distinguishable features in the transmission.

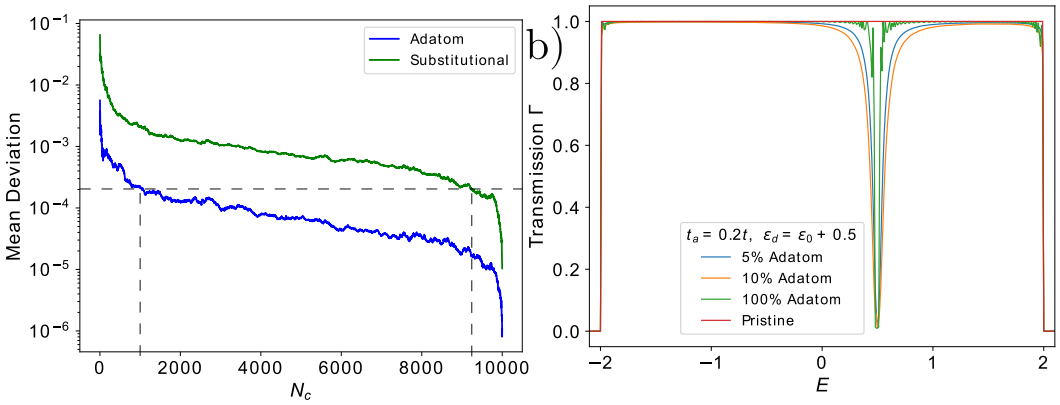


Figure 4.3: **a)** Average convergence comparison between adsorbed impurities and substitutional at 5% concentration in relation to the average done with ten thousand curves. Each step on the horizontal axis signifies an increase in the number of configurations used to compose the probing average. Note that the adatom case converges more rapidly at first, reaching at 1000 configurations the same level of conversion that the substitutional case reaches at around 9000. **b)** Comparison between average transmission of systems with adsorbed orbitals. Each curve is an average of ten thousand configurations with adsorption concentrations: 0% (Pristine), 5%, 10% and 100%, showing curves with very similar signatures almost on top of each other.

As we have noted, this is a simplified case in a basic system that serves to illustrate that the signature of adsorption is weaker when compared to substitution. To get a more realistic description, however, we have to model our complex systems to account for the structural impact of this type of disorder on the lattice.

4.3 Supercell Approach

To map the effect that the gold functionalization will have in our lattice, we need to expand our *ab initio* description of our system, from which we acquire the TB model parameters, as was discussed in Chapter 2. Now, instead of concerning ourselves with a unit cell composed of one primitive lattice cell, we use DFT (with the help of our collaborators at Universidade Estadual Paulista) to calculate the structural configuration of a set of primitive cells located around the functionalization, as illustrated in Fig. 4.1a. This set of 3×4 primitive cells we call a supercell and assumes the dimensions of 9.77 Å $\times$ 11.28 Å and with 3.22 Å of thickness after the DFT relaxation process. Disordered supercells are those containing the functionalization placed at the center while pristine supercells are composed solely of primitive MoS_2 sites. In the disordered case, the presence of the $AuCl_3$ coordinated complex will dislocate the surrounding Mo and S atoms, modifying their relative distances and, consequently, their hopping energies. Here, one $AuCl_3$ complex is included in the supercell with the gold atom positioned 2.69 Å (after relaxation) above a S atom, as shown in Fig. 4.1a. The total-energy and electronic structure results were obtained via DFT as implemented in the SIESTA code [228]. From the minimization of the localized Wannier functions [78, 79] of this structure via the Wannier90 code [181, 182], we can then obtain the TB parametrization which agrees with the DFT calculations as shown in Fig. 4.1b. With the new parametrization, we can repeat our calculation steps to simulate large systems.

Note, that, for modelling sake, the redefinition of the lattice in this way demands a reinterpretation of the hoppings - some hoppings that before were connecting neighbouring unit cells, now connect sites within one supercell, as illustrated in Fig. 4.4. This is important to keep in mind when constructing our lattice for the KITE [65, 175–177] environment via the PyBinding [229] lattice building scripts. Just as the index of the orbitals outside the primitive cell changes so they can fit within one supercell, the hopping towards orbitals occupying neighbouring supercells will have their relative number changed as well. A methodical construction of the supercell is necessary to accommodate these changes.

Once we perform this transformation in our lattice representation, the definition of disorder in our lattice also comes with extra caveats. Now, we have to account for the effect of considering a large unit cell (the supercell) as the

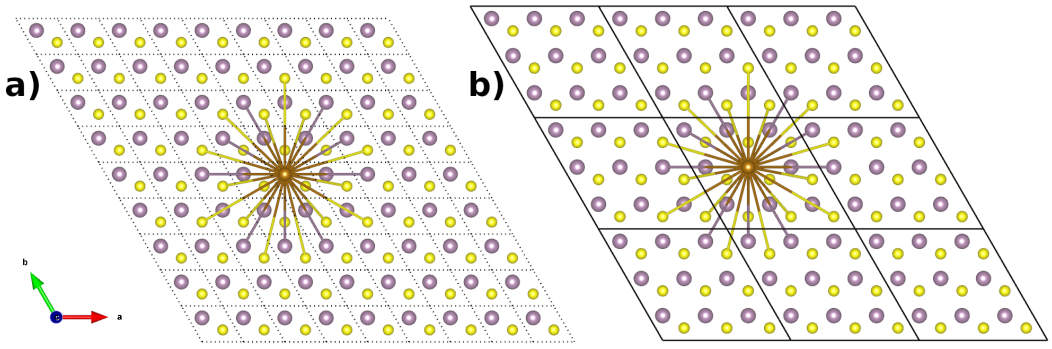


Figure 4.4: Difference between unit cell hopping reach in the cases of a lattice composed of **a)** primitive cells and **b)** supercells. Here, only the hoppings for the central Mo atom are shown to facilitate visualisation.

subject of disorder on the practical concentration and distribution, since the disorder-adding mechanism of KITE is unit-cell oriented. If we wish to subject our system to a certain vacancy concentration x, for example, it is no longer enough to implement a disorder of concentration x for the whole system for this would result in an effective concentration of $x_{eff} = \frac{x}{12}$. At first glance, we may attempt to address this issue simply by increasing the concentration of the disorder in the whole system twelve times. This, however, has an immediate limitation since $x_{eff} * 12 <= 1$, so the highest effective concentration value we can achieve would be $x_{eff_MAX} \approx 8.3\%$. Not only that, but if we impose the highest concentration, we will form a sub-grid of disorder, turning our disordered system into a crystal composed of equally disordered supercells.

To solve both these issues, we have to approach the introduction of disorder in a different way - each supercell is subject to multiple individual disorder types, each of which would be responsible for one set of orbitals and occurring in the right concentration. In other words, now we are no longer concerned with simply one concentration of S vacancies, but a set of vacancy concentrations $\{S_1, S_2, S_3, \cdots, S_{24}\}$, since the supercell grid contain 12 MoS_2, or 24 S atoms. For the case of the adsorbed disorder, since the geometry of the surroundings is relevant, we cannot modify its relative location within the supercell without requiring a fresh DFT calculation for each scenario. In this case, the limitations expressed above are present, so during the simulations, one has to be careful not to approach the extreme cases of application of this disorder.

4.4 Obtaining Gold Concentration via Inversion

Similarly to the previous chapter, we consider here the projections of p_x, p_y and p_z orbitals of the chalcogen atoms and the five d orbitals of Mo, and now we also account for the s and all the p orbitals of Au and Cl, respectively, adding to a total of 132 orbitals for the pristine and 142 for the disordered one. The DFT-derived parameters corresponding to a pristine MoS_2 unit supercell (all the onsite potentials for each orbital as well as all the second-nearest-neighbors inter-orbital hoppings of the 3x4 set of primitive MoS_2 cells) serve to establish the repetition base for a pristine description of the MoS_2 system.

In the KITE environment, we are unable to produce extra orbitals once our lattice is set, so to account for the possible instances in which our pristine supercells are subject to defects, we add to the pristine description ten empty, disconnected orbitals. Because they are isolated, these orbitals have no impact on the supercell or the calculation of the spectral quantities, but they reserve a scope in the modelling of the unit cell to later house the adsorbed impurities in case the given supercell is selected to be disordered. In this case, the energies and connections relative to the adsorbed atoms replace the orbitals previously held as mock orbitals.

The supercells are repeated to form 54067nm^2 systems with randomly placed impurities in different sites with predetermined concentrations. Our built systems comprise approximately 7.1 10^6 orbitals on a 64x64 unit cell grid containing various disorder concentrations. In each DC conductivity calculation, we used an expansion of 2048 moments of the Chebyshev polynomials for 3 different random trace vector iterations. Note that the number of necessary polynomials now has increased tenfold, which increases the cost of full-spectrum calculations by one hundredfold (since the system size is too big to store all necessary random vectors in memory). This problem also introduces a drastic increase in the size of our Hamiltonian and, in some cases, it may be more interesting to calculate fewer energy points instead of the whole spectrum to save computational resources. This can be done via the single-shot energy approach [175] as illustrated in one of the branches of the conductivity calculation algorithm of Appendix A. For our case, however, the more energy points we can avail of, the more accurate will be our inversion due to the underlying ergodicity of the method, as previously discussed in Chapter 2.

Fig. 4.5 shows the effect of $AuCl_3$ complexes and vacancies on the DC con-

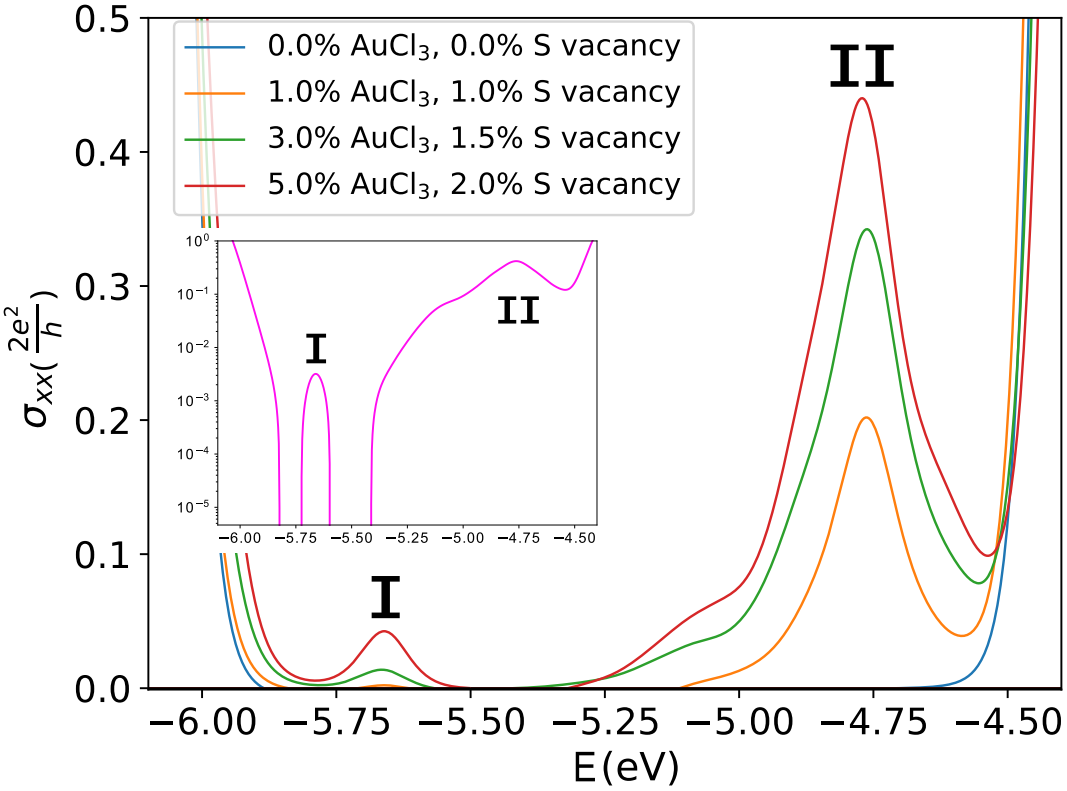


Figure 4.5: Intra-gap effect of the disorder shown in averages over 40 configurations. The heights of the peaks **I** are proportional to the increased presence of $AuCl_3$. The concentrations of $AuCl_3$ are exaggerated to illustrate both peaks in the same scale. The heights of the peaks **II** are proportional to the increased presence of S vacancies. In the inset, we can see the case for typical concentrations of 1% $AuCl_3$ and 2% S vacancies in the purple log-linear plot.

ductivity band-gap. The very occurrence of the unique peaks produced by the presence of disorder illustrates how the CAs with different disorder concentrations provide unique curves that populate the space of possible input signals, as more thoroughly illustrated in Fig. 2.9. Here, the concentration of $AuCl_3$ is exaggerated to make the peaks visible on the same scale - for the scenarios in this thesis Au concentrations will typically stay below 1%, however, systems with higher disorder concentration can also be fabricated (although our simulated concentrations peak at $x_{eff_MAX} \approx 8.3\%$). The separation between the characteristic vacancy and gold peak positions in the transmission gap region indicates independence between the types of disorder. Such orthogonality guarantees that $AuCl_3$ inversions and S vacancy inversions can be performed independently and simultaneously in the same system, avoiding the exponential scaling of the inversion procedure cost when a new disorder is introduced

in the inversion procedure as discussed previously in Chapter 2.

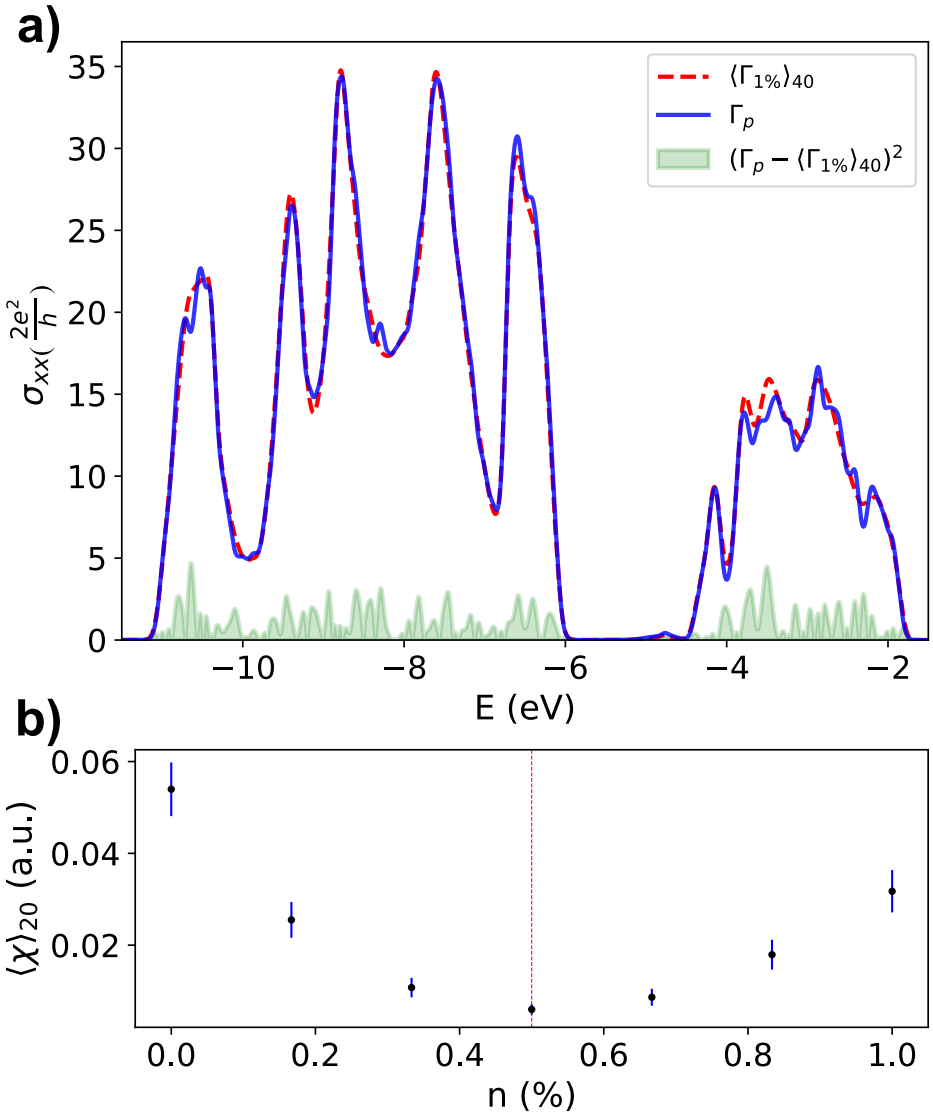


Figure 4.6: **a)** Longitudinal conductivity at temperature $T = 300$K comparison (filled green region) between 1% $AuCl_3$ concentration CA (dashed red line) and input configuration signal (solid blue line) containing unknown $AuCl_3$ concentration. The CA is composed of 40 configurations and all systems have a 1% concentration of S vacancies. **b)** Misfit function $\chi(n)$ in arbitrary units averaged over 20 distinct inversion instances with minima at 0.5% $AuCl_3$ concentration. The vertical (red) line indicates the real concentration of the input configurations.

Fig. 4.6a displays in green the integrand in the right-hand side of Eq.(2.66) calculated over the whole spectrum, depicting the CA in red and the input signal in blue, both for the case of theoretically calculated conductivity for

MoS_2 containing vacancies and coordinated gold complexes. To isolate the effect of the presence of $AuCl_3$ coordinated complexes, every system in these calculations was subject to the same S vacancy concentration of 1%. Each CA was calculated over configurations containing a certain concentration of $AuCl_3$ from 0% to 1%. The dashed red line in Fig. 4.6a represents one of these CAs, which was calculated over configurations containing 1% concentration of $AuCl_3$ impurity. The input function in blue has a concealed $AuCl_3$ concentration, to be determined via the inversion from the misfit depicted in green. Fig. 4.6b shows the resulting misfit function, with a very distinctive minimum. The minimum indicates the impurity concentration which produces the smallest discrepancy when compared to the synthetic input signal and is the most likely disorder concentration value of the original input signal. The CA defined in Eq.(2.65) was calculated here using only $N_c = 40$ configurations for each of the seven different disorder concentration values n, seen on the horizontal axis. Given the large integration range of this particular inversion, a relatively low N_c number is enough to compute a high accuracy inversion considering the ergodic properties of the problem as we discussed before.

We select an arbitrary disorder concentration (in this case 0.5%, indicated by the vertical red dashed line) to characterize our synthetically generated input function $\Gamma(E)$ and compared it with the previously obtained CAs calculated via Eq.(2.66). Repeating this procedure for multiple input functions with the same disorder concentration, we generate the average misfit values and respective standard deviations indicated by the error bars around the data points. The presence of such a clear minimum that coincides with the red line indicates that the inversion was successful. Furthermore, from the minimum relative depth and the respective standard deviations, we can conclude that the inversion was not only successful but also very accurate.

This remarkable result reveals that our inversion methodology is indeed capable of resolving the contribution of a minute concentration of adsorbed atoms and molecules to the conductivity of a disordered structure, even when such complexes weakly affect the charge mobility signature of the system. This configures an expansion of the applicability of the method now encompassing a new type of complex disorder, also testifying to its general accuracy and robustness. It is important to emphasize, however, that in cases where the target system is subject to impurities with extremely weak signatures, the accuracy of the method relies heavily on the precision and resolution of the input

function and the CAs. Our success reported in this chapter was possible due to the increase in complexity of the system modelling and respective calculations, allowing us to resolve the minute impact of the coordinated complexes on the conductivity spectrum. If one would attempt an inversion of an experimental signal containing $AuCl_3$ complexes, for example, the conductivity experimental measurements must be correspondingly sensitive to the characteristic signatures of this type of disorder. At this higher level of precision not only the characterization of disorder concentration of $AuCl_3$ is needed to evaluate the accuracy of the method, but also characterizations of the other possible impurities that may have stronger signatures, such as vacancies.

4.5 Summary

In this chapter, we approached the MoS_2 TMD in the light of a new type of disorder - functionalized $AuCl_3$ coordinated complexes. Due to the weak signature of this disorder on the analysed spectral quantities, its presence introduced a novel set of challenges both for our modelling and our calculations. We approached these challenges by implementing techniques such as the first-principles supercell description and by enhancing the complexity of our calculations via the increase of system size and number of polynomial moments, allowing for DC conductivity results with magnified resolution.

The presence of this weak scatterer in our target systems ultimately probes the extent of the application of our inversion method. By successfully characterizing the concentration of a disorder which exhibited no measurable change in carrier mobility, we demonstrate that the inversion method is capable of obtaining structural information about systems even in cases where the same would be hard to do from experimental measurements. This reiterates that this inversion methodology offers a powerful complementary tool for device characterization and that it is capable of tackling any type of disorder.

In the next chapter, we will shift a few of our paradigms to tackle a drastically different type of system. We will analyse nano-wire networks of memristors and apply the inversion method to obtain the parameters of the network which are decisive for the emergence of a specific type of behaviour.

Chapter 5

Inversion on Neuromorphic Systems

So far we have employed our inversion method to tackle disordered crystalline systems, but this technique is not structure-dependent. In fact, it is the opposite - it finds application precisely where there is a lack of structure or when there is the presence of disorder. That is to say that we do not need to limit ourselves to work on lattice-structured materials and, as long as we can extract information via a calculable measurement, we can perform an inversion. This is precisely what we will see in this chapter - now, our devices of interest are random nano-wire networks (NWN) built from random placement of wires without any prior structure. In this context, we now face disorder on a fundamental level - the very construction of the material is random, and disordered by definition. This innate disorder implies that every single system will display a different signature. Yet, the intrinsic properties that define the electrical transmission in these devices can be obtained via our inversion method.

Before I present the application of our inversion methodology, let me introduce our new system, the impact of certain parameters and the inverse problem in question.

5.1 Memristive Nanowire Networks

Nanowire networks (NWNs) have attracted the interest of solid-state research in the last decade due to their exceptional mechanical strength and flexibility

[230, 231], electrical conductance [232, 233], and catalytic activity [234, 235]. Randomly dispersed nanowires as depicted in Fig. 5.1, usually comprised of core metallic nanowires coated with a dielectric layer, exploit such properties to be used as sensors [236, 237], memory devices [238, 239], thin-film solar cells [240–242], energy storage [243], and transparent conductors [244–249], to name a few. When metallic nanowires are coated with a dielectric material, one can observe the emergence of memristive properties [250–254], which is to say that their electrical conductance depends on the history of the applied voltage. Such memristive property is at the heart of the development of brain-inspired neuromorphic architectures because it reflects an adaptive resistive behaviour similar to our current model of neuronal activity in the human brain. As a result, such memristive systems can be used to inspire the development of novel brain-like hardware or neuromorphic systems. [255–261]. In other words, when attempting to mimic neuromorphic behaviours, such networks of memristive systems exhibit adaptive activation behaviours in which the conductance of a memristive channel or junction is modulated by the current or charge flowing through it.

It is important to emphasize that, despite the title of this chapter, we do not currently have complete information about the functioning of the brain and brain cells. Notwithstanding the great advances in neuroscience, the mechanisms behind how the brain learns and stores information remain a mystery. When we say that these NWNs display neuromorphic behaviour here, we are referring mostly to the mimicking of *artificial neural networks* employed in machine learning. These networks are composed of artificial neurons and the way they interact with each other inside such networks resembles an extremely simplified version of our model for the behaviour of biological brain cells. Compared to biological neurons, artificial neuron networks ignore major environmental factors such as brain hormones, neuron taxonomy (morphology, physiology, signature, *etc.*), and the variety of computational operations that real neurons can do. A more faithful computational description of neurons is studied in the field of computational neuroscience, in which scientists create complex and resource-intensive models of the various kinds of neurons [262–264]. That said, one can hardly call artificial neurons biologically neuromorphic structures, but due to historical reasons, this nomenclature has persisted and along with it brought terms such as artificial "neuromorphic behaviour". Having clarified this terminology, one still has to acknowledge the

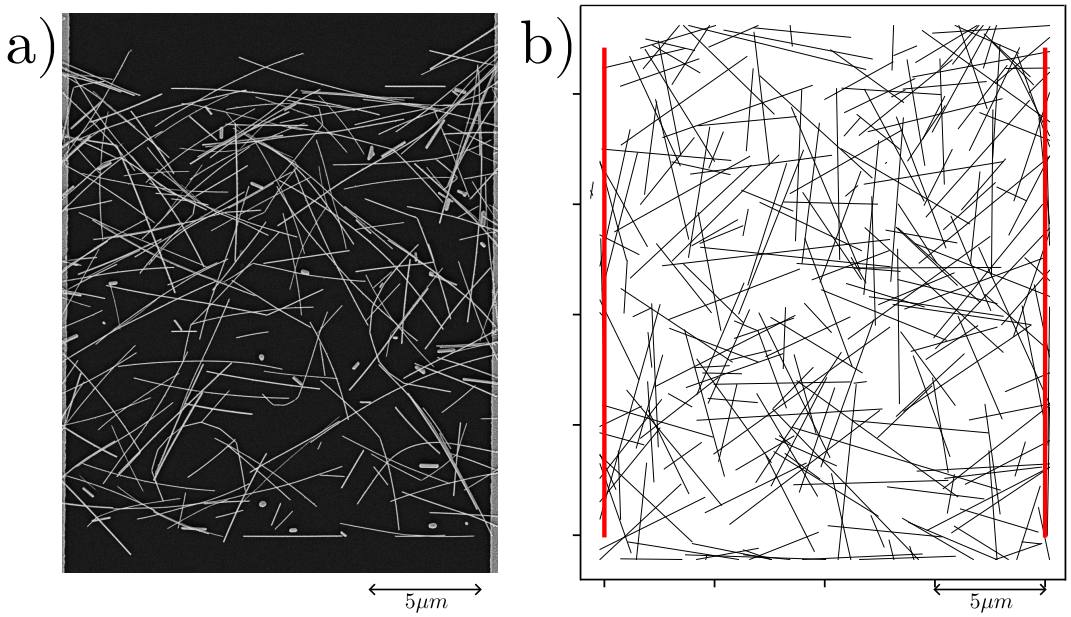


Figure 5.1: **a)** Scanning electron microscopy image of an NWN made of Ag/PVP core-shell nanowires with wire density of 0.49 nanowires/μm^2. Courtesy of the authors of reference [232]. **b)** Computationally generated random nanowire network geometry with a density of 0.67 nanowires/μm^2. The black lines represent the coated metal nanowires (in our case simulated to be Ag/PVP core-shell nanowires). The red vertical lines represent the metallic leads acting as electrodes.

power of artificial neural networks and all the emergent properties that arise from combining these simple structures as demonstrated particularly in the machine learning field of deep learning. With this in mind, discovering and studying physical systems capable of mimicking those artificial neuromorphic networks is vastly valuable for it can offer solutions to various computational challenges in the machine learning field.

5.2 The Winner Takes All Identification Problem

For the case of the NWNs studied here, the contact point or junction between two touching nanowires behaves as a memristive unit. When many of these memristive junctions are organized in a network, they may compete with one another for activation during a conductance evolution process, where the network is subject to increased voltage between the terminals. Activation here

is the process in which a junction will have its resistance decreased due to the passing of increasing current, as we will see later in greater detail. This competition can lead to a highly selective conducting state in which just a few junctions in the network take the load of propagating the majority of the current being sourced in the system. As in a mechanism to minimize power dissipation, under specific conditions, this state reveals a single conducting path formed of nanowires arranged as memristors in series. This selective conducting strategy coincides with artificial intelligence neuromorphic algorithms such as the "winner takes all" (WTA) implemented in computational neural network models, offering an *in materia* counterpart to the algorithm where the memory states are stored in the variable resistance states of the NWN [259, 265–268].

Manning et al. [265] provided experimental confirmation for WTA conducting pathways in NWNs formed with Ag nanowires coated with polyvinylpyrrolidone (PVP). To experimentally verify that a NWN would form a single WTA path, the authors used passive voltage contrast scanning electron microscopy imaging technique that depicted wires being "short-circuited" in the WTA path with distinguished colour contrast. This imaging process, however, requires the activation of the system at least up until the formation of the WTA path. It would be useful to predict if a NWN will develop a WTA path or not prior to the path formation to optimize the NWN use. Most importantly, we wish to perform this prediction in the absence of sophisticated and costly microscopy imaging methods. To perform this prediction is exactly the inverse problem we have in our hands. In contrast to the other inverse problems we have seen so far, in this case, we do not have access to the entire signature (the entire conductance current evolution), instead, we are tasked with predicting the future of the signature by analysing its initial behaviour and characterizing its network.

Manning et al. [265] performed extensive work on Ag/PVP NWNs which are prone to WTA states, but there is a wide range of other core-shell material combinations that can be tested for WTA. With this in mind, by solving this inverse problem, we will be able to predict the emergence of WTA before any experimentation and for a wide variety of materials, correlating the initial conditions and intrinsic characteristics of the NWNs with the final (potential) WTA state.

In summary, we need to decode the final WTA conductance state by in-

ferring the inputs and initial conditions that can lead to such a state. This inference is done with minimum information about how the NWNs are initially prepared. The formation of a WTA in a NWN system depends on various factors such as the properties of the junctions, the materials composing the core-shell nanowires, the overall network connectivity, and the junction density of the NWN, some of which are not accessible experimentally. It becomes relevant to devise a way of characterizing the appropriate parameters goading these events through indirect observation. In this chapter, I will adapt the inversion method we have been working with in the previous chapters for that goal. We will be able to extract NWN junction parameters that are crucially linked to the formation of WTA as well as parameters that are useful for the overall electrical characterization of the network junctions. As a result, we will obtain a robust computational framework that can directly complement experimental microscopy means to characterize NWNs, including their material and overall network features. To perform this task, we will need to first be able to simulate the NWN conductance evolution, which will be used to construct the CAs and input functions for our inversion technique.

5.3 The Junction Power Law Conductance Model

Now that the problem is enunciated, let us understand more thoroughly the systems in question (NWNs prone to WTA states) and define their main parameters used to model such conducting emergent features. We will also revise the main stages in the conductance evolution of a NWN subjected to increased current excitation that may lead to the formation of a WTA state.

Fig. 5.2 shows a circuit representation of a simple NWN motif made of just three nanowires for illustration. Multiple interconnected nanowires can be mapped as a network made of nodes and edges. In this representation, named Multi-Nodal Representation, the nodes are the points on each wire that share a contact with another wire. This contact point is represented by lumped circuit elements. In the case of memristive NWNs, the elements we use to describe their conduction properties are static Ohmic resistors and dynamic memristive units. Nodal voltage points located on the same wire will be connected by an inner "edge" resistor described by the standard law $R_{in} = \rho\ell/\Omega$ with ρ being the resistivity of the core metal, ℓ is the length segment between the two voltage nodal points, and Ω is the wire cross-sectional area. These inner resistances

are considered static or Ohmic in nature and are shown in orange in Fig. 5.2. A pair of nodes in different wires that share the same contact position defines a "junction" - the region of contact between two wires, and the point where the memristive properties of the dielectric coating are relevant. These junctions are described by memristive units whose resistance (R_j) changes as a function of the amount of current flowing through them and the history of the voltage applied across them.

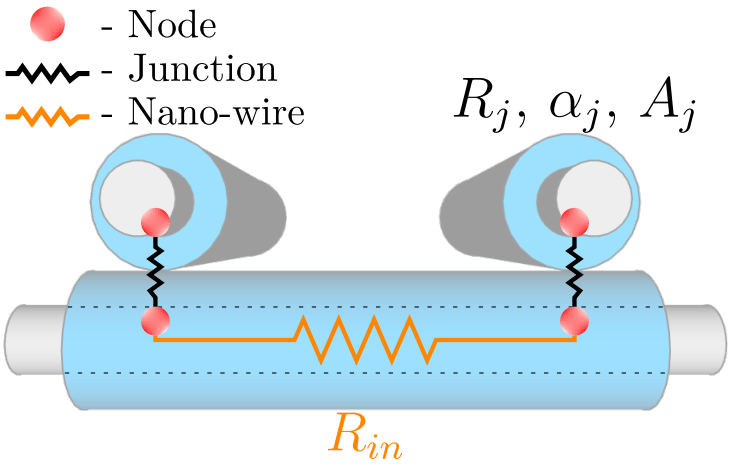


Figure 5.2: Schematics of core-shell nanowire contact points depicting the main resistance contributions in our circuit model. Three nanowires made of a metallic core (internal silver cylinders) are coated by a dielectric material (outer blue cylinders) and are in direct contact at two locations: at left and right positions with respect to the bottom nanowire depicted horizontally. At each contact point, two distinct voltage nodes or terminals are created (red spheres). The resistance inside a wire segment (orange resistor symbol) is described by a static Ohmic resistance given by $R_{in} = \rho\ell/\Omega$ with ρ being the resistivity of the core metallic material, ℓ the length segment between the two voltage nodal points, and Ω the wire cross-sectional area. A variable resistive junction j used to model the inter-wire dynamic conduction is represented by the black resistor symbols and is characterized by a junction resistance R_j which is a function of the parameters A_j and α_j defining the phenomenological power law $R_j = I^{-\alpha_j}/A_j$ being I the amount of current flowing through the junction.

We can verify experimentally that certain nanomaterial systems whose transport properties are dominated by junctions display self-similarity, which is to say that each nanowire junction possesses similar power scaling to that of the collective behaviour of the NWN junctions [265,266]. Following the model used in previous works, the interwire junction resistance R_j or its reciprocal conductance $\Gamma_j = 1/R_j$ can change from a low resistance state (LRS) to a high

resistance state (HRS) via an activation process ruled by a phenomenological power law given by $\Gamma_j = A_j I^{\alpha_j}$ in which I is the current flowing through the junction and A_j and α_j are power law parameters that characterize the intrinsic properties of the junction. Our power-law junction model has cut-offs in which the junction resistance cannot be larger than $R_{HRS} \sim 10^4$ kΩ and cannot be smaller than $R_{LRS} = 12.9$ kΩ which is equivalent to the quantum of resistance $R_q = h/2e^2$ with h being the Planck constant and e the elementary charge. These cut-offs were established based on previous experimental results in which 10^4 kΩ is already a sufficiently high resistance for the kinds of dielectric coatings considered and 12.9 kΩ is based on the assumption that the amount of current compliance set in the experiments is enough to form one single quantum of conductance channel inside the junction.

The parameters A_j and α_j that dictate the conductivity evolution of the nanowire junction j are associated with the electric properties and geometry of the materials composing the nanowires and the dielectric layers. From experimental measurements of individual nanowires and nanowire networks [265], we can determine that A_j is associated with the charge mobility of the nanowire material and the width of the junction whereas α_j is related to the nonlinearity in the memristive evolution of the dielectric diffusion barrier. This nonlinearity is present in the ion-drifting that occurs in the dielectric layer as the current changes [269]. The ion-drifting describes an extension of the conducting filament from the accumulation of ions within the dielectric material which decreases the distance between the nanowire contacts and consequently increases the tunnelling chance of charge between the capacitor formed by the metal-dielectric-metal junction. This affects the conductivity measured between the wires and its effects can be mapped on the A_j and α_j parameters. In some materials, we can observe that this ion-drifting is not linear [270–272], causing the emergence of hysteresis in the resistance variation of the memristor as well as an exponential parameter $\alpha_j \neq 1$ for the junction conductivity evolution.

The junction power law model with cut-offs as discussed above for fixed α_j values and scanned as a function of A_j and I (source current) can be visualized in Fig. 5.3 as colourmap surfaces. The three panels correspond to the cases in which $\alpha_j = 1.3$ (top panel), $\alpha_j = 1$ (middle panel), and $\alpha_j = 0.7$ (bottom panel). This figure shows clearly the regions of high and low conductance for a range of A_j at a fixed exponent α_j. We can see that when $\alpha_j < 1$, the activation of the junction, *i.e.*, when Γ_j starts to increase above the cut-off

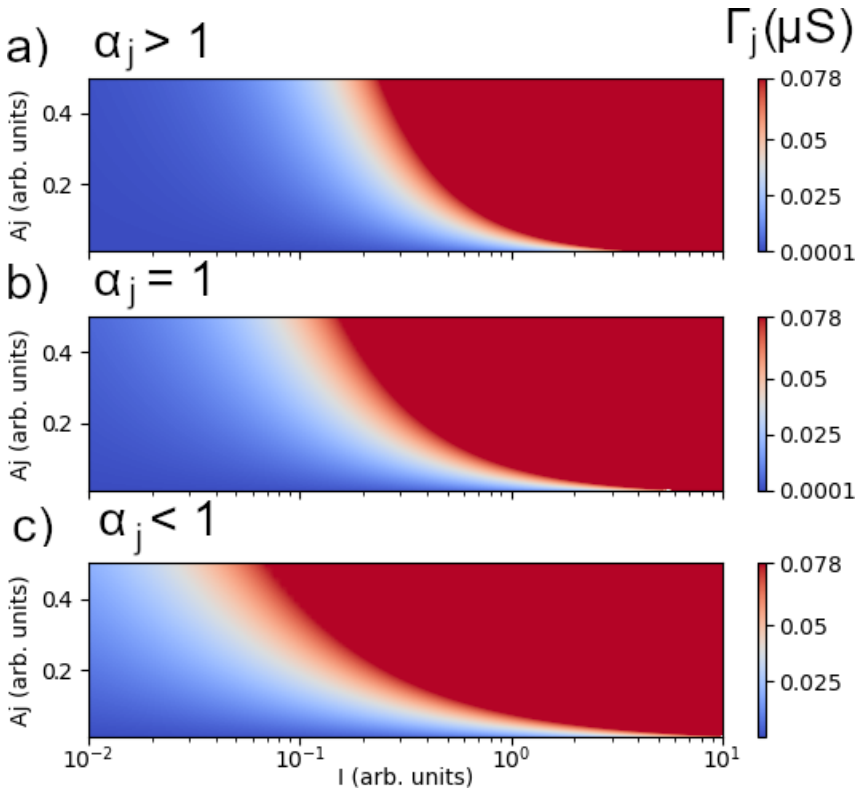


Figure 5.3: Surface colourmaps of the conductance junction model as a function of source current (I) and A_j, parameters in the junction conductance power law given by $\Gamma_j = A_j I^{\alpha_j}$. This conductance value is capped by two cut-off values defining an HRS and an LRS that the junction can endure. The resistance of the junction $R_j = 1/\Gamma_j$ cannot be larger than $R_{HRS} \sim 10^4$ kΩ and cannot be lower than $R_{LRS} = 12.9$ kΩ known as the quantum of resistance. The three panels show three important junction model cases that one needs to consider to subsequently understand the formation or not of WTA states in NWNs: **a)** $\alpha_j = 1.3$, illustrating junctions with $\alpha_j > 1$, **b)** $\alpha_j = 1$, and **c)** $\alpha_j = 0.7$, illustrating junctions with $\alpha_j < 1$.

$\Gamma_{HRS} = 1/R_{HRS}$, initiates at lower current values but its conductance growth is slower or sublinear. Setting $\alpha_j = 1$ or > 1 will result in the junction activating at higher currents but its conductance growth will be faster, linear and supralinear, respectively. These features in the single junction model will render complex emergent outcomes when incorporated in a NWN frame and it is key to the realization (or not) of WTA states.

5.4 The Network Conductance Evolution

Once the single conductance junction model is understood, we can incorporate it into a NWN circuit simulation framework with which we can monitor how the overall conductance of the NWN evolves as source current is gradually increased in between the terminals. The conductance evolution curves are a result of the NWN memristive-based dynamics formulated in terms of the junction power law model introduced in the previous section. In this model, the junction conductances in the NWN are not static, rather they vary in accordance with the phenomenological power law model given by $\Gamma_j = A_j\, I_{n,m}^{\alpha_j}$ in which $\{A_j, \alpha_j\}$ are parameters that depend on the intrinsic properties of the junction, and $I_{n,m}$ is the amount of current flowing between the two terminal nodal points in the junction (n, m). The conductances along the nanowire segments are considered static given by $\Gamma_{in} = 1/R_{in}$ with R_{in} being the nanowire inner resistance. We assume the nanowire metal cores are composed of the same material with a fixed inner resistivity of $\rho = 22.6$ nΩm (relative to the silver nanowires) and the nanowire diameters fixed at 60 nm.

The NWN conductance evolution simulation starts by setting the initial conditions for all junction resistances at R_{HRS} and considering that a minute amount of current (I_{min}) is being initially sourced in the metallic electrodes, electrically probing the NWN. Accounting for all NWN connectivity information and Kirchhoff's circuit laws, one can build the conductance Kirchhoff matrix $\hat{M}_\Gamma$ based on our resistances graph and apply it to Ohm's law written in matrix form as [265, 273]

$$\hat{M}_\Gamma \hat{\mathrm{U}} = \hat{I} \quad . \tag{5.1}$$

Here, $\hat{M}_\Gamma$ has the dimension $N \times N$, where N is the number of nodes in the graph representation. $\hat{I}$ is a vector $N \times 1$ storing the amount of current being passed through each node. At the start of every iteration, $\hat{I}$ is set to zero, except for the nodes representing the terminals, which will contain the values of current being sourced at each input terminal and extracted (negative value) at each output terminal. In our case, we have a NWN subjected to a two-terminal electrode setup, meaning that one of the electrode nodes acts as the source and the other acts as the drain of current. Given $\hat{M}_\Gamma$ and $\hat{I}$, the matrix equation above can be solved for $\hat{\mathrm{U}}$ which is the potential vector of dimension $N \times 1$, storing the electrical potential at each node of the network. Once $\hat{\mathrm{U}}$

is determined at this initial step, we can calculate the amount of current (in absolute value) flowing through each junction with terminals (n, m) given by

$$I_{n,m} = \frac{\mid \mathrm{U}_n - \mathrm{U}_m \mid}{R_j^{n,m}} \quad . \tag{5.2}$$

This junction current-flow value, in turn, is then used to update all junction conductance values using

$$\Gamma_{n,m} = A_j \, I_{n,m}^{\alpha_j} \quad . \tag{5.3}$$

The new values of $\Gamma_{n,m}$ define reciprocally the new resistances and compose the $\hat{M}_\Gamma$ matrix for the next evolution step. Note that $\Gamma_{n,m}$ values are bounded by the reciprocal limits $[R_{LRS}, R_{HRS}]$ to emulate the fact that junction conductances cannot increase or decrease indefinitely. More notably, the value $\Gamma_{s,d}$ between the source node s and the drain node d, indicate the global conductance of the network. The next evolution step is conducted by incrementing the source current by a sufficiently small value ΔI and repeating the process from equation (5.1). The NWN conductance evolution is carried on until a predefined maximum current source (I_{max}) value is reached. How large I_{max} is will determine if the NWN evolution will cover all transport characteristic regimes.

Because the NWN is composed of static and adaptive dynamical resistors, its conductance will evolve in a nonlinear manner as a function of the source current. Considering that the NWN starts at an OFF state in which all junction resistances are set at R_{HRS} and the current source starts increasing the current flow in small current increments, the NWN will pass over three other characteristic regimes which we named transient growth (TG), power law, and post-power-law. Depending on the choice of A_j and α_j values in the power law conductance junction model, each of these phases can be very distinguishable when analyzing the equivalent conductance of the NWN versus sourced current. This can be seen in Fig. 5.4 which shows some conductance curve evolution examples for the NWN structure presented in Fig. 5.1b. One can see that for $\alpha_j > 1$, the conductance evolution starts at a conductance plateau (OFF state), followed by a nonlinear conductance increase (TG), a power law regime marked by multiple discontinuities, and finally, the curve slowly converging into a linear Ohmic behaviour, characterizing the post-power law state. For $\alpha_j < 1$, the NWN conductance evolution curves depict a rather monotonic

growth (in log-log scale) in which the TG and power law stages are not easily discernible.

Most importantly, the exponential (power law) regime carries in its slope the information regarding the α_j junction parameter, however, our inverse problem is to identify this property before we reach this stage, *i.e.* at the transient growth stage. Therefore we can enunciate our inverse problem as:

> *Considering that we only have access to the NWN evolution up to the transient growth (TG) stage, would it be possible to characterize the intrinsic junction power law conductance model parameters (A_j, α_j), without a priori knowledge, allowing the prediction of the subsequent stages of the NWN conductance evolution and a possible WTA behaviour?*

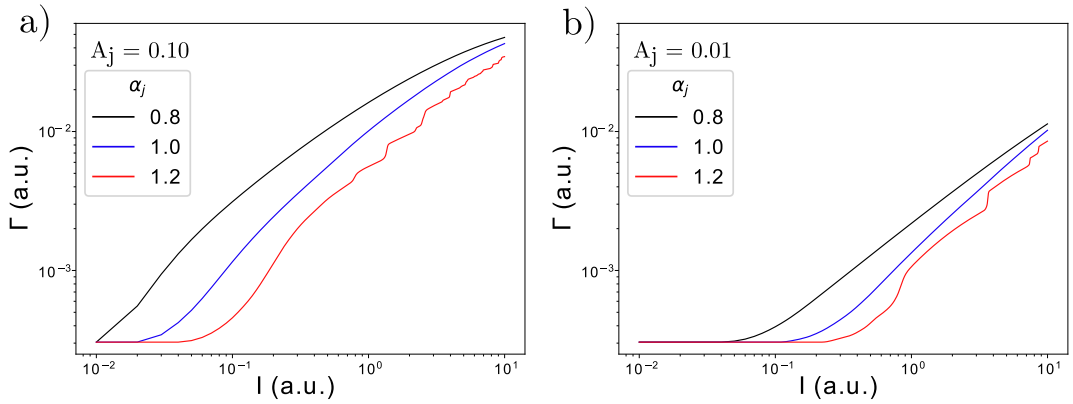


Figure 5.4: Log-log plots of the NWN conductance evolution as a function of the sourced current. The NWN geometry adopted here is shown in Fig. 5.1b. The junction power law conductance model parameters (given in arbitrary units) used in **a)** are for fixed $A_j = 0.01$ and three distinct curves taken for $\alpha_j = 0.8, 1.0, 1.2$. In **b)**, A_j was reduced (and fixed) to $A_j = 0.1$ and the same α_j exponent values as in a) were used.

Percolation in the Conductance Evolution

Nanowire networks have been thoroughly studied in light of percolation theory given that these networks can be equivalently described by their node connectivity and the slight change in the network connections leads to big changes in its electrical and optical-electrical properties [274–278]. In our case, the number of nanowires and their spacial configuration in the system is fixed, but thanks to the memristive properties of our junctions, their geometry changes

on a small scale, which leads to a statistical geometrical phase transition when we view the network as whole.

The different activation speeds of the junction detailed in the previous section hint at a percolation effect behind the formation of conductive paths in our nanowire networks. In Fig. 5.4, one can see clearly the percolation transitions happening, particularly in the cases for $\alpha_j > 1$. In these curves, the continuous change in the junction activation (given by the ion-drifting conductive filament augmentation) leads to the sudden formation of new conductivity paths, which are captured by the occurrence of the plateaus in the conductivity evolution graphs. This suggests that one can study the formation of the first stand-alone path (which we define as the WTA) as a percolation transition from the low-conductive state to the first plateau of conductivity. In our particular case, since we are interested in the transient growth regime of the conductivity evolution before the formation of the plateaus (before the actual percolation transitions), we did avail of percolation theory in the analysis of our inversion results.

5.5 Inversion of Conductance Evolutions

Now we have all the ingredients to perform our inversion. We begin by populating the configurational average space of the parameters we are interested in (A_j or α_j). Since each different NWN geometry will yield a different curve, our CAs here are the averages of the conductance evolution curve over N_c random NWN with unique geometries - $\langle \Gamma(I, A_j, \alpha_j) \rangle = (1/N_c) \sum_{m=1}^{N_c} \Gamma_m(I, A_j, \alpha_j)$. As before, for each configuration average (CA) the parameter of interest is slightly changed, allowing for a thorough mapping of the parameter space where it will be encoded the characteristic signatures of the parameter amount. The input function, in this case, is the NWN conductance evolution of a network with unknown α_j values $\Gamma_{in}(I)$.

To computationally generate enough network samples so that we could perform the parametric simulations in this work, we extracted the typical wire lengths, nanowire densities, and network sizes from real NWNs synthesized in the laboratory and devised a random NWN generation algorithm that would supply us with different synthetic NWNs while keeping essential similarities to the experimental ones. The computationally generated NWNs for the CAs resemble realistic NWN samples because their materials and structural features

are based on experimental micrograph images from past works [232]. While computationally generating the NWNs, the main spatial parameters and constraints set for the pseudo-random generator are:

- Length of electrodes and distance between them; those were set to create squared shape NWNs of 20 $\times$ 20 μm;
- The length of nanowires sorted in a given configurational sample is taken from a Gaussian distribution of average length 5.5 μm $\pm$2 μm standard deviation;
- The total number of nanowires, which were set to maintain the chosen standard of 900 wire-wire junctions (N_j), representing approximately the average junction density of the observed micrograph images. The number of placed wires also has to guarantee that the electrodes are electrically shortened;
- Each configuration (NWN) has a unique spatial distribution with nanowires being randomly placed at each generation.

Now we have as an input a truncated conductance evolution curve up to the TG regime from which the NWN (A_j, α_j) values are concealed or unknown. By obtaining the junction model parameters (A_j, α_j) we can infer if the NWN under study is prone to WTA conduction or not. To infer the power law exponent value, we calculate CAs for the set of networks possessing a systematically varied α_j value. In the misfit equation (5.4), we calculate the discrepancy between the partal input evolution Γ_{in} of a NWN system and the CAs $\langle\Gamma(I, \alpha_j)\rangle$ and integrated within the truncated evolution range $[I_{min}, I_{max}]$ as

$$\chi(\alpha_j) = \frac{1}{I_{max} - I_{min}} \int_{I_{min}}^{I_{max}} dI \; \left[\Gamma_{in}(I) - \langle\Gamma(I, \alpha_j)\rangle\right]^2 . \tag{5.4}$$

The point where χ versus α_j exhibits a minimum corresponds to the unknown α_j value that most likely generated the input NWN conductance evolution curve. Once α_j is unveiled, we can extrapolate information about WTA path formation: if $\alpha_j > 1$, we have an indication that a WTA is likely to be formed in that NWN. In the next section, we will see the prediction capabilities of the misfit method in such a way that the power law junction model parameters can be estimated from the partial NWN conductance evolution. In this scenario,

the minimization of the χ function allows us to infer the future of the NWN under study.

5.6 Determining Winner Takes All Occurance

To determine WTA occurrence, we first need to characterize the network junction parameters via the inversion method as explained in the previous section. At first, we assume the junction parameters are homogeneous throughout the network, in such a way that one can effectively consider these to be a global network parameter. We also assume A_j constant and attempt the characterization on α_j. We create CAs with $N_c = 100$ NWN conductance evolutions, each network set with a fixed $A_j = 0.05$ and α_j values varying from 0.6 up to 1.6 in increments of $\Delta\alpha_j = 0.05$. It is worth mentioning for the sake of simplicity, we are keeping all model parameters in arbitrary units meaning that conductance and current information are also given in arbitrary units. Realistic physical units can be set with appropriate scaling factors that result in conductances in S (Siemens) and currents in the nA (nano amperes).

Fig. 5.5a shows a colour band representation to illustrate the range of CAs with different α_j values. The dashed line on the same plot is the conductance versus current curve for an input NWN system that we wish to determine its a priori unknown α_j value. We apply the misfit minimization to unveil the unknown exponent α_j adopted in the input simulation. We have the resulting misfit plotted as a $\log(\chi)$ as a function of α_j, appearing in Fig 5.5b. The current limits of integration used in Equation (5.4) are consistent with including only the OFF and the TG regimes in the χ function. Note that χ as a function of α_j curve evidences a clear minimum at $\alpha_{min} = 1.1$ which agrees with the exponent of the input conductance curve that significantly overlaps with the yellow/green bands in Fig. 5.5a corresponding precisely to exponents in the range of $[1.0, 1.2]$.

We repeat this process for 60 input functions with concealed $\alpha_j = 1.1$ as the input as shown in Fig. 5.6 to obtain the statistical accuracy of this inversion. Once more, we can see the presence of a well-defined minimum with reasonable error bars, indicating a high-accuracy inversion. We conclude then that from the conductivity response of the system, one can predict an intrinsic parameter or initial condition of the system.

The result for this set of inversions indicates a supralinear exponent ($\alpha_j >$

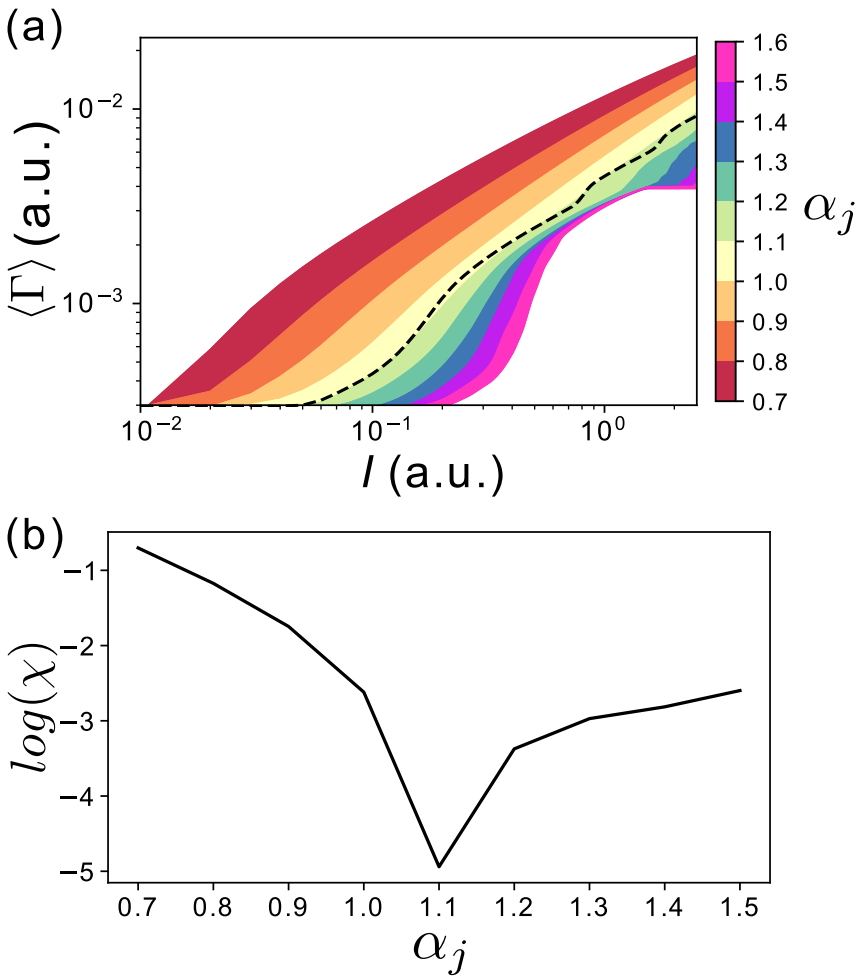


Figure 5.5: **a)** Colour band representation depicting the CAs composed of 100 configurations, which was used in the misfit minimization. Each colour band is defined between two CA curves. The configurations had $A_j = 0.05$ and distinct α_j values as depicted by the colour code. The dashed line is the input conductance evolution for a NWN evolved only up to the TG stage with an unknown α_j exponent. **b)** Misfit function $\log(\chi)$ versus α_j curve, with a clear minimum at $\alpha_{min} = 1.1$, revealing the correct exponent used in the input conductance curve before the power-law regime in the evolution.

1) and, as a result, one can expect the formation of a WTA even though the input function has not reached the power law stage yet. To verify this, one needs to explicitly visualize current pathways, *i.e.*, to visualize how the NWN is distributing the source current through its network structure. This can be done through current colour mapping plots as in Fig. 5.7. In the figure, nanowire segments carrying larger amounts of current are depicted in brighter colours. Each current colour mapping depicts a state of the NWN in the evolution

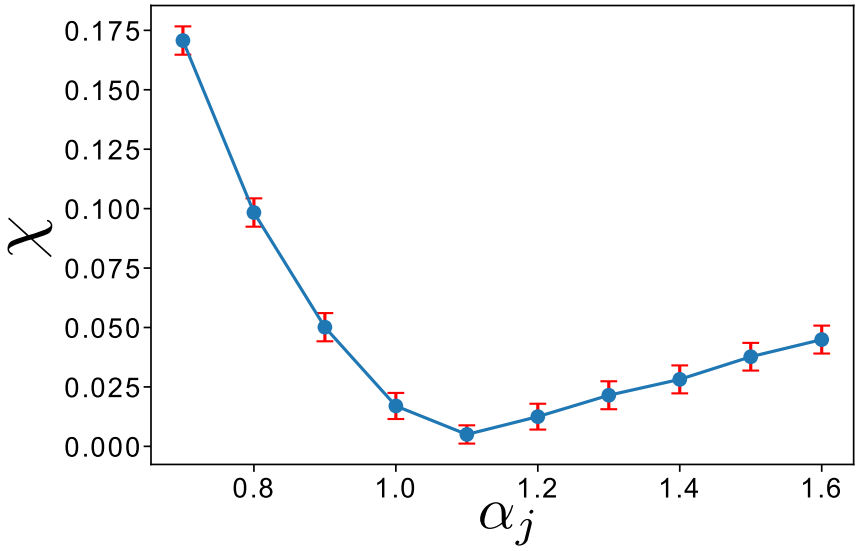


Figure 5.6: Average misfit function χ plotted as a function of exponent α_j, developing a minimum at $\alpha_{min} = 1.1$, corresponding to the actual value of the input systems. The current limits of integration considered in the calculation of χ for the inversion is $I_{min} = 0$ to $I_{max} = 0.2$ (arbitrary units) and fixed $A_j = 0.05$ (arbitrary units). The error bars correspond to the standard deviation in χ computed over an ensemble of 60 inversions.

curve of Γ versus I; for the results in Fig. 5.7, we fixed $I = 0.25$ (arbitrary units) which corresponds to a relatively early stage in the evolution as shown in Fig. 5.5a. To demonstrate the contrast between a WTA and a non-WTA (multiple paths) situation, we obtained current maps for $\alpha_j = 0.9$, $\alpha_j = 1$, and $\alpha_j = 1.1$ for a NWN of fixed spatial structure as depicted in Fig. 5.7a. In the cases of $\alpha_j \leq 1$, we observe various nanowire segments coloured, indicating that the current sourced into the electrodes is being distributed to distinct sections of the NWN. For $\alpha_j > 1$ however, a single current pathway is highlighted characterizing the early stages of WTA formation, which the misfit method could correctly predict without the need for current visualization maps.

The conductance evolution of a NWN subjected to a current source depends on numerous other parameters such as its connectivity pattern (*e.g.*, wire density that can define how sparse or dense a NWN is), junction density, material resistivity, nanowire length, *etc.* The procedure can be adapted to infer other variables as well, as we will see for the case of the power law prefactor A_j. Equation (5.4) can be rewritten in terms of A_j as the parameters to be inferred from the minimization scheme, *i.e.*, χ is a function of A_j instead. Furthermore, we can go one step further and conduct a dual-parameter

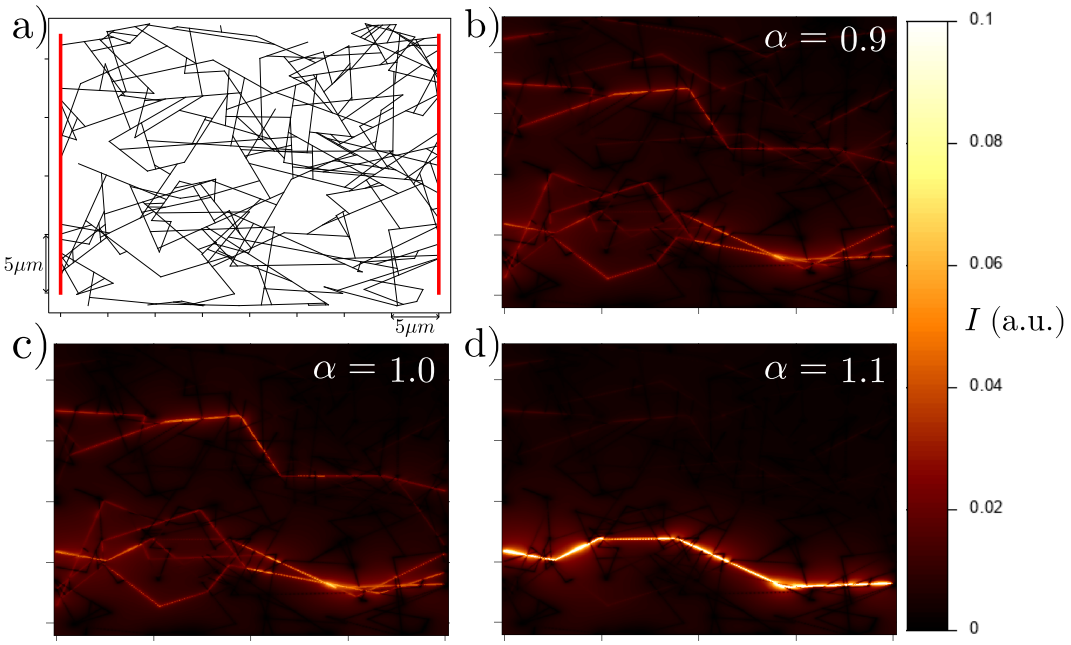


Figure 5.7: **a)** The same NWN as in Fig. 5.1b. Here only the nanowire segments between junctions are shown - nanowire "dead ends" are not depicted. **b-d)** Current maps obtained at the conductance state at $I = 0.25$ which corresponds to a state at the transient regime (TG) (see Fig. 5.5a). The power law prefactor was fixed at $A_j = 0.05$. Each panel shows the current color map for a given α_j value: b) $\alpha_j = 0.9$, c) $\alpha_j = 1.0$, and d) $\alpha_j = 1.1$. In the panels, $\alpha \equiv \alpha_j$. $\alpha_j > 1$ evidences the early stages of a WTA scenario whereas in the cases where $\alpha_j \leq 1$, a multiple path scenario is seen.

minimization, done in terms of both parameters A_j and α_j, as we mention to be possible in Chapter 2 and extended in reference [22]. This inversion requires us to populate a two-dimensional configuration space of $\alpha_j \times A_j$ with the NWN CAs, so naturally, it will demand more computations - the computational cost of populating the configuration space grows exponentially with the dimensionality of the space. The misfit values associated with each CA can then be depicted as a surface contour plot. We sweep this space with $N_c = 100$ CAs having A_j values ranging from 0.03 to 0.09 and α_j values ranging from 0.6 to 1.6 and applied the multivariable version of Equation (5.4) to calculate χ. The result is shown in Fig. 5.8, evidencing a $\log(\chi)$ minimum at $(\alpha_j = 1.1, A_j = 0.05)$, matching the power law model specifications of the input NWN system. Slicing this surface at $\alpha_j = 1.1$, we can visualize the minimum of χ as a function of A_j with clarity at $A_j = 0.05$ as shown in Fig. 5.9. The χ values are averages taken over 60 different inversion calculations from

which we also computed the standard deviations shown as error bars in the plot.

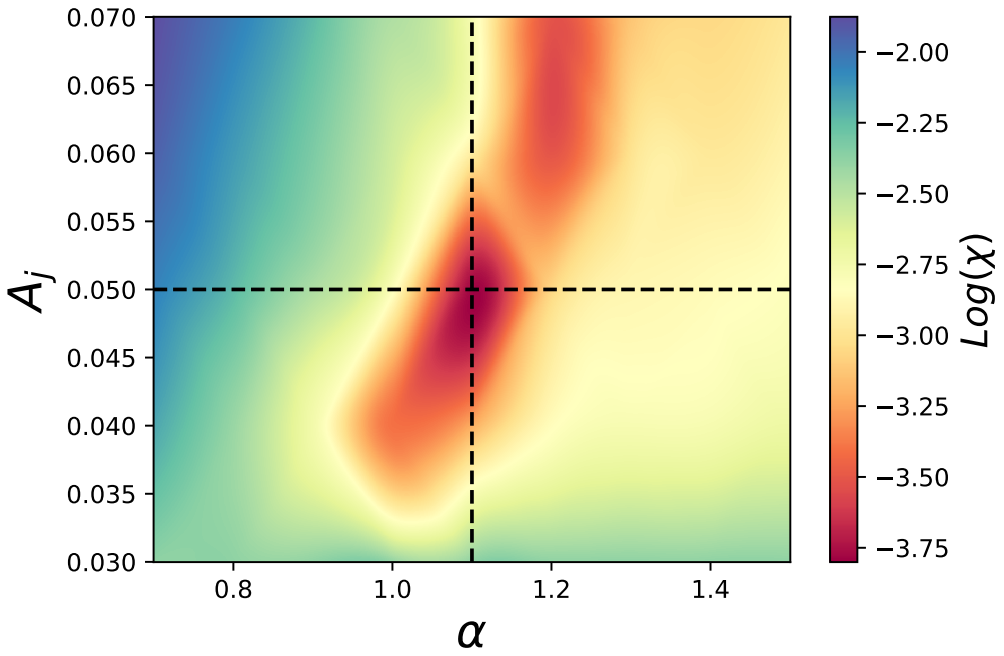


Figure 5.8: Surface contour plot of the logarithm of the misfit function in terms of α_j and A_j. The crossing of the horizontal and vertical dashed lines indicate the minimum of the $\log(\chi)$ surface, matching the parameters initially set for the input NWN system which were $\alpha_j = 1.1$ and $A_j = 0.05$.

5.7 Multiple-Material Network Characterization

Having established the efficacy of the inversion method in characterizing the exponent and the power law prefactor modelling nanowire junctions in NWNs, we explore now a special case in which a NWN may be composed of different types of nanowire. In this case, we consider that NWN would contain two types of junctions modelled as (dropping the junction subscript $_j$): $\Gamma_1 = A_1\, I^{\alpha_1}$ and $\Gamma_2 = A_2\, I^{\alpha_2}$. Here we focus the analysis on the exponents keeping $A_1 = A_2$ and $\alpha_1 \neq \alpha_2$ with α_1 and α_2 in the sublinear and supralinear regimes, respectively. This modelling consideration accounts for the fact that some junctions may activate faster (higher exponents) than others due to various microscopic factors, *e.g.*, differences in the ionic mobilities of the charge carriers inside the junctions, differences in sizes of the nanowire coating layers, to

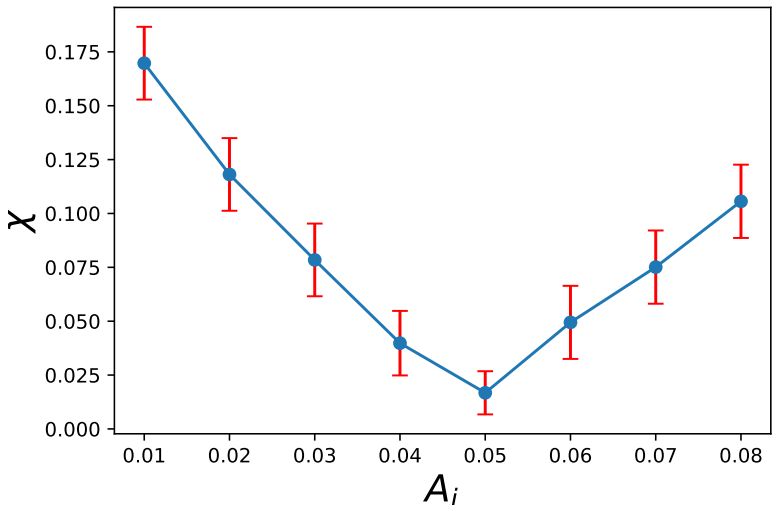


Figure 5.9: Fixing $\alpha_j = 1.1$ in Fig. 5.8, one can visualize the misfit function (average) plotted in terms of A_j; the minimum is located at $A_{min} = 0.05$, corresponding to the original prefactor set in the input NWN system. The distribution of χ was computed from 60 different inversions with standard deviations shown as error bars.

name but a few. Fig. 5.10 shows the misfit function result to identify these two parameters from an input NWN with $\alpha_1 = 0.9$ and $\alpha_2 = 1.2$. Note the presence of the two equivalent minima - given that there is no differentiation between α_1 and α_2 by the inversion method, so both configurations of $\alpha_1 = 0.9$ and $\alpha_2 = 1.2$ and $\alpha_1 = 1.2$ and $\alpha_2 = 0.9$ are equiprobable.

The bimodal calculation above can be expanded to consider more than two exponents in the power law model, increasing the complexity of the NWNs. Consequently, the dimensionality of the problem increases and the computational cost for the misfit procedure also increases. However, if we are smart about the parameters we aim to characterize, we can consider the construction of a more realistic NWN with a low cost. For instance, we can expect that, in the process of nanowire fabrication, the dielectric coating around the wire will not be uniform for every nanowire. Since the memristive property of our junctions comes from the dielectric coating, we can assume that the junction parameters of a specific wire determination will in reality follow a Gaussian distribution between a mean with a standard deviation. Considering this, could we obtain the information that characterizes this distribution solely from the inversion of the conductance evolution? We can simulate this

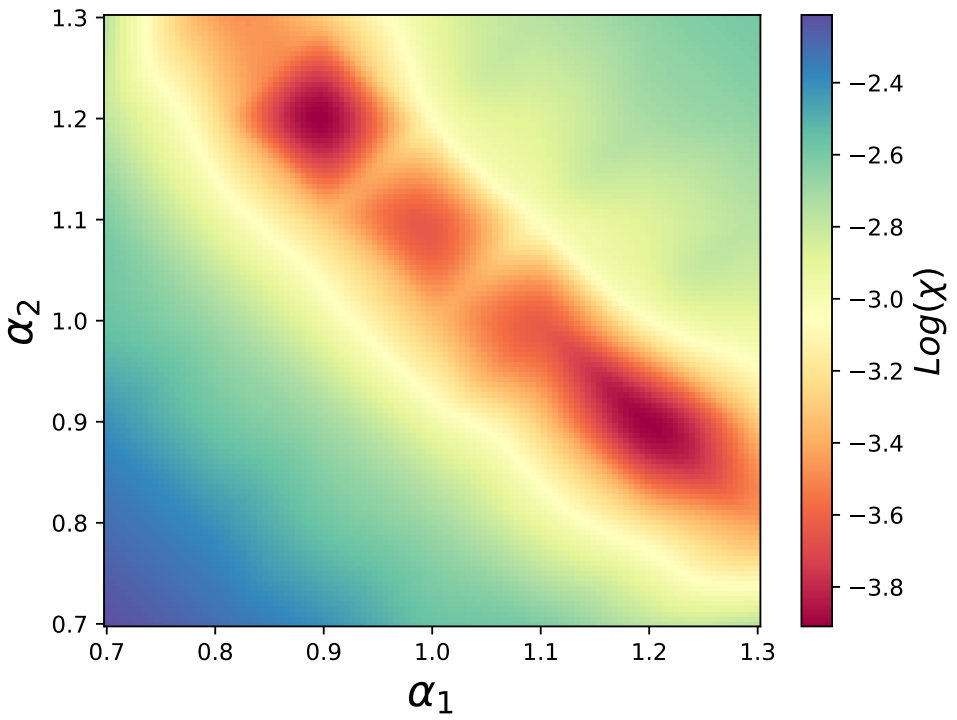


Figure 5.10: Surface contour plot of the logarithm of the misfit function in terms of α_1 and α_2. In this case, the power law exponents for each junction in the NWN case were arbitrarily assigned to $\alpha_1 = 0.9$ and $\alpha_2 = 1.2$. Note that now, since the misfit function cannot differentiate between the variables, this graph will be symmetric along the identity line (save some oscillations from the stochastic CA calculations). This implies that we have two possible minima, one at $\alpha_1 = 0.9$ and $\alpha_2 = 1.2$ and the symmetric one at $\alpha_1 = 1.2$ and $\alpha_2 = 0.9$.

by considering that each α_j value is randomly assigned following an unknown Gaussian distribution of mean α_μ and standard deviation α_σ. We then construct NWN CAs in terms of the Gaussian distribution parameters, which will be used in the minimization of the misfit function written in terms of α_μ and α_σ. Fig. 5.11 shows a $\log(\chi)$ surface as a function of α_μ and α_σ using CAs generated with $N_c = 300$ conifguraitons. Once more, the dashed lines crossing marks the minimum in $\log(\chi)$ found at $\alpha_\mu^{min} = 1.2$ and $\alpha_\sigma^{min} = 0.2$.

This last example demonstrates that the misfit minimization method can effectively predict parametric distribution features that characterize more complex NWNs with a wide variety of junction characteristics and material properties within the same NWN structure. In other words, this parametric distribu-

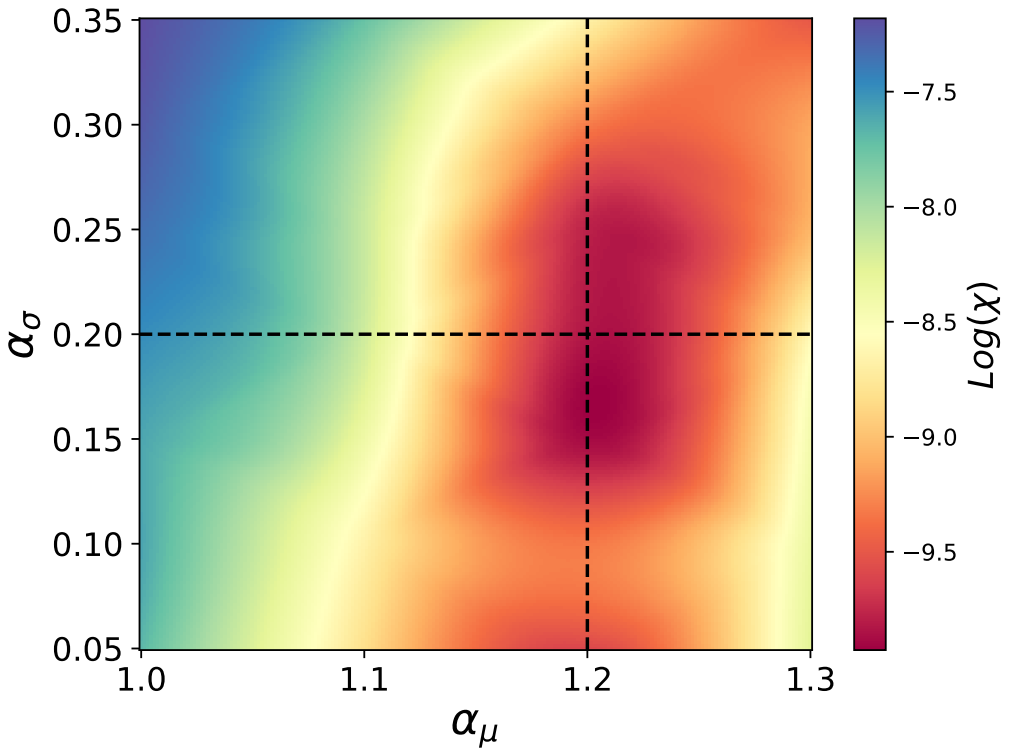


Figure 5.11: Surface contour plot of the logarithm of the misfit function in terms of α_μ and α_σ. In this case, the power law exponents for each junction in the NWN case were randomly assigned following a Gaussian distribution of mean α_μ and standard deviation α_σ. The crossing of the horizontal and vertical dashed lines indicates the minimum of the $\log(\chi)$ surface, matching the Gaussian parameters initially set for the input NWN system which were $\alpha_\mu = 1.2$ and $\alpha_\sigma = 0.2$.

tion feature analysis allows the investigation of NWNs that are not as idealized as the first examples studied in this chapter with all nanowire junctions with the same exponent and prefactor values. This enables the inference of more realistic settings as NWN intrinsic properties and initial conditions can fluctuate significantly from sample to sample. Naturally, this is not system-dependent and is an intrinsic capability of the inversion method that can be applied to any other system that may be constructed with parameters following a natural distribution. Note that by approaching the parameter probability distribution instead of the parameters themselves, we were able to encompass the identification of a range of different parameter values using only two variables in our misfit function, optimizing the inversion procedure for this general case.

5.8 Summary

In this chapter, we approached a drastically different system compared to the previous chapters. Here we tackled the challenging problem of characterizing complex systems in the form of memristive random NWNs whose disorder is expressed from the very geometry of the device construction. We tackled the identification of the winner takes all (WTA) path formation in these devices as a result of the current evolution through memristive junctions. By inverting conductance versus current curves, we were able to determine the junction parameters of the network via the inversion method. The identification of these parameters serves for the overall characterization of the NWN, whose features are often not directly accessible, *i.e.*, we cannot infer the features of a single interwire junction amidst the whole intricate interconnect structure that random NWNs characteristically have. Most importantly, these parameters serve as predictors of the WTA path formation, allowing us to anticipate the future of the network evolution.

The identification of α_j, in particular, is very important in the context of memristive NWNs because that gives information about the conduction strategy the NWN is prone to use: it may use a single current pathway to propagate nearly 100% of the sourced current if $\alpha_j > 1$ or it may spread the sourced current into multiple paths if $\alpha_j \leq 1$. The inversion method is capable of predicting with which exponent an input NWN system will portray by only using information from its early activation stages.

Later, we demonstrated that the methodology can be extended to make parametric predictions in two-dimensional phase space. This includes the identification of meta-parameters defining the junction parametric distribution in the network. This allows us to tackle more interesting scenarios of networks composed of multiple types of nanowires, as well as the realistic case of a network whose junctions are defined within a normal distribution.

This concludes the series of works in this thesis that cover the application of our devised inversion methodology for the characterization of disordered systems.

Chapter 6

Conclusion

6.1 Thesis Summary

In this thesis, we studied the inverse problem presented in the context of condensed matter systems characterization. This problem is a particular member of a family containing many other inverse problems encompassing multiple disciplines. We explore a proposed method for solving such a problem, consolidating its application and, at the same time, expanding its scope.

In Chapter 2, we established the theoretical foundation necessary for the work reported in this thesis and it can be separated into two parts. Firstly we analyse the theoretical methods of modeling disordered condensed matter systems with a crystalline lattice. We are introduced to the Tight Binding modelling paradigm necessary to theoretically represent our devices. Then, we get familiar with the concept of Green's Functions and its application in Dyson's Equations in order to perform transmission calculations within the Kubo formalism. This framework is applied to generate transmission curves that serve as proof of concept of our inversion method later in this chapter. We also implement it to perform the calculations of other quantities of interest in Appendices B and C. These appendices cover some peripheral cases of application of the inverse method - they present in a nutshell relevant problems at the edge of its application namely the inversion of the Magnetic Susceptibility quantity of systems with magnetic disorder and the Phononic Transmission in disordered systems (which handles the transmission of a bosonic particle). Later in this part, we introduced the Green's Function Chebyshev Polynomial method based on the tight binding model, which avails of some approximations

to calculate conductivity spectral quantities of disordered large and complex devices with low computational cost. The algorithm for the implementation of this method is presented in Appendix A.

The second part of Chapter 2 concerns the introduction of inverse problems and careful inspection of the problem at hand. We laid down our systematic approach to solving this problem as well as introduced concepts such as the ill-posedness of inverse problems and the ergodicity of our method. The inverse method was exemplified in simple systems such as the linear chain and the bi-dimensional single-orbital-carbon graphene.

In Chapter 3, we face our first characterization problem in a complex system - films of MoS_2 transition metal dichalcogenide with chalcogen vacancies. Here we use the methods introduced in Chapter 2 to simulate and invert DC and Optical electrical conductivity signals in order to obtain the value of vacancy concentration in different devices. We also use the assembled data to perform a qualitative characterization of transconductivity signals of MoS_2 film samples with native defects. Lastly, we use the flexibility of CPGF spectral calculations to validate the ergodic assumption behind our inversion. This establishes a precedent for the application of the method in real systems and enables further exploration in the front.

Chapter 4 presents a distinctive challenge that tests our method in an extreme scenario. Now our scatterers in question are the functionalized $AuCl_3$ complexes, which have a weak signature on the transport properties of our device. We present a toy model for adatom modelling and techniques to simulate coordinated complexes in realistic systems. The presence of this new disorder increases the complexity of the material simulation and demands a higher resolution from our polynomial expansions. To deal with the higher complexity in the lattice, we employ the supercell description technique, which allows for the implementation of structural disorder with longer-range impact in the system. Despite these obstacles, the inversion method is capable of quantifying the disorder concentration from conductivity signals, confirming its reliability.

Finally in Chapter 5, we shift our definition of disorder from structural defects and adatoms on a crystalline lattice to disorder in the form of the very geometry of the device. Now we deal with memristive random nanowire networks that may display a *winner takes all* neuromorphic behaviour, and via the inversion, we quantify the crucial junction parameters responsible for the emergence of this behaviour. The new geometry implies a new approach

to modelling and simulation via Matrice Kirchhoff's equations, in contrast to tight binding for regular lattices. In this chapter, we are able to obtain from the network global conductance evolution the parameters responsible for the rate of activation of single junctions, which are the main predictors of the emergence of the winner-takes-all behaviour. This was done by analysing an early stage of the conductance evolution before the network evolution entered the self-similar power-law stage. In this way, we were able to predict the future evolution of the input network. Our inversion method was then used to characterize other meaningful parameters of the network both independently and jointly in a multi-parameter inversion. Later we also consider the characterization of a multi-material network - a network composed of different wires or coatings - and successfully recovered the network junction parameters. Finally, we considered the case in which the power-law exponent parameter of the junctions was not determined by a single value but, instead, followed a Gaussian distribution. By applying our multi-variable inversion method, we were able to characterize the mean and standard deviation of the parameter distribution.

6.2 Future Work

6.2.1 Quantitative Experimental Assessment

The work laid out in Chapter 3 left open the question of qualitative measurement of the inversion accuracy in real systems. This question branched a new collaboration with the experimental Nanofabrication Group of Trinity College Dublin. By generating MoS_2 films at different temperatures, one can systematically regulate the concentration of native chalcogen vacancy in the final device [279, 280]. By combining this with a low-degree-of-freedom form of measurement such as scanning transmission electron microscopy, we can obtain a quantitative measurement of the concentration of vacancies in each sample. This can then be compared to the result of the inversion procedure when analysing an experimentally measured conductivity signal of that same device, which will finally give us a qualitative measurement of the accuracy of our inversion method.

6.2.2 Material Design

The mission behind the field of material science is to obtain devices that satisfy specific conditions, usually for the sake of their electronic and photo-electronics properties for direct application in different technological fields. These conditions can be arbitrarily complex and are rarely met in materials found in nature or in pristine, crystalline materials synthesized in laboratories. One often has to tinker with known stable systems to encourage the emergence of such desired properties. Many tools can be used to arrive at this result - some external like temperature and pressure, and some structural like vacancies, substitution impurities, shearing, or modification of its geometry or topology. In other words, material science tackles the problem of finding the correct combination and quantity of elements that, in a specific configuration, will perform with certain properties or characteristics.

One can certainly approach this problem via intense exploration, experimentation through educated trials and errors, and insight. However, one would benefit immensely from a methodology that can systematically generate novel materials with specific desired properties. One example of a question asked in this endeavour is:

> *Given an arbitrary spectral signal, what should be the structural configuration of a material so that its measurement displays such a signal?*

You may have noticed by now that this is also a form of inverse problem. In fact, this problem is very closely related to the characterization problem - as if they were siblings in a family of inverse problems. The difference between them is that in signal characterization you want to obtain structural information of an arbitrary device based on spectral measurements, whereas in material design you want to obtain a specific device whose spectral measurement will behave like an arbitrarily proposed signal.

This fundamental difference is responsible for a small, but consequential change in the way we approach the solution for the problem. Notice that now we know how we want the measured signal of the designed device to look, whereas, in the case of signal characterization, we do not know what possible signal we will be tasked with inverting. This makes it so that the approach for signal characterization has to be universal - the sweep of the configuration space by the CAs has to be thorough and general enough to accommodate

a signal at any point in this space. In the case of material design, however, we know our target is in one certain point of the configuration space and the problem becomes finding that device configuration which yields the minimum discrepancy.

Because we have to ensure the universality of solutions for the case of signal characterization, we are compromising some part of the uniqueness of a disordered signal. Our CAs are able to capture the average disorder signature, but the unique oscillations of each separate configuration signal that composes our CA get averaged out. In this sense, we are losing some information to guarantee that there is no bias in the characterization process. However, in the case of material design, this extra bit of information would be very useful to pinpoint the potential candidates that have a spectral signature close to the target one. We can adjust our misfit function of Eq.(2.66) to take this into consideration and write

$$\chi_G = \int dE \ (\Gamma_T - \Gamma_G)^2 \ , \tag{6.1}$$

where Γ_T is the target signature, Γ_G is the spectral measurement of the guessed configuration and χ_G is the misfit of that particular guess.

Of course, we shall not approach this guessing blindly. Firstly, we can treat our target signature as a device with an unknown disorder concentration and use the signal characterization method on it, narrowing down the space of likely configurations. Then, we can avail of stochastic techniques such as the criteria-based Monte Carlo method [281] to probe the reduced configurational space randomly while setting aside those guesses that came very close to the target, as measured by the value of the misfit functional criterion.

Mind you this is but one suggestion of how to address the inverse problem of material design. Even if we can obtain an ideal theoretical Hamiltonian, we would still need to take into consideration the feasibility of fabricating material with optimum configuration, which brings about its own set of challenges. In the process of research, these ideas will be constantly evolving.

6.3 Final Words

Having firmly established the applicability of our inversion methodology in multiple scenarios and with a variety of signals, I feel confident to say such a

method can be a reliable aid to the structural characterization of devices, both in conjunction with different characterization instruments as well as in extreme scenarios where such tools are not available. It is worth highlighting that the complete characterization of a device is an extensive task and includes obtaining information about different properties, some of which were not covered in this thesis. These include structural characterization via procedures like crystallography, optical characterization via photoluminescence spectroscopy, and magnetic characterization via magnetometry to name a few. The study cases presented in this thesis can certainly aid some aspects of device characterization, but most importantly, they serve to showcase the power and application of the proposed inversion methodology.

The research on inverse problems has a large scope and encompasses many areas of physics. In particular, the area of material design symbolizes a pathway into an era in which we hold complete control over the physical devices and bend these structures to behave according to our will, as was the ambition of the alchemists of the past. This thesis offers a humble contribution for humanity to the gargantuan task of obtaining domain over matter.

Appendix A

Chebyshev Polynomial Green's Function Algorithm

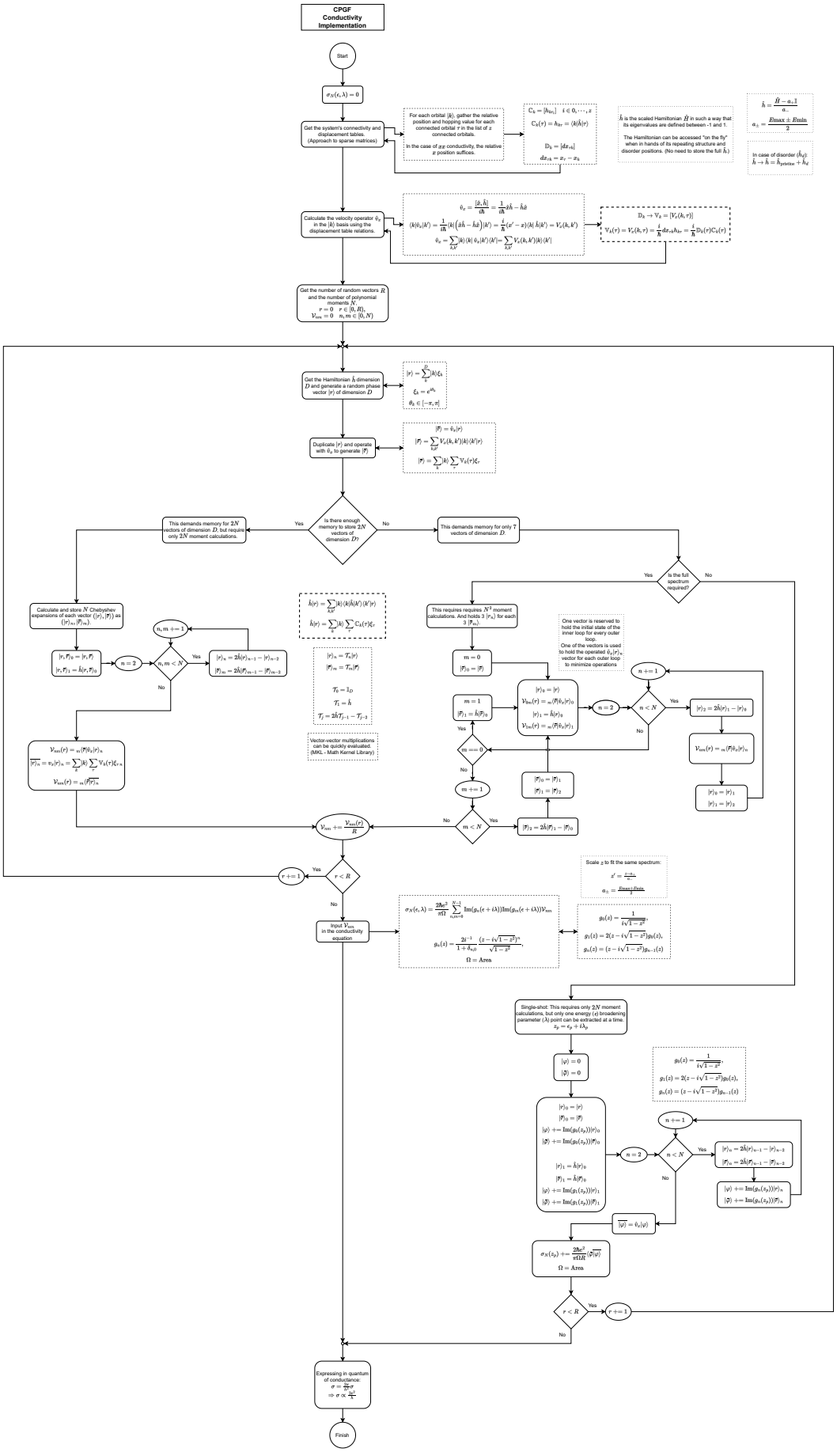
Below you will find the algorithm for the numerical implementation of the Chebyshev Polynomial Green's Function method that calculates the DC conductivity of a system as introduced in Chapter and section 2.1.6. This algorithm offers three different ways of performing the calculation depending on the available memory or CPU hours.

1. The direct method is the fastest, requiring $2N$ calculations, where N is the number of Chebyshev polynomial moments, but requires memory to store $2NRD$ complex floating point numbers. This approach calculates the entire spectrum at once.

2. When dealing with large systems, there might not be enough memory to store all this data. A memory-cheap approach is to store only 6 random vectors each time, but this increases the number of necessary calculations to N^2 to obtain the entire spectrum, since the moments are now calculated iteratively for each pair of random vector calculations.

3. The last approach is the Single-shot approach, using the same amount of memory as before, but with the goal of calculating only one energy point at a time with the cost of $2N$ operations per point.

Please access this document via the PDF format in order to be able to zoom in on the figure, or make use of a magnifying glass.


CPGF Conductivity Implementation
Start
Get the system's connectivity and displacement tables. (Approach to sparse matrices)
Calculate the velocity operator $\hat{v}_x$ in the $|k\rangle$ basis using the displacement table relations.
Get the number of random vectors R, and the number of polynomial moments N.
Get the Hamiltonian $\hat{h}$ dimension D and generate a random phase vector $|r\rangle$ of dimension D
Duplicate $|r\rangle$ and operate with $\hat{v}_x$ to generate $|\bar{r}\rangle$
Is there enough memory to store $2N$ vectors of dimension D?
Yes
No
This demands memory for $2N$ vectors of dimension D, but require only $2N$ moment calculations.
This demands memory for only 7 vectors of dimension D.
Is the full spectrum required?
Yes
No
Calculate and store N Chebyshev expansions of each vector $(|r\rangle_n, |\bar{r}\rangle_n)$.
This requires requires N^2 moment calculations. And holds 3 $|r\rangle_n$ for each 3 $|\bar{r}\rangle_n$).
One vector is reserved to hold the initial state of the inner loop for every outer loop.
One of the vectors is used to hold the operated $\hat{v}_x|r\rangle_n$ vector for each outer loop to minimize operations
Vector-vector multiplications can be quickly evaluated. (MKL - Math Kernel Library)
Input $\mathcal{V}_{nm}$ in the conductivity equation
Scale z to fit the same spectrum:
Single-shot: This requires only $2N$ moment calculations, but only one energy (ϵ) broadening parameter (λ) point can be extracted at a time. $z_p = \epsilon_p + i\lambda_p$
Expressing in quantum of conductance: $\sigma = \frac{\Omega e^2}{\pi \hbar} \sigma$ $\Rightarrow \sigma \propto \frac{\Omega e^2}{h}$
Finish

Appendix B

Magnetic Susceptibility Inversion

Among the types of disorder that we may want to introduce to our systems, a common one is a disorder of magnetic type or impurities that possess a magnetic moment. Let us explore in this appendix if we can use the measurement of magnetic susceptibility of a system with magnetic impurities to obtain information regarding the configuration of that system using our inversion method.

Materials such as graphene and TMDs have promising applications in the spintronics field [282–284] where long-distance interactions are particularly relevant. One mechanism by which these interactions occur is by having the magnetic dipole alignment states propagated via the electrons in the media. Similarly, dipole oscillations are also carried through the medium and this magnetic moment precession induces a spin polarization in other magnetic impurities of the system which will align ferro or anti-ferro magnetically with the source [285–287]. This polarization is quantified by the magnetic susceptibility quantity χ that expresses how the spin degrees of freedom of a system will respond to a magnetic excitation. The magnetic susceptibility can be expressed in the frequency domain using random phase approximation as:

$$\chi(\omega) = \frac{\chi^0(\omega)}{1 + U\chi^0(\omega)}\,, \tag{B.1}$$

where U is an onsite interaction present exclusively on sites with magnetic disorder and χ^0 is Hartree-Fock susceptibility. The matrix elements of χ^0 expressing the amplitude of the spin precession on the site r as a response to

a induced precession at site i is given by [288, 289]:

$$\chi^0_{r,i}(\omega) = I_1 + I_2 + I_3\,, \tag{B.2a}$$

$$I_1 = \frac{i}{2\pi}\int_{-\infty}^{+\infty} dE' f(E')\mathcal{G}^+_{r,i}(E')\mathcal{G}^+_{i,r}(E'+\hbar\omega)\,, \tag{B.2b}$$

$$I_2 = -\frac{i}{2\pi}\int_{-\infty}^{+\infty} dE' f(E')\mathcal{G}^-_{i,r}(E')\mathcal{G}^-_{r,i}(E'-\hbar\omega)\,, \tag{B.2c}$$

$$I_3 = \frac{i}{2\pi}\int_{-\infty}^{+\infty} dE' \left[f(E'+\hbar\omega) - f(E')\right]\mathcal{G}^-_{i,r}(E')\mathcal{G}^+_{r,i}(E'+\hbar\omega)\,. \tag{B.2d}$$

Here $f(E)$ is the Fermi-Dirac distribution and $\mathcal{G}^+$ and $\mathcal{G}^-$ are the retarded and advanced Green's functions for the pristine system which can be calculated using the methods of Chapter 2.

Having the magnetic susceptibility as an experimentally measurable quantity [290–292] and having a way of calculating it from synthetic simulated materials, it appeared to be a good candidate for the spectral quantity of our inversion procedure. Naturally, we enquired if it was possible to characterize the synthetic system via this quantity - if it was possible to recover the quantity of magnetic impurities present in the system from its magnetic susceptibility measurement. However, as illustrated in Fig. B.1b, the inversion results in a flat misfit function, which is an indication that no minima could be obtained.

Figure B.1 illustrates the inversion for the $\chi^0_{0,0}$ quantity, which represents the response read in the site 0 when a precession induced in the site 0 interacts with the entirety of the system. The CAs shown in Fig. B.1a were formed with 2000 configurations, but when compared to one random input configuration plotted in black, one can observe that the input configuration does not visually follow the trend of any of the CAs for most of the spectrum. This is because, for each disorder configuration of the same amount of magnetic impurities, the peaks of the magnetic susceptibility signal will change drastically from one case to the other depending on the separation between the magnetic moments, not only that, but some disorder configurations will have the peaks on the negative side of the spectrum if the resultant interaction is anti-ferromagnetic instead of ferromagnetic. This results in CAs that carry no information about the number of impurities in the system and there is no use comparing them with individual input signals for the purpose of characterization.

As mentioned in Chapter 2, one of the core assumptions behind the working

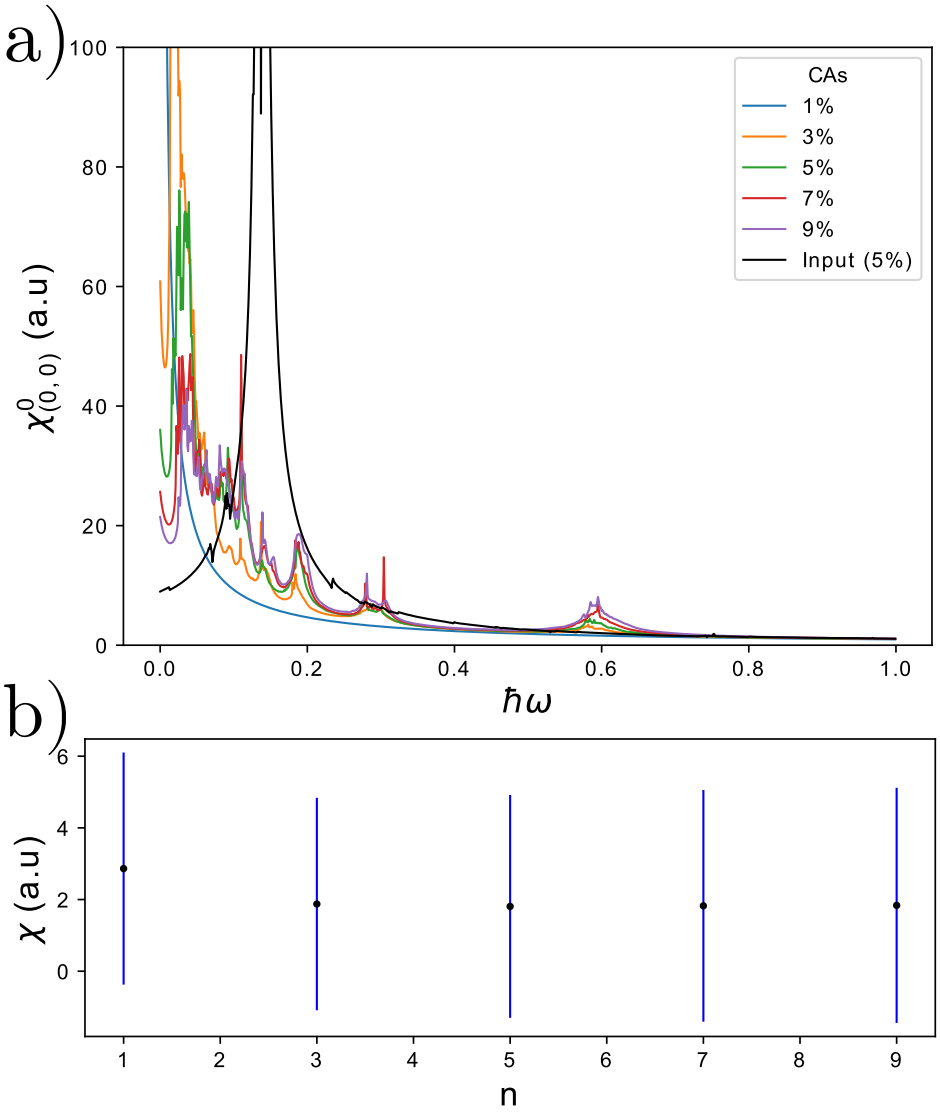


Figure B.1: Magnetic susceptibility calculation for a one-dimensional lattice of 1.000 sites with varied concentrations of magnetic disorder. **a)** CAs for different disorder concentrations and the plot of one input signal with a 5% concentration of magnetic impurities (black). **b)** The misfit function distribution of 500 minimization samples with input functions containing 5% concentration of disorder.

of this inversion method is the isotropy in the system in such a way that a mean-field approximation of the degrees of freedom of the scatterer positions is possible. However, when we introduce an interaction that depends so strongly on the inter-scatterer separation, this approximation no longer holds. The test case of magnetic susceptibility presented here illustrates this clearly.

Appendix C

Inversion of Phononic Quantities

Having already established the inversion protocol for quantities such as electronic DC conductivity and optical conductivity in Chapter 2, I propose in this appendix that we explore how well the inversion method fares when dealing with a different particle, namely phonons. Associated with the vibrational modes in the lattice, phonons are bosonic particles whose transmission contributes to the thermal conductivity of the system. To model the transmission of phonons, let us explore how we would define the phononic Hamiltonian of a linear chain of atoms.

In this new framework, we are concerned with the transverse vibrations of our atoms and their propagation through the network. This leads us to model our system as a series of coupled harmonic oscillators, which makes it so that the laws of motion for the i^{th} atom in the chain depicted in Fig C.1a is given by:

$$m_i\ddot{x}_i = -\kappa(x_i - x_{i-1}) - \kappa(x_i - x_{i+1}) \quad \Rightarrow \tag{C.1a}$$

$$\ddot{x}_i = \frac{\kappa}{m_i}(-2x_i + x_{i-1} + x_{i+1})\,, \tag{C.1b}$$

where $\ddot{x}_i$ is the second derivative with respect to time of the position of the i^{th} atom, m_i its mass, and κ the elastic constant associated with the parabolic approximation of the near-equilibrium part of the Born–Landé potential. In the pristine case where all atoms possess the same mass, we could write a solution for the lattice vibration as Bloch waves

$$x_j = Ae^{i(kaj-\omega t)}\,, \tag{C.2}$$

where a is the lattice constant. The quantized equations of motion of a N-orbital system would then result in

$$\omega(n) = 2\omega_0 \left|\sin\left(\frac{\pi n}{N}\right)\right| \text{, with} \tag{C.3}$$

$$\omega_0 = \sqrt{\frac{\kappa}{m}} \text{, and } n = \frac{kaN}{2\pi}\,. \tag{C.4}$$

Resulting in the acoustic dispersion relations (and optical when considering a diatomic periodic chain).

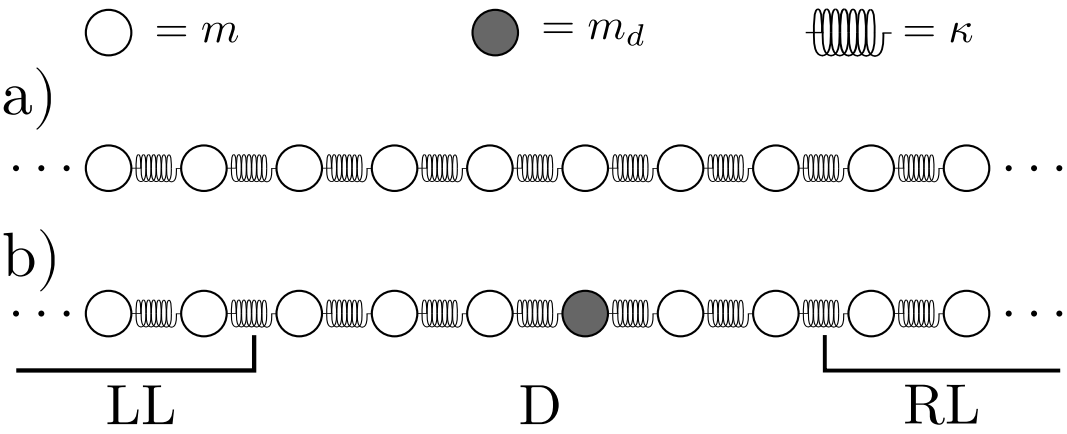


Figure C.1: **a**) Pristine infinite linear chain of harmonic oscillators with mass m and elastic constant κ. **b**) Disordered case with the transmission setting including right and left leads. Here the disorder is represented by a single impurity of mass m_d.

However, as thoroughly stated throughout this thesis, we are more concerned with the disordered case rather than the pristine one. In this scenario, a disorder in the system is configured as an orbital in the lattice with a different $\frac{\kappa}{m}$ ratio. For simplicity, we will consider all springs to be equal and to ease the notation, let us consider $\kappa = 1$ and the pristine mass $m = 1$. Now, what determines the disorder is the value of its mass m_d. If we wish to preserve the plane wave assumption, our equivalent Hamiltonian matrix is defined as:

$$\left[\omega^2\hat{\mathbb{I}} - \hat{H}\right]\hat{x} = 0\,. \tag{C.5a}$$

Considering a disorder in one of the sites as illustrated in Fig C.1b and using Eq.(C.1b), the Hamiltonian reads:

$$\langle \hat{H} \rangle = \begin{bmatrix} \ddots & \ddots & & & & & \\ \ddots & 2 & -1 & & & 0 & \\ & -1 & 2 & -1 & & & \\ & & -\frac{1}{m_d} & \frac{2}{m_d} & -\frac{1}{m_d} & & \\ & & & -1 & 2 & -1 & \\ & 0 & & & -1 & 2 & \ddots \\ & & & & & \ddots & \ddots \end{bmatrix} . \tag{C.5b}$$

Here we can see that the Hamiltonian is no longer hermitian. This makes the energy spectrum for ω^2 have a non-zero imaginary part, implying that there will be extra vibrational modes within the system and, in the case of an isolated finite system, the energy alternates between them.

We can still implement the calculations for the transmission derived in Chapter 2 making use of the Dyson equations and the iterative Green function method. Extra care now has to be taken when considering the connecting perturbation terms, since, in the case of this disorder, $V_{01} \neq V_{10}$. Observing the transmission for the real energies for different concentration configurational averages of disorder with $m_d = 2m$, we obtain the result shown in Fig. C.2a. By performing the inversion on these transmission functions directly and repeating it for ten thousand input configurations, we obtain the result in Fig. C.2b. Despite the minimum at the correct place, the error bars in this figure indicate that the CA distributions are too wide in relation to their relative separations. This statistical interference ultimately decreases the accuracy of the inversion. Fig. C.2c illustrates the distributions of the transmission values for the CAs at a specific energy value and the overlaps between these distributions point to low accuracy in the inversion.

Let us now see what the steps would be for calculating the inversion based on the phononic contribution to the thermal conductivity. This contribution, ignoring other contributions such as the electron-phonon or phonon-phonon interactions, is given by [293, 294]:

$$\sigma = \int_{-\infty}^{\infty} d\omega \, \frac{\hbar\omega}{2\pi} \Xi(\omega) \left[f(\omega, T_2) - f(\omega, T_1) \right] , \tag{C.6a}$$

where Ξ is the transmission calculated above given by Eq.(2.25). f is the Bose-Einstein distribution of the bosonic states for the thermal baths with temperature T_1 and T_2. In first order approximation,

$$f(\omega, T_2) - f(\omega, T_1) \approx \frac{\partial f(\omega, T)}{\partial T} \Delta T = \Delta T \frac{e^{\frac{\hbar\omega}{k_B T}}}{\left(e^{\frac{\hbar\omega}{k_B T}} - 1 \right)^2} \frac{\hbar\omega}{k_B T^2} \Rightarrow \tag{C.6b}$$

$$\sigma = \frac{k_B \Delta T}{2\pi} \int_{-\infty}^{\infty} d\omega \, \Xi(\omega) \Upsilon(\omega, T) \, . \tag{C.6c}$$

$$\Upsilon(\omega, T) = x^2 \frac{e^x}{\left(e^x - 1 \right)^2} = \frac{1}{4} x^2 csch^2 \left(\frac{x}{2} \right) \quad \text{,with} \quad x = \frac{\hbar\omega}{k_B T}. \tag{C.6d}$$

The integral of Eq.(C.6c), does not need to go from minus infinity to plus infinity since $\Xi(\omega)$ is only defined for $\omega > 0$ and $\Upsilon(\omega, T)$ decay very quickly with ω. For typical temperatures of $T = 300K$, $\Upsilon(\omega = 0.3, T = 300) \approx 0$.

Most importantly the change of particle distribution from Fermi to Bose-Einstein leads us to a change of paradigm from analysing the Fermi energy of the spectrum to the temperature. This brings about a change in the integration parameter for our misfit function since the energy (dictated by ω) no longer gives us information about the transmission spectrum. Rather, what determines the width of the modulating function is the temperature. As the temperature increases, the modulating function $\Upsilon(\omega, T)$ will broaden, allowing for probing of different parts of the transmission spectrum. With that, we can inspect the temperature spectrum in the light of our inversion methodology and use the temperature as our parameter of integration:

$$\chi(n) = \frac{1}{T_f - T_0} \int_{T_0}^{T_f} dT \, \left[\sigma(T) - \langle \sigma(T, n) \rangle \right]^2 , \tag{C.7}$$

where $\langle \sigma(T, n) \rangle$ is the CAs.

The low accuracy in the inversion of the transmission case seen in Fig. C.2b will most likely translate to a low accuracy in the inversion of the conductivity. This is because the Bose-Einstein distribution modulating function Υ restricts the amount of information we can obtain from the transmission signatures as-

sociated with different concentration. This simple example, however, is not representative of all devices from which we can obtain phononic transmission information, rather it serves as a proof of concept for the application of the inverse method for bosonic particles. In some devices, *e.g.* higher dimensional systems, the accuracy may be better since the transmission configuration distributions are often narrower, allowing for better resolution of the inversion. Another important factor that may impact the inversion accuracy is the other contributions to the thermal conductivity that were ignored in the above description. Nonetheless, we can observe the configurational averages and the resulting misfit function for the thermal conductivity calculations in Fig. C.3. Despite the lower accuracy, as expected, the inversion method remains precise, given that on average the minimum of the misfit functions still rests at the correct place. This is yet another sign that, in different conditions with improved configurational distributions, the misfit function will yield the correct result with good accuracy.

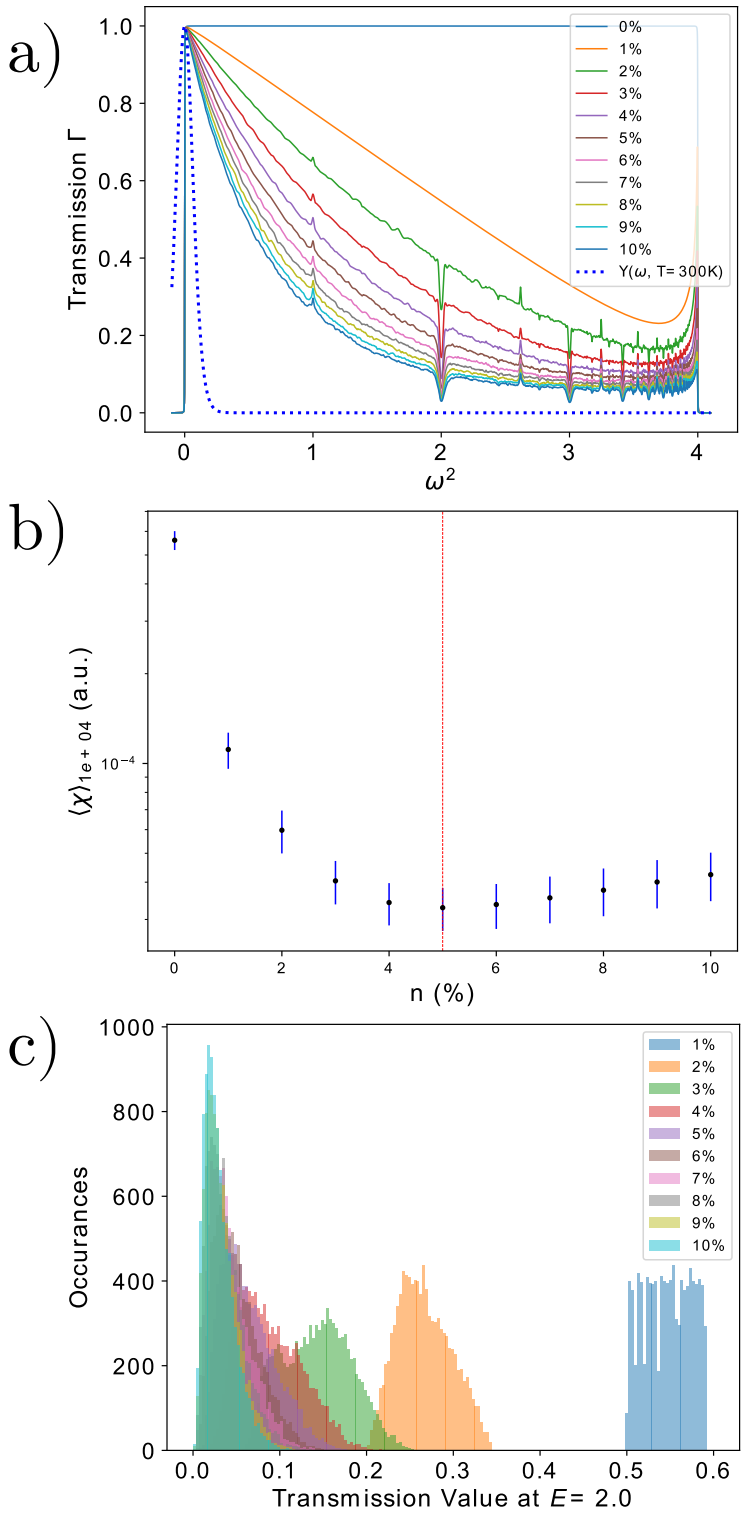


Figure C.2: **a**) Phonon transmission CAs for different concentrations of disorder ($m_d = 2m$). We can also see the function $\Upsilon(\omega, T = 300K)$ that will later modulate the transmission for the thermal conductivity calculation. **b**) Misfit function averages and standard deviations for ten thousand input functions and minimum at 5% concentration, marked by red line. **c**) CA distributions at $E = 2.0$.

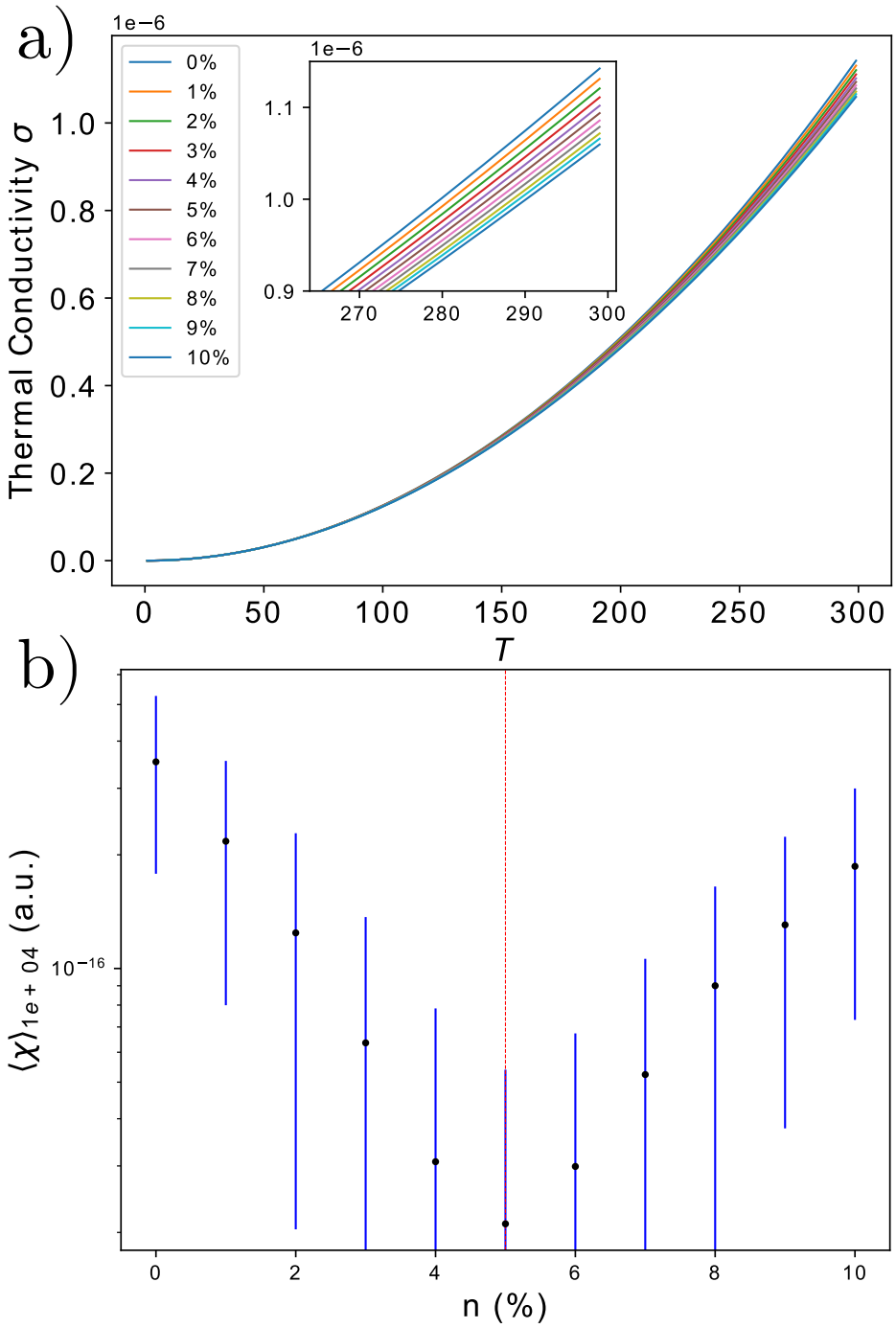


Figure C.3: **a**) CAs for the phononic contribution to the thermal conductivity of linear chain of harmonic oscillators with different concentrations of disorder. **b**) Misfit function averages and standard deviations for ten thousand input functions and minimum at 5% concentration, marked by red line.

Bibliography

[1] G. Bertone and D. Hooper, "History of dark matter," *Reviews of Modern Physics*, vol. 90, no. 4, p. 045002, 2018.

[2] K. Chadan, D. Colton, L. Päivärinta, and W. Rundell, *An introduction to inverse scattering and inverse spectral problems*. SIAM, 1997.

[3] C. W. Groetsch and C. Groetsch, *Inverse problems in the mathematical sciences*, vol. 52. Springer, 1993.

[4] Y. Song, L. Shen, L. Xing, and S. Ermon, "Solving inverse problems in medical imaging with score-based generative models," *arXiv preprint arXiv:2111.08005*, 2021.

[5] A. Louis, "Medical imaging: state of the art and future development," *Inverse Problems*, vol. 8, no. 5, p. 709, 1992.

[6] D. Kundur and D. Hatzinakos, "Blind image deconvolution," *IEEE signal processing magazine*, vol. 13, no. 3, pp. 43–64, 1996.

[7] L. Xu, J. S. Ren, C. Liu, and J. Jia, "Deep convolutional neural network for image deconvolution," *Advances in neural information processing systems*, vol. 27, 2014.

[8] H. Tsushima, R. Hino, Y. Tanioka, F. Imamura, and H. Fujimoto, "Tsunami waveform inversion incorporating permanent seafloor deformation and its application to tsunami forecasting," *Journal of Geophysical Research: Solid Earth*, vol. 117, no. B3, 2012.

[9] N. Hirata and M. Matsu'ura, "Maximum-likelihood estimation of hypocenter with origin time eliminated using nonlinear inversion technique," *Physics of the Earth and Planetary Interiors*, vol. 47, pp. 50–61, 1987.

[10] R. Brauchler, J.-T. Cheng, P. Dietrich, M. Everett, B. Johnson, R. Liedl, and M. Sauter, "An inversion strategy for hydraulic tomography: Coupling travel time and amplitude inversion," *Journal of hydrology*, vol. 345, no. 3-4, pp. 184–198, 2007.

[11] A. Tarantola, "Theoretical background for the inversion of seismic waveforms, including elasticity and attenuation," *Scattering and attenuations of seismic waves, part i*, pp. 365–399, 1988.

[12] J. Virieux, A. Asnaashari, R. Brossier, L. Métivier, A. Ribodetti, and W. Zhou, "An introduction to full waveform inversion," in *Encyclopedia of exploration geophysics*, pp. R1–1, Society of Exploration Geophysicists, 2017.

[13] G. Bal, "Introduction to inverse problems," *Lecture Notes-Department of Applied Physics and Applied Mathematics, Columbia University, New York*, 2012.

[14] P. J. Shaw and D. J. Rawlins, "The point-spread function of a confocal microscope: its measurement and use in deconvolution of 3-d data," *Journal of Microscopy*, vol. 163, no. 2, pp. 151–165, 1991.

[15] A. N. Tikhonov, "On the solution of ill-posed problems and the method of regularization," in *Doklady akademii nauk*, vol. 151, 3, pp. 501–504, Russian Academy of Sciences, 1963.

[16] M. Bertero, P. Boccacci, and C. De Mol, *Introduction to inverse problems in imaging*. CRC press, 2021.

[17] F. D. M. Neto and A. J. da Silva Neto, *An introduction to inverse problems with applications*. Springer Science & Business Media, 2012.

[18] A. Tarantola, *Inverse problem theory and methods for model parameter estimation*. SIAM, 2005.

[19] M. S. Zhdanov, *Geophysical inverse theory and regularization problems*, vol. 36. Elsevier, 2002.

[20] S. Mukim, F. P. Amorim, A. R. Rocha, R. B. Muniz, C. Lewenkopf, and M. S. Ferreira, "Disorder information from conductance: a quantum inverse problem," *Physical Review B*, vol. 102, no. 7, p. 075409, 2020.

[21] S. Mukim, C. Lewenkopf, and M. Ferreira, "Spatial mapping of disordered 2d systems: The conductance sudoku," *Carbon*, vol. 188, pp. 360–366, 2022.

[22] S. Mukim, J. O'Brien, M. Abarashi, M. S. Ferreira, and C. G. Rocha, "Decoding the conductance of disordered nanostructures: a quantum inverse problem," *Journal of Physics: Condensed Matter*, vol. 34, no. 8, p. 085901, 2021.

[23] M. Kasim, T. Galligan, J. Topp-Mugglestone, G. Gregori, and S. Vinko, "Inverse problem instabilities in large-scale modeling of matter in extreme conditions," *Physics of Plasmas*, vol. 26, no. 11, 2019.

[24] G. Bertaina, D. E. Galli, and E. Vitali, "Statistical and computational intelligence approach to analytic continuation in quantum monte carlo," *Advances in Physics: X*, vol. 2, no. 2, pp. 302–323, 2017.

[25] L. Yu, R. S. Kokenyesi, D. A. Keszler, and A. Zunger, "Inverse design of high absorption thin-film photovoltaic materials," *Advanced Energy Materials*, vol. 3, no. 1, 2013.

[26] A. Franceschetti and A. Zunger, "The inverse band-structure problem of finding an atomic configuration with given electronic properties," *Nature*, vol. 402, no. 6757, pp. 60–63, 1999.

[27] L. Zhang, J.-W. Luo, A. Saraiva, B. Koiller, and A. Zunger, "Genetic design of enhanced valley splitting towards a spin qubit in silicon," *Nature communications*, vol. 4, no. 1, p. 2396, 2013.

[28] M. d'Avezac, J.-W. Luo, T. Chanier, and A. Zunger, "Genetic-algorithm discovery of a direct-gap and optically allowed superstructure<? format?> from indirect-gap si and ge semiconductors," *Physical review letters*, vol. 108, no. 2, p. 027401, 2012.

[29] K. Hansen, G. Montavon, F. Biegler, S. Fazli, M. Rupp, M. Scheffler, O. A. Von Lilienfeld, A. Tkatchenko, and K.-R. Muller, "Assessment and validation of machine learning methods for predicting molecular atomization energies," *Journal of chemical theory and computation*, vol. 9, no. 8, pp. 3404–3419, 2013.

[30] V. Mlinar, "Utilization of inverse approach in the design of materials over nano-to macro-scale," *Annalen der Physik*, vol. 527, no. 3-4, pp. 187–204, 2015.

[31] R. Vargas-Hernández, Y. Guan, D. Zhang, and R. Krems, "Bayesian optimization for the inverse scattering problem in quantum reaction dynamics," *New Journal of Physics*, vol. 21, no. 2, p. 022001, 2019.

[32] V. K. Sangwan and M. C. Hersam, "Neuromorphic nanoelectronic materials," *Nature nanotechnology*, vol. 15, no. 7, pp. 517–528, 2020.

[33] D. Marković, A. Mizrahi, D. Querlioz, and J. Grollier, "Physics for neuromorphic computing," *Nature Reviews Physics*, vol. 2, no. 9, pp. 499–510, 2020.

[34] J. Lazzaro, S. Ryckebusch, M. A. Mahowald, and C. A. Mead, "Winner-take-all networks of o (n) complexity," *Advances in neural information processing systems*, vol. 1, 1988.

[35] K. Burke and L. O. Wagner, "Dft in a nutshell," *International Journal of Quantum Chemistry*, vol. 113, no. 2, pp. 96–101, 2013.

[36] P. Koskinen and V. Mäkinen, "Density-functional tight-binding for beginners," *Computational Materials Science*, vol. 47, no. 1, pp. 237–253, 2009.

[37] R. J. Bartlett and J. F. Stanton, "Applications of post-hartree—fock methods: A tutorial," *Reviews in computational chemistry*, pp. 65–169, 1994.

[38] P. Echenique and J. L. Alonso, "A mathematical and computational review of hartree–fock scf methods in quantum chemistry," *Molecular Physics*, vol. 105, no. 23-24, pp. 3057–3098, 2007.

[39] F. Bloch, "Quantum mechanics of electrons in crystal lattices," *Z. Phys*, vol. 52, pp. 555–600, 1928.

[40] J. C. Slater and G. F. Koster, "Simplified lcao method for the periodic potential problem," *Physical review*, vol. 94, no. 6, p. 1498, 1954.

[41] C. Goringe, D. Bowler, and E. Hernandez, "Tight-binding modelling of materials," *Reports on Progress in Physics*, vol. 60, no. 12, p. 1447, 1997.

[42] S. H. Simon, *The Oxford solid state basics*. OUP Oxford, 2013.

[43] E. N. Economou, *Green's functions in quantum physics*, vol. 7. Springer Science & Business Media, 2006.

[44] J. J. Sakurai and E. D. Commins, "Modern quantum mechanics, revised edition," 1995.

[45] R. Kubo, "Statistical-mechanical theory of irreversible processes. i. general theory and simple applications to magnetic and conduction problems," *Journal of the physical society of Japan*, vol. 12, no. 6, pp. 570–586, 1957.

[46] J. Mathon, "Large enhancement of the perpendicular giant magnetoresistance in pseudorandom magnetic multilayers," *Physical Review B*, vol. 54, no. 1, p. 55, 1996.

[47] P. A. Lee and D. S. Fisher, "Anderson localization in two dimensions," *Physical Review Letters*, vol. 47, no. 12, p. 882, 1981.

[48] Y. Imry, *Introduction to mesoscopic physics*. Oxford university press, 2002.

[49] A. Weiße, G. Wellein, A. Alvermann, and H. Fehske, "The kernel polynomial method," *Reviews of modern physics*, vol. 78, no. 1, p. 275, 2006.

[50] R. Silver and H. Röder, "Densities of states of mega-dimensional hamiltonian matrices," *International Journal of Modern Physics C*, vol. 5, no. 04, pp. 735–753, 1994.

[51] S. Sota and M. Itoh, "Fast and accurate scheme for green functions and eigenvectors: Regulated polynomial expansion without gibbs oscillation," *Journal of the Physical Society of Japan*, vol. 76, no. 5, pp. 054004–054004, 2007.

[52] D. Jackson, "On approximation by trigonometric sums and polynomials," *Transactions of the American Mathematical society*, vol. 13, no. 4, pp. 491–515, 1912.

[53] A. Ferreira and E. R. Mucciolo, "Critical delocalization of chiral zero energy modes in graphene," *Physical review letters*, vol. 115, no. 10, p. 106601, 2015.

[54] A. Braun and P. Schmitteckert, "Numerical evaluation of green's functions based on the chebyshev expansion," *Physical Review B*, vol. 90, no. 16, p. 165112, 2014.

[55] J. H. García, L. Covaci, and T. G. Rappoport, "Real-space calculation of the conductivity tensor for disordered topological matter," *Physical review letters*, vol. 114, no. 11, p. 116602, 2015.

[56] J. P. Boyd, *Chebyshev and Fourier spectral methods*. Courier Corporation, 2001.

[57] T. Cysne, T. Rappoport, A. Ferreira, J. V. P. Lopes, and N. Peres, "Numerical calculation of the casimir-polder interaction between a graphene sheet with vacancies and an atom," *Physical Review B*, vol. 94, no. 23, p. 235405, 2016.

[58] H. Tal-Ezer and R. Kosloff, "An accurate and efficient scheme for propagating the time dependent schrödinger equation," *The Journal of chemical physics*, vol. 81, no. 9, pp. 3967–3971, 1984.

[59] I. S. Gradshteyn and I. M. Ryzhik, *Table of integrals, series, and products*. Academic press, 2014.

[60] A. Bastin, C. Lewiner, O. Betbeder-Matibet, and P. Nozieres, "Quantum oscillations of the hall effect of a fermion gas with random impurity scattering," *Journal of Physics and Chemistry of Solids*, vol. 32, no. 8, pp. 1811–1824, 1971.

[61] D. A. Drabold and O. F. Sankey, "Maximum entropy approach for linear scaling in the electronic structure problem," *Physical review letters*, vol. 70, no. 23, p. 3631, 1993.

[62] O. F. Sankey, D. A. Drabold, and A. Gibson, "Projected random vectors and the recursion method in the electronic-structure problem," *Physical Review B*, vol. 50, no. 3, p. 1376, 1994.

[63] T. Iitaka and T. Ebisuzaki, "Random phase vector for calculating the trace of a large matrix," *Physical Review E*, vol. 69, no. 5, p. 057701, 2004.

[64] A. Weisse, "Chebyshev expansion approach to the ac conductivity of the anderson model," *The European Physical Journal B-Condensed Matter and Complex Systems*, vol. 40, no. 2, pp. 125–128, 2004.

[65] S. M. João, M. Andelkovic, L. Covaci, T. Rappoport, J. M. Lopes, and A. Ferreira, "Kite: high-performance accurate modelling of electronic structure and response functions of large molecules, disordered crystals and heterostructures," *arXiv preprint arXiv:1910.05194*, 2019.

[66] S. João and J. Lopes, "Non-linear optical response of non-interacting systems with spectral methods," *J. Phys.: Condens. Matter*, vol. 32, p. 125901, 2020.

[67] P. Hohenberg and W. Kohn, "Inhomogeneous electron gas," *Physical review*, vol. 136, no. 3B, p. B864, 1964.

[68] W. Kohn and L. J. Sham, "Self-consistent equations including exchange and correlation effects," *Physical review*, vol. 140, no. 4A, p. A1133, 1965.

[69] W. M. C. Foulkes and R. Haydock, "Tight-binding models and density-functional theory," *Physical review B*, vol. 39, no. 17, p. 12520, 1989.

[70] V. Gavini, K. Bhattacharya, and M. Ortiz, "Quasi-continuum orbital-free density-functional theory: A route to multi-million atom non-periodic dft calculation," *Journal of the Mechanics and Physics of Solids*, vol. 55, no. 4, pp. 697–718, 2007.

[71] P. Suryanarayana, V. Gavini, T. Blesgen, K. Bhattacharya, and M. Ortiz, "Non-periodic finite-element formulation of kohn–sham density functional theory," *Journal of the Mechanics and Physics of Solids*, vol. 58, no. 2, pp. 256–280, 2010.

[72] J. Jung and A. H. MacDonald, "Accurate tight-binding models for the π bands of bilayer graphene," *Physical Review B*, vol. 89, no. 3, p. 035405, 2014.

[73] P. Garcia-Fernandez, J. C. Wojdeł, J. Iniguez, and J. Junquera, "Second-principles method for materials simulations including electron and lattice degrees of freedom," *Physical Review B*, vol. 93, no. 19, p. 195137, 2016.

[74] F. Spiegelman, N. Tarrat, J. Cuny, L. Dontot, E. Posenitskiy, C. Martí, A. Simon, and M. Rapacioli, "Density-functional tight-binding: basic concepts and applications to molecules and clusters," *Advances in physics: X*, vol. 5, no. 1, p. 1710252, 2020.

[75] K. F. Garrity and K. Choudhary, "Database of wannier tight-binding hamiltonians using high-throughput density functional theory," *Scientific data*, vol. 8, no. 1, p. 106, 2021.

[76] L. A. Agapito, S. Ismail-Beigi, S. Curtarolo, M. Fornari, and M. B. Nardelli, "Accurate tight-binding hamiltonian matrices from ab initio calculations: Minimal basis sets," *Physical Review B*, vol. 93, no. 3, p. 035104, 2016.

[77] N. Marzari, A. A. Mostofi, J. R. Yates, I. Souza, and D. Vanderbilt, "Maximally localized wannier functions: Theory and applications," *Reviews of Modern Physics*, vol. 84, no. 4, p. 1419, 2012.

[78] N. Marzari and D. Vanderbilt, "Maximally localized generalized Wannier functions for composite energy bands," *Phys. Rev. B - Condens. Matter Mater. Phys.*, vol. 56, no. 20, pp. 12847–12865, 1997.

[79] I. Souza, N. Marzari, and D. Vanderbilt, "Maximally localized Wannier functions for entangled energy bands," *Phys. Rev. B - Condens. Matter Mater. Phys.*, vol. 65, no. 3, pp. 1–13, 2002.

[80] S. Mukim, F. P. Amorim, A. R. Rocha, R. B. Muniz, C. Lewenkopf, and M. S. Ferreira, "Disorder information from conductance: A quantum inverse problem," *Phys. Rev. B*, vol. 102, p. 075409, Aug 2020.

[81] G. D. Birkhoff, "Proof of the ergodic theorem," *Proceedings of the National Academy of Sciences*, vol. 17, no. 12, pp. 656–660, 1931.

[82] S. Z. Butler, S. M. Hollen, L. Cao, Y. Cui, J. A. Gupta, H. R. Gutiérrez, T. F. Heinz, S. S. Hong, J. Huang, A. F. Ismach, *et al.*, "Progress, challenges, and opportunities in two-dimensional materials beyond graphene," *ACS nano*, vol. 7, no. 4, pp. 2898–2926, 2013.

[83] H. Zhang, "Ultrathin two-dimensional nanomaterials," *ACS nano*, vol. 9, no. 10, pp. 9451–9469, 2015.

[84] J. C. Meyer, A. K. Geim, M. I. Katsnelson, K. S. Novoselov, T. J. Booth, and S. Roth, "The structure of suspended graphene sheets," *Nature*, vol. 446, no. 7131, p. 60, 2007.

[85] M. Katsnelson, K. Novoselov, and A. Geim, "Chiral tunnelling and the klein paradox in graphene," *Nature physics*, vol. 2, no. 9, p. 620, 2006.

[86] S. Y. Lee, D. L. Duong, Q. A. Vu, Y. Jin, P. Kim, and Y. H. Lee, "Chemically modulated band gap in bilayer graphene memory transistors with high on/off ratio," *Acs Nano*, vol. 9, no. 9, pp. 9034–9042, 2015.

[87] M. Y. Han, B. Özyilmaz, Y. Zhang, and P. Kim, "Energy band-gap engineering of graphene nanoribbons," *Physical review letters*, vol. 98, no. 20, p. 206805, 2007.

[88] S. Xiao, J.-H. Chen, S. Adam, E. D. Williams, and M. S. Fuhrer, "Charged impurity scattering in bilayer graphene," *Physical Review B*, vol. 82, no. 4, p. 041406, 2010.

[89] J. Son, S. Lee, S. J. Kim, B. C. Park, H.-K. Lee, S. Kim, J. H. Kim, B. H. Hong, and J. Hong, "Hydrogenated monolayer graphene with reversible and tunable wide band gap and its field-effect transistor," *Nature communications*, vol. 7, no. 1, p. 13261, 2016.

[90] T. Takahashi, K. Sugawara, E. Noguchi, T. Sato, and T. Takahashi, "Band-gap tuning of monolayer graphene by oxygen adsorption," *Carbon*, vol. 73, pp. 141–145, 2014.

[91] Y. Wu, C. Cao, C. Qiao, Y. Wu, L. Yang, and W. Younas, "Bandgap-tunable phosphorus-doped monolayer graphene with enhanced visible-light photocatalytic h 2-production activity," *Journal of Materials Chemistry C*, vol. 7, no. 34, pp. 10613–10622, 2019.

[92] W. Choi, N. Choudhary, G. H. Han, J. Park, D. Akinwande, and Y. H. Lee, "Recent development of two-dimensional transition metal dichalcogenides and their applications," *Materials Today*, vol. 20, no. 3, pp. 116–130, 2017.

[93] M. Chhowalla, Z. Liu, and H. Zhang, "Two-dimensional transition metal dichalcogenide (tmd) nanosheets," *Chemical Society Reviews*, vol. 44, no. 9, pp. 2584–2586, 2015.

[94] X. Duan, C. Wang, A. Pan, R. Yu, and X. Duan, "Two-dimensional transition metal dichalcogenides as atomically thin semiconductors: opportunities and challenges," *Chemical Society Reviews*, vol. 44, no. 24, pp. 8859–8876, 2015.

[95] D. Akinwande, N. Petrone, and J. Hone, "Two-dimensional flexible nanoelectronics," *Nature communications*, vol. 5, p. 5678, 2014.

[96] H. Huang, X. Fan, D. J. Singh, and W. Zheng, "Recent progress of tmd nanomaterials: phase transitions and applications," *Nanoscale*, vol. 12, no. 3, pp. 1247–1268, 2020.

[97] Z. Li, X. Meng, and Z. Zhang, "Recent development on mos2-based photocatalysis: A review," *Journal of Photochemistry and Photobiology C: Photochemistry Reviews*, vol. 35, pp. 39–55, 2018.

[98] J. Nieminen, S. Dhara, W.-C. Chiu, E. R. Mucciolo, and A. Bansil, "Atomistic modeling of a superconductor–transition metal dichalcogenide–superconductor josephson junction," *Physical Review B*, vol. 107, no. 17, p. 174524, 2023.

[99] J. H. Garcia, J. You, M. García-Mota, P. Koval, P. Ordejón, R. Cuadrado, M. J. Verstraete, Z. Zanolli, and S. Roche, "Electrical control of spin-polarized topological currents in monolayer wte 2," *Physical Review B*, vol. 106, no. 16, p. L161410, 2022.

[100] F. Xia, H. Wang, D. Xiao, M. Dubey, and A. Ramasubramaniam, "Two-dimensional material nanophotonics," *Nature Photonics*, vol. 8, no. 12, p. 899, 2014.

[101] Z. Zheng, M. Cox, and B. Li, "Surface modification of hexagonal boron nitride nanomaterials: a review," *Journal of Materials Science*, vol. 53, no. 1, pp. 66–99, 2018.

[102] Z.-Q. Wang, T.-Y. Lü, H.-Q. Wang, Y. P. Feng, and J.-C. Zheng, "Review of borophene and its potential applications," *Frontiers of Physics*, vol. 14, no. 3, p. 33403, 2019.

[103] A. Carvalho, M. Wang, X. Zhu, A. S. Rodin, H. Su, and A. H. C. Neto, "Phosphorene: from theory to applications," *Nature Reviews Materials*, vol. 1, no. 11, pp. 1–16, 2016.

[104] M. Houssa, A. Dimoulas, and A. Molle, "Silicene: a review of recent experimental and theoretical investigations," *Journal of Physics: Condensed Matter*, vol. 27, no. 25, p. 253002, 2015.

[105] A. Acun, L. Zhang, P. Bampoulis, M. Farmanbar, A. van Houselt, A. Rudenko, M. Lingenfelder, G. Brocks, B. Poelsema, M. Katsnelson, *et al.*, "Germanene: the germanium analogue of graphene," *Journal of physics: Condensed matter*, vol. 27, no. 44, p. 443002, 2015.

[106] M. Khazaei, A. Ranjbar, M. Arai, T. Sasaki, and S. Yunoki, "Electronic properties and applications of mxenes: a theoretical review," *Journal of Materials Chemistry C*, vol. 5, no. 10, pp. 2488–2503, 2017.

[107] H. Li, S. Wang, H. Sawada, G. G. Han, T. Samuels, C. S. Allen, A. I. Kirkland, J. C. Grossman, and J. H. Warner, "Atomic structure and dynamics of single platinum atom interactions with monolayer mos2," *ACS nano*, vol. 11, no. 3, pp. 3392–3403, 2017.

[108] H. Li, J. Wu, Z. Yin, and H. Zhang, "Preparation and applications of mechanically exfoliated single-layer and multilayer mos2 and wse2 nanosheets," *Accounts of chemical research*, vol. 47, no. 4, pp. 1067–1075, 2014.

[109] N. Liu, P. Kim, J. H. Kim, J. H. Ye, S. Kim, and C. J. Lee, "Large-area atomically thin mos2 nanosheets prepared using electrochemical exfoliation," *ACS nano*, vol. 8, no. 7, pp. 6902–6910, 2014.

[110] Y.-H. Lee, X.-Q. Zhang, W. Zhang, M.-T. Chang, C.-T. Lin, K.-D. Chang, Y.-C. Yu, J. T.-W. Wang, C.-S. Chang, L.-J. Li, *et al.*, "Synthesis of large-area mos2 atomic layers with chemical vapor deposition," *arXiv preprint arXiv:1202.5458*, 2012.

[111] J. Jeon, S. K. Jang, S. M. Jeon, G. Yoo, Y. H. Jang, J.-H. Park, and S. Lee, "Layer-controlled cvd growth of large-area two-dimensional mos 2 films," *Nanoscale*, vol. 7, no. 5, pp. 1688–1695, 2015.

[112] K. F. Mak, C. Lee, J. Hone, J. Shan, and T. F. Heinz, "Atomically thin mos 2: a new direct-gap semiconductor," *Physical review letters*, vol. 105, no. 13, p. 136805, 2010.

[113] S. Tongay, H. Sahin, C. Ko, A. Luce, W. Fan, K. Liu, J. Zhou, Y.-S. Huang, C.-H. Ho, J. Yan, *et al.*, "Monolayer behaviour in bulk res 2 due to electronic and vibrational decoupling," *Nature communications*, vol. 5, p. 3252, 2014.

[114] Q. H. Wang, K. Kalantar-Zadeh, A. Kis, J. N. Coleman, and M. S. Strano, "Electronics and optoelectronics of two-dimensional transition metal dichalcogenides," *Nature nanotechnology*, vol. 7, no. 11, p. 699, 2012.

[115] H.-M. Li, D. Lee, D. Qu, X. Liu, J. Ryu, A. Seabaugh, and W. J. Yoo, "Ultimate thin vertical p–n junction composed of two-dimensional layered molybdenum disulfide," *Nature communications*, vol. 6, no. 1, pp. 1–9, 2015.

[116] W. Xin-Ran, S. Yi, and Z. Rong, "Field-effect transistors based on two-dimensional materials for logic applications," *Chinese Physics B*, vol. 22, no. 9, p. 098505, 2013.

[117] B. Radisavljevic, A. Radenovic, J. Brivio, V. Giacometti, and A. Kis, "Single-layer mos 2 transistors," *Nature nanotechnology*, vol. 6, no. 3, p. 147, 2011.

[118] K. F. Mak and J. Shan, "Photonics and optoelectronics of 2d semiconductor transition metal dichalcogenides," *Nature Photonics*, vol. 10, no. 4, p. 216, 2016.

[119] A. Splendiani, L. Sun, Y. Zhang, T. Li, J. Kim, C.-Y. Chim, G. Galli, and F. Wang, "Emerging photoluminescence in monolayer mos2," *Nano letters*, vol. 10, no. 4, pp. 1271–1275, 2010.

[120] T. Sohier, P. M. de Melo, Z. Zanolli, and M. J. Verstraete, "The impact of valley profile on the mobility and kerr rotation of transition metal dichalcogenides," *2D Materials*, vol. 10, no. 2, p. 025006, 2023.

[121] H. Zeng and X. Cui, "An optical spectroscopic study on two-dimensional group-vi transition metal dichalcogenides," *Chemical Society Reviews*, vol. 44, no. 9, pp. 2629–2642, 2015.

[122] G.-B. Liu, D. Xiao, Y. Yao, X. Xu, and W. Yao, "Electronic structures and theoretical modelling of two-dimensional group-vib transition metal dichalcogenides," *Chemical Society Reviews*, vol. 44, no. 9, pp. 2643–2663, 2015.

[123] S. A. Vitale, D. Nezich, J. O. Varghese, P. Kim, N. Gedik, P. Jarillo-Herrero, D. Xiao, and M. Rothschild, "Valleytronics: Opportunities, challenges, and paths forward," *Small*, vol. 14, no. 38, p. 1801483, 2018.

[124] X. Zhang, X.-F. Qiao, W. Shi, J.-B. Wu, D.-S. Jiang, and P.-H. Tan, "Phonon and raman scattering of two-dimensional transition metal dichalcogenides from monolayer, multilayer to bulk material," *Chemical Society Reviews*, vol. 44, no. 9, pp. 2757–2785, 2015.

[125] Y. Chen, C. Tan, H. Zhang, and L. Wang, "Two-dimensional graphene analogues for biomedical applications," *Chemical Society Reviews*, vol. 44, no. 9, pp. 2681–2701, 2015.

[126] S. Varghese, S. Varghese, S. Swaminathan, K. Singh, and V. Mittal, "Two-dimensional materials for sensing: graphene and beyond," *Electronics*, vol. 4, no. 3, pp. 651–687, 2015.

[127] C. Tan, Z. Liu, W. Huang, and H. Zhang, "Non-volatile resistive memory devices based on solution-processed ultrathin two-dimensional nanomaterials," *Chemical society reviews*, vol. 44, no. 9, pp. 2615–2628, 2015.

[128] H. Wang, H. Yuan, S. S. Hong, Y. Li, and Y. Cui, "Physical and chemical tuning of two-dimensional transition metal dichalcogenides," *Chemical Society Reviews*, vol. 44, no. 9, pp. 2664–2680, 2015.

[129] C. Tan and H. Zhang, "Two-dimensional transition metal dichalcogenide nanosheet-based composites," *Chemical Society Reviews*, vol. 44, no. 9, pp. 2713–2731, 2015.

[130] Q. Ji, Y. Zhang, Y. Zhang, and Z. Liu, "Chemical vapour deposition of group-vib metal dichalcogenide monolayers: engineered substrates from

amorphous to single crystalline," *Chemical Society Reviews*, vol. 44, no. 9, pp. 2587–2602, 2015.

[131] Y. Shi, H. Li, and L.-J. Li, "Recent advances in controlled synthesis of two-dimensional transition metal dichalcogenides via vapour deposition techniques," *Chemical Society Reviews*, vol. 44, no. 9, pp. 2744–2756, 2015.

[132] D. Wang, W. Zhou, R. Zhang, J. Zeng, Y. Du, S. Qi, C. Cong, C. Ding, X. Huang, G. Wen, *et al.*, "Mass production of large-sized, nonlayered 2d nanosheets: Their directed synthesis by a rapid "gel-blowing" strategy, and applications in li/na storage and catalysis," *Advanced Materials*, vol. 30, no. 43, p. 1803569, 2018.

[133] C. Zhang, J. Tan, Y. Pan, X. Cai, X. Zou, H.-M. Cheng, and B. Liu, "Mass production of 2d materials by intermediate-assisted grinding exfoliation," *National Science Review*, vol. 7, no. 2, pp. 324–332, 2020.

[134] M. S. Sokolikova and C. Mattevi, "Direct synthesis of metastable phases of 2d transition metal dichalcogenides," *Chemical Society Reviews*, vol. 49, no. 12, pp. 3952–3980, 2020.

[135] B. Zhao, D. Shen, Z. Zhang, P. Lu, M. Hossain, J. Li, B. Li, and X. Duan, "2d metallic transition-metal dichalcogenides: structures, synthesis, properties, and applications," *Advanced Functional Materials*, vol. 31, no. 48, p. 2105132, 2021.

[136] K. Lasek, J. Li, S. Kolekar, P. M. Coelho, M. Zhang, Z. Wang, M. Batzill, *et al.*, "Synthesis and characterization of 2d transition metal dichalcogenides: Recent progress from a vacuum surface science perspective," *Surface Science Reports*, vol. 76, no. 2, p. 100523, 2021.

[137] X. Li and H. Zhu, "Two-dimensional mos2: Properties, preparation, and applications," *Journal of Materiomics*, vol. 1, no. 1, pp. 33–44, 2015.

[138] A. N. Enyashin, M. Bar-Sadan, L. Houben, and G. Seifert, "Line defects in molybdenum disulfide layers," *The Journal of Physical Chemistry C*, vol. 117, no. 20, pp. 10842–10848, 2013.

[139] U. Krishnan, M. Kaur, K. Singh, M. Kumar, and A. Kumar, "A synoptic review of mos2: Synthesis to applications," *Superlattices and Microstructures*, vol. 128, pp. 274–297, 2019.

[140] E. Gourmelon, O. Lignier, H. Hadouda, G. Couturier, J. Bernede, J. Tedd, J. Pouzet, and J. Salardenne, "Ms2 (m= w, mo) photosensitive thin films for solar cells," *Solar energy materials and solar cells*, vol. 46, no. 2, pp. 115–121, 1997.

[141] W. Ho, J. C. Yu, J. Lin, J. Yu, and P. Li, "Preparation and photocatalytic behavior of mos2 and ws2 nanocluster sensitized tio2," *Langmuir*, vol. 20, no. 14, pp. 5865–5869, 2004.

[142] S. Mahatha, K. Patel, and K. S. Menon, "Electronic structure investigation of mos2 and mose2 using angle-resolved photoemission spectroscopy and ab initio band structure studies," *Journal of Physics: Condensed Matter*, vol. 24, no. 47, p. 475504, 2012.

[143] C. Ataca and S. Ciraci, "Functionalization of single-layer mos2 honeycomb structures," *The Journal of Physical Chemistry C*, vol. 115, no. 27, pp. 13303–13311, 2011.

[144] E. Cappelluti, R. Roldán, J. Silva-Guillén, P. Ordejón, and F. Guinea, "Tight-binding model and direct-gap/indirect-gap transition in single-layer and multilayer mos 2," *Physical Review B*, vol. 88, no. 7, p. 075409, 2013.

[145] R. Roldán, M. P. López-Sancho, F. Guinea, E. Cappelluti, J. Silva-Guillén, and P. Ordejón, "Momentum dependence of spin–orbit interaction effects in single-layer and multi-layer transition metal dichalcogenides," *2D Materials*, vol. 1, no. 3, p. 034003, 2014.

[146] W. Feng, Y. Yao, W. Zhu, J. Zhou, W. Yao, and D. Xiao, "Intrinsic spin hall effect in monolayers of group-vi dichalcogenides: A first-principles study," *Physical Review B*, vol. 86, no. 16, p. 165108, 2012.

[147] W.-Y. Shan, H.-Z. Lu, and D. Xiao, "Spin hall effect in spin-valley coupled monolayers of transition metal dichalcogenides," *Physical Review B*, vol. 88, no. 12, p. 125301, 2013.

[148] C. Patterson, "Role of defects in ferromagnetism in zn 1- x co x o: A hybrid density-functional study," *Physical Review B—Condensed Matter and Materials Physics*, vol. 74, no. 14, p. 144432, 2006.

[149] D. Mogilevtsev, F. Pinheiro, R. Dos Santos, S. Cavalcanti, and L. Oliveira, "Light propagation and anderson localization in disordered superlattices containing dispersive metamaterials: effects of correlated disorder," *Physical Review B—Condensed Matter and Materials Physics*, vol. 84, no. 9, p. 094204, 2011.

[150] J. Yang, F. Bussolotti, H. Kawai, and K. E. J. Goh, "Tuning conductivity type in monolayer ws2 and mos2 by sulfur vacancies," *physica status solidi (RRL)–Rapid Research Letters*, 2020.

[151] D. Liu, Y. Guo, L. Fang, and J. Robertson, "Sulfur vacancies in monolayer mos2 and its electrical contacts," *Applied Physics Letters*, vol. 103, no. 18, p. 183113, 2013.

[152] Y. Zhou, P. Yang, H. Zu, F. Gao, and X. Zu, "Electronic structures and magnetic properties of mos 2 nanostructures: atomic defects, nanoholes, nanodots and antidots," *Physical Chemistry Chemical Physics*, vol. 15, no. 25, pp. 10385–10394, 2013.

[153] Y. Ma, Y. Dai, M. Guo, C. Niu, J. Lu, and B. Huang, "Electronic and magnetic properties of perfect, vacancy-doped, and nonmetal adsorbed mose 2, mote 2 and ws 2 monolayers," *Physical Chemistry Chemical Physics*, vol. 13, no. 34, pp. 15546–15553, 2011.

[154] D. Yang, X. Fan, F. Zhang, Y. Hu, and Z. Luo, "Electronic and magnetic properties of defected monolayer wse 2 with vacancies," *Nanoscale research letters*, vol. 14, no. 1, pp. 1–9, 2019.

[155] Z. Lin, B. R. Carvalho, E. Kahn, R. Lv, R. Rao, H. Terrones, M. A. Pimenta, and M. Terrones, "Defect engineering of two-dimensional transition metal dichalcogenides," *2D Materials*, vol. 3, p. 022002, Apr. 2016.

[156] B. Schuler, D. Y. Qiu, S. Refaely-Abramson, C. Kastl, C. T. Chen, S. Barja, R. J. Koch, D. F. Ogletree, S. Aloni, A. M. Schwartzberg, *et al.*, "Large spin-orbit splitting of deep in-gap defect states of engineered

sulfur vacancies in monolayer ws 2," *Physical review letters*, vol. 123, no. 7, p. 076801, 2019.

[157] Q. Liang, Q. Zhang, X. Zhao, M. Liu, and A. T. Wee, "Defect engineering of two-dimensional transition-metal dichalcogenides: applications, challenges, and opportunities," *ACS nano*, vol. 15, no. 2, pp. 2165–2181, 2021.

[158] E. Mitterreiter, B. Schuler, A. Micevic, D. Hernangómez-Pérez, K. Barthelmi, K. A. Cochrane, J. Kiemle, F. Sigger, J. Klein, E. Wong, *et al.*, "The role of chalcogen vacancies for atomic defect emission in mos2," *Nature communications*, vol. 12, no. 1, p. 3822, 2021.

[159] M. Ghorbani-Asl, A. N. Enyashin, A. Kuc, G. Seifert, and T. Heine, "Defect-induced conductivity anisotropy in mos 2 monolayers," *Physical Review B*, vol. 88, no. 24, p. 245440, 2013.

[160] S. Tongay, J. Suh, C. Ataca, W. Fan, A. Luce, J. S. Kang, J. Liu, C. Ko, R. Raghunathanan, J. Zhou, *et al.*, "Defects activated photoluminescence in two-dimensional semiconductors: interplay between bound, charged and free excitons," *Scientific reports*, vol. 3, no. 1, pp. 1–5, 2013.

[161] X. Wang, J. Wu, Y. Zhang, Y. Sun, K. Ma, Y. Xie, W. Zheng, Z. Tian, Z. Kang, and Y. Zhang, "Vacancy defects in 2d transition metal dichalcogenide electrocatalysts: From aggregated to atomic configuration," *Advanced Materials*, vol. 35, no. 50, p. 2206576, 2023.

[162] H. Zhu, Q. Wang, L. Cheng, R. Addou, J. Kim, M. J. Kim, and R. M. Wallace, "Defects and surface structural stability of mote2 under vacuum annealing," *Acs Nano*, vol. 11, no. 11, pp. 11005–11014, 2017.

[163] R. Walker, T. Shi, E. Silva, I. Jovanovic, and J. Robinson, "Radiation effects on two-dimensional materials," *physica status solidi (a)*, vol. 213, no. 12, pp. 3065–3077, 2016.

[164] M. Schleberger and J. Kotakoski, "2d material science: Defect engineering by particle irradiation," *Materials*, vol. 11, no. 10, p. 1885, 2018.

[165] H.-P. Komsa, J. Kotakoski, S. Kurasch, O. Lehtinen, U. Kaiser, and A. V. Krasheninnikov, "Two-dimensional transition metal dichalcogenides un-

der electron irradiation: defect production and doping," *Physical review letters*, vol. 109, no. 3, p. 035503, 2012.

[166] S. Kretschmer, H.-P. Komsa, P. Bøggild, and A. V. Krasheninnikov, "Structural transformations in two-dimensional transition-metal dichalcogenide mos2 under an electron beam: insights from first-principles calculations," *The Journal of Physical Chemistry Letters*, vol. 8, no. 13, pp. 3061–3067, 2017.

[167] Y. Guo, D. Liu, and J. Robertson, "Chalcogen vacancies in monolayer transition metal dichalcogenides and fermi level pinning at contacts," *Applied Physics Letters*, vol. 106, no. 17, 2015.

[168] P. Vancsó, G. Z. Magda, J. Pető, J.-Y. Noh, Y.-S. Kim, C. Hwang, L. P. Biró, and L. Tapasztó, "The intrinsic defect structure of exfoliated mos 2 single layers revealed by scanning tunneling microscopy," *Scientific reports*, vol. 6, p. 29726, 2016.

[169] L. Xie, "Two-dimensional transition metal dichalcogenide alloys: preparation, characterization and applications," *Nanoscale*, vol. 7, no. 44, pp. 18392–18401, 2015.

[170] H. Li, C. Yoo, T.-J. Ko, J. H. Kim, and Y. Jung, "Atomic-scale characterization of structural heterogeny in 2d tmd layers," *Materials Advances*, vol. 3, no. 3, pp. 1401–1414, 2022.

[171] R. Saito, Y. Tatsumi, S. Huang, X. Ling, and M. Dresselhaus, "Raman spectroscopy of transition metal dichalcogenides," *Journal of Physics: Condensed Matter*, vol. 28, no. 35, p. 353002, 2016.

[172] X. Zhang, Q.-H. Tan, J.-B. Wu, W. Shi, and P.-H. Tan, "Review on the raman spectroscopy of different types of layered materials," *Nanoscale*, vol. 8, no. 12, pp. 6435–6450, 2016.

[173] W. Shi, M.-L. Lin, Q.-H. Tan, X.-F. Qiao, J. Zhang, and P.-H. Tan, "Raman and photoluminescence spectra of two-dimensional nanocrystallites of monolayer ws2 and wse2," *2D Materials*, vol. 3, no. 2, p. 025016, 2016.

[174] S. Yuan, R. Roldán, M. Katsnelson, and F. Guinea, "Effect of point defects on the optical and transport properties of mos 2 and ws 2," *Physical Review B*, vol. 90, no. 4, p. 041402, 2014.

[175] S. M. João, M. Anđelković, L. Covaci, T. G. Rappoport, J. M. Lopes, and A. Ferreira, "Kite: high-performance accurate modelling of electronic structure and response functions of large molecules, disordered crystals and heterostructures," *Royal Society Open Science*, vol. 7, no. 2, p. 191809, 2020.

[176] S. M. João, J. V. P. Lopes, and A. Ferreira, "High-resolution real-space evaluation of the self-energy operator of disordered lattices: Gade singularity, spin–orbit effects and p-wave superconductivity," *Journal of Physics: Materials*, vol. 5, no. 4, p. 045002, 2022.

[177] H. Veiga, S. João, J. Pinho, J. Pires, and J. Lopes, "Unambiguous simulation of diffusive charge transport in disordered nanoribbons," *arXiv preprint arXiv:2311.03983*, 2023.

[178] P. Giannozzi, S. Baroni, N. Bonini, M. Calandra, R. Car, C. Cavazzoni, D. Ceresoli, G. L. Chiarotti, M. Cococcioni, I. Dabo, A. Dal Corso, S. de Gironcoli, S. Fabris, G. Fratesi, R. Gebauer, U. Gerstmann, C. Gougoussis, A. Kokalj, M. Lazzeri, L. Martin-Samos, N. Marzari, F. Mauri, R. Mazzarello, S. Paolini, A. Pasquarello, L. Paulatto, C. Sbraccia, S. Scandolo, G. Sclauzero, A. P. Seitsonen, A. Smogunov, P. Umari, and R. M. Wentzcovitch, "QUANTUM ESPRESSO: a modular and open-source software project for quantum simulations of materials," *Journal of Physics: Condensed Matter*, vol. 21, no. 39, p. 395502, 2009.

[179] D. R. Hamann, "Optimized norm-conserving Vanderbilt pseudopotentials," *Physical Review B*, vol. 88, p. 085117, aug 2013.

[180] M. van Setten, M. Giantomassi, E. Bousquet, M. Verstraete, D. Hamann, X. Gonze, and G.-M. Rignanese, "The PseudoDojo: Training and grading a 85 element optimized norm-conserving pseudopotential table," *Computer Physics Communications*, vol. 226, pp. 39–54, may 2018.

[181] G. Pizzi, V. Vitale, R. Arita, S. Blügel, F. Freimuth, G. Géranton, M. Gibertini, D. Gresch, C. Johnson, T. Koretsune, J. Ibañez-Azpiroz, H. Lee, J. M. Lihm, D. Marchand, A. Marrazzo, Y. Mokrousov, J. I. Mustafa, Y. Nohara, Y. Nomura, L. Paulatto, S. Poncé, T. Ponweiser, J. Qiao, F. Thöle, S. S. Tsirkin, M. Wierzbowska, N. Marzari, D. Vanderbilt, I. Souza, A. A. Mostofi, and J. R. Yates, "Wannier90 as

a community code: New features and applications," *J. Phys. Condens. Matter*, vol. 32, no. 16, 2020.

[182] G. Pizzi, V. Vitale, R. Arita, S. Bluegel, F. Freimuth, G. Géranton, M. Gibertini, D. Gresch, C. Johnson, T. Koretsune, J. Ibanez, H. Lee, J.-M. Lihm, D. Marchand, A. Marrazzo, Y. Mokrousov, J. I. Mustafa, Y. Nohara, Y. Nomura, L. Paulatto, S. Ponce, T. Ponweiser, J. Qiao, F. Thöle, S. S. Tsirkin, M. Wierzbowska, N. Marzari, D. Vanderbilt, I. Souza, A. A. Mostofi, and J. R. Yates, "Wannier90 as a community code: new features and applications," *Journal of Physics: Condensed Matter*, 2019.

[183] A. Molina-Sánchez, K. Hummer, and L. Wirtz, "Vibrational and optical properties of mos2: From monolayer to bulk," *Surface Science Reports*, vol. 70, no. 4, pp. 554 – 586, 2015.

[184] D. Vanderbilt, *The PythTB Package*, p. 327–362. Cambridge University Press, 2018.

[185] L. M. Canonico, T. P. Cysne, A. Molina-Sanchez, R. Muniz, and T. G. Rappoport, "Orbital hall insulating phase in transition metal dichalcogenide monolayers," *Physical Review B*, vol. 101, no. 16, p. 161409, 2020.

[186] E. Cappelluti, R. Roldán, J. A. Silva-Guillén, P. Ordejón, and F. Guinea, "Tight-binding model and direct-gap/indirect-gap transition in single-layer and multilayer mos_2," *Phys. Rev. B*, vol. 88, p. 075409, Aug 2013.

[187] S. Yuan, R. Roldán, M. I. Katsnelson, and F. Guinea, "Effect of point defects on the optical and transport properties of mos_2 and ws_2," *Phys. Rev. B*, vol. 90, p. 041402, Jul 2014.

[188] E. Ridolfi, D. Le, T. S. Rahman, E. R. Mucciolo, and C. H. Lewenkopf, "A tight-binding model for MoS2monolayers," *Journal of Physics: Condensed Matter*, vol. 27, p. 365501, Aug. 2015.

[189] S. Fang, R. Kuate Defo, S. N. Shirodkar, S. Lieu, G. A. Tritsaris, and E. Kaxiras, "Ab initio tight-binding hamiltonian for transition metal dichalcogenides," *Phys. Rev. B*, vol. 92, p. 205108, Nov 2015.

[190] S. M. João, M. Andelkovic, L. Covaci, T. G. Rappoport, J. M. V. P. Lopes, and A. Ferreira, "KITE: high-performance accurate modelling of electronic structure and response functions of large molecules, disordered crystals and heterostructures," *Royal Society Open Science*, vol. 7, p. 191809, Feb. 2020.

[191] Z. Fan, J. H. Garcia, A. W. Cummings, J. E. Barrios-Vargas, M. Panhans, A. Harju, F. Ortmann, and S. Roche, "Linear scaling quantum transport methodologies," *arXiv preprint arXiv:1811.07387*, 2018.

[192] J. H. García, B. Uchoa, L. Covaci, and T. G. Rappoport, "Adatoms and anderson localization in graphene," *Phys. Rev. B*, vol. 90, p. 085425, Aug 2014.

[193] L. M. Canonico, T. G. Rappoport, and R. B. Muniz, "Spin and charge transport of multiorbital quantum spin hall insulators," *Phys. Rev. Lett.*, vol. 122, p. 196601, May 2019.

[194] S. M. João and J. M. V. P. Lopes, "Basis-independent spectral methods for non-linear optical response in arbitrary tight-binding models," *Journal of Physics: Condensed Matter*, vol. 32, p. 125901, Dec. 2019.

[195] J. Silva-Guillén, P. San-Jose, and R. Roldán, "Electronic band structure of transition metal dichalcogenides from ab initio and slater–koster tight-binding model," *Applied Sciences*, vol. 6, p. 284, Oct. 2016.

[196] Z. Li and J. P. Carbotte, "Longitudinal and spin-valley hall optical conductivity in single layer mos_2," *Phys. Rev. B*, vol. 86, p. 205425, Nov 2012.

[197] S. Mouri, Y. Miyauchi, and K. Matsuda, "Tunable photoluminescence of monolayer mos2 via chemical doping," *Nano letters*, vol. 13, no. 12, pp. 5944–5948, 2013.

[198] M. Ementchouk, M. Khan, and M. N. Leuenberger, "Optical signatures of states bound to vacancy defects in monolayer mos 2," *Physical Review B*, vol. 92, no. 12, p. 121401, 2015.

[199] A. Hötger, T. Amit, J. Klein, K. Barthelmi, T. Pelini, A. Delhomme, S. Rey, M. Potemski, C. Faugeras, G. Cohen, *et al.*, "Spin-defect charac-

teristics of single sulfur vacancies in monolayer mos2," *npj 2D Materials and Applications*, vol. 7, no. 1, p. 30, 2023.

[200] D. S. Schulman, A. J. Arnold, and S. Das, "Contact engineering for 2d materials and devices," *Chemical Society Reviews*, vol. 47, pp. 3037–3058, 2018.

[201] J. Hong, Z. Hu, M. Probert, K. Li, D. Lv, X. Yang, L. Gu, N. Mao, Q. Feng, L. Xie, *et al.*, "Exploring atomic defects in molybdenum disulphide monolayers," *Nature communications*, vol. 6, no. 1, p. 6293, 2015.

[202] S. M. Gali, A. Pershin, A. Lherbier, J.-C. Charlier, and D. Beljonne, "Electronic and transport properties in defective mos2: impact of sulfur vacancies," *The Journal of Physical Chemistry C*, vol. 124, no. 28, pp. 15076–15084, 2020.

[203] S. Roy, W. Choi, S. Jeon, D.-H. Kim, H. Kim, S. J. Yun, Y. Lee, J. Lee, Y.-M. Kim, and J. Kim, "Atomic observation of filling vacancies in monolayer transition metal sulfides by chemically sourced sulfur atoms," *Nano Letters*, vol. 18, no. 7, pp. 4523–4530, 2018.

[204] S. Datta, *Electronic Transport in Mesoscopic Systems*. Cambridge: Cambridge University Press, 1995.

[205] A. Mikhailiuk and A. Faul, "Deep learning applied to seismic data interpolation," in *80th EAGE Conference and Exhibition 2018*, vol. 2018, pp. 1–5, European Association of Geoscientists & Engineers, 2018.

[206] A. Lopez-Bezanilla and O. A. von Lilienfeld, "Modeling electronic quantum transport with machine learning," *Phys. Rev. B*, vol. 89, p. 235411, Jun 2014.

[207] D. Voiry, A. Goswami, R. Kappera, C. d. C. C. e. Silva, D. Kaplan, T. Fujita, M. Chen, T. Asefa, and M. Chhowalla, "Covalent functionalization of monolayered transition metal dichalcogenides by phase engineering," *Nature chemistry*, vol. 7, no. 1, pp. 45–49, 2015.

[208] Q. Ding, K. J. Czech, Y. Zhao, J. Zhai, R. J. Hamers, J. C. Wright, and S. Jin, "Basal-plane ligand functionalization on semiconducting 2h-mos2 monolayers," *ACS applied materials & interfaces*, vol. 9, no. 14, pp. 12734–12742, 2017.

[209] N. Martín, N. Tagmatarchis, Q. H. Wang, and X. Zhang, "Chemical functionalization of 2d materials," 2020.

[210] L. Ries, E. Petit, T. Michel, C. C. Diogo, C. Gervais, C. Salameh, M. Bechelany, S. Balme, P. Miele, N. Onofrio, *et al.*, "Enhanced sieving from exfoliated mos2 membranes via covalent functionalization," *Nature Materials*, vol. 18, no. 10, pp. 1112–1117, 2019.

[211] W. Yin, L. Yan, J. Yu, G. Tian, L. Zhou, X. Zheng, X. Zhang, Y. Yong, J. Li, Z. Gu, *et al.*, "High-throughput synthesis of single-layer mos2 nanosheets as a near-infrared photothermal-triggered drug delivery for effective cancer therapy," *ACS nano*, vol. 8, no. 7, pp. 6922–6933, 2014.

[212] S. W. Han, G.-B. Cha, Y. Park, and S. Hong, "Hydrogen physisorption based on the dissociative hydrogen chemisorption at the sulphur vacancy of mos2 surface," *Scientific reports*, vol. 7, no. 1, p. 7152, 2017.

[213] S. S. Chou, Y.-K. Huang, J. Kim, B. Kaehr, B. M. Foley, P. Lu, C. Dykstra, P. E. Hopkins, C. J. Brinker, J. Huang, *et al.*, "Controlling the metal to semiconductor transition of mos2 and ws2 in solution," *Journal of the American Chemical Society*, vol. 137, no. 5, pp. 1742–1745, 2015.

[214] L. David, R. Bhandavat, U. Barrera, and G. Singh, "Polymer-derived ceramic functionalized mos2 composite paper as a stable lithium-ion battery electrode," *Scientific reports*, vol. 5, no. 1, p. 9792, 2015.

[215] E. P. Nguyen, B. J. Carey, J. Z. Ou, J. Van Embden, E. D. Gaspera, A. F. Chrimes, M. Spencer, S. Zhuiykov, K. Kalantar-Zadeh, and T. Daeneke, "Electronic tuning of 2d mos2 through surface functionalization.," *Advanced Materials (Deerfield Beach, Fla.)*, vol. 27, no. 40, pp. 6225–6229, 2015.

[216] A. Stergiou and N. Tagmatarchis, "Molecular functionalization of two-dimensional mos2 nanosheets," *Chemistry–A European Journal*, vol. 24, no. 69, pp. 18246–18257, 2018.

[217] W. Zhou, H. Gong, X. Jin, Y. Chen, H. Li, and S. Liu, "Recent progress of two-dimensional transition metal dichalcogenides for thermoelectric applications," *Frontiers in Physics*, vol. 10, p. 842789, 2022.

[218] T. N. Nguyen Le, K. Kondratenko, I. Arbouch, A. Moreac, J.-C. L. Breton, C. van Dyck, J. Cornil, D. Vuillaume, and B. Fabre, "Electronic properties of electroactive ferrocenyl-functionalized mos2," *The Journal of Physical Chemistry C*, 2024.

[219] S. Presolski and M. Pumera, "Covalent functionalization of mos2," *Materials Today*, vol. 19, no. 3, pp. 140–145, 2016.

[220] D. Saha, S. Angizi, M. Darestani-Farahani, J. Dalmieda, P. R. Selvaganapathy, and P. Kruse, "Tuning the chemical and mechanical properties of conductive mos2 thin films by surface modification with aryl diazonium salts," *Langmuir*, vol. 38, no. 12, pp. 3666–3675, 2022.

[221] J. Luo, C. Shi, L. Yin, K. Gong, X. Qian, and K. Zhou, "Surface engineering and functionalization of mos2-based nanoarchitecture for constructing epoxy composites with excellent fire resistance and mechanical properties," *Applied Surface Science*, vol. 640, p. 158447, 2023.

[222] X. Chen and A. R. McDonald, "Functionalization of two-dimensional transition-metal dichalcogenides," *Advanced Materials*, vol. 28, no. 27, pp. 5738–5746, 2016.

[223] M. Chhowalla, H. S. Shin, G. Eda, L.-J. Li, K. P. Loh, and H. Zhang, "The chemistry of two-dimensional layered transition metal dichalcogenide nanosheets," *Nature chemistry*, vol. 5, no. 4, pp. 263–275, 2013.

[224] Y. Zhao, S. M. Gali, C. Wang, A. Pershin, A. Slassi, D. Beljonne, and P. Samori, "Molecular functionalization of chemically active defects in wse2 for enhanced opto-electronics," *Advanced Functional Materials*, vol. 30, no. 45, p. 2005045, 2020.

[225] M. Yarali, H. Brahmi, Z. Yan, X. Li, L. Xie, S. Chen, S. Kumar, M. Yoon, K. Xiao, and A. Mavrokefalos, "Effect of metal doping and vacancies on the thermal conductivity of monolayer molybdenum diselenide," *ACS applied materials & interfaces*, vol. 10, no. 5, pp. 4921–4928, 2018.

[226] S. Wang, A. Robertson, and J. H. Warner, "Atomic structure of defects and dopants in 2d layered transition metal dichalcogenides," *Chemical Society Reviews*, vol. 47, no. 17, pp. 6764–6794, 2018.

[227] H. Liu, D. Grasseschi, A. Dodda, K. Fujisawa, D. Olson, E. Kahn, F. Zhang, T. Zhang, Y. Lei, R. B. N. Branco, *et al.*, "Spontaneous chemical functionalization via coordination of au single atoms on monolayer mos2," *Science advances*, vol. 6, no. 49, p. eabc9308, 2020.

[228] J. M. Soler, E. Artacho, J. D. Gale, A. García, J. Junquera, P. Ordejón, and D. Sánchez-Portal, "The SIESTA method for ab initio order-N materials simulation," *J. Phys. Condens. Matter*, vol. 14, no. 11, pp. 2745–2779, 2002.

[229] D. Moldovan, M. Andelkovic, and F. Peeters, "pybinding v0.9.4: a Python package for tight- binding calculations," July 2017. This work was supported by the Flemish Science Foundation (FWO-Vl) and the Methusalem Funding of the Flemish Government.

[230] H. Sohn, C. Park, J.-M. Oh, S. W. Kang, and M.-J. Kim, "Silver nanowire networks: Mechano-electric properties and applications," *Materials*, vol. 12, no. 16, p. 2526, 2019.

[231] S. Imtiaz, I. S. Amiinu, D. Storan, N. Kapuria, H. Geaney, T. Kennedy, and K. M. Ryan, "Dense silicon nanowire networks grown on a stainless-steel fiber cloth: A flexible and robust anode for lithium-ion batteries," *Advanced Materials*, vol. 33, no. 52, p. 2105917, 2021.

[232] C. G. da Rocha, H. G. Manning, C. O'Callaghan, C. Ritter, A. T. Bellew, J. J. Boland, and M. S. Ferreira, "Ultimate conductivity performance in metallic nanowire networks," *Nanoscale*, vol. 7, no. 30, pp. 13011–13016, 2015.

[233] Q. Huang and Y. Zhu, "Patterning of metal nanowire networks: methods and applications," *ACS Applied Materials & Interfaces*, vol. 13, no. 51, pp. 60736–60762, 2021.

[234] M. Chirea, A. Freitas, B. S. Vasile, C. Ghitulica, C. M. Pereira, and F. Silva, "Gold nanowire networks: synthesis, characterization, and catalytic activity," *Langmuir*, vol. 27, no. 7, pp. 3906–3913, 2011.

[235] N. Ulrich, M. Schafer, M. Romer, S. D. Straub, S. Zhang, J. Brootz, C. Trautmann, C. Scheu, B. J. Etzold, and M. E. Toimil-Molares, "Cu nanowire networks with well-defined geometrical parameters for catalytic

electrochemical co2 reduction," *ACS Applied Nano Materials*, vol. 6, no. 6, pp. 4190–4200, 2023.

[236] I. Paulowicz, V. Hrkac, S. Kaps, V. Cretu, O. Lupan, T. Braniste, V. Duppel, I. Tiginyanu, L. Kienle, R. Adelung, *et al.*, "Three-dimensional sno2 nanowire networks for multifunctional applications: From high-temperature stretchable ceramics to ultraresponsive sensors," *Advanced Electronic Materials*, vol. 1, no. 8, p. 1500081, 2015.

[237] D.-L. Wen, P. Huang, B.-Y. Li, Y. Qiu, Y.-L. Wang, X.-R. Zhang, H.-T. Deng, and X.-S. Zhang, "Silk fibroin/ag nanowire-based multifunctional sensor for wearable self-powered wireless multi-sensing microsystems," *Nano Energy*, vol. 113, p. 108569, 2023.

[238] A. T. Bellew, A. P. Bell, E. K. McCarthy, J. A. Fairfield, and J. J. Boland, "Programmability of nanowire networks," *Nanoscale*, vol. 6, no. 16, pp. 9632–9639, 2014.

[239] R. Fang, W. Zhang, K. Ren, P. Zhang, X. Xu, Z. Wang, and D. Shang, "In-materio reservoir computing based on nanowire networks: Fundamental, progress, and perspective," *Materials Futures*, 2023.

[240] J. Liu, D. Jia, J. M. Gardner, E. M. Johansson, and X. Zhang, "Metal nanowire networks: Recent advances and challenges for new generation photovoltaics," *Materials Today Energy*, vol. 13, pp. 152–185, 2019.

[241] K. Chen, B. Zhao, L. Wu, T. Hu, Y. Xiang, T. Chen, and G. Pei, "Silver nanowire networks on textured silicon as low-emissivity coatings for photovoltaic/thermal applications," *Solar Energy*, vol. 267, p. 112253, 2024.

[242] H. Lu, J. Lin, N. Wu, S. Nie, Q. Luo, C.-Q. Ma, and Z. Cui, "Inkjet printed silver nanowire network as top electrode for semi-transparent organic photovoltaic devices," *Applied Physics Letters*, vol. 106, no. 9, 2015.

[243] G. Zhou, L. Xu, G. Hu, L. Mai, and Y. Cui, "Nanowires for electrochemical energy storage," *Chemical reviews*, vol. 119, no. 20, pp. 11042–11109, 2019.

[244] D. Tan, C. Jiang, Q. Li, S. Bi, and J. Song, "Silver nanowire networks with preparations and applications: a review," *Journal of Materials Science: Materials in Electronics*, vol. 31, pp. 15669–15696, 2020.

[245] D. Langley, G. Giusti, C. Mayousse, C. Celle, D. Bellet, and J.-P. Simonato, "Flexible transparent conductive materials based on silver nanowire networks: a review," *Nanotechnology*, vol. 24, no. 45, p. 452001, 2013.

[246] H. Du, T. Wan, B. Qu, F. Cao, Q. Lin, N. Chen, X. Lin, and D. Chu, "Engineering silver nanowire networks: from transparent electrodes to resistive switching devices," *ACS Applied Materials & Interfaces*, vol. 9, no. 24, pp. 20762–20770, 2017.

[247] J. Kim, M. Kim, H. Jung, J. Park, and Y. Lee, "Ultrastable 2d material-wrapped copper nanowires for high-performance flexible and transparent energy devices," *Nano Energy*, vol. 106, p. 108067, 2023.

[248] K. Esteki, D. Curic, H. G. Manning, E. Sheerin, M. S. Ferreira, J. J. Boland, and C. G. Rocha, "Thermo-electro-optical properties of seamless metallic nanowire networks for transparent conductor applications," *Nanoscale*, vol. 15, no. 24, pp. 10394–10411, 2023.

[249] K. Esteki, H. G. Manning, E. Sheerin, M. S. Ferreira, J. J. Boland, and C. G. da Rocha, "Tuning the electro-optical properties of nanowire networks," *Nanoscale*, vol. 13, no. 36, pp. 15369–15379, 2021.

[250] P. N. Nirmalraj, A. T. Bellew, A. P. Bell, J. A. Fairfield, E. K. McCarthy, C. O'Kelly, L. F. Pereira, S. Sorel, D. Morosan, J. N. Coleman, *et al.*, "Manipulating connectivity and electrical conductivity in metallic nanowire networks," *Nano letters*, vol. 12, no. 11, pp. 5966–5971, 2012.

[251] D. S. Jeong, R. Thomas, R. Katiyar, J. Scott, H. Kohlstedt, A. Petraru, and C. S. Hwang, "Emerging memories: resistive switching mechanisms and current status," *Reports on Progress in Physics*, vol. 75, no. 7, p. 076502, 2012.

[252] G. Milano, S. Porro, I. Valov, and C. Ricciardi, "Recent developments and perspectives for memristive devices based on metal oxide nanowires," *Advanced Electronic Materials*, vol. 5, no. 9, p. 1800909, 2019.

[253] J. Resende, A. Sekkat, V. H. Nguyen, T. Chatin, C. Jiménez, M. Burriel, D. Bellet, and D. Muñoz-Rojas, "Planar and transparent memristive devices based on titanium oxide coated silver nanowire networks with tunable switching voltage," *Small*, vol. 17, no. 21, p. 2007344, 2021.

[254] L. A. Moisés and A. J. Chiquito, "Enhancing the memristive effects in sno2 nanowire networks," *Current Applied Physics*, vol. 53, pp. 165–171, 2023.

[255] D. V. Christensen, R. Dittmann, B. Linares-Barranco, A. Sebastian, M. Le Gallo, A. Redaelli, S. Slesazeck, T. Mikolajick, S. Spiga, S. Menzel, *et al.*, "2022 roadmap on neuromorphic computing and engineering," *Neuromorphic Computing and Engineering*, vol. 2, no. 2, p. 022501, 2022.

[256] Z. Kuncic and T. Nakayama, "Neuromorphic nanowire networks: principles, progress and future prospects for neuro-inspired information processing," *Advances in Physics: X*, vol. 6, no. 1, p. 1894234, 2021.

[257] Z. Kuncic, O. Kavehei, R. Zhu, A. Loeffler, K. Fu, J. Hochstetter, M. Li, J. M. Shine, A. Diaz-Alvarez, A. Stieg, *et al.*, "Neuromorphic information processing with nanowire networks," in *2020 IEEE International Symposium on Circuits and Systems (ISCAS)*, pp. 1–5, IEEE, 2020.

[258] K. Fu, R. Zhu, A. Loeffler, J. Hochstetter, A. Diaz-Alvarez, A. Stieg, J. Gimzewski, T. Nakayama, and Z. Kuncic, "Reservoir computing with neuromemristive nanowire networks," in *2020 International Joint Conference on Neural Networks (IJCNN)*, pp. 1–8, IEEE, 2020.

[259] G. Milano, G. Pedretti, K. Montano, S. Ricci, S. Hashemkhani, L. Boarino, D. Ielmini, and C. Ricciardi, "In materia reservoir computing with a fully memristive architecture based on self-organizing nanowire networks," *Nature materials*, vol. 21, no. 2, pp. 195–202, 2022.

[260] A. Loeffler, A. Diaz-Alvarez, R. Zhu, N. Ganesh, J. M. Shine, T. Nakayama, and Z. Kuncic, "Neuromorphic learning, working memory, and metaplasticity in nanowire networks," *Science Advances*, vol. 9, no. 16, p. eadg3289, 2023.

[261] R. Zhu, S. Lilak, A. Loeffler, J. Lizier, A. Stieg, J. Gimzewski, and Z. Kuncic, "Online dynamical learning and sequence memory with neu-

romorphic nanowire networks," *Nature Communications*, vol. 14, no. 1, p. 6697, 2023.

[262] L. Kanari, H. Dictus, A. Chalimourda, A. Arnaudon, W. Van Geit, B. Coste, J. Shillcock, K. Hess, and H. Markram, "Computational synthesis of cortical dendritic morphologies," *Cell Reports*, vol. 39, no. 1, 2022.

[263] N. Kriegeskorte and P. K. Douglas, "Cognitive computational neuroscience," *Nature neuroscience*, vol. 21, no. 9, pp. 1148–1160, 2018.

[264] H. Zeng and J. R. Sanes, "Neuronal cell-type classification: challenges, opportunities and the path forward," *Nature Reviews Neuroscience*, vol. 18, no. 9, pp. 530–546, 2017.

[265] H. G. Manning, F. Niosi, C. G. da Rocha, A. T. Bellew, C. O'Callaghan, S. Biswas, P. F. Flowers, B. J. Wiley, J. D. Holmes, M. S. Ferreira, and J. J. Boland, "Emergence of winner-takes-all connectivity paths in random nanowire networks," *Nature Communications*, vol. 9, no. 1, p. 3219, 2018.

[266] C. O'Callaghan, C. G. da Rocha, F. Niosi, H. G. Manning, J. J. Boland, and M. S. Ferreira, "Collective capacitive and memristive responses in random nanowire networks: Emergence of critical connectivity pathways," *Journal of Applied Physics*, vol. 124, no. 15, 2018.

[267] J. J. Wang, Q. Yu, S. G. Hu, Y. Liu, R. Guo, T. P. Chen, Y. Yin, and Y. Liu, "Winner-takes-all mechanism realized by memristive neural network," *Applied Physics Letters*, vol. 115, no. 24, 2019.

[268] Q. Li, A. Diaz-Alvarez, R. Iguchi, J. Hochstetter, A. Loeffler, R. Zhu, Y. Shingaya, Z. Kuncic, K.-i. Uchida, and T. Nakayama, "Dynamic electrical pathway tuning in neuromorphic nanowire networks," *Advanced Functional Materials*, vol. 30, no. 43, p. 2003679, 2020.

[269] D. B. Strukov, G. S. Snider, D. R. Stewart, and R. S. Williams, "The missing memristor found," *nature*, vol. 453, no. 7191, pp. 80–83, 2008.

[270] Z. Biolek, D. Biolek, and V. Biolkova, "Spice model of memristor with nonlinear dopant drift.," *Radioengineering*, vol. 18, no. 2, 2009.

[271] T. Prodromakis, B. P. Peh, C. Papavassiliou, and C. Toumazou, "A versatile memristor model with nonlinear dopant kinetics," *IEEE transactions on electron devices*, vol. 58, no. 9, pp. 3099–3105, 2011.

[272] S. Alialy, K. Esteki, M. S. Ferreira, J. J. Boland, and C. G. da Rocha, "Nonlinear ion drift-diffusion memristance description of tio 2 rram devices," *Nanoscale Advances*, vol. 2, no. 6, pp. 2514–2524, 2020.

[273] C. J. O'Callaghan, *Transport Properties of Disordered Nanowire Networks: From Conducting Thin Films to Neuromorphic Applications*. PhD thesis, Trinity College Dublin, 2018.

[274] R. K. Daniels and S. A. Brown, "Nanowire networks: how does small-world character evolve with dimensionality?," *Nanoscale Horizons*, vol. 6, no. 6, pp. 482–488, 2021.

[275] R. M. Mutiso, M. C. Sherrott, A. R. Rathmell, B. J. Wiley, and K. I. Winey, "Integrating simulations and experiments to predict sheet resistance and optical transmittance in nanowire films for transparent conductors," *ACS nano*, vol. 7, no. 9, pp. 7654–7663, 2013.

[276] D. P. Langley, M. Lagrange, N. D. Nguyen, and D. Bellet, "Percolation in networks of 1-dimensional objects: Comparison between monte carlo simulations and experimental observations," *Nanoscale Horizons*, vol. 3, no. 5, pp. 545–550, 2018.

[277] S. I. White, R. M. Mutiso, P. M. Vora, D. Jahnke, S. Hsu, J. M. Kikkawa, J. Li, J. E. Fischer, and K. I. Winey, "Electrical percolation behavior in silver nanowire–polystyrene composites: simulation and experiment," *Advanced Functional Materials*, vol. 20, no. 16, pp. 2709–2716, 2010.

[278] T. Sannicolo, D. Munoz-Rojas, N. D. Nguyen, S. Moreau, C. Celle, J.-P. Simonato, Y. Bréchet, and D. Bellet, "Direct imaging of the onset of electrical conduction in silver nanowire networks by infrared thermography: Evidence of geometrical quantized percolation," *Nano letters*, vol. 16, no. 11, pp. 7046–7053, 2016.

[279] P. Maguire, J. Jadwiszczak, M. O'Brien, D. Keane, G. S. Duesberg, N. McEvoy, and H. Zhang, "Defect-moderated oxidative etching of mos2," *Journal of Applied Physics*, vol. 126, no. 16, 2019.

[280] S. Aldana, I. Spiridon, L. Wang, and H. Zhang, "Understanding substrate effects on two-dimensional mos2 growth: a kinetic monte carlo approach," *arXiv preprint arXiv:2401.01661*, 2024.

[281] R. Toral and P. Colet, *Stochastic numerical methods: an introduction for students and scientists*. John Wiley & Sons, 2014.

[282] W. Han, R. K. Kawakami, M. Gmitra, and J. Fabian, "Graphene spintronics," *Nature nanotechnology*, vol. 9, no. 10, pp. 794–807, 2014.

[283] Y. P. Feng, L. Shen, M. Yang, A. Wang, M. Zeng, Q. Wu, S. Chintalapati, and C.-R. Chang, "Prospects of spintronics based on 2d materials," *Wiley Interdisciplinary Reviews: Computational Molecular Science*, vol. 7, no. 5, p. e1313, 2017.

[284] E. C. Ahn, "2d materials for spintronic devices," *npj 2D Materials and Applications*, vol. 4, no. 1, p. 17, 2020.

[285] A. M. Black-Schaffer, "Rkky coupling in graphene," *Physical Review B*, vol. 81, no. 20, p. 205416, 2010.

[286] E. Šimánek and B. Heinrich, "Gilbert damping in magnetic multilayers," *Physical Review B*, vol. 67, no. 14, p. 144418, 2003.

[287] F. Guimaraes, D. Kirwan, A. Costa, R. Muniz, D. Mills, and M. Ferreira, "Carbon nanotube: A low-loss spin-current waveguide," *Physical Review B*, vol. 81, no. 15, p. 153408, 2010.

[288] S. Power, F. Guimaraes, A. Costa, R. Muniz, and M. Ferreira, "Dynamic rkky interaction in graphene," *Physical Review B*, vol. 85, no. 19, p. 195411, 2012.

[289] R. Muniz and D. Mills, "Theory of spin excitations in fe (110) monolayers," *Physical Review B*, vol. 66, no. 17, p. 174417, 2002.

[290] M. Costache, S. Watts, C. Van Der Wal, and B. Van Wees, "Electrical detection of spin pumping: dc voltage generated by ferromagnetic resonance at ferromagnet/nonmagnet contact," *Physical Review B*, vol. 78, no. 6, p. 064423, 2008.

[291] N. Tombros, C. Jozsa, M. Popinciuc, H. T. Jonkman, and B. J. Van Wees, "Electronic spin transport and spin precession in single graphene layers at room temperature," *nature*, vol. 448, no. 7153, pp. 571–574, 2007.

[292] Y. Tserkovnyak, A. Brataas, G. E. Bauer, and B. I. Halperin, "Nonlocal magnetization dynamics in ferromagnetic heterostructures," *Reviews of Modern Physics*, vol. 77, no. 4, p. 1375, 2005.

[293] L. Medrano Sandonas, R. Gutierrez, A. Pecchia, A. Croy, and G. Cuniberti, "Quantum phonon transport in nanomaterials: combining atomistic with non-equilibrium green's function techniques," *Entropy*, vol. 21, no. 8, p. 735, 2019.

[294] Z. Tong, S. Li, X. Ruan, and H. Bao, "Comprehensive first-principles analysis of phonon thermal conductivity and electron-phonon coupling in different metals," *Physical review B*, vol. 100, no. 14, p. 144306, 2019.